Alma Mater Studiorum – Università di Bologna

Dottorato di ricerca in
Fisica
Ciclo XXXI

Settore Concorsuale: 02/A1
Settore Scientifico disciplinare: FIS/01

CP violation in $D^0 \to K^+K^-$ and $D^0 \to \pi^+\pi^-$ decays and lepton-flavour universality test with the decay $B^0 \to D^{*-}\tau^+\nu_\tau$

Presentata da: Federico Betti

Coordinatore Dottorato
Prof.ssa Silvia Arcelli

Supervisore
Prof. Angelo Carbone

Co-supervisore
Dott. Vincenzo Maria Vagnoni

Esame finale anno 2019

Abstract

The LHCb experiment has been designed to exploit the potential of heavy-flavour production in highly energetic pp collisions at the Large Hadron Collider, in order to look for indirect signs of physics beyond the Standard Model of particle physics. The experiment has been performing a number of measurements with a plethora of physics observables, notably including CP-violating asymmetries and lepton-flavour universality probes. This thesis presents two distinct measurements performed using LHCb data. The first is that of the ratio of branching fractions $\mathcal{R}(D^*) \equiv \mathcal{B}(B^0 \to D^{*-}\tau^+\nu_\tau)/\mathcal{B}(B^0 \to D^{*-}\ell^+\nu_\ell)$, with the τ lepton decaying to final states containing three charged pions, performed using a data sample of pp collisions at the centre-of-mass energies of 7 and 8 TeV, corresponding to $3\,\text{fb}^{-1}$ of integrated luminosity. The result is

$$\mathcal{R}(D^*) = 0.291 \pm 0.019 \pm 0.026 \pm 0.013,$$

where the first uncertainty is statistical, the second systematic and the third due to the knowledge of the $B^0 \to D^{*-}\pi^+\pi^-\pi^+$ branching fraction, as this decay is used in the analysis as a normalisation for the intermediate measurement of $\mathcal{B}(B^0 \to D^{*-}\tau^+\nu_\tau)$. This corresponds to one of the most precise single measurements of $\mathcal{R}(D^*)$ and to the first performed with the three-prong decay of the τ lepton to date. The measured value of $\mathcal{R}(D^*)$ is compatible with previous determinations and with the Standard Model expectation. The second measurement presented in this thesis is that of the difference between the CP asymmetries in $D^0 \to K^+K^-$ and $D^0 \to \pi^+\pi^-$ decays, performed using a data sample of pp collisions at the centre-of-mass energy of 13 TeV, corresponding to $6\,\text{fb}^{-1}$ of integrated luminosity. The value of $\Delta A_{CP} \equiv A_{CP}(K^+K^-) - A_{CP}(\pi^+\pi^-)$, measured by reconstructing D^0 mesons which originate from $D^{*+} \to D^0\pi^+$ decays or from $B \to D^0\mu\nu X$ decays, is

$$\Delta A_{CP} = (-17.1 \pm 3.0 \pm 1.0) \cdot 10^{-4},$$

where the first uncertainty is statistical and the second systematic. By combining this result with previous LHCb measurements based on Run-1 data, the value of ΔA_{CP} results to be

$$\Delta A_{CP} = (-15.4 \pm 2.9) \cdot 10^{-4},$$

which differs from zero by 5.3 standard deviations. This is the first observation of CP violation in the decay of a charm hadron.

Contents

Introduction

Our current knowledge of fundamental particles and interactions, excluding gravity, is described by the Standard Model (SM) of particle physics, *i.e.* a quantum-field theory which has been able to provide outstanding predictions and describe accurately a huge harvest of experimental results. However, despite its undisputable success, the SM has to be considered as an effective theory which is valid up to a certain energy scale, and not as the ultimate theory. A series of open questions needs to be answered, such as: how did antimatter particles disappear in the early universe leaving a tiny amount of residual matter particles alone? What is the nature of dark matter and dark energy, which make up 95% of the universe? How to incorporate a coherent description of gravity into a quantum-mechanical framework?

The incompleteness of the SM implies that some kind of new physics (NP) should exist above a certain energy scale, where the SM ceases to be an effective description of reality. The search for NP is the most important goal of particle physics and can be pursued directly, *e.g.* by producing possible new particles in high-energy collisions, or indirectly, *i.e.* by studying low-energy processes in which some physics observables, such as decay rates or *CP* asymmetries, might be affected by the presence of virtual particles not accounted for in the SM. Such new particles would manifest their existence by altering SM predictions of given particle properties.

The first run of the Large Hadron Collider (LHC), with 7 and 8 TeV pp collisions, led to the fundamental discovery of the Higgs boson. Although no hint of the existence of other new particles has been found yet, some anomalies have been emerging in the heavy-flavour sector, which may turn out to be indications of first cracks in the SM.

Lepton-flavour universality (LFU), *i.e.* an accidental symmetry of the SM according to which the coupling between leptons and electroweak bosons does not depend on the lepton family, implies that the observation of any effect discriminating different lepton families (besides those due to the different masses

of the leptons) would be a clear sign of NP. Recently, hints of LFU violation have been observed in measurements of branching fractions and angular observables of rare $b \to s\ell^+\ell^-$ decays [1–5], as well as in measurements of branching fractions of decays involving $b \to c\ell\nu$ transitions. In particular, the ratios of branching fractions $\mathcal{R}(D^{(*)-}) \equiv \mathcal{B}(B^0 \to D^{(*)-}\tau^+\nu_\tau)/\mathcal{B}(B^0 \to D^{(*)-}\ell^+\nu_\ell)$ and $\mathcal{R}(D^{(*)0}) \equiv \mathcal{B}(B^- \to D^{(*)0}\tau^+\nu_\tau)/\mathcal{B}(B^- \to D^{(*)0}\ell^+\nu_\ell)$ show a discrepancy between measurements and SM expectations by about 3.5 standard deviations [6].

On a different subject, measurements of observables related to the violation of the *CP* symmetry are important to understand the baryon asymmetry of the universe and to put constraints on possible NP contributions. In particular, *CP* violation in the charm sector has not been observed yet. The difference between the *CP* asymmetries in $D^0 \to K^+K^-$ and $D^0 \to \pi^+\pi^-$ decays, $\Delta A_{CP} \equiv A_{CP}(K^+K^-) - A_{CP}(\pi^+\pi^-)$, is a physics observable that is experimentally very robust against possible systematic effects, and is expected to be measured with an uncertainty approaching $\mathcal{O}(10^{-4})$ using the full data sample collected by LHCb during Run 1 and Run 2. As the SM expectation for the value of ΔA_{CP} is around $10^{-3} - 10^{-4}$ [7–10], LHCb has the potential to measure a deviation from zero in a statistically significant way.

The most recent measurements of $\mathcal{R}(D^*)$ and ΔA_{CP} performed using LHCb data are the subjects of this thesis, which is organised as follows. In Chapter 1, after a brief overview of the SM, semitauonic B decays are introduced, with a focus on the theoretical and experimental status of $\mathcal{R}(D^*)$. Then a theoretical description of *CP* violation in neutral-meson decays is given, and some emphasis is given to $D^0 \to K^+K^-$ and $D^0 \to \pi^+\pi^-$ decays, notably describing the present experimental picture. A short description of the LHC accelerator complex and the LHCb detector is given in Chapter 2. Chapter 3 is devoted to the measurement of $\mathcal{R}(D^*)$, while the measurement of ΔA_{CP} is described in Chapter 4. Finally, the results are summarised and conclusions are drawn.

Chapter 1

Theory of *CP* violation and semileptonic decays

The Glashow-Weinberg-Salam (GWS) model is a Yang-Mills non-abelian quantum field theory based on the SU(2) $\times$ U(1) gauge symmetry group, and provides a unified and experimentally established picture of electroweak interactions. The Standard Model (SM) of particle physics is obtained expanding the GWS model with the SU(3) symmetry of strong interactions and the Brout-Englert-Higgs spontaneous symmetry breaking mechanism. The SM describes all the known elementary particles (quarks, leptons, gauge and Higgs bosons) and their fundamental interactions, with the exception of gravity. The GWS model is explained in Sec. 1.1, and a brief description of the SU(3) component of the SM, *i.e.* the quantum chromodynamics Lagrangian, is given in Sec. 1.3. In Sec. 1.4 an overview of the theoretical and experimental status of lepton-universality tests in $B^0 \to D^{*-}\tau^+\nu_\tau$ decays is given, and in Sec. 1.5 the phenomenology of *CP* violation in neutral mesons is described, with a particular focus on charged two-body decays of neutral D mesons.

1.1 The Glashow-Weinberg-Salam model

The Lagrangian of the GWS model can be divided into four main terms [11–13]

$$\mathcal{L} = \mathcal{L}_B + \mathcal{L}_f + \mathcal{L}_H + \mathcal{L}_Y. \tag{1.1}$$

Here $\mathcal{L}_B$ is the kinetic term of the four gauge fields: W^a_μ (the weak isospin fields with $(a = 1, 2, 3)$) and B_μ (the hypercharge field). Denoting $W^a_{\mu\nu}$ and $B_{\mu\nu}$ as their

field strength tensors, this term is equal to

$$\mathcal{L}_B = -\frac{1}{4}W^{a\mu\nu}W^a_{\mu\nu} - \frac{1}{4}B^{\mu\nu}B_{\mu\nu}. \tag{1.2}$$

The second term describes the kinetics of the fermions and how they interact with the gauge bosons

$$\mathcal{L}_f = \overline{Q}^j i\not{D}_L Q^j + \overline{u}^j_R i\not{D}_R u^j_R + \overline{d}^j_R i\not{D}_R d^j_R + \overline{L}^j i\not{D}_L L^j + \overline{e}^j_R i\not{D}_R e^j_R, \tag{1.3}$$

where Q^j are the left-handed SU(2) quark doublets, u^j_R and d^j_R are the up and down right-handed quark singlets, while L^j are the left-handed lepton doublets and e^j_R the right-handed charged-lepton singlets. The contracted form $\not{D} = \gamma^\mu D_\mu$ is used, where γ^μ is the Dirac matrix. The explicit form of the doublets involves the left-handed fields u^j_L, d^j_L, ν^j_L and e^j_L

$$Q^j = \begin{pmatrix} u^j_L \\ d^j_L \end{pmatrix}, \tag{1.4}$$

$$L^j = \begin{pmatrix} \nu^j_L \\ e^j_L \end{pmatrix}. \tag{1.5}$$

In Eq. (1.3), a sum over j is assumed, where j is the flavour (or generation) index, which runs from 1 to 3. The presence of $D_{L\mu}$ and $D_{R\mu}$, that are the covariant derivatives for the left-handed and right-handed fermion fields, is needed to keep the Lagrangian invariant under the SU(2) × U(1) local gauge transformation. The covariant derivatives are defined differently depending on which field they are applied to

$$D_{L\mu} = \partial_\mu + igW^a_\mu \frac{\sigma^a}{2} + ig'\frac{Y}{2}B_\mu, \tag{1.6a}$$

$$D_{R\mu} = \partial_\mu + ig'\frac{Y}{2}B_\mu, \tag{1.6b}$$

where Y is the hypercharge of the field on which D_μ operates, σ^a are the Pauli matrices, g and g' are the coupling constants.

Since Q^j and L^j are SU(2) doublets, they have weak isospin $T = 1/2$, with third component $T_3 = \pm 1/2$ for up- and down-type fields, respectively. The right-handed fermion fields are SU(2) singlets, so they have $T = 0$. The electromagnetic charge Q of a field can be expressed in terms of its hypercharge Y and third component of weak isospin T_3 as

$$Q = \frac{Y}{2} + T_3. \tag{1.7}$$

Table 1.1: Third component of the weak isospin T_3, hypercharge Y and electromagnetic charge Q of leptons and quarks.

Fermion	T_3	Y	Q
u_L	$1/2$	$1/3$	$2/3$
d_L	$-1/2$	$1/3$	$-1/3$
u_R	0	$4/3$	$2/3$
d_R	0	$-2/3$	$-1/3$
ν_L	$1/2$	-1	0
e_L	$-1/2$	-1	-1
e_R	0	-2	-1

The values of the hypercharges of all fermionic doublets and singlets can therefore be obtained according to their electromagnetic charge. The values of T_3, Y and Q of the fermion fields are reported in Table 1.1.

The third term of Eq. (1.1) describes the Higgs field and its coupling with the gauge bosons [14] [15]

$$\begin{aligned}\mathcal{L}_H &= (D^\mu\phi^\dagger)(D_\mu\phi) - V(\phi^\dagger\phi) = \\ &= (D^\mu\phi^\dagger)(D_\mu\phi) - \left(-\mu^2\phi^\dagger\phi + \frac{\lambda^2}{2}(\phi^\dagger\phi)^2\right),\end{aligned} \tag{1.8}$$

where λ and μ are positive real parameters and ϕ is the SU(2) Higgs doublet with hypercharge 1

$$\phi = \begin{pmatrix}\phi^+ \\ \phi^0\end{pmatrix}, \tag{1.9}$$

with ϕ^+ and ϕ^0 electromagnetic charged and neutral complex scalar fields. Since ϕ is a SU(2) doublet with hypercharge 1, the covariant derivative that operates on it is

$$D_\mu = \partial_\mu + igW_\mu^a\frac{\sigma^a}{2} + \frac{1}{2}ig'B_\mu. \tag{1.10}$$

The Yukawa interaction between the fermion fields and ϕ, needed to generate the fermion masses, is given by the last term of Eq. (1.1)

$$\mathcal{L}_Y = -\lambda_d^{ij}\overline{Q}^i\phi d_R^j - \lambda_u^{ij}\overline{Q}^i(i\sigma^2\phi)u_R^j - g_e^i\overline{L}^i\phi e_R^i + \text{h.c.}, \tag{1.11}$$

where a sum over indices i and j is assumed, g_e^i are coupling constants and $\lambda_{d,u}^{ij}$ are general complex-valued matrices.

The Higgs potential $V(\phi^\dagger\phi)$ is at its minimum value when $\phi^\dagger\phi = \mu^2/\lambda^2 \equiv v^2/2$, where $v/\sqrt{2}$ is the vacuum expectation value (VEV) of ϕ ($v \simeq 246\,\text{GeV}$). The SU(2)

gauge invariance allows the four degrees of freedom of ϕ to be reduced to one. Hence the Higgs doublet can be written in the unitarity gauge and expanded around its own VEV

$$\phi = \frac{1}{\sqrt{2}} \begin{pmatrix} 0 \\ v + H(x) \end{pmatrix}, \tag{1.12}$$

where $H(x)$ is the Higgs field, that is scalar and real. In this way a specific direction of vacuum has been chosen, so the symmetry has been spontaneously broken and the Lagrangian is no longer SU(2) invariant.

The physical gauge fields are defined as

$$W_\mu^\pm = \frac{W_\mu^1 \mp i W_\mu^2}{\sqrt{2}}, \tag{1.13a}$$

$$Z_\mu = W_\mu^3 \cos\theta_\mathrm{W} - B_\mu \sin\theta_\mathrm{W}, \tag{1.13b}$$

$$A_\mu = W_\mu^3 \sin\theta_\mathrm{W} + B_\mu \cos\theta_\mathrm{W}, \tag{1.13c}$$

where θ_W is the Weinberg angle ($\sin^2\theta_\mathrm{W} \simeq 0.23$). The mass terms of the gauge fields are then obtained by substituting Eq. (1.12) in Eq. (1.8)

$$-\frac{1}{8} g^2 v^2 (W^{+\mu} W_\mu^+ + W^{-\mu} W_\mu^-) - \frac{1}{8} v^2 (g^2 + g'^2) Z^\mu Z_\mu - \frac{1}{2} \lambda^2 v^2 H^2. \tag{1.14}$$

From Eq. (1.14) it is apparent that the masses of the gauge and H bosons are

$$M_H = \lambda v, \tag{1.15a}$$

$$M_W = \frac{1}{2} g v, \tag{1.15b}$$

$$M_Z = \frac{1}{2} \sqrt{g^2 + g'^2}\, v, \tag{1.15c}$$

$$M_\gamma = 0. \tag{1.15d}$$

The three weak bosons acquire mass, while the photon remains massless. By substituting Eq. (1.12) in Eq. (1.11) one obtains

$$\mathcal{L}_Y = -\frac{v}{\sqrt{2}} \lambda_d^{ij} \overline{d}_L^i d_R^j - \frac{v}{\sqrt{2}} \lambda_u^{ij} \overline{u}_L^i u_R^j - \frac{v}{\sqrt{2}} g_e^i e_L^i e_R^i + \text{h.c.}, \tag{1.16}$$

i.e. the mass of e^i is equal to

$$\frac{v}{\sqrt{2}} g_e^i, \tag{1.17}$$

proportional to the coupling between the electron (muon, tau) and the Higgs boson, while the neutrinos remain massless. For a long time it was believed that neutrinos

were massless, making them very different from the other SM fermions. However, since last two decades a number of crucial observations have firmly established that neutrinos not only have mass, but also mix amongst themselves, leading to the phenomenon of neutrino oscillations [16–22]. The flavour or weak eigenstates are then related to the mass eigenstates by

$$\nu_L^i = \sum_j U_{ij} \nu_{m,L}^j, \tag{1.18}$$

where U is the neutrino mixing matrix, also called Pontecorvo-Maki-Nakagawa-Sakata (PMNS) matrix, analogous to the quark mixing matrix discussed in more detail in the coming section. This matrix characterises the weak charged current for leptons

$$\frac{g}{2\sqrt{2}} \overline{e}_L^i U_{ij} \gamma_\mu (1+\gamma_5) \nu_{m,L}^j W^{-\mu} + \text{h.c.} \tag{1.19}$$

1.2 The Cabibbo-Kobayashi-Maskawa matrix

The u^i and d^i fields are not the physical fermions seen experimentally. The mass terms for physical quarks are obtained by diagonalising the $\lambda_{u,d}$ matrices introduced in Eq. (1.11). In order to do that, unitary matrices $S_{u,d}$, $T_{u,d}$ are defined such that

$$\lambda_{u,d} \lambda_{u,d}^\dagger = S_{u,d} D_{u,d}^2 S_{u,d}^\dagger, \tag{1.20a}$$
$$\lambda_{u,d}^\dagger \lambda_{u,d} = T_{u,d} D_{u,d}^2 T_{u,d}^\dagger, \tag{1.20b}$$

where $D_{u,d}$ are diagonal matrices. This leads to

$$\lambda_{u,d} = S_{u,d} D_{u,d} T_{u,d}^\dagger. \tag{1.21}$$

The physical quark fields can now be defined in the following way

$$u_L^i = S_u^{i,j} u_L^{j,phys}, \tag{1.22a}$$
$$u_R^i = T_u^{i,j} u_R^{j,phys}, \tag{1.22b}$$
$$d_L^i = S_d^{i,j} d_L^{j,phys}, \tag{1.22c}$$
$$d_R^i = T_d^{i,j} d_R^{j,phys}, \tag{1.22d}$$

which, together with Eq. (1.21), allows one to get in Eq. (1.16) the terms

$$-\frac{v}{\sqrt{2}} D_u^{ii} \overline{u}^{i,phys} u^{i,phys} - \frac{v}{\sqrt{2}} D_d^{ii} \overline{d}^{i,phys} d^{i,phys}. \tag{1.23}$$

The quark masses are then defined as

$$m^i_{u,d} = \frac{v}{\sqrt{2}} D^{ii}_{u,d}. \tag{1.24}$$

Besides the replacement of weak eigenstates with mass eigenstates, the presence of $W_{u,d}$ and $U_{u,d}$ has an important effect in the weak charged current. It is possible to prove that in Eq. (1.3) there are the following terms

$$-\frac{g}{\sqrt{2}}\left(J^{+\mu}W^+_\mu + J^{-\mu}W^-_\mu\right) - \frac{g}{\cos\theta_{\mathrm{W}}} J^{N\mu} Z_\mu, \tag{1.25}$$

where $J^{\pm\mu}$ and $J^{N\mu}$ are the charged and neutral currents

$$J^{+\mu} = \overline{\nu}^a_L \gamma^\mu e^a_L + \overline{u}^a_L \gamma^\mu d^a_L, \tag{1.26a}$$

$$J^{-\mu} = \text{h.c.}(J^{+\mu}), \tag{1.26b}$$

$$J^{N\mu} = \sum_{a,f} \overline{f}^a \frac{\gamma^\mu}{2}\left[T_3 - (T_3 - 2\sin^2\theta_{\mathrm{W}} Q)\gamma^5\right] f^a, \tag{1.26c}$$

with f^a standing for a generic fermion (neutrino, electron, quark) of the a-th generation, Q its electromagnetic charge and T_3 its weak isospin . Using Eq. (1.22), the terms involving quarks in Eq. (1.26a) can be written as

$$\overline{u}^{i,phys}_L (S^\dagger_u S_d)^{ij} \gamma^\mu d^{j,phys}_L. \tag{1.27}$$

The matrix ($S^\dagger_u S_d \equiv V_{CKM}$) is called the Cabibbo-Kobayashi-Maskawa matrix (CKM) [23, 24].

The charged-current interaction Lagrangian for quarks can finally be written as

$$\mathcal{L}_{cc,quarks} = -\frac{g}{\sqrt{2}} \begin{pmatrix} \overline{u}_L & \overline{c}_L & \overline{t}_L \end{pmatrix} \begin{pmatrix} V_{ud} & V_{us} & V_{ub} \\ V_{cd} & V_{cs} & V_{cb} \\ V_{td} & V_{ts} & V_{tb} \end{pmatrix} \gamma^\mu \begin{pmatrix} d_L \\ s_L \\ b_L \end{pmatrix} W^+_\mu + \text{h.c.}, \tag{1.28}$$

where the spinors denote the physical quark fields. From this it is clear that the $W^\pm$ bosons mediate interactions between up-type and down-type quarks also between different families, and so the quark flavour can change in weak interactions. Every element of the CKM matrix describes the coupling strength between two different quarks, for example $|V_{tb}| \simeq 1$ and $|V_{ub}| \simeq 0.004$ means that the coupling between t and b is much stronger than that between u and b.

A complex unitary $n \times n$ matrix contains n^2 independent real parameters, of which $n(n-1)/2$ correspond to the independent rotation angles between the n basis

vectors, and the other $n(n+1)/2$ are complex phases. The phase of $2n-1$ quark fields can be redefined leaving the Lagrangian unaffected. Hence the number of physical phases is $(n-1)(n-2)/2$. For $n=2$, *i.e.* for only two families, there is one mixing angle, the Cabibbo angle, and no complex phases. The CKM matrix ($n=3$) can be instead parameterised by means of three mixing angles θ_{12}, θ_{13}, θ_{23} and a phase δ, which is responsible for *CP* violation in weak interactions, as explained in Sec. 1.5. By defining $s_{ij} \equiv \sin\theta_{ij}$ and $c_{ij} \equiv \cos\theta_{ij}$, the CKM matrix can be written as

$$V_{CKM} = \begin{pmatrix} c_{12}c_{13} & s_{12}c_{13} & s_{13}e^{-i\delta} \\ -s_{12}c_{23} - c_{12}s_{23}s_{13}e^{i\delta} & c_{12}c_{23} - s_{12}s_{23}s_{13}e^{i\delta} & s_{23}c_{13} \\ s_{12}s_{23} - c_{12}c_{23}s_{13}e^{i\delta} & -c_{12}s_{23} - s_{12}c_{23}s_{13}e^{i\delta} & c_{23}c_{13} \end{pmatrix} + \mathcal{O}(\lambda^4), \quad (1.29)$$

The strong hierarchy of the CKM matrix elements can be made explicit by adopting the parameterisation initially proposed by Wolfenstein [25], based on an expansion in terms of the four parameters λ, A, ρ and η, where the expansion parameter $\lambda \simeq 0.226$ is the sine of the Cabibbo angle

$$V_{CKM} = \begin{pmatrix} 1-\lambda^2/2 & \lambda & A\lambda^3(\rho - i\eta) \\ -\lambda & 1-\lambda^2/2 & A\lambda^2 \\ A\lambda^3(1-\rho-i\eta) & -A\lambda^2 & 1 \end{pmatrix} + \mathcal{O}(\lambda^4), \quad (1.30)$$

where

$$s_{12} = \lambda = \frac{|V_{us}|}{\sqrt{|V_{ud}|^2 + |V_{us}|^2}}, \quad (1.31a)$$

$$s_{23} = A\lambda^2 = \lambda \left| \frac{V_{cb}}{V_{us}} \right|, \quad (1.31b)$$

$$s_{13}e^{i\delta} = A\lambda^3(\rho + i\eta) = V_{ub}^*. \quad (1.31c)$$

According to the experimental measurements [26], the magnitudes of the elements of the CKM matrix are

$$\begin{pmatrix} 0.97446 \pm 0.00010 & 0.22452 \pm 0.00044 & 0.00365 \pm 0.00012 \\ 0.22438 \pm 0.00044 & 0.97359^{+0.00010}_{-0.00011} & 0.04214 \pm 0.00076 \\ 0.00896^{+0.00024}_{-0.00023} & 0.04133 \pm 0.00074 & 0.999105 \pm 0.000032 \end{pmatrix}. \quad (1.32)$$

Owing to the unitarity of $U_{u,d}$ and $W_{u,d}$, in neutral-current interactions a fermion interacts with its antiparticle or with an identical fermion, as can be seen substituting Eq. (1.22) in Eq. (1.26c). Therefore the transition between different quark families does not take place in neutral currents. This means that the SM does not foresee flavour-changing neutral currents (FCNC) processes at tree level [27].

1.3 Quantum chromodynamics

Quantum chromodynamics (QCD) is the theory that describes the strong interactions between quarks and gluons, and, along with the GWS model, constitutes the SM. QCD is a Yang-Mills non-abelian quantum-field theory based on the exact colour-SU(3) local gauge symmetry [26]. The QCD Lagrangian is

$$\mathcal{L}_{QCD} = \sum_F \overline{\psi}_F \left(i\gamma^\mu \partial_\mu - g_s \gamma^\mu \frac{\lambda^C}{2} A^C_\mu - m_F \right) \psi_F - \frac{1}{4} A^{C\mu\nu} A^C_{\mu\nu}, \tag{1.33}$$

where ψ_F is a triplet in the SU(3) space of quark spinors of flavour F and mass m_F, g_s is the QCD coupling constant, λ^C are the eight Gell-Mann matrices (generators of the SU(3) group), A^C_μ are the massless gluon fields ($C = 1, ..., 8$) and $A^{C\mu\nu}$ are the gluon-field strength tensors.

The strong coupling constant $\alpha_s = g_s^2/4\pi$ has, at one-loop level, a dependence on the exchanged momentum q^2 in a given process

$$\alpha_s(q^2) = \frac{4\pi}{\left(11 - \frac{2}{3} n_f\right) \log \frac{q^2}{\Lambda^2_{QCD}}}, \tag{1.34}$$

where n_f is the number of flavours and Λ_{QCD} is the energy scale of strong interactions, which experimentally is known to be $\Lambda_{QCD} \simeq 200\,\text{MeV}$. Equation (1.34) shows that the magnitude of the coupling constant decreases with increasing q^2 (or with decreasing distance). Hence at high energies, *i.e.* $q \gg \Lambda_{QCD}$, quarks and gluons behave as quasi-free particles and quark-gluon interactions can be treated perturbatively. Conversely, at low energies ($q \ll \Lambda_{QCD}$) the coupling constant becomes very high and a perturbation expansion in series of α_s has no practical meaning.

In order to perform non-perturbative treatments of QCD problems, lattice QCD (LQCD) is used [28]. In LQCD, Euclidean spacetime is discretised on a hypercubic lattice with a certain spacing, with quark fields placed on sites and gauge fields on the links between sites. The quantum-field theory is therefore finite, and the lattice spacing plays the role of the ultraviolet regulator. With this approach, non-perturbative calculations are made possible by numerical evaluation of the path integral which defines the theory. The continuum theory is then recovered by taking the limit of vanishing lattice spacing. The main limitation of LQCD calculations is represented by the availability of computational resources and by the efficiency of the algorithms.

The strong interaction between a single heavy quark (b or c) and a lighter quark can be described through a heavy quark effective theory (HQET) [29–32]. The key idea of HQET consists in considering as infinite the mass of the heavy quark, m_Q, such that the heavy quark acts like a stationary point source of colour charge. The QCD Lagrangian is then expanded in a power series of $1/m_Q$, neglecting higher-order terms, in order to obtain the HQET Lagrangian. The expansion holds as far as $m_Q \gg \Lambda_{QCD}$. As explained more in detail in Sec. 1.4.1, HQET is particularly useful to calculate the form factors of decays involving $B \to D$ transitions, because the velocity transferred between the b and c quark is small, due to their large masses, leaving the colour source stationary to a good approximation.

Decays involving light quarks, like $c \to s$ and $c \to d$ transitions, are not well described by HQET. In this case the light cone sum rules (LCSR) method is used [33–36]. In LCSR the limit considered is that of large hadron momentum, and an expansion is made around the large energy limit in powers of the distance between partons in the direction transverse to the hadron momentum.

1.4 Lepton flavour universality in semitauonic B decays

In the SM, lepton-flavour universality (LFU) is an accidental symmetry broken only by the Yukawa interactions. From Eq. (1.25) it is clear that the coupling between leptons and electroweak bosons does not depend on the lepton family. Therefore differences between the branching fractions of semileptonic decays into the three lepton families are expected to be caused only by the different masses of the charged leptons, and further deviations from LFU would be a signature of NP. The couplings of Z and W bosons to light leptons, which were mainly measured by LEP and SLC experiments, are compatible with LFU, but a difference at the 2.8σ level exists between the measurement of the branching fraction of the $W^+ \to \tau^+\nu_\tau$ decay and those of the branching fractions of $W^+ \to \mu^+\nu_\mu$ and $W^+ \to e^+\nu_e$ decays [37]. Recently, hints of LFU violation have been observed in measurements of branching fractions and angular observables of rare $b \to s\ell^+\ell^-$ decays [1–5] and in measurements of branching fractions of decays involving $b \to c\ell\nu$ transitions.

In the following, the $B^0 \to D^{*-}\tau^+\nu_\tau$ decay is discussed more in detail. In Sec. 1.4.1, the main steps which lead to the calculation of the $\mathcal{R}(D^*)$ observable are illustrated, while in Sec. 1.4.2 an overview of the experimental status of $\mathcal{R}(D)$ and

$\mathcal{R}(D^*)$ is reported.

1.4.1 $\mathcal{R}(D^*)$ in the Standard Model

If in the semileptonic decay of a meson M_{Qq} of momentum p into a state containing a meson $M_{q'q}$ of momentum p', the exchanged four-momentum $q = p - p'$ between the two mesons is much smaller than the mass M_W of the $W^{\pm}$ boson, the decay amplitude can be written as

$$\mathcal{M} = -i\frac{G_F}{\sqrt{2}} V_{Qq'} L^{\mu} H_{\mu}, \tag{1.35}$$

where G_F is the Fermi constant, L^{μ} is the leptonic current

$$L^{\mu} = \overline{\ell}\gamma^{\mu}(1-\gamma_5)\nu_{\ell}, \tag{1.36}$$

and H_{μ} is the hadronic current

$$H_{\mu} = \langle M_{q'q}(p')|j_{\mu}^{H}|M_{Qq}(p)\rangle. \tag{1.37}$$

Here j_{μ}^{H} can be expressed in terms of Lorentz-invariant quantities that are combinations of q_{μ}, q^2 and $(p_{\mu} + p'_{\mu})$. The two mesons interact also strongly, so the hadronic current contains some terms which parameterise the non-perturbative behaviour of the QCD. These terms, called form factors, depend on the given initial and final state and, for some decays, can be measured experimentally. When form factors cannot be extracted from data, one must rely on various theory inputs to calculate them.

The $b \to c\ell\overline{\nu}_{\ell}$ transition can be described by the effective Hamiltonian [38]

$$\mathcal{H}_{eff} = \frac{4G_F V_{cb}}{\sqrt{2}} J_{bc,\mu} \sum_{\ell=e,\mu,\tau} \left(\overline{\ell}\gamma^{\mu} P_L \nu_{\ell}\right) + \text{h.c.}, \tag{1.38}$$

where $J_{bc,\mu}$ is the effective SM $b \to c$ charged current

$$J_{bc,\mu} = \overline{c}\gamma_{\mu} P_L b. \tag{1.39}$$

From this Hamiltonian the differential decay rate of $B^0 \to D^{*-}\tau^+\nu_{\tau}$ as function of $q^2 = (p_B - p_{D^*})^2$ is calculated

$$\begin{aligned}\frac{d\Gamma_{\ell}}{dq^2} =& \frac{G_F^2 \left|V_{cb}\right|^2 |\mathbf{p}| q^2}{96\pi^3 m_B^2} \left(1 - \frac{m_{\ell}^2}{q^2}\right)^2 \times \\ & \left[\left(|H_{++}|^2 + |H_{--}|^2 + |H_{00}|^2\right)\left(1 + \frac{m_{\ell}^2}{2q^2}\right) + \frac{3m_{\ell}^2}{2q^2}|H_{0t}|^2\right],\end{aligned} \tag{1.40}$$

where $\mathbf{p}$ is the three-momentum of the D^{*-} meson in the B^0 rest frame

$$|\mathbf{p}| = \frac{\sqrt{\lambda(m_B^2, m_{D^*}^2, q^2)}}{2m_B}, \tag{1.41}$$

$$\lambda(a,b,c) \equiv a^2 + b^2 + c^2 - 2(ab + bc + ca). \tag{1.42}$$

Finally, H_{mn} are the relevant hadronic helicity amplitudes

$$H_{\pm\pm}(q^2) = (m_B + m_{D^*})A_1(q^2) \mp \frac{2m_B}{m_B + m_{D^*}}|\mathbf{p}|V(q^2), \tag{1.43a}$$

$$H_{00}(q^2) = \frac{1}{2m_{D^*}\sqrt{q^2}}\times \left[(m_B^2 - m_{D^*}^2 - q^2)(m_B + m_{D^*})A_1(q^2) - \frac{4m_B^2|\mathbf{p}|^2}{m_B + m_{D^*}}A_2(q^2)\right], \tag{1.43b}$$

$$H_{0t}(q^2) = \frac{2m_B|\mathbf{p}|}{\sqrt{q^2}}A_0(q^2), \tag{1.43c}$$

where $A_{0,1,2}(q^2)$, $V(q^2)$ are the form factors of this process, which need to be calculated. Since the last term of Eq. (1.40) is proportional to m_ℓ^2/q^2, it is relevant only for decays involving τ leptons. In order to reduce most theoretical uncertainties due to the evaluation of the form factors, it is useful to normalise the branching fraction of the $B^0 \to D^{*-}\tau^+\nu_\tau$ decay to the modes with a light lepton (ℓ) in place of τ in the final state. Hence an interesting observable is the ratio[1]

$$\mathcal{R}(D^*) = \frac{\mathcal{B}(B^0 \to D^{*-}\tau^+\nu_\tau)}{\mathcal{B}(B^0 \to D^{*-}\ell^+\nu_\ell)}. \tag{1.44}$$

In order to compute the value of $\mathcal{R}(D^*)$, the four form factors introduced in Eq. (1.43) must be computed. This task can be achieved by using HQET. In fact, according to HQET, in the $m_Q \to \infty$ limit the hadronic matrix element describing the scattering process can be expressed as a function of an universal form factor $\xi(w)$, called Isgur-Wise function [39, 40], where

$$w = v_B \cdot v_{D^*} = \frac{m_B^2 + m_{D^*}^2 - q^2}{2m_B m_{D^*}}, \tag{1.45}$$

with v_B, v_{D^*} the four-velocities of the B^0 and D^{*-} mesons. At the zero-recoil limit $w = 1$, *i.e.* $q^2 = (m_B - m_{D^*})^2$, the Isgur-Wise function is normalised to 1: $\xi(1) = 1$.

[1] Assuming isospin symmetry, the study of the $B^0 \to D^{*-}\tau^+\nu_\tau$ decay is equivalent to that of $B^+ \to \overline{D}^{*0}\tau^+\nu_\tau$, and in the following $\mathcal{R}(D^*)$ refers to both $\mathcal{R}(D^{*-})$ and $\mathcal{R}(\overline{D}^{*0})$, which are equal.

In the infinite-mass limit the properties of mesons containing a single heavy quark are insensitive to the spin and flavour of the heavy quark. This heavy-quark spin symmetry leads to additional relations among form factors, so matrix elements involving vector mesons can be related to those involving pseudoscalar mesons. Therefore, according to the CLN parameterisation [41], the form factors can be expressed in terms of a universal form factor

$$h_{A_1}(w) = A_1(q^2)\frac{2}{M(w+1)} \tag{1.46}$$

and three ratios R_0, R_1, R_2

$$A_0(q^2) = \frac{R_0(w)}{M}h_{A_1}(w), \tag{1.47a}$$

$$A_2(q^2) = \frac{R_2(w)}{M}h_{A_1}(w), \tag{1.47b}$$

$$V(q^2) = \frac{R_1(w)}{M}h_{A_1}(w), \tag{1.47c}$$

where $M = 2\sqrt{m_B m_{D^*}}/(m_B + m_{D^*})$. At the heavy quark limit, *i.e.* considering only the leading Isgur-Wise function, the w dependence of these quantities is given by

$$h_{A_1}(w) = h_{A_1}(1)[1 - 8\rho^2 z + (53\rho^2 - 15)z^2 - (231\rho^2 - 91)z^3], \tag{1.48a}$$

$$R_0(w) = R_0(1) - 0.11(w-1) + 0.01(w-1)^2, \tag{1.48b}$$

$$R_1(w) = R_1(1) - 0.12(w-1) + 0.05(w-1)^2, \tag{1.48c}$$

$$R_2(w) = R_2(1) + 0.11(w-1) - 0.06(w-1)^2, \tag{1.48d}$$

where $z = (\sqrt{w+1} - \sqrt{2})/(\sqrt{w+1} + \sqrt{2})$. $\mathcal{R}(D^*)$ does not depend on $h_{A_1}(1)$, since it is common to all hadronic currents, while the parameters ρ^2, $R_1(1)$, $R_2(1)$ can be measured by fitting the $B^0 \to D^{*-}\ell^+\nu_\ell$ decay distributions [42]. Those measured values are used as inputs to some HQET calculations in order to extract the value of $R_0(1)$, which cannot be directly measured, as the sensitivity to this parameter is minimal in the $B^0 \to D^{*-}\ell^+\nu_\ell$ decay. At the heavy quark limit, the SM expectation for $\mathcal{R}(D^*)$ is [38]

$$\mathcal{R}(D^*) = 0.252 \pm 0.003.$$

New predictions of $\mathcal{R}(D^*)$ have been recently obtained including terms proportional to $\Lambda_{QCD}/m_{c,b}$ and α_s. In this case three more universal subleading Isgur-Wise functions are needed to describe all form factors. Including these additional terms, using QCD sum rule predictions [43–45] and up-to-date lattice calculations of form

factors and experimental results from Belle [46], the calculated value of $\mathcal{R}(D^*)$ is equal to [47]

$$\mathcal{R}(D^*) = 0.257 \pm 0.003,$$

which is about 1 standard deviation higher than the previous prediction. This last result takes also into account the theoretical uncertainties of the slopes and curvatures of Eqs. (1.48c) and (1.48d), which was not done in Ref. [38].

One further analysis [48], which includes theoretical uncertainties due to higher order corrections in $R_{1,2}(w)$, reports an expected value of $\mathcal{R}(D^*)$ equal to

$$\mathcal{R}(D^*) = 0.260 \pm 0.008.$$

In this case the form factors are described with the BGL parameterisation [49], which takes into account sub-threshold singularities not considered by the CLN parameterisation. A similar study [50], in which missing high-order corrections in the form-factor ratios are parameterised by introducing terms which are determined from data and lattice calculations, finds a consistent result

$$\mathcal{R}(D^*) = 0.257 \pm 0.005.$$

Similar calculations have been made for $\mathcal{R}(D)$, which is defined in the same way as $\mathcal{R}(D^*)$ but with the D meson in place of the D^*. A summary of the SM predictions for $\mathcal{R}(D)$ and $\mathcal{R}(D^*)$ is reported in Table 1.2. Both central values and uncertainties of the SM expectations are expected to evolve in the future as more precise measurements of $B \to \overline{D}^{(*)}\tau^+\nu_\tau$ spectra and new calculations will become available. The theoretical uncertainty, mainly due to assumptions on the pseudoscalar form factor, is currently under debate in the community. This disagreement will be settled down when calculations of the $B \to D^*$ form factor beyond the zero-recoil limit and more information on the pseudoscalar form factor will become available [6].

1.4.2 Experimental status of $\mathcal{R}(D^*)$

The observables $\mathcal{R}(D^{0,-})$, $\mathcal{R}(D^{*-,0})$ and their averages $\mathcal{R}(D)$ and $\mathcal{R}(D^*)$ have been measured by the BaBar and Belle collaborations. The BaBar collaboration reported a combined discrepancy of $\mathcal{R}(D)$ and $\mathcal{R}(D^*)$ from the values predicted in Ref. [38] at 3.4σ level [53, 54], arousing large interest in the community. The measurements performed by the Belle collaboration [55–58] are compatible with the expectations.

Table 1.2: Summary of SM predictions for $\mathcal{R}(D)$ and $\mathcal{R}(D^*)$.

$\mathcal{R}(D)$	$\mathcal{R}(D^*)$	Reference
0.300 ± 0.008	-	[51]
-	0.252 ± 0.003	[38]
0.299 ± 0.003	-	[52]
0.299 ± 0.003	0.257 ± 0.003	[47]
-	0.260 ± 0.008	[48]
0.299 ± 0.004	0.257 ± 0.005	[50]

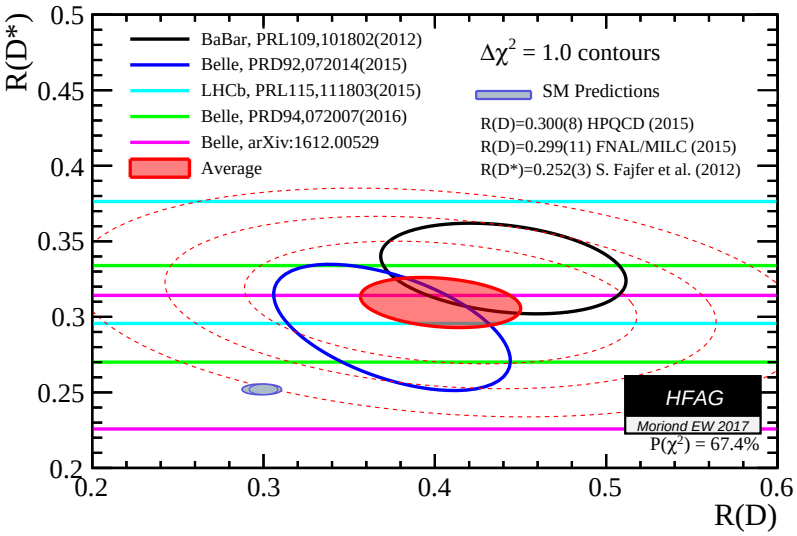

Figure 1.1: Graphical view of the status prior to the analysis reported in this thesis of experimental measurements and theoretical predictions of $\mathcal{R}(D^*)$ and $\mathcal{R}(D)$.

The LHCb collaboration reported a measurement of $\mathcal{R}(D^*)$ [59] 2.1σ larger than the value calculated in Ref. [38]. The combination of all these measurements, summarised in Fig. 1.1, gives

$$\mathcal{R}(D^*) = 0.310 \pm 0.015 \text{ (stat)} \pm 0.008 \text{ (syst)},$$
$$\mathcal{R}(D) = 0.403 \pm 0.040 \text{ (stat)} \pm 0.024 \text{ (syst)}.$$

The measured values of both $\mathcal{R}(D)$ and $\mathcal{R}(D^*)$ are all higher than the SM expectations. The difference between the average of the measured values of $\mathcal{R}(D)$ and the combination of the three most recent predictions of this observable corresponds to 2.2σ. The average value of $\mathcal{R}(D^*)$ differs by 2.7σ from the prediction with the largest theoretical uncertainty. The combination of $\mathcal{R}(D)$ and $\mathcal{R}(D^*)$, which takes

into account the correlation $\rho = -0.23$ between their average values [6], differs from the SM predictions by about 3.5σ.

All the measurements listed here have been performed by reconstructing the τ lepton in its leptonic decay mode. The last measurement of $\mathcal{R}(D^*)$, performed by the LHCb collaboration reconstructing the τ in the $\tau^+ \to \pi^+\pi^-\pi^+(\pi^0)\overline{\nu}_\tau$, is the subject of this thesis and is described in detail in Chapter 3.

1.5 *CP* violation in the Standard Model

The discrete transformation denoted as *CP* is the combination of charge conjugation C, which interchanges particles and antiparticles, and parity transformation P, which flips the signs of the spatial coordinates. Strong and electromagnetic interactions conserve C and P symmetries separately, thus they do not violate CP[2]. By contrast, weak interaction maximally violates C and P as well as, tinily, *CP*.

Measurements of *CP*-violating quantities place strong constraints on the flavour parameters of the SM. Future measurements of *CP* observables will provide additional constraints and more strongly probe the presence of possible new physics (NP) effects.

As explained in Sec. 1.1, the CKM matrix can be parameterised in terms of three mixing angles and a complex phase. Even if in different parameterisations the complex phase moves to different matrix elements, its position in the matrix is not physically significant. In fact, a *CP*-violating quantity can be defined independently of the parameterisation [61]. For example the Jarlskog invariant J_{CKM}, is defined through the relation

$$\Im(V_{ij}V_{kl}V_{il}^*V_{kj}^*) = J_{CKM}\sum_{m,n=1}^{3}\epsilon_{ikm}\epsilon_{jln} \quad (i,j,k,l = 1,2,3), \tag{1.49}$$

and can be written as

$$J_{CKM} = s_{12}s_{13}s_{23}c_{12}c_{23}c_{13}^2\sin\delta. \tag{1.50}$$

It can be shown that a necessary and sufficient condition for the existence of *CP* violation in the quark sector is

$$(m_t^2 - m_c^2)(m_t^2 - m_u^2)(m_c^2 - m_u^2)(m_b^2 - m_s^2)(m_b^2 - m_d^2)(m_s^2 - m_d^2)J_{CKM} \neq 0. \tag{1.51}$$

[2]Formally speaking, the QCD Lagrangian contains terms which naturally violate the *CP* symmetry. Since this is not observed experimentally in strong interactions, the reason why such *CP*-violating terms are ineffective is still an open problem in particle physics. Some explanations have been found, notably including the Peccei-Quinn theory [60], which predicts the existence of the axion.

Hence, in order to have *CP* violation in the SM, there must not be mass degeneracy between any up-type or down-type quarks, all of the three mixing angles must be different from 0 or $\pi/2$ and the phase must not be 0 or π. Moreover Eq. (1.49) shows that, in order to have *CP* violation in a certain process, at least four different quarks must be involved in the transition.

For a generic meson M and its *CP* conjugate $\overline{M}$, the following decay amplitudes in the final state f and its *CP*-conjugate $\overline{f}$ are defined

$$A_f = \langle f|\mathcal{H}|M\rangle, \quad A_{\overline{f}} = \langle \overline{f}|\mathcal{H}|M\rangle, \quad \overline{A}_f = \langle f|\mathcal{H}|\overline{M}\rangle, \quad \overline{A}_{\overline{f}} = \langle \overline{f}|\mathcal{H}|\overline{M}\rangle, \tag{1.52}$$

where $\mathcal{H}$ is the effective decay Hamiltonian. Two types of phases are involved in these amplitudes. The phases occurring in the couplings of the $W^{\pm}$ bosons, called *weak phases*, appear in complex conjugate form in the *CP*-conjugate amplitude. Other phases originate from the possible contribution from intermediate on-shell states in the decay process, usually due to strong interactions, hence called *strong phases*. Since the strong interaction is *CP*-invariant, the strong phases do not change between A_f and $\overline{A}_{\overline{f}}$.

CP violation in the decay (*i.e.* $|A_f| \neq |\overline{A}_{\overline{f}}|$), is a result of the interference between terms in the amplitude, and it takes place only if at least two terms have different weak and strong phases. In fact, if an amplitude is given by the sum of several contributions

$$A_f = \sum_i |A_i| e^{i(\delta_i + \phi_i)}, \tag{1.53}$$

where $|A_i|$, δ_i and ϕ_i are, respectively, the magnitude, strong phase and weak phase of each contribution, the difference between the squared amplitude $|A_f|^2$ and $|\overline{A}_{\overline{f}}|^2$ is equal to

$$|A_f|^2 - |\overline{A}_{\overline{f}}|^2 = -2 \sum_{i \neq j} |A_i||A_j| \sin(\delta_i - \delta_j) \sin(\phi_i - \phi_j). \tag{1.54}$$

1.5.1 *CP* violation in neutral mesons

The phenomenology of *CP* violation in neutral mesons is enriched by the presence of flavour mixing or oscillation, *i.e.* the $M^0 \leftrightarrow \overline{M}^0$ transition. In fact, due to the structure of the weak interaction, an initially pure flavour eigenstate develops a component of the opposite flavour before decaying. Four neutral mesons can mix: K^0, D^0, B^0 and B_s^0.

A state which is initially a superposition of $|M^0\rangle$ and $|\overline{M}^0\rangle$

$$|\psi(t=0)\rangle = a(0)|M^0\rangle + b(0)|\overline{M}^0\rangle \tag{1.55}$$

will evolve in time as

$$|\psi(t)\rangle = a(t)|M^0\rangle + b(t)|\overline{M}^0\rangle + \sum_i c_i(t)|f_i\rangle, \tag{1.56}$$

where f_i are all the possible decay final states. The mixing in the subspace defined by $|M^0\rangle$ and $|\overline{M}^0\rangle$ is described by the Schrödinger equation

$$i\frac{\partial}{\partial t}\begin{pmatrix} a(t) \\ b(t) \end{pmatrix} = \left(\mathbf{M} - \frac{i}{2}\mathbf{\Gamma}\right)\begin{pmatrix} a(t) \\ b(t) \end{pmatrix}, \tag{1.57}$$

where the elements of the mass matrix $\mathbf{M}$ are defined as

$$M_{ij} = m_0\delta_{i,j} + \langle M_i|\mathcal{H}_{\mathrm{w}}|M_j\rangle + \sum_k \mathrm{P}\left(\frac{\langle M_i|\mathcal{H}_{\mathrm{w}}|f_k\rangle\langle f_k|\mathcal{H}_{\mathrm{w}}|M_j\rangle}{m_0 - E_{f_k}}\right), \tag{1.58}$$

and the elements of the decay matrix $\mathbf{\Gamma}$ are

$$\Gamma_{ij} = 2\pi\sum_k \delta(m_0 - E_{f_k})\langle M_i|\mathcal{H}_{\mathrm{w}}|f_k\rangle\langle f_k|\mathcal{H}_{\mathrm{w}}|M_j\rangle, \tag{1.59}$$

with $M_1 = M^0$, $M_2 = \overline{M}^0$, $\mathcal{H}_{\mathrm{w}}$ is the weak Hamiltonian and m_0 is the M^0 mass. Both $\mathbf{M}$ and $\mathbf{\Gamma}$ are Hermitian, while $\mathbf{H} = \mathbf{M} - \frac{i}{2}\mathbf{\Gamma}$ is not Hermitian, otherwise the mesons would only oscillate and not decay. The matrix $\mathbf{M}$ is associated with transitions via off-shell (dispersive) intermediate states, while $\mathbf{\Gamma}$ with on-shell (absorptive) intermediate states. While diagonal elements of $\mathbf{H}$ are associated with flavour-conserving transitions, the off-diagonal elements describe flavour-changing transitions. The conservation of the *CPT* symmetry requires that $M_{11} = M_{22}$ and $\Gamma_{11} = \Gamma_{22}$.

The eigenvectors of $\mathbf{H}$, called $|M_H\rangle$ and $|M_L\rangle$, have defined masses (m_H and m_L) and decay widths (Γ_H and Γ_L). The eigenvectors are equal to

$$|M_H\rangle = p|M^0\rangle - q|\overline{M}^0\rangle, \tag{1.60a}$$

$$|M_L\rangle = p|M^0\rangle + q|\overline{M}^0\rangle, \tag{1.60b}$$

where p and q are complex parameters with $|p|^2 + |q^2| = 1$ and

$$\frac{q}{p} = \sqrt{\frac{M_{12}^* - \frac{i}{2}\Gamma_{12}^*}{M_{12} - \frac{i}{2}\Gamma_{12}}}. \tag{1.61}$$

The corresponding eigenvalues are

$$\lambda_{H,L} = M_{11} - \frac{i}{2}\Gamma_{11} \pm \frac{q}{p}\left(M_{12} - \frac{i}{2}\Gamma_{12}\right). \tag{1.62}$$

The masses of the eigenstates are the real part of the eigenvalues, while the decay widths are proportional to the imaginary part

$$m_{H,L} = \Re(\lambda_{H,L}) = M_{11} \pm \Re\left[\frac{q}{p}\left(M_{12} - \frac{i}{2}\Gamma_{12}\right)\right], \tag{1.63a}$$

$$\Gamma_{H,L} = -2\Im(\lambda_{H,L}) = \Gamma_{11} \mp 2\Im\left[\frac{q}{p}\left(M_{12} - \frac{i}{2}\Gamma_{12}\right)\right]. \tag{1.63b}$$

If a state is an initially pure $|M^0\rangle$ or $|\overline{M}^0\rangle$, at time t one has

$$|M^0(t)\rangle = g_+(t)|M^0\rangle - \frac{q}{p}\, g_-(t)|\overline{M}^0\rangle, \tag{1.64a}$$

$$|\overline{M}^0(t)\rangle = g_-(t)|\overline{M}^0\rangle - \frac{p}{q}\, g_+(t)|M^0\rangle, \tag{1.64b}$$

where

$$g_\pm = \frac{1}{2}\left(e^{-im_H t - \frac{1}{2}\Gamma_H t} \pm e^{-im_L t - \frac{1}{2}\Gamma_L t}\right). \tag{1.65}$$

This means that the time-dependent decay rate of an initially pure $|M^0\rangle$ state is

$$\begin{aligned}\Gamma(M^0(t) \to f) = \Gamma\Bigg[&\left(|A_f|^2 + \left|\frac{q}{p}\,\overline{A}_f\right|^2\right)\cosh(y\Gamma t) \\ &+ \left(|A_f|^2 - \left|\frac{q}{p}\,\overline{A}_f\right|^2\right)\cos(x\Gamma t) \\ &+ 2\Re\left(\frac{q}{p}\, A_f^*\overline{A}_f\right)\sinh(y\Gamma t) - 2\Im\left(\frac{q}{p}\, A_f^*\overline{A}_f\right)\sin(x\Gamma t)\Bigg],\end{aligned} \tag{1.66}$$

where x, y and λ_f are defined as

$$\Gamma = \frac{\Gamma_H + \Gamma_L}{2}, \tag{1.67a}$$

$$x = \frac{\Delta m}{\Gamma} = \frac{m_H - m_L}{\Gamma}, \tag{1.67b}$$

$$y = \frac{\Delta\Gamma}{2\Gamma} = \frac{\Gamma_H - \Gamma_L}{2\Gamma}. \tag{1.67c}$$

In an analogous way

$$\Gamma(\overline{M}^0(t)\to f) = \Gamma\left[\left(|\overline{A}_f|^2 + \left|\frac{p}{q}\,A_f\right|^2\right)\cosh(y\Gamma t)\right.$$
$$+\left(|\overline{A}_f|^2 - \left|\frac{p}{q}\,A_f\right|^2\right)\cos(x\Gamma t)$$
$$\left.+2\Re\left(\frac{p}{q}\,\overline{A}_f^* A_f\right)\sinh(y\Gamma t) - 2\Im\left(\frac{p}{q}\,\overline{A}_f^* A_f\right)\sin(x\Gamma t)\right], \qquad (1.68)$$

In Eqs. (1.66) and (1.68) the terms proportional to $|A_f|^2$ and $|\overline{A}_f|^2$ are associated to decays taking place without any oscillations, while the terms proportional to $|(q/p)\ \overline{A}_f|^2$ and $|(p/q)\ A_f|^2$ are associated to decays following an oscillation. The other terms, proportional to $\sinh(y\Gamma t)$ and $\sin(x\Gamma t)$, are associated to the interference between decays with and without oscillation. The decay rates in the $\overline{f}$ state can be obtained by replacing A_f ($\overline{A}_f$) with $A_{\overline{f}}$ ($\overline{A}_{\overline{f}}$) in Eqs. (1.66) and (1.68). The corresponding time-integrated rates, obtained by calculating the integral $\int_0^\infty \Gamma(M^0/\overline{M}^0(t)\to f)\Gamma e^{-\Gamma t}\mathrm{d}t$, are

$$\Gamma(M^0\to f) = \Gamma\left[\left(|A_f|^2 + \left|\frac{q}{p}\,\overline{A}_f\right|^2\right)\frac{1}{1-y^2} + \left(|A_f|^2 - \left|\frac{q}{p}\,\overline{A}_f\right|^2\right)\frac{1}{1+x^2}\right.$$
$$\left.+2\Re\left(\frac{q}{p}\,A_f^*\overline{A}_f\right)\frac{y}{1-y^2} - 2\Im\left(\frac{q}{p}\,A_f^*\overline{A}_f\right)\frac{x}{1+x^2}\right], \qquad (1.69a)$$

$$\Gamma(\overline{M}^0\to f) = \Gamma\left[\left(|\overline{A}_f|^2 + \left|\frac{p}{q}\,A_f\right|^2\right)\frac{1}{1-y^2} + \left(|\overline{A}_f|^2 - \left|\frac{p}{q}\,A_f\right|^2\right)\frac{1}{1+x^2}\right.$$
$$\left.+2\Re\left(\frac{p}{q}\,\overline{A}_f^* A_f\right)\frac{y}{1-y^2} - 2\Im\left(\frac{p}{q}\,\overline{A}_f^* A_f\right)\frac{x}{1+x^2}\right]. \qquad (1.69b)$$

CP violation in neutral-meson decays can be classified as

1. *CP* violation in the decay, happening when $\left|A_f/\overline{A}_{\overline{f}}\right| \neq 1$. This is the only source present also in charged-meson decays. The *CP* asymmetry is defined as
$$A_{CP}(f) = \frac{\Gamma(M\to f) - \Gamma(\overline{M}\to\overline{f})}{\Gamma(M\to f) + \Gamma(\overline{M}\to\overline{f})} = \frac{1-|\overline{A}_{\overline{f}}/A_f|^2}{1+|\overline{A}_{\overline{f}}/A_f|^2}. \qquad (1.70)$$

2. *CP* violation in mixing, which takes place when $|q/p| \neq 1$. In this case a useful observable is the time-dependent version of Eq. (1.70)
$$A_{CP}(f,t) = \frac{\Gamma(M^0(t)\to f) - \Gamma(\overline{M}^0(t)\to\overline{f})}{\Gamma(M^0(t)\to f) + \Gamma(\overline{M}^0(t)\to\overline{f})}. \qquad (1.71)$$

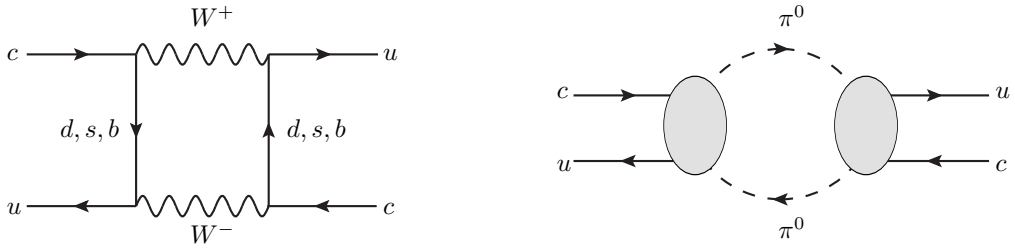

Figure 1.2: Examples of Feynman diagrams describing (left) short- and (right) long-distance contributions in the D^0 oscillation amplitude.

3. *CP* violation in the interference between decay and oscillation. This occurs when the final state is common to both M^0 and $\overline{M}^0$, and when $\Im(\lambda_f) \neq 0$, with

$$\lambda_f = \frac{q}{p}\,\frac{\overline{A}_f}{A_f}. \tag{1.72}$$

   Due to the presence of an interference term, the *CP* symmetry can be violated even when $\left|A_f/\overline{A}_f\right| = 1$ and $|q/p| = 1$, *i.e.* when there is no *CP* violation in the decay nor in the mixing.

CP violation in the decay is usually called *direct CP* violation, while the last two are referred to as *indirect CP* violation.

CP violation has been observed at more than 5 standard deviations in the decays of the K, B and B_s^0 mesons. All three types of *CP* violation have been observed in $K \to \pi\pi$ decays, while, concerning the B mesons, direct *CP* violation has been observed for example in the $B^0 \to K^+\pi^-$ channel and *CP* violation due to interference between decay with and without mixing has been observed in the $B^0 \to J/\psi\, K^0_{\rm S}$ decay. Direct *CP* violation has been observed in the $\overline{B}^0_s \to K^+\pi^-$ decay as well. *CP* violation in the decays of the D^0 meson has not been seen yet.

1.5.2 *CP* violation in charged two-body decays of D^0 mesons

The existence of oscillations in the D^0-meson system has been established in recent years. The average values of the mixing parameters, when *CP* violation is simultaneously measured, are $x = (0.36^{+0.21}_{-0.16})\%$ and $y = (0.67^{+0.06}_{-0.13})\%$ [6]. According to the SM, mixing in the D^0 system takes place through a double weak-boson exchange (*short-distance* contribution) or intermediate states accessible to D^0 and $\overline{D}^0$ (*long-distance* contribution), as illustrated in Fig. 1.2. The long-distance contributions are non-perturbative, so the SM predictions for the D^0 mixing parameters

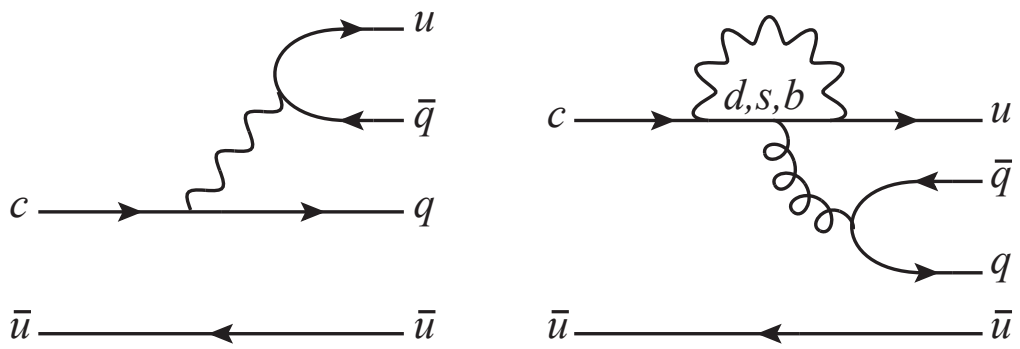

Figure 1.3: Examples of Feynman diagrams contributing to the amplitude of charged two-body D^0-meson decays: (left) tree and (right) one-loop penguin.

are difficult to calculate. Therefore the measurement of D^0 oscillation parameters does not provide at present strong constraints to the CKM parameters. In fact current measurements are on the upper end of most theory predictions, which span several orders of magnitude [62, 63].

D^0-meson decays to the *CP* eigenstates K^+K^- and $\pi^+\pi^-$ proceed through singly-Cabibbo-suppressed transitions, as illustrated in Fig. 1.3. The $D^0/\overline{D}^0 \to h^+h^-$ (where $h^\pm = K^\pm, \pi^\pm$) decay amplitudes are dominated by tree diagrams, and they can be written as

$$A_f = |A_f^T| e^{i\phi_f^T} \left[1 + r_f e^{i(\delta_f + \phi_f)}\right], \tag{1.73a}$$

$$\eta_{CP}(f)\overline{A}_f = |A_f^T| e^{-i\phi_f^T} \left[1 + r_f e^{i(\delta_f - \phi_f)}\right], \tag{1.73b}$$

where $|A_f^T| e^{i\phi_f^T}$ is the tree-level contribution to A_f, $r_f \ll 1$ and δ_f are the module ratio and the strong phase difference between the subleading and the tree-level contribution, ϕ_f is the weak phase of the subleading contribution and η_{CP} is equal to 1 (-1) for a *CP*-even (*CP*-odd) eigenstate f [7]. The tree-level Feynman diagrams of the $D^0 \to h^+h^-$ decays involve the CKM terms $V_{us}^* V_{cs}$ and $V_{ud}^* V_{cd}$, which, in the Wolfenstein parameterisation, are real up to $\mathcal{O}(\lambda^4)$ (see Eq. (1.30)). The tree-level phase can therefore be neglected and λ_f can be written as [64]

$$\lambda_f = \left|\frac{q}{p}\right| e^{i\phi_D}, \tag{1.74}$$

where ϕ_D is a universal (*i.e.* independent of the final state) phase and $\eta_{CP}(f) = 1$, since K^+K^- and $\pi^+\pi^-$ are *CP*-even eigenstates. Since x, y and r_f have small

values, Eq. (1.69) can be expanded to leading order in these parameters, resulting in Eq. (1.70) to become:

$$A_{CP}(f) = A_{CP}^{\text{dir}}(f) + A_{CP}^{\text{mix}} + A_{CP}^{\text{int}} = A_{CP}^{\text{dir}}(f) + A_{CP}^{\text{ind}}, \tag{1.75}$$

where

$$A_{CP}^{\text{dir}}(f) = -2r_f \sin\phi_f \sin\delta_f \tag{1.76}$$

is associated to direct *CP* violation,

$$A_{CP}^{\text{mix}} = -\frac{y}{2}\left(\left|\frac{q}{p}\right| - \left|\frac{p}{q}\right|\right)\cos\phi_D \tag{1.77}$$

refers to *CP* violation in mixing ($|q/p| \neq 1$) and

$$A_{CP}^{\text{int}} = \frac{x}{2}\left(\left|\frac{q}{p}\right| + \left|\frac{p}{q}\right|\right)\sin\phi_D \tag{1.78}$$

is associated to *CP* violation in the interference between decay and mixing. The effect of direct *CP* violation can therefore be isolated defining the observable

$$\Delta A_{CP} = A_{CP}(K^+K^-) - A_{CP}(\pi^+\pi^-) = A_{CP}^{\text{dir}}(K^+K^-) - A_{CP}^{\text{dir}}(\pi^+\pi^-). \tag{1.79}$$

Due to the universality of indirect *CP* violation, the observation of a difference between $A_{CP}(K^+K^-)$ and $A_{CP}(\pi^+\pi^-)$ means that direct *CP* violation is present. Direct and indirect *CP* violation effects can be separated in the time-dependent *CP* asymmetry as well. By expanding Eqs. (1.66) and (1.68) in x, y, r_f, it is possible to write Eq. (1.71) as a linear function of time

$$A_{CP}(f,t) = A_{CP}^{\text{dir}}(f) + \Gamma t A_{CP}^{\text{ind}}. \tag{1.80}$$

Since $x, y \ll 1$, the time dependence can be recast into a purely exponential form with the effective decay widths

$$\Gamma_{D^0\to f} = \Gamma\left[1 + \left|\frac{q}{p}\right|(y\cos\phi_D - x\sin\phi_D)\right], \tag{1.81a}$$

$$\Gamma_{\bar{D}^0\to f} = \Gamma\left[1 + \left|\frac{p}{q}\right|(y\cos\phi_D + x\sin\phi_D)\right]. \tag{1.81b}$$

Introducing the A_Γ parameter as the asymmetry of the effective decay widths

$$\begin{aligned} A_\Gamma &= \frac{\Gamma_{D^0\to f} - \Gamma_{\bar{D}^0\to f}}{\Gamma_{D^0\to f} + \Gamma_{\bar{D}^0\to f}} \\ &\simeq \frac{\Gamma_{D^0\to f} - \Gamma_{\bar{D}^0\to f}}{2\Gamma}, \end{aligned} \tag{1.82}$$

Eq. (1.80) can be rewritten as

$$A_{CP}(f,t) = A_{CP}^{\text{dir}}(f) - \Gamma t A_{\Gamma}, \tag{1.83}$$

and so A_Γ is simply

$$A_{\Gamma} = -A_{CP}^{\text{ind}}. \tag{1.84}$$

If a measurement reports $A_\Gamma \neq 0$, it means that *CP* violation is present either in mixing or the interference between decay and mixing.

A residual contribution from indirect *CP* violation must be taken into account in calculating ΔA_{CP} when there is a different experimental decay-time acceptance between $D^0 \to K^+K^-$ and $D^0 \to \pi^+\pi^-$ decays. In fact, the observed distribution of the decay time could be different from the pure exponential $\Gamma e^{-\Gamma t}$. In the presence of an experimental acceptance function $\varepsilon(t)$, the distribution of the decay time becomes $D(t) = \Gamma\varepsilon(t)e^{-\Gamma t}$, and Eq. (1.69) must be calculated by doing the integral $\int_0^\infty \Gamma(M^0/\overline{M}^0(t) \to f)D(t)\mathrm{d}t$. Hence the terms which are linear in t in Eqs. (1.66) and (1.68) will be proportional to the average value of the observed decay time

$$\int_0^\infty tD(t)\mathrm{d}t = \langle t \rangle . \tag{1.85}$$

This means that if the acceptance is different between reconstructed $D^0 \to K^+K^-$ and $D^0 \to \pi^+\pi^-$ decays, ΔA_{CP} will contain a contribution from indirect *CP* violation

$$\Delta A_{CP} = \Delta A_{CP}^{\text{dir}} - \Gamma A_{\Gamma} \Delta \langle t \rangle ,^{3} \tag{1.86}$$

where $\Delta \langle t \rangle = \langle t \rangle_{K^+K^-} - \langle t \rangle_{\pi^+\pi^-}$. In experiments where the reconstruction efficiency does not depend on the decay time, like BaBar and Belle as there is no need to apply decay-time biasing requirements to reject the background, $\langle t \rangle$ is equal to the nominal lifetime τ of the D^0 meson, resulting in sensitivity only to direct *CP* violation. In the analysis described in this thesis, and in general in all analyses performed in LHCb involving charm mesons, some selection criteria introduce an acceptance on the decay time. Hence $\langle t \rangle$ must be measured in order to understand the effect of the indirect *CP* violation in the measurement of ΔA_{CP}, as explained in detail in Sec. 4.6.

No *CP* violation has been observed so far in the decays of charmed mesons, neither direct nor indirect. The agreement of the combination, prior to the analysis

[3] A small correction to Eq. (1.86) is $\Delta A_{CP} = \Delta A_{CP}^{\text{dir}}(1 + \Gamma y_{CP}\overline{\langle t \rangle}) - \Gamma A_\Gamma \Delta \langle t \rangle$, where $y_{CP} = (\Gamma_{D^0 \to f} + \Gamma_{\overline{D}^0 \to f})/2\Gamma - 1$ and $\overline{\langle t \rangle} = (\langle t \rangle_{K^+K^-} + \langle t \rangle_{\pi^+\pi^-})/2$ [65].

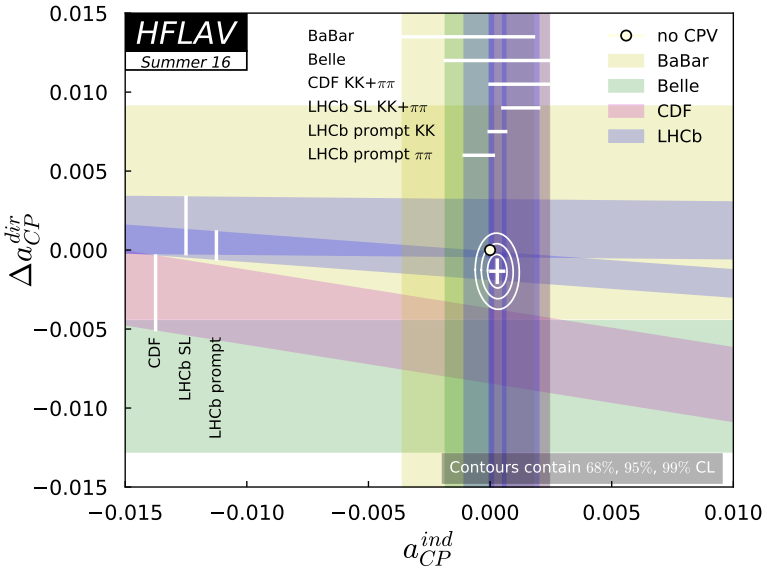

Figure 1.4: Experimental status in the $(\Delta A_{CP}, A_\Gamma)$ plane. The point of no *CP* violation is shown as a filled circle. The overall average is represented by a cross surrounded by ellipses denoting the contours at 68%, 95% and 99.7% confidence levels. For details on the measurements reported in this plot see Ref. [6].

described in this thesis, of the measurements of A_Γ and ΔA_{CP}, reported in Fig. 1.4, with the no-*CP* violation hypothesis has a p-value of about $9.3 \cdot 10^{-2}$. The average values of A_{CP}^{ind} and $\Delta A_{CP}^{\text{dir}}$ are [6]

$$A_{CP}^{\text{ind}} = (0.030 \pm 0.026)\%,$$
$$\Delta A_{CP}^{\text{dir}} = (-0.134 \pm 0.070)\%.$$

The most precise measurements of ΔA_{CP} were performed by LHCb using data collected during the LHC Run 1 [66, 67]:

$$\Delta A_{CP}^{\text{SL}} = (0.14 \pm 0.16\ (\text{stat}) \pm 0.08\ (\text{syst}))\%,$$
$$\Delta A_{CP}^{\text{prompt}} = (-0.10 \pm 0.08\ (\text{stat}) \pm 0.03\ (\text{syst}))\%,$$

in particular $\Delta A_{CP}^{\text{SL}}$ was measured on a sample of D^0 mesons produced from the semileptonic decays of B mesons, while $\Delta A_{CP}^{\text{prompt}}$ was measured using a sample of D^0 mesons promptly produced in pp interactions.

As mentioned before, the calculation of the decay amplitudes of the D^0 decay is difficult because of the presence of long-distance contributions. Anyway, it is

possible to have an estimate of the *CP* asymmetries in charged two-body D^0-meson decays, which result to be around $10^{-3} - 10^{-4}$ [7–10]. In particular, by using LCSR to estimate the hadronic matrix elements involved in the calculation of the $D^0 \to h^+h^-$ decay amplitudes, *CP* asymmetries can be computed without relying on any flavour-symmetry or model-inspired amplitude decomposition, but on the assumption of quark-hadron duality. The *CP* asymmetries and their difference calculated in this way are at the 10^{-4} level. However, to the admission of the authors, the assumption of quark-hadron duality introduces a systematic uncertainty that cannot be estimated reliably.

Chapter 2

The LHCb experiment at the LHC

2.1 The Large Hadron Collider

The Large Hadron Collider (LHC) [68] is a 26.7 km-long hadron synchrotron, located near Geneva across the French and Swiss border, installed about 100 m underground inside the tunnel formerly used for the Large Electron Positron collider. The machine is designed to collide protons up to a centre-of-mass energy of 14 TeV with a luminosity exceeding $10^{34}\,\mathrm{cm}^{-2}\,\mathrm{s}^{-1}$ and lead ions at 2.76 TeV per nucleon with a luminosity of $10^{27}\,\mathrm{cm}^{-2}\,\mathrm{s}^{-1}$. The hadron beams circulate in opposite directions in two accelerating rings and are forced to collide into four interaction points, where LHCb and the three other main CERN experiments (ATLAS, CMS and ALICE) are installed. Since it is not possible to accelerate protons from a quasi-rest condition up to 7 TeV, protons are injected into the LHC from the chain of preaccelerators Linac2 - Proton Synchrotron Booster (PSB) - Proton Synchrotron (PS) - Super Proton Synchrotron (SPS). The linear accelerator Linac2 accelerates the protons up to 50 MeV and injects them into the PSB, which raises their energy to 1.4 GeV. The protons are then passed to the PS, which increases their energy to 25 GeV and forms proton bunches, each containing about 10^{11} protons, which are transferred to the SPS. After being accelerated to 450 GeV, the proton bunches are injected from the SPS into the LHC, where their energy is finally increased to 7 TeV. The complex of CERN accelerators is schematically shown in Fig. 2.1.

During the first run (Run 1) of data taking, LHC operated at centre-of-mass energies of $\sqrt{s} = 7$ and 8 TeV in 2011 and 2012, respectively, with pp collisions. For the second run (Run 2), the collision energy is $\sqrt{s} = 13$ TeV for the years 2015–2018.

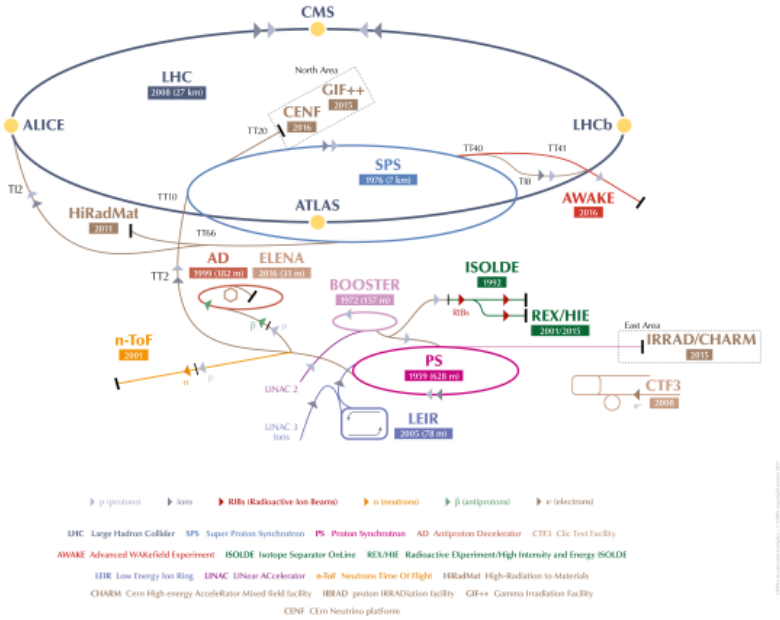

Figure 2.1: The CERN accelerator complex [69].

2.2 The LHCb detector

The LHCb experiment [70] is mainly dedicated to the study of flavour physics, more specifically the physics of beauty and charm hadrons. The main purpose of LHCb is the search for physics processes beyond SM through the study of *CP* violation in b or c decays, the measurement of rare processes and more recently the test of lepton-flavour universality.

LHCb is a single-arm forward spectrometer with a geometrical acceptance of $[10, 250]$mrad in the vertical plane and $[10, 300]$mrad in the horizontal plane. LHCb detects particles with pseudorapidity η [1] ranging between 1.6 and 4.9.

The particular geometry of the LHCb detector has been chosen because most of the $b\bar{b}$ pairs produced in pp interactions hadronise to b hadrons which are highly boosted towards the forward (or backward) beam direction, with a small angle

[1] The pseudorapidity of a particle with θ as polar angle with respect to the beam axis is defined as

$$\eta = -\log\tan\frac{\theta}{2}.$$

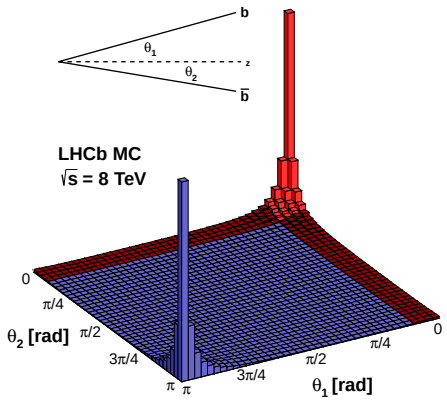

Figure 2.2: Production angles of a $b\bar{b}$ pair with respect to the beam direction

with respect to the beam axis, as can be seen in Fig. 2.2. The $b\bar{b}$ production cross-section measured by LHCb in the pseudorapidity range $2 < \eta < 5$ at centre-of-mass-energies of $\sqrt{s} = 7$ and 13 TeV are $\sigma\left(pp \to b\bar{b}X\right)_{\sqrt{s}=7\,\text{TeV}} = (72.0 \pm 0.3 \pm 6.8)\,\mu\text{b}$ and $\sigma\left(pp \to b\bar{b}X\right)_{\sqrt{s}=13\,\text{TeV}} = (144 \pm 1 \pm 21)\,\mu\text{b}$, respectively [71]. LHCb is optimal also for the study of charm physics, with the additional bonus that the $c\bar{c}$ production cross-section is much larger than the $b\bar{b}$ one, namely $\sigma\left(pp \to c\bar{c}X\right)_{\sqrt{s}=7\,\text{TeV}} = (1419 \pm 12 \pm 116 \pm 65)\,\mu\text{b}$ and $\sigma\left(pp \to c\bar{c}X\right)_{\sqrt{s}=13\,\text{TeV}} = (2369 \pm 3 \pm 152 \pm 118)\,\mu\text{b}$ [72, 73].

In order to keep a low pile-up and to reduce radiation damage of the detector elements closer to the beam pipe, the luminosity at the interaction point of LHCb is kept below the maximum deliverable from LHC by tuning the transverse separation between the beams. To this end, a luminosity levelling technique [74] is used: the beams are progressively brought closer to each other in the transverse plane, such that the rate of collisions is kept constant over the beam lifetime. The instantaneous luminosity was set around $3 \cdot 10^{32}\,\text{cm}^{-2}\text{s}^{-1}$ in 2011, $4 \cdot 10^{32}\,\text{cm}^{-2}\text{s}^{-1}$ in 2012, 2015, 2016, 2017 and about $5 \cdot 10^{32}\,\text{cm}^{-2}\text{s}^{-1}$ in 2018. The total integrated luminosity collected by LHCb is summarised in Fig. 2.3.

LHCb is comprised of multiple sub-detectors, as illustrated in the sketch of Fig. 2.4. They can be divided into two classes based on their purpose

- Tracking system, made up of the the Vertex Locator (VELO), the magnet, the Tracker Turicensis (TT) and three tracking stations (T1-T3).

- Particle identification system, consisting of two ring imaging Cherenkov de-

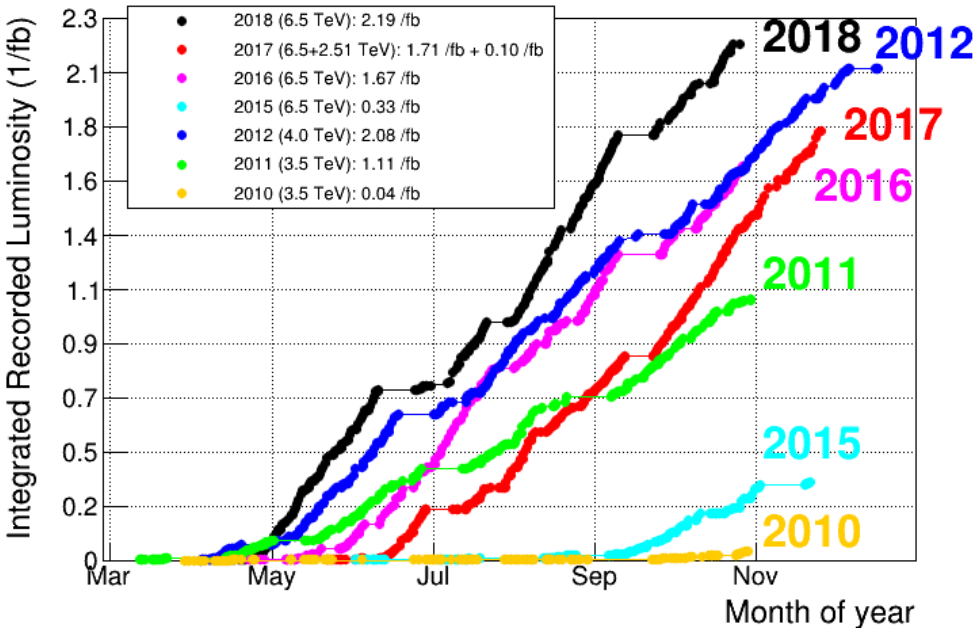

Figure 2.3: Integrated luminosity collected at LHCb, divided by years of data taking.

tectors (RICH1 and RICH2), the electromagnetic calorimeter (SPD, PS and ECAL), the hadronic calorimeter (HCAL) and five muon stations (M1-M5).

A brief description of each sub-detector is given in the following sections.

2.3 The LHCb tracking system

The LHCb tracking system is designed to reconstruct tracks of charged particles and measure their momentum, starting from the VELO in the very proximity of the interaction point. The silicon trackers measure the coordinates of particles flying close to the beam axis, while the external acceptance is covered by the outer tracker made of straw-tubes. The presence of the dipole magnet allows the particle momentum to be measured with very high precision.

2.3.1 The Vertex Locator

Weakly-decaying beauty and charm hadrons travel about 1 cm inside the LHCb detector before decay. For this reason the presence of secondary vertices is a

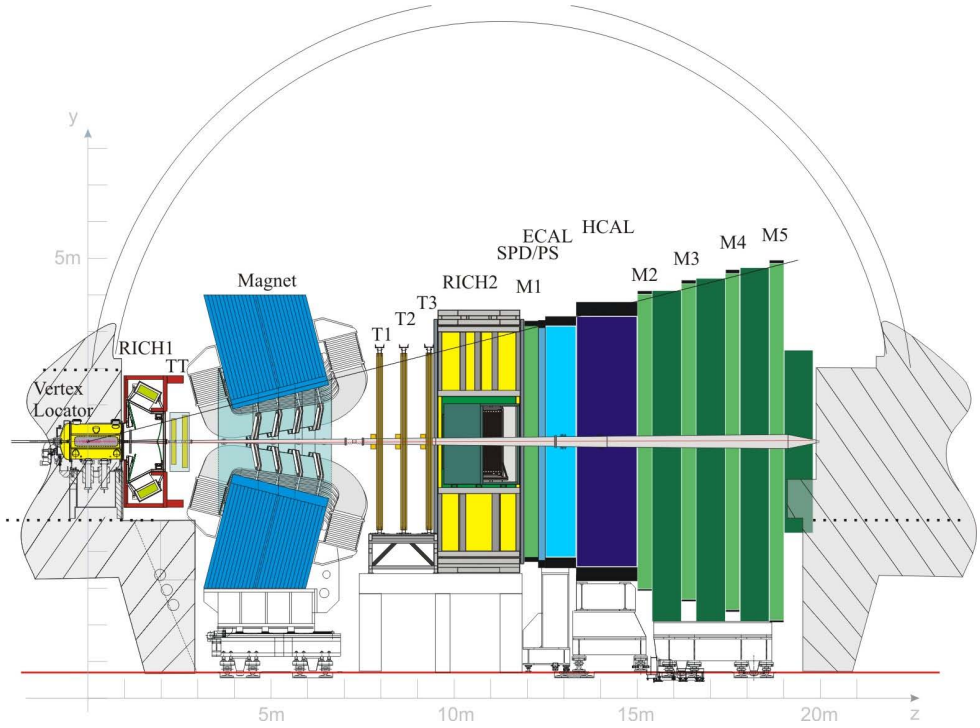

Figure 2.4: The LHCb apparatus. Starting from left, the following sub-components are visible: Vertex Locator (VELO), ring imaging Cherenkov detector RICH1, Tracker Turicensis (TT), dipole magnet, tracking stations (T1-T3), RICH2, first muon station (M1), electromagnetic calorimeter (ECAL), hadronic calorimeter (HCAL), final muon stations (M2-M5).

distinctive feature of b-hadron decays. Their reconstruction with micro-metric precision is therefore fundamental in order to select signal events while rejecting most of the background. The very high spatial resolution is also needed to perform time-dependent analyses, which rely on the precise measurement of particle lifetimes. The VELO detector [75,76], which is the sub-detector placed closest to the interaction point, fulfills these requirements. Its main features are

- The resolution on the position of the primary vertex (PV), as an example reconstructed with 25 tracks, is 70 μm along the z-axis (beam direction) and 13 μm in the transverse plane.
- The resolution on the impact parameter (IP) of charged tracks, calculated with respect to PV along the x (horizontal) or y (vertical) direction, is about 12 μm at high transverse momentum (p_{T}).
- The decay length of heavy-flavoured hadrons is calculated with a resolution ranging from 220 μm to 370 μm.

This sub-detector is comprised of 23 modules placed orthogonally to the beam, each of them made by radiation-tolerant silicon strip sensors, 300 μm thick. Each station, split in a left and a right part, measures the radial coordinate and the azimuthal angle of the charged tracks using two different types of modules. Two of these stations are equipped with only radial sensors and placed upstream of the interaction point, in order to measure the number of interactions per collision and produce the pile-up information for the trigger. The two parts are moved to a safety distance of 3 cm from the beam during LHC injection, and to a distance of only 7 mm during collisions of stable beams. The modules are placed in a vacuum vessel which is separated from the beam vacuum by a 0.5 mm aluminum sheet. A schematic representation of the VELO is reported in Figs. 2.5 and 2.6.

2.3.2 The Tracker Turicensis

The TT is a system composed of four detection layers located after RICH1 and before the magnet, approximately 2.4 m after the beam interaction region. The four layers, 150 cm wide and 130 cm high, are grouped in two stations, TTa and TTb, placed at a distance of about 30 cm from each other. Each layer is made of 500 μm thick silicon vertical micro-strips organised into either two or three readout sectors. In the first and fourth layers the micro-strips are parallel to the vertical axis, while

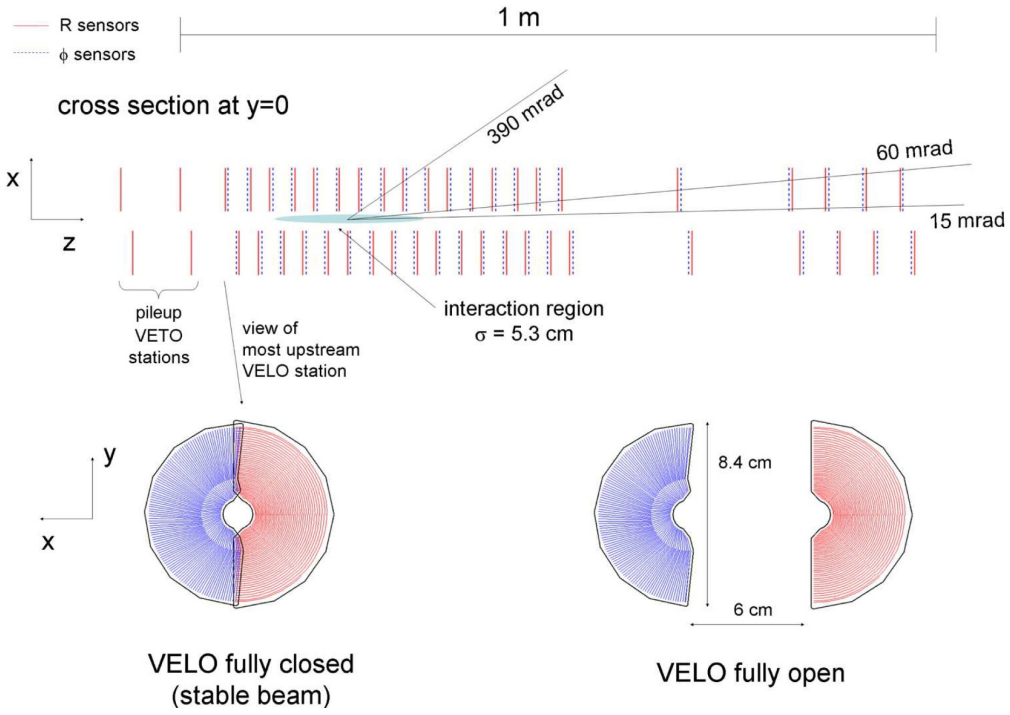

Figure 2.5: Cross-section in the (x, z) plane of the VELO silicon sensors, at $y = 0$, with the detector in the fully closed position. The front face of the first modules is illustrated in both the closed and open positions. The two pile-up veto stations are located upstream of the VELO sensors.

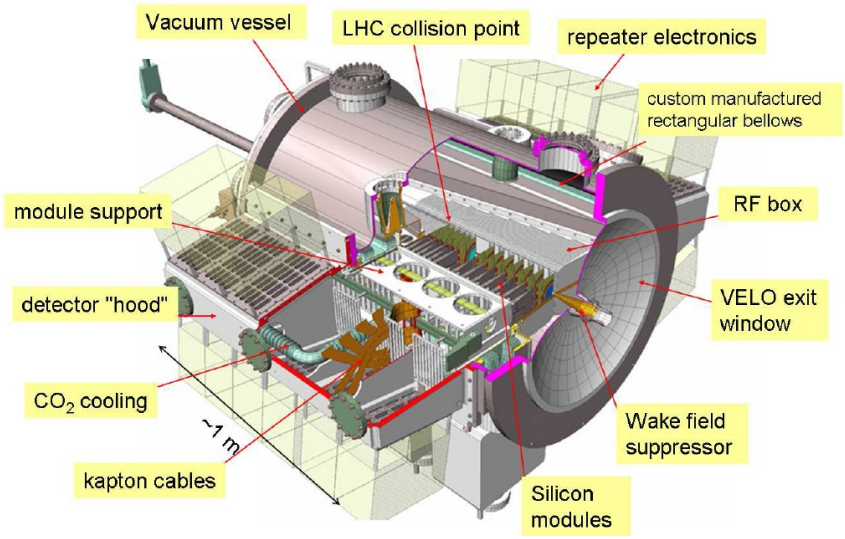

Figure 2.6: Overview of the VELO vacuum vessel.

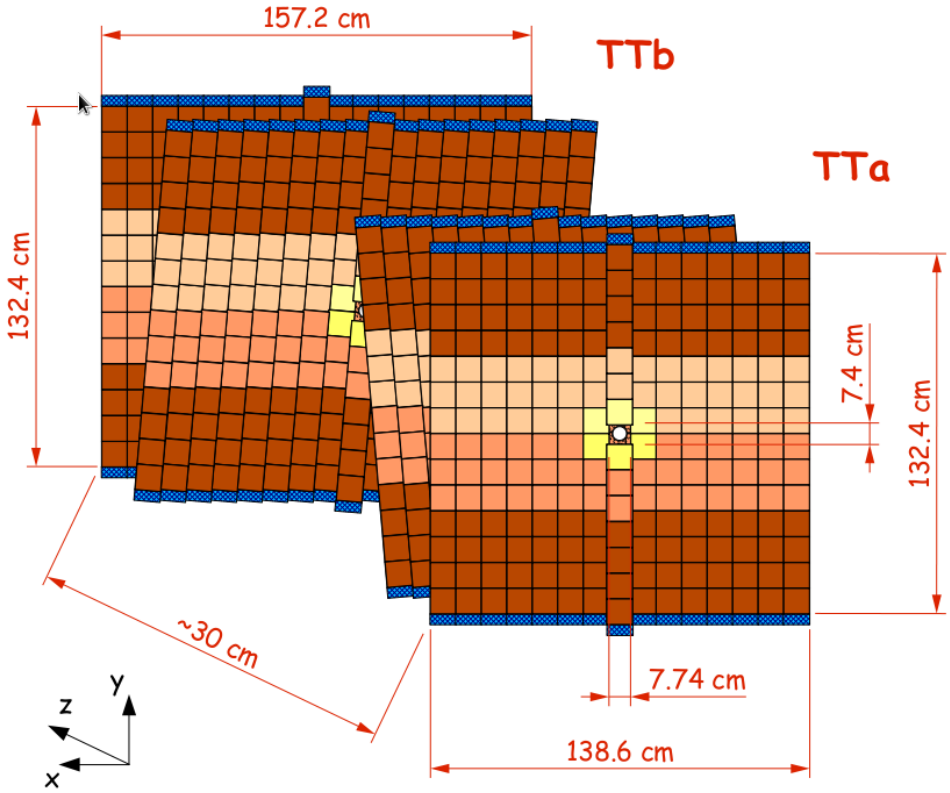

Figure 2.7: Layout of the four detection layers of the TT station.

in the second and third layers the strips are rotated by $+5°$ and $-5°$. The single hit resolution of the TT reaches about 60 µm. A scheme of this sub-detector is shown in Fig. 2.7.

The TT provides reference segments used to combine the track reconstructed in the VELO with those reconstructed in the tracking stations, in order to improve the momentum and coordinate resolution and reduce the number of fake tracks (ghosts).

2.3.3 The tracking stations

The three tracking stations T1, T2 and T3, placed behind the magnet, are divided in two parts which adopt different technologies: the inner part of the tracking stations, made of silicon micro-strip sensors, is called Inner Tracker (IT), while the outer part, composed by drift straw tubes, is called Outer Tracker (OT).

The IT [77] consists of four individual detector boxes placed around the beam

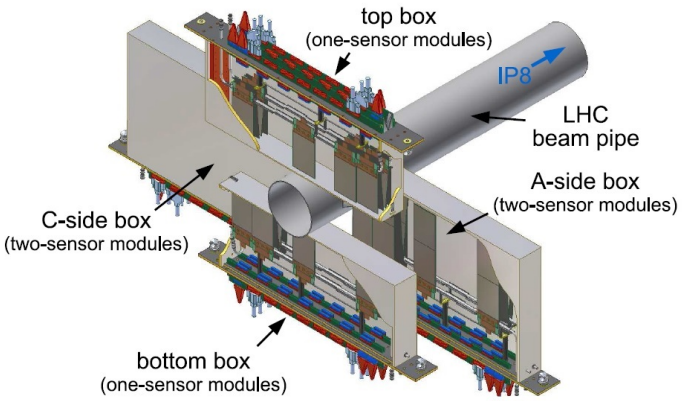

Figure 2.8: View of the four IT detector boxes arranged around the LHC beam pipe.

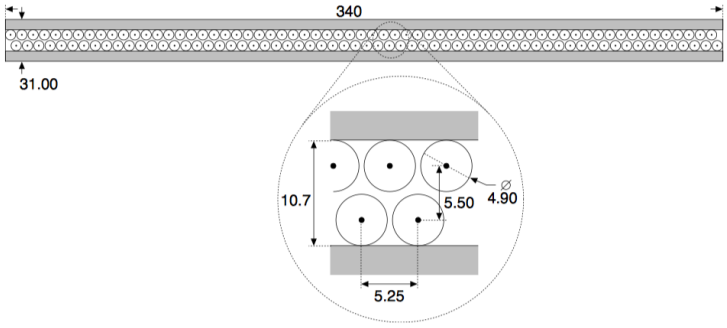

Figure 2.9: Cross-section of an OT plane with a zoom on the straw-tubes. The dimensions are in mm.

pipe, as illustrated in Fig. 2.8. Each box contains four detection layers arranged in the same way as the TT. Each layer is formed by seven modules with one or two sensors, depending on the position. The single hit resolution is about 50 μm.

The OT [78] consists of three stations, each of them made by four modules of straw-tubes arranged with the same geometry as the micro-strips in the IT and the TT. Each module is made up by two rows arranged in a honeycomb structure, as shown in Fig. 2.9. The diameter of each single tube is 4.9 mm. The tubes are filled with a mixture of Argon (70%) and CO_2 (30%), which enables a drift time below 50 ns and a drift-coordinate resolution of 200 mm to be achieved.

2.3.4 The magnet

A warm dipole magnet is used in LHCb to measure the momentum of the charged particles. The magnet, located between the TT and the tracking stations, is formed

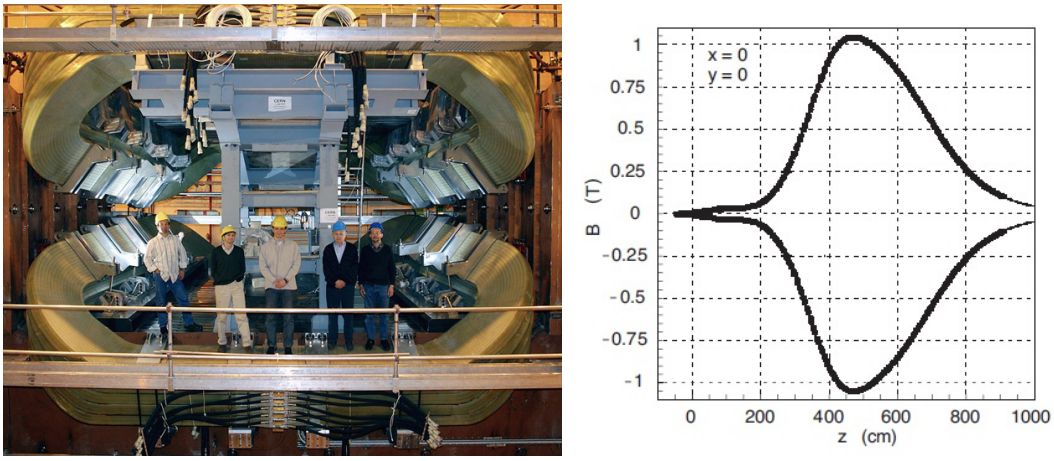

Figure 2.10: (left) Perspective view of the LHCb dipole magnet. (right) Magnetic field intensity along the z axis.

by two identical saddle-shaped coils, bent at 45° on the two transverse sides and mounted inside an iron yoke. The shape of the magnet gap has been designed to follow the detector acceptance. The maximum current in the coils is 6.6. kA, and the total weights of the yoke and the coils are 1500 tons and 54 tons, respectively.

The magnetic field has a vertical direction, in order to deflect charged particles in the horizontal plane (x, z). The strength of the field is variable along the z-axis: it is less than 2 mT in the regions occupied by the RICH detectors and about 1 T between the TT and the tracking stations. The integrated magnetic field is equal to 4 Tm.

The direction of the magnetic field is reversed every few weeks of data taking in order to minimise systematic effects depending on particle charge. In fact, since positive and negative charged particles are bent to opposite directions under the effect of the magnetic field, any variation in the detection efficiency between the left and the right part of the detector could affect *CP* asymmetry measurements. The magnetic-field intensity as a function of the z coordinate and a schematic view of the magnet are reported in Fig. 2.10.

The momentum resolution $\delta p/p$ as a function of the momentum p, measured by studying $J/\psi \to \mu^+\mu^-$ decays [79], is reported in Fig. 2.11. The momentum resolution is about 0.5% for particle momenta below 20 GeV/c and around 0.8% for momenta around 100 GeV/c.

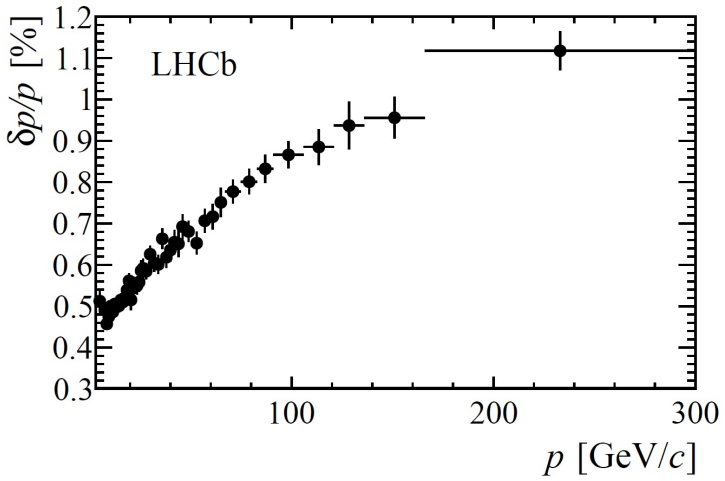

Figure 2.11: Relative momentum resolution versus momentum for tracks traversing the entire detector.

2.4 The LHCb particle identification system

Particle identification is a fundamental task of the LHCb detector. The discrimination between pions, kaons and protons is realised by RICH1 and RICH2. Electron and photons are detected by the calorimeter system, while muons are identified in the muon stations.

2.4.1 The ring imaging Cherenkov detectors

The two RICH detectors [80], RICH1 located between the VELO and the TT and RICH2 between T3 and the first station of the muon detector, play a fundamental role in the particle identification. This structure is sketched in Fig. 2.12. Their working principle is Cherenkov radiation, which is the light emitted by a charged particle when it travels through a medium with a velocity greater than the speed of light in that medium. Cherenkov photons are emitted on a cone of angle θ_c which depends on the refractive index n of the medium and the particle velocity βc

$$\cos\theta_c = \frac{1}{n\beta}. \tag{2.1}$$

By measuring the Cherenkov angle and the momentum of the particle it is then possible to infer its mass.

In order to cover complementary momentum ranges, the two RICH use different radiators. During Run 1 of data taking RICH1 used two radiators: a layer of aerogel,

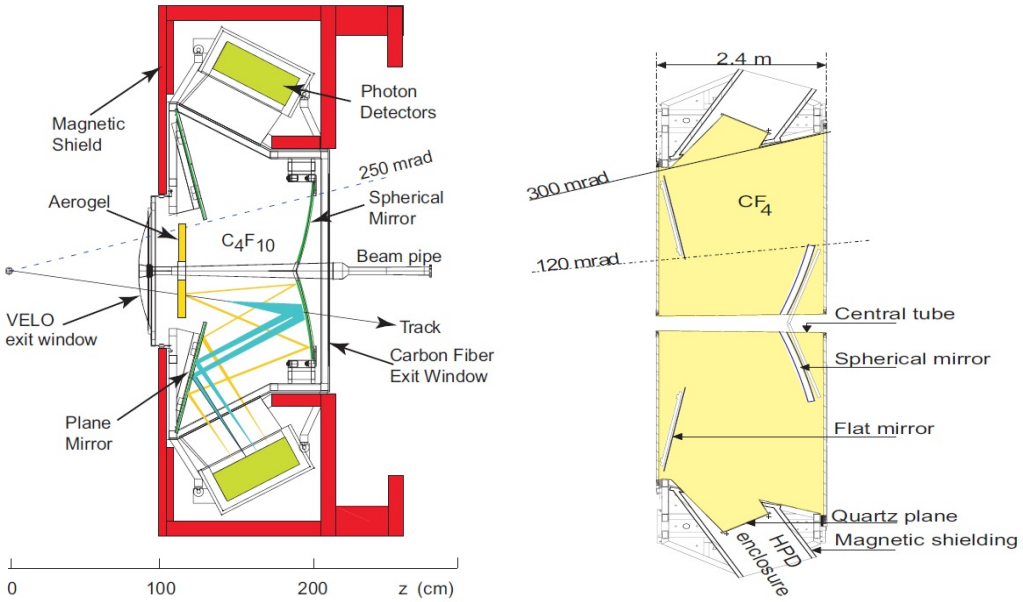

Figure 2.12: (left) Side view of the RICH1 detector. (right) Top view of the RICH2 detector.

suitable for low momentum particles, and fluorobutane (C_4F_{10}), which fills the remaining part of the tank and is needed for higher momentum particles. The layer of aerogel has been removed between Run 1 and Run 2. The tetrafluoromethane (CF_4) has been chosen as radiator for RICH2. RICH1 covers the low momentum range $[1, 60]\,\text{GeV}/c$ and the full LHCb acceptance, while RICH2 covers the high momentum range from $15\,\text{GeV}/c$ to beyond $100\,\text{GeV}/c$, with a limited angular acceptance of $[15, 120]$ mrad in the horizontal plane and up to 100 mrad in the vertical plane.

In both RICH1 and RICH2 detectors a combination of spherical and flat mirrors reflects the Cherenkov light, taking the image onto a lattice of Hybrid Photon Detectors (HPDs), which are located out of the spectrometer acceptance, in a region shielded against the residual magnetic field. The HPDs are vacuum photon detectors in which the photoelectrons, released from the incident photons in a photocathode, are accelerated by an applied high voltage of typically 10 to 20 kV onto a reverse-biased silicon detector. The generated current is then read by the readout electronics, which is able to detect single photoelectrons.

Figure 2.13 shows the dependence of the Cherenkov angle on the particle momentum for different particle species. Different Cherenkov angles produce different rings in the HPD plane, each with radius proportional to θ_c. By measuring the

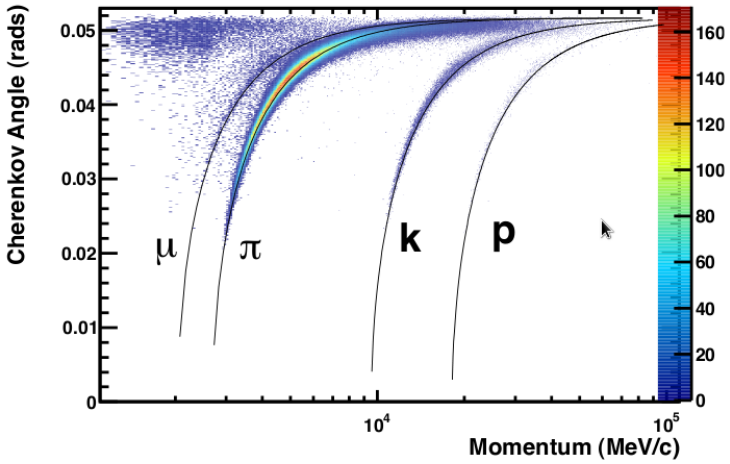

Figure 2.13: Reconstructed Cherenkov angle as a function of particle momentum in RICH1 for μ, π, K and p. The expected curves (solid lines) are superimposed to the experimental results.

Cherenkov angle and the momentum of each particle, the various mass hypotheses can be discriminated. Due to resolution effects, the presence of photons coming from other particles in the event and the complexity of the problem, a dedicated algorithm is adopted to obtain optimal performances. A different approach is needed in order to obtain a good particle discrimination. First of all, for each mass hypothesis, the probability for a single photon produced by a certain particle to be detected by a single HPD is computed Then a likelihood is calculated combining the expected probabilities of all sources and the observed number of photons in the various HPDs. The mass hypotheses which are considered are: pion, kaon, proton, electron, muon. Since the computation of the likelihood for all tracks with all mass hypotheses would be unfeasible, a first global likelihood is computed assigning the pion mass hypothesis to them. Then, for one particle at a time, the mass hypothesis is changed and the difference (called DLL), in the global likelihood is computed. The chosen hypothesis is the one giving the maximum improvement in the global likelihood. The process is then repeated until no further improvement is seen in the likelihood. As an example, the variable $\mathrm{DLL}_{K\pi}$ for the particle h is defined as

$$\mathrm{DLL}_{K\pi}(h) \equiv \log \mathcal{L}_K(h) - \log \mathcal{L}_\pi(h). \tag{2.2}$$

Hence the larger is $\mathrm{DLL}_{K\pi}$ of a particle, the higher is the probability that that particle is a kaon instead of a pion. The performances of the DLL variables for pion, kaons and protons are reported in Fig. 2.14 [81].

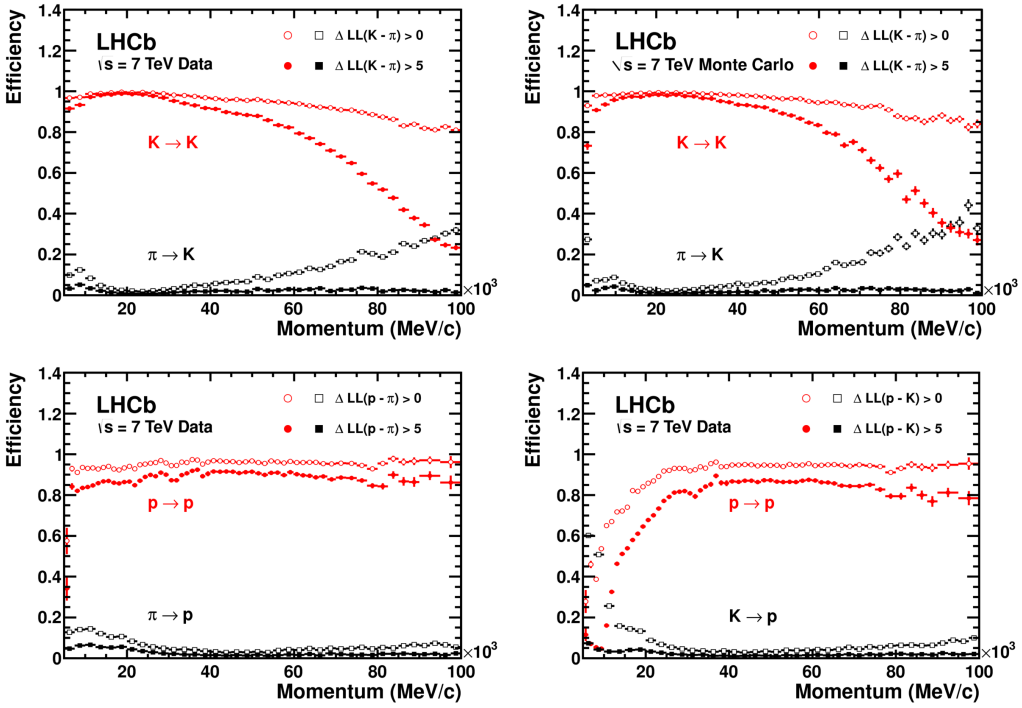

Figure 2.14: (top) Pion mis-identification rate and kaon identification efficiency as a function of the track momentum for (left) data and (right) simulated events. (bottom) Proton identification efficiency for (left) pions and (right) kaons froml data.

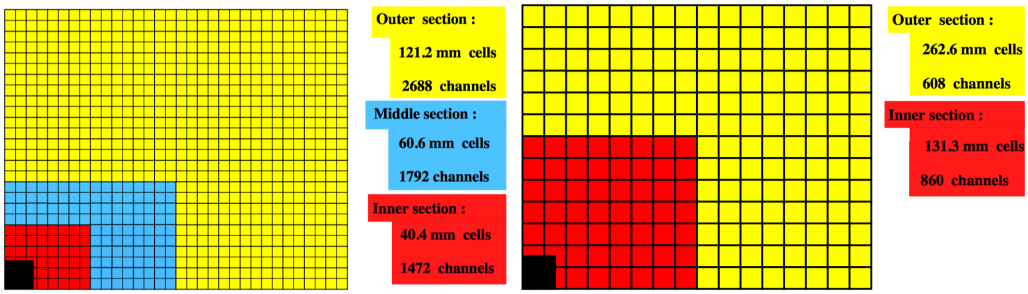

Figure 2.15: Lateral segmentation of one quadrant of (left) ECAL and SPD/PS and (right) HCAL. Cell sizes and number of channels are given for (left) ECAL and (right) HCAL.

2.4.2 The calorimeters

The LHCb calorimeter system [82], placed between the stations M1 and M2 of the muon system, identifies hadron, electron and photon candidates, providing important information for the Level-0 trigger by measuring their transverse energy or momentum. The calorimeter system is composed of (starting from the interaction point): scintillating pad detector (SPD), a lead converter, preshower (PS), electromagnetic calorimeter (ECAL) and hadronic calorimeter (HCAL). Each calorimeter is made of alternating layers of scintillating material and absorbing material. The particles traversing the absorbing material lose energy via electromagnetic or hadronic cascades, which excite the molecules of the scintillating material that emit ultraviolet radiation in an amount proportional to the energy of the particle. The light is then carried away by wavelength-shifting (WLS) fibres to some multi-anode photomultipliers (MAPMTs) located outside the detector.

Since the hit density varies by two orders of magnitude over the surface of the calorimeters, they are split in cells with a variable lateral segmentation, as shown in Fig. 2.15. ECAL and SPD/PS are divided into three different sections, HCAL in two.

The SPD/PS system consists of a 15 mm thick, *i.e.* 2.5 radiation length (X_0), lead converter sandwiched between two identical planes of polystyrene-based scintillating pads with thickness of 15 mm. The SPD allows charged and neutral particles to be distinguished, since charged particles produce light in the scintillator material, while neutrals do not. The PS instead is used to obtain a discrimination between electrons and pions. The sensitive area of this detector is $7.6 \times 6.2\,\mathrm{m}^2$.

Full containment of the electromagnetic showers is needed in order to get the

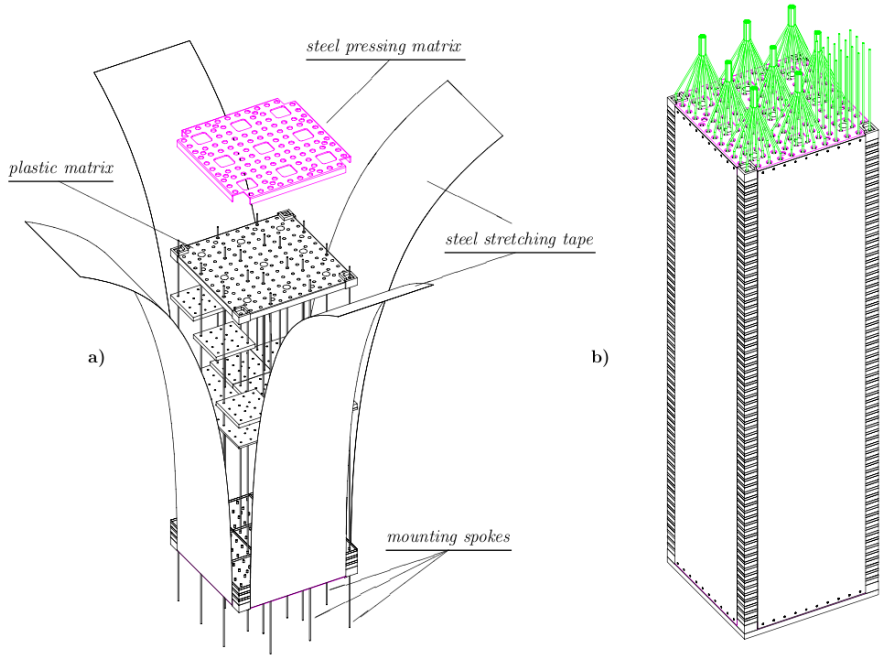

Figure 2.16: (left) Exploded view of one ECAL module. (right) The assembled stack, with the inserted fibres.

optimal energy resolution. For this reason the ECAL thickness is 25 X_0. The ECAL, based on the shashlik technology, consists of 66 lead slices of 2 mm thickness, each one sandwiched between two 4 mm thick polystyrene-based scintillator plates, with each layer incorporating a pattern of holes to house the WLS fibres, as illustrated in Fig. 2.16. The total area of this detector is $7.76 \times 6.30\,\mathrm{m}^2$. The energy resolution of the ECAL is given by

$$\frac{\sigma_E}{E} = \frac{9.5\%}{\sqrt{E}} \oplus 1\%, \tag{2.3}$$

where E is expressed in GeV.

Trigger requirements do not need high energy resolution in the HCAL, so a full containment of the hadronic showers is not necessary. Because of this, the HCAL thickness is 1.2 m, corresponding to 5.6 interaction lengths (λ_{int}). The HCAL alternates 4 mm scintillator planes to 16 mm iron plates, with the tiles installed parallel to the beam, as shown in Fig. 2.17. The energy resolution of the HCAL is

$$\frac{\sigma_E}{E} = \frac{(72.9 \pm 2.9)\%}{\sqrt{E}} \oplus (10.11 \pm 0.45)\%, \tag{2.4}$$

with E expressed in GeV.

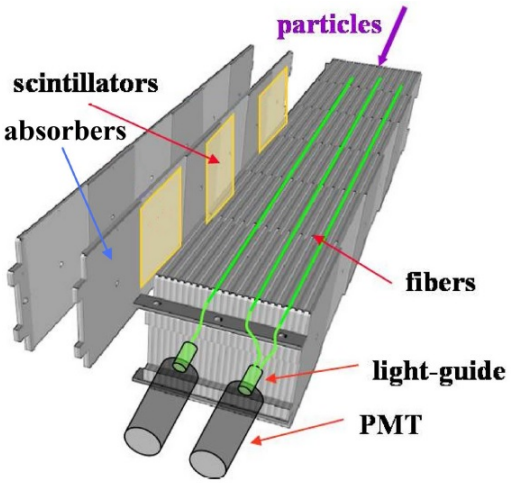

Figure 2.17: A schematic view of a module of HCAL, where two ejected layers show its structure.

Similarly to what happens for RICH, a DLL variable is defined in order to discriminate between hadrons and electrons, which gets information from the ECAL, the HCAL and the PS

$$\mathrm{DLL}_{eh}^{\mathrm{CALO}} = \mathrm{DLL}_{eh}^{\mathrm{ECAL}} + \mathrm{DLL}_{eh}^{\mathrm{HCAL}} + \mathrm{DLL}_{eh}^{\mathrm{PS}}. \tag{2.5}$$

The performance of $\mathrm{DLL}_{eh}^{\mathrm{CALO}}$ is illustrated in Fig. 2.18. By requiring $\mathrm{DLL}_{eh}^{\mathrm{CALO}}$ to be greater than 2, about 90% electron efficiency and 3% $e \to h$ mis-identification rate are achieved.

2.4.3 The muon system

Identification of muons is of great importance in LHCb, because they are present in many sensitive *CP*-violating decays, such as the "golden modes" $B^0 \to J/\psi\,(\mu^+\mu^-)K^0_{\mathrm{S}}$ and $B^0_s \to J/\psi\,(\mu^+\mu^-)\phi$, or in rare decays like $B^0_s \to \mu^+\mu^-$ and $B^0 \to \overline{K}^{*0}\mu^+\mu^-$, which could be sensitive to physics beyond the SM. Muon identification also enables the flavour of the b and c hadrons to be tagged, like in the $\overline{B} \to D^0\mu^-\overline{\nu}_\mu X$ decay.

The LHCb muon system [83] consists of five rectangular stations M1-M5, covering an angular acceptance of ±300 mrad in the horizontal plane and ±200 mrad in the vertical plane, as illustrated in Fig. 2.19. M1 is located before the calorimeters, while the other four stations are after them, at the end of the LHCb detector. M2-M5 are separated from each other by 80 cm thick iron absorbers, in order to select the most

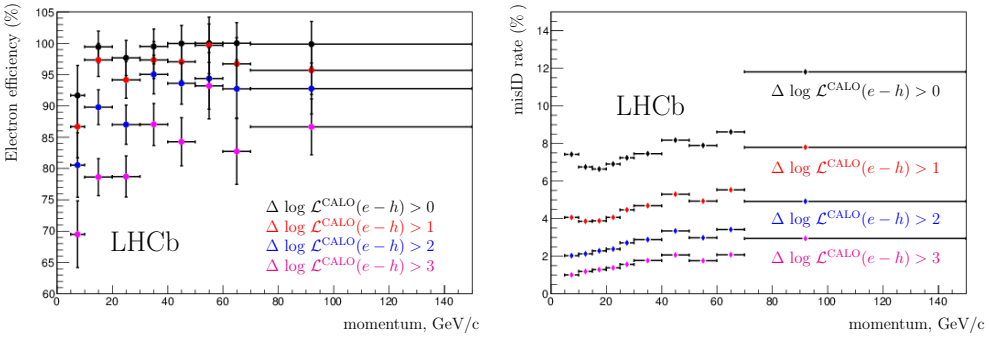

Figure 2.18: (left) Electron identification rate and (right) $e \to h$ mis-identification as a function of momentum, for different requirements on $\mathrm{DLL}_{eh}^{\mathrm{CALO}}$.

penetrating muons. Each station is divided in four concentric regions (R1-R4, where R1 is the closest to the beam pipe), whose linear dimensions and segmentations scale as 1:2:4:8. The particle flux is expected to be about the same over the four regions of a given station. The spatial resolution along the bending plane is higher in the first three stations, in order to define the track direction and to calculate the p_{T} of the candidate muon with a resolution of 20%. The minimum value of momentum needed to a muon to cross all the stations is 6 GeV/c.

The muon system is made of multi wire proportional chambers (MWPCs), except for region R1 of the station M1, where there are 12 chambers composed by two triple GEM detectors. The MWPCs, 1368 in total, have four overlapped gaps of 5 mm filled with a combination of carbon dioxide, tetrafluoromethane and argon, and a wire plane of 2 mm spacing placed in the middle of each gap. They have a time resolution of about 5 ns. Each GEM consists of three gas electron-multiplier foils sandwiched between cathode and anode planes, and can sustain a rate up to 500 kHz/ cm^2 of charged particles, with a time resolution better than 3 ns. Ageing effects of the GEMs due to radiation are expected to be negligible in 10 years of data taking. Figure 2.20 shows the division of each station in chambers and logical pads that define the spatial resolution along x and y.

There are three steps in the muon identification procedure [84]. The first requirement, called *IsMuon*, performs a loose selection on the muon candidate according to the number of muon stations traversed as a function of its momentum. A likelihood is then computed for the muon candidates passing the *IsMuon* selection, taking into account the pattern of the hits around the tracks extrapolated from the

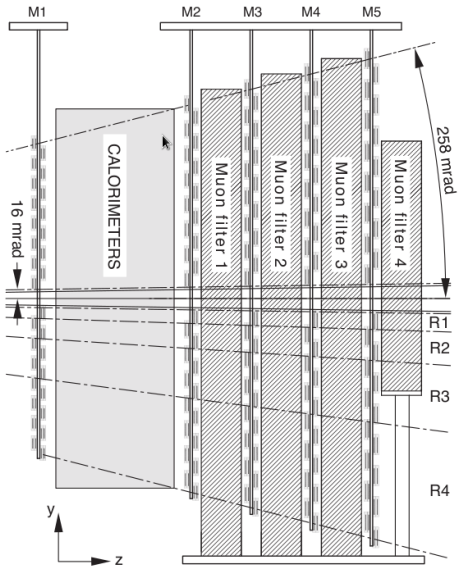

Figure 2.19: Schematic side view of the muon system.

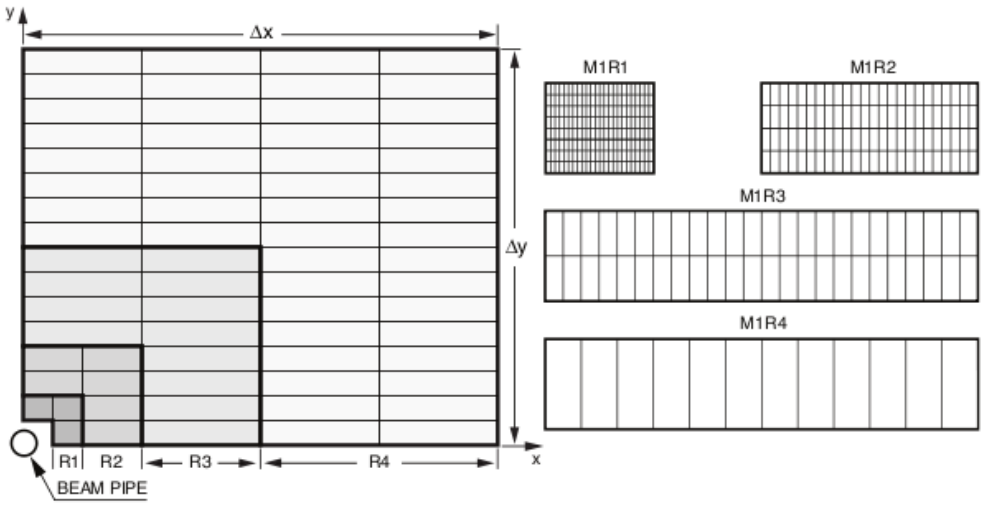

Figure 2.20: (left) Front view of a quadrant of a muon station. Each rectangle represents one chamber. (right) Division into logical pads of four chambers belonging to the M1 station.

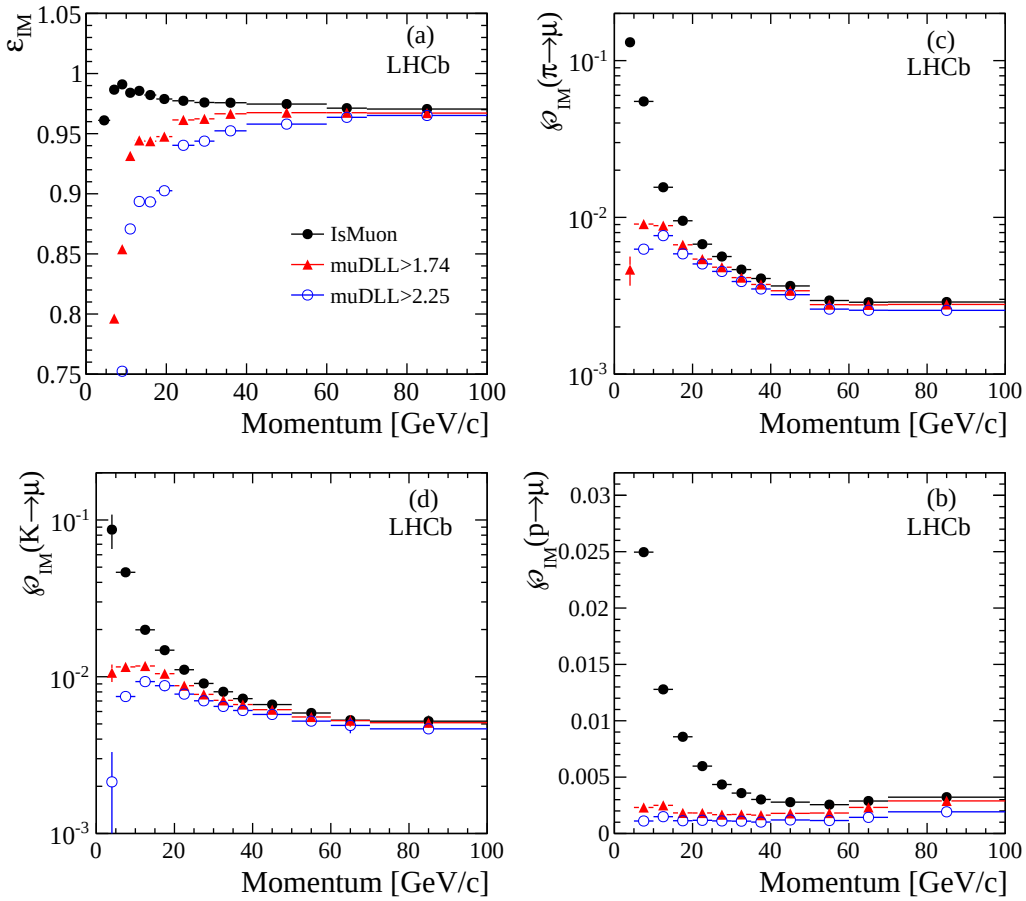

Figure 2.21: (top left) Muon identification efficiency and (top right) pion, (bottom left) kaon and (bottom right) proton mis-identification rates as a function of the track momentum. Various combinations of the *IsMuon* and muDLL requirements are shown.

tracking system to the muon chambers. The ratio between the likelihoods for the muon and the non-muon hypotheses is called muDLL and allows to discriminate between muons and hadrons. The performances of *IsMuon* and muDLL are illustrated in Fig. 2.21.

2.5 The LHCb trigger

The LHCb trigger [85] is a system which allows the interactions seen by the detector to be skimmed, in order to accept only interesting events while rejecting time most of the vastly dominant background, before sending data to mass storage. This

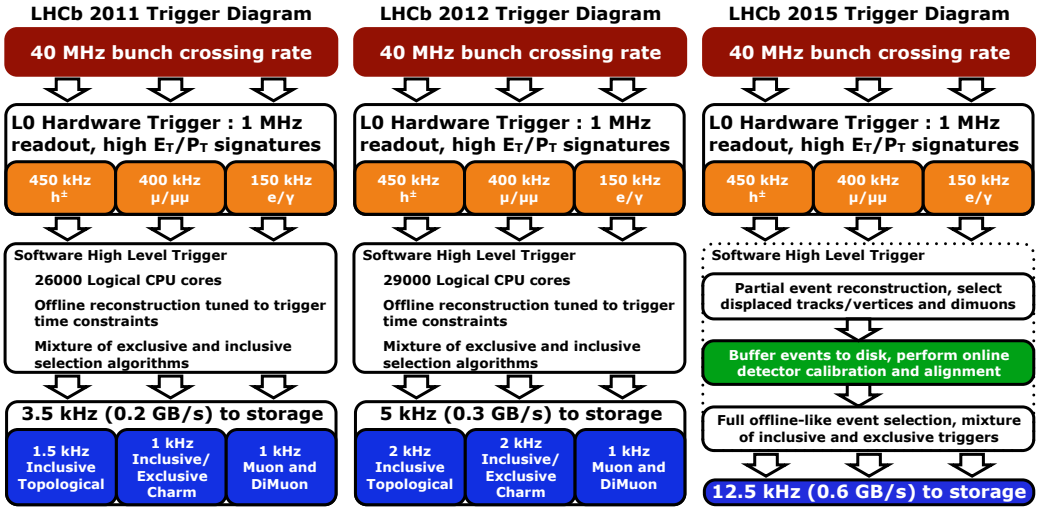

Figure 2.22: Trigger layout during (left) 2011, (centre) 2012 and (right) 2015. The layout used during Run 2 is the same as in 2015.

complex task is performed through three levels, each one processing the output of the previous one

Level-0 (L0): this level is implemented in hardware, based on custom electronics. It is synchronous with the bunch crossing rate of the LHC (40 MHz), and it reduces the event rate to about 1 MHz.

High Level Trigger 1 (HLT1): this level, software-based, filters the events in an inclusive way, reducing the rate to 150 kHz.

High Level Trigger 2 (HLT2): this is the last trigger level, software-based as the HLT1. By applying inclusive and exclusive selections of beauty and charm decays, it reduced the rate to about 3.5–5 kHz in Run 1 and 12.5 kHz in Run 2.

A schematic view of the trigger layout for the various years of data taking is reported in Fig. 2.22. Each of these levels is described more in details in the following sections.

2.5.1 Level-0

Decay products of the b hadrons often have large transverse momentum and transverse energy (E_{T}). The L0 is therefore designed to select events where particles with high p_{T} and E_{T} are present. The L0 is divided in three parts, each of them connected to

its own detector: L0 pile-up, L0 calorimeter and L0 muon. L0 pile-up, which gets information from the two pile-up modules of the VELO, is mainly used to aid the determination of the luminosity and it does not participate in the L0 decisions.

The calorimeter component of L0 measures the E_{T} released in clusters of 2×2 cells of ECAL or HCAL and selects the candidate with the highest E_{T}. If that value of E_{T} is higher than a certain threshold, the event is kept by the L0 trigger. There are three independent triggers which use information from the calorimeter

Hadron trigger (`L0Hadron`): selects the candidate with the highest E_{T} in a cluster of HCAL. If the highest E_{T} of ECAL is located in front of the HCAL cluster, it is added to the candidate E_{T}.

Photon trigger (`L0Photon`): selects the candidate with the highest E_{T} in ECAL, with at most 2 (or 4 in the inner region) PS hits in front of the cluster and no hits in the SPD cells aligned with the PS ones.

Electron trigger (`L0Electron`): has the same requirements as the `L0Photon`, but with at least one additional hit in the SPD cell in front of the cluster.

Typical thresholds for E_{T} are 4 GeV for hadrons and 2.7 GeV for electrons and photons.

The `L0Muon` reconstructs tracks in the muon stations in the following way. It starts from a *seed* hit in M3, extrapolates the direction of the muon, define fields of interest (FOI) around extrapolation points in the other stations and searches for hits in the FOI. The direction defined by the associated hits in M1 and M2 enables the p_{T} of the muon to be determined with a precision of about 20%. The L0 keeps the event if the highest p_{T} is above a certain threshold, whose typical value ranges between 1 GeV/c and 1.8 GeV/c.

The information coming from the various L0 triggers is then processed by a decision unit (DU), which takes the final decision. The L0 latency is 4 µs, *i.e.* the L0 decision must be taken within 4 µs from the bunch crossing.

2.5.2 High Level Trigger 1

The HLT software runs on the event filter farm (EFF), which consists of about 1700 nodes with 27000 physical cores, and a total of 10 PB of hard disk space.

The HLT1 is the first step in the event reconstruction. First of all, the VELO tracks and the PVs are reconstructed, requiring the track to have a minimum number

of hits and large IP with respect to the closest PV. VELO tracks are then matched to hits in the TT, in order to have a first estimate of track charge and momentum and require minimal p and p_{T} thresholds. After this, the track candidates are reconstructed with the information of the remaining tracking stations and fitted using a Kalman filter [86], which takes into account multiple scattering and corrects for energy losses due to ionisation. Finally other requirements on the track χ^2 and the IP significance (χ^2_{IP}) are applied.

A sequence of reconstruction algorithms and selections defines a certain *trigger line*. Combinations of trigger lines together with a L0 configuration form a unique trigger configuration key (TCK), that is a 32 bit word pointing to the database that stores all the parameters which configure the trigger lines.

2.5.3 High Level Trigger 2

The HLT2 performs an event reconstruction similar to the off-line reconstruction, using also information from RICH detectors and calorimeters. The HLT2 includes some hundred trigger lines, which can be grouped as in the following

Inclusive trigger lines, designed to trigger on partially reconstructed b-hadron decays through topological requirements, for example asking at least for two charged tracks coming from a displaced decay vertex fulfilling requirements on track χ^2, IP and particle identification. Two-body objects are built requiring small distance of closest approach (DOCA) between the two decay particles, and in the same way n-body objects are built combining the $(n-1)$-body candidate with another particle.

Exclusive trigger lines, designed for specific final states, requiring all particles to be reconstructed. These lines are tipically used for c hadrons directly produced in pp interactions.

During Run 2, a new data stream was introduced in HLT2, called Turbo stream [87]. This stream is suitable for decays that are fully reconstructed in HLT2. In fact, the information from the rest of the event is discarded to save storage space, in contrast to what happens for the Full stream (*i.e.* the default way of storing data, which allows dedicated event reconstructions to be re-run). The events stored in the Turbo stream have in general a smaller size with respect to those in the Full stream. No offline reconstruction is required prior to physics analysis, since sufficient information

is saved from the HLT2. Turbo will become the default way of processing and storing data in Run 3 after the upgrade of the LHCb detector.

Chapter 3

Measurement of $\mathcal{R}(D^*)$ with three-prong τ decays

In this chapter a detailed description of the measurement of $\mathcal{R}(D^*)$ performed using LHCb data with the three-prong τ decays is given. The signal is the $B^0 \to D^{*-}\tau^+\nu_\tau$ decay, where the D^{*-} is reconstructed through the $D^{*-} \to \overline{D}^0\pi^-$ decay, with $\overline{D}^0 \to K^+\pi^-$, and the τ^+ decay channel is $\tau^+ \to \pi^+\pi^-\pi^+(\pi^0)\overline{\nu}_\tau$[1]. Neutral pions and neutrinos are not reconstructed in this analysis, hence the visible final state consists of five pions plus a kaon. The $B^0 \to D^{*-}3\pi$ decay[2] has the same visible final state as the signal, thus it is chosen as a normalisation channel to minimise experimental systematic uncertainties. It is experimentally convenient to measure the branching fraction $\mathcal{B}(B^0 \to D^{*-}\tau^+\nu_\tau)$ as

$$\mathcal{B}(B^0 \to D^{*-}\tau^+\nu_\tau) = \mathcal{K}(D^*) \cdot \mathcal{B}(B^0 \to D^{*-}3\pi), \tag{3.1}$$

where $\mathcal{K}(D^*)$ is

$$\mathcal{K}(D^*) = \frac{\mathcal{B}(B^0 \to D^{*-}\tau^+\nu_\tau)}{\mathcal{B}(B^0 \to D^{*-}3\pi)}. \tag{3.2}$$

The number of reconstructed signal events after the selection is

$$\begin{aligned} N_{\text{sig}} = 2 \cdot \mathcal{L} \cdot \sigma(pp \to b\bar{b}) \cdot P(b \to B^0) \cdot \mathcal{B}(B^0 \to D^{*-}\tau^+\nu_\tau) \cdot \mathcal{B}(D^{*-} \to \overline{D}^0\pi^-) \\ \cdot \mathcal{B}(\overline{D}^0 \to K^+\pi^-) \cdot [\mathcal{B}(\tau^+ \to 3\pi\overline{\nu}_\tau) + \mathcal{B}(\tau^+ \to 3\pi\pi^0\overline{\nu}_\tau)] \cdot \varepsilon_{\text{sig}}, \end{aligned} \tag{3.3}$$

where $\mathcal{L}$ is the integrated luminosity, $\sigma(pp \to b\bar{b})$ is the $b\bar{b}$ production cross-section and $P(b \to B^0)$ is the probability that b hadronises into a B^0 meson. The reconstruction

[1] Charge conjugated decay modes are implied throughout, unless stated otherwise.
[2] The $\pi^+\pi^-\pi^+$ system is hereafter referred to as 3π.

and selection efficiency $\varepsilon_{\rm sig}$ is the weighted average of the efficiencies on $\tau^+ \to 3\pi\overline{\nu}_\tau$ and $\tau^+ \to 3\pi\pi^0\overline{\nu}_\tau$ decays according to their branching fractions

$$\varepsilon_{\rm sig} = \frac{\mathcal{B}(\tau^+ \to 3\pi\overline{\nu}_\tau) \cdot \varepsilon_{{\rm sig},3\pi\overline{\nu}_\tau} + \mathcal{B}(\tau^+ \to 3\pi\pi^0\overline{\nu}_\tau) \cdot \varepsilon_{{\rm sig},3\pi\pi^0\overline{\nu}_\tau}}{\mathcal{B}(\tau^+ \to 3\pi\overline{\nu}_\tau) + \mathcal{B}(\tau^+ \to 3\pi\pi^0\overline{\nu}_\tau)}. \tag{3.4}$$

In a similar way, the number of normalisation events is

$$\begin{aligned} N_{\rm norm} = 2 \cdot \mathcal{L} \cdot \sigma(pp \to b\bar{b}) \cdot P(b \to B^0) \cdot \mathcal{B}(B^0 \to D^{*-}3\pi) \\ \cdot \mathcal{B}(D^{*-} \to \overline{D}^0\pi^-) \cdot \mathcal{B}(\overline{D}^0 \to K^+\pi^-) \cdot \varepsilon_{\rm norm}. \end{aligned} \tag{3.5}$$

Following Eqs. (3.3) and (3.5), Eq. (3.2) can be written as

$$\mathcal{K}(D^*) = \frac{N_{\rm sig}}{N_{\rm norm}} \cdot \frac{\varepsilon_{\rm norm}}{\mathcal{B}(\tau^+ \to 3\pi\overline{\nu}_\tau) \cdot \varepsilon_{{\rm sig},3\pi\overline{\nu}_\tau} + \mathcal{B}(\tau^+ \to 3\pi\pi^0\overline{\nu}_\tau) \cdot \varepsilon_{{\rm sig},3\pi\pi^0\overline{\nu}_\tau}}. \tag{3.6}$$

As the efficiencies are calculated on the simulated sample, possible correction factors must be taken into account in the efficiency ratio if the simulation does not reproduce the data with sufficient accuracy. If $\varepsilon_{\rm norm,MC}$, $\varepsilon_{{\rm sig},3\pi\overline{\nu}_\tau,{\rm MC}}$ and $\varepsilon_{{\rm sig},3\pi\pi^0\overline{\nu}_\tau,{\rm MC}}$ are the efficiencies evaluated on the simulated sample and r is the product of the various correction factors applied to match the signal-to-normalisation efficiency ratios as observed in data, $\mathcal{K}(D^*)$ is equal to

$$\mathcal{K}(D^*) = \frac{N_{\rm sig}}{N_{\rm norm}} \cdot \frac{\varepsilon_{\rm norm,MC}}{\mathcal{B}(\tau^+ \to 3\pi\overline{\nu}_\tau) \cdot \varepsilon_{{\rm sig},3\pi\overline{\nu}_\tau,{\rm MC}} + \mathcal{B}(\tau^+ \to 3\pi\pi^0\overline{\nu}_\tau) \cdot \varepsilon_{{\rm sig},3\pi\pi^0\overline{\nu}_\tau,{\rm MC}}} \cdot \frac{1}{r}. \tag{3.7}$$

Once $\mathcal{K}(D^*)$ is measured, the average of the measurements of $\mathcal{B}(B^0 \to D^{*-}3\pi)$ available in literature [88–90] enables the value of $\mathcal{B}(B^0 \to D^{*-}\tau^+\nu_\tau)$ to be determined, and then, by using the known value of $\mathcal{B}(B^0 \to D^{*-}\mu^+\nu_\mu)$ [6], a measurement of $\mathcal{R}(D^*)$ is obtained.

The largest background source in this analysis, consisting of inclusive decays of b hadrons to $D^*3\pi X$, is suppressed by requiring a significant displacement between the τ^+ and the B^0 decay vertices and a set of topological and kinematic requirements which are described in Sec. 3.2.3. In order to discriminate from signal the remaining background, mainly due to B decays with a D^{*-} and another charm hadron in the final state, a multivariate analysis, described in Sec. 3.2.5, is used. The output of the multivariate analysis, along with other two variables obtained with a partial reconstruction of the decay kinematics described in Sec. 3.2.4, is used to perform a template fit to extract the signal yield in the data sample, as explained in Sec. 3.5.2. Since the templates representing the various expected contributions in data are built

from simulated samples, some corrections are applied to the simulation in order to adjust possible mismodelling of distributions and efficiencies, as illustrated in Sec. 3.4. Some corrections are performed with the help of the normalisation sample and other control samples whose derivation from data is described in Sec. 3.3. The normalisation yield is obtained by fitting the $D^{*-}3\pi$ invariant-mass distribution in the B^0 peak region, after reverting the τ^+ vertex requirement, as explained in Sec. 3.5.1. The systematic uncertainties associated to the modelling of signal and background and to the various steps of the analysis are evaluated with the procedure described in Sec. 3.6. Finally, the measured values of $\mathcal{K}(D^*)$, $\mathcal{B}(B^0 \to D^{*-}\tau^+\nu_\tau)$ and $\mathcal{R}(D^*)$ are reported in Sec. 3.7.

3.1 Overview of background sources

The most dominant background for this analysis is represented by $B \to D^{*-}3\pi X$ inclusive decays where the 3π system is produced directly from the B decay vertex. From studies on simulated events, the number of B^0 candidates due to this kind of background is expected to be about 100 times higher than that due to signal decays.

Other background decays can be categorised in two classes, depending on whether or not the three pions originate from the same vertex. In the first case, the background consists of B decays with a D^{*-} and another charm hadron in the final state, *i.e. double-charm* decays, which have a topology similar to that of the signal. The most dominant contribution in this class of decays is the $B \to D^{*-}D_s^+(X)$ decay, with $D_s^+ \to 3\pi(X)$. Other important double-charm decays are $B \to D^{*-}D^0(X)$, with $D^0 \to K^-3\pi$, since the K^- of the D^0 final state is not reconstructed, and the $B \to D^{*-}D^+(X)$, with $D^+ \to K^-\pi^+\pi^+$, which can be reconstructed as signal when the K^- of the D^0 final state is misidentified as a pion. Prompt charm decays can also contribute to the background, as for example when the $\overline{D}^0$ is produced directly in the pp interaction and not from the B decay, and is combined with a 3π system. The second category, referred to as *combinatorial* background, mostly consists of decays where two pions originate from the same vertex, while the third comes from the other b hadron produced at the PV, or from a different intermediate particle in the decay chain of the same b hadron, or directly from the PV, or from a different PV.

As explained in Sec. 3.2, various requirements and techniques are implemented to suppress and control all these various sources of background.

3.2 Data and simulated samples

The measurement is performed on a pp-collision data sample collected by LHCb during Run 1, corresponding to $3.0\,\text{fb}^{-1}$ of integrated luminosity. Simulated samples of signal, normalisation and background decays are needed in all steps of the analysis to understand the different background sources, evaluate and optimise the selection efficiency and extract the yields of the various contributions in data. In all simulated samples, generated with 2011 and 2012 data-taking conditions, the six charged tracks of the final state are required to be in the LHCb acceptance.

In the signal simulation, the τ^+ is requested to decay in both $3\pi\overline{\nu}_\tau$ and $3\pi\pi^0\overline{\nu}_\tau$ modes, following the TAUOLA model [91, 92], with the hadronic currents described by the resonance chiral Lagrangian whose parameters are tuned on data collected by BaBar [93, 94]. The B^0 decay is generated according to the ISGW2 model [95]. In order to study the double-charm background, various semi-inclusive samples are used, where B^0, B^+, B_s^0 mesons generally decay into D^*X_cX, with the D^* meson decaying as in the signal mode and the charmed meson $X_c = D_s^+, D^+, D^0, D_{sJ}$ to three charged mesons plus extra particles. Contributions from semileptonic decays where excited D^{**} mesons are present are studied with a simulated sample of $B^0 \to D^{**-}\tau^+\nu_\tau$. A sample of $B^0 \to D^{*-}\tau^+\nu_\tau$, where the τ^+ decays inclusively, is used to evaluate the contamination of τ^+ decays in final states that are different from $3\pi(\pi^0)\overline{\nu}_\tau$. In order to understand the effect of other possible sources of background, an inclusive sample of events where a b hadron decays to the final state $D^{*-}3\pi X$ is used.

3.2.1 Stripping selection

As explained in Sec. 2.5.3, the events selected by the HLT2 are recorded in the Full and in the Turbo streams. The reconstruction and selection of the candidates from the events stored in the Full stream is performed centrally by the *stripping lines*, which are algorithms that build various decay chains and save them in the LHCb standard format (DST). A stripping line contains therefore a set of requirements on kinematic and geometrical properties of final-state particles and reconstructed composite candidates.

The stripping line used for this analysis reconstructs the τ^+ lepton from the combination of three charged tracks identified as pions, that originate from a common vertex which is detached from the PV. The $\overline{D}^0$ meson, made up of two oppositely charged tracks, one identified as a pion and the other as a kaon, is combined with

a slow pion to form a D^{*-}. Finally, the B^0 candidate is obtained by combining the D^{*-} with the τ^+. The various selection requirements imposed by the stripping line on the final-state particles are listed in Table 3.1. The variables involved in the selection are the transverse momentum p_{T}, the total momentum p, the χ^2_{IP} (*i.e.* the difference in the PV fit χ^2 with and without the track), the χ^2 of the fit used to determine the track from the information given by the tracking system (χ^2_{track}), the probability of the track to be reconstructed from random combinations of hits in the detector $P_{\mathrm{track}}(\mathrm{Ghost})$ and the $\mathrm{DLL}_{K\pi}$, defined in Sec. 2.4.1. Table 3.2 reports the selection criteria for the intermediate reconstructed particles and the B^0 candidate. Requirements are imposed on the invariant mass m, the transverse momentum p_{T}, the χ^2_{vtx} of the vertex fit, the distance of closest approach (DOCA) of the child particles, the vertex distance from the PV measured in terms of χ^2 (χ^2_{VD}), and the cosine of the angle between the momentum of the particle and its flight direction (DIRA). Finally, the stripping line requires that at least one track used to reconstruct the B^0 fires the trigger line `Hlt1TrackAllL0`, defined in Sec. 3.2.2. Another stripping line is used to select *wrong-sign* events, *i.e.* events where the D^{*-} candidate is combined with a $\pi^-\pi^+\pi^-$ system, with the same requirements as the nominal stripping line. This wrong-sign sample is useful to study the combinatorial background.

The stripping efficiencies for the signal $B^0 \to D^{*-}\tau^+(\to 3\pi\overline{\nu}_\tau)\nu_\tau$, $B^0 \to D^{*-}\tau^+(\to 3\pi\pi^0\overline{\nu}_\tau)\nu_\tau$ and the normalisation $B^0 \to D^{*-}3\pi$ are evaluated from simulation and are equal to 0.826%, 0.729% and 1.382%, respectively.

3.2.2 Trigger selection

A trigger can be fired by tracks belonging to the signal candidate or to a certain intermediate particle in the signal decay chain. In these cases one talks about trigger on signal (TOS). If a trigger is fired by tracks which do not come from signal decay, it is said to be trigger independent of signal (TIS). The following trigger requirements are applied to the events surviving the stripping selection

L0 trigger: `L0Hadron_TOS` on the D^{*-} or `L0Global_TIS` on the B^0, *i.e.* the event is accepted if at least one track from the D^{*-} fires the `L0Hadron` or other particles not belonging to the B^0 fire any L0 trigger.

HLT1: `Hlt1TrackAllL0_TOS` on the B^0, which means that the event is accepted if at least one track used to build the B^0 fires the `Hlt1TrackAllL0` line, which

Table 3.1: Stripping requirements applied to the tracks of the final state.

Particle	Variable	Selection requirement
K^+, π^- from $\overline{D}^0$	p_{T}	$> 250\,\mathrm{MeV}/c$
	χ^2_{IP}	> 10
	p	$> 2000\,\mathrm{MeV}/c$
	$P_{\mathrm{track}}(\mathrm{Ghost})$	< 0.4
	$\chi^2_{\mathrm{track}}/\mathrm{ndof}(K^+)$	< 30
	$\chi^2_{\mathrm{track}}/\mathrm{ndof}(\pi^-)$	< 3
	$\mathrm{DLL}_{K\pi}(K^+)$	> -3
	$\mathrm{DLL}_{K\pi}(\pi^-)$	< 50
π^- from D^{*-}	p_{T}	$> 50\,\mathrm{MeV}/c$
	$\chi^2_{\mathrm{track}}/\mathrm{ndof}$	< 30
	$P_{\mathrm{track}}(\mathrm{Ghost})$	< 0.6
π^+, π^-, π^+ from τ^+	p_{T}	$> 250\,\mathrm{MeV}/c$
	χ^2_{IP}	> 4
	$\chi^2_{\mathrm{track}}/\mathrm{ndof}$	< 3
	$P_{\mathrm{track}}(\mathrm{Ghost})$	< 0.4
	$\mathrm{DLL}_{K\pi}$	< 8

has certain requirements on VELO hits, p, p_{T}, $\chi^2_{\mathrm{track}}/\mathrm{ndof}$ and χ^2_{IP} [96].

HLT2: `Hlt2Topo*` and one between `Hlt2CharmHadD02HH_D02KPi_TOS` on the $\overline{D}^0$ and `Hlt2Topo2(3)(4)BodyBBDT_TOS` on the B^0 is fired. This requires any topological line in the event to be fired and the presence of either a two-track vertex consistent with a $D^0 \to K^-\pi^+$ decay, or a two-, three-, or four-track secondary vertex consistent with the decay of a b hadron, with a significant displacement from any PV.

3.2.3 "Cut"-based selection

The first step of the offline selection applied to the events filtered by the stripping line described in Sec. 3.2.1 and the trigger selection reported in Sec. 3.2.2 consists of a set of requirements involving different properties of the reconstructed particles. The list of requirements is reported in Table 3.3.

As explained in Sec. 3.1, the dominant background consists of candidates where the 3π system originates directly from the B decay vertex, *i.e.* $B \to D^{*-}3\pi X$ inclusive decays. Such a background is highly suppressed by requiring the distance between the 3π and the B^0 vertices along the beam direction, $\Delta z(3\pi, B^0) = \mathrm{vtx}_z(3\pi) - \mathrm{vtz}_z(B^0)$,

Table 3.2: Stripping requirements applied on the intermediate particles and the B candidate.

Particle	Variable	Selection requirement
$\overline{D}^0$	p_{T}	$> 1200\,\mathrm{MeV}/c$
	m	$\in [1825, 1905]\ \mathrm{MeV}/c^2$
	χ^2_{vtx}	< 10
	χ^2_{VD}	> 36
	$p_{\mathrm{T}}(\pi^-) + p_{\mathrm{T}}(K^+)$	$> 1200\,\mathrm{MeV}/c$
	$\mathrm{DOCA}(K^+, \pi^-)$	$< 0.5\,\mathrm{mm}$
	$\chi^2_{\mathrm{DOCA}}(K^+, \pi^-)$	< 15
	$\cos(\mathrm{DIRA})$	> 0.995
D^{*-}	p_{T}	$> 1250\,\mathrm{MeV}/c$
	m	$\in [1960, 2060]\ \mathrm{MeV}/c^2$
	χ^2_{vtx}	< 25
	$m(D^{*-}) - m(\overline{D}^0)$	$\in [135, 150]\ \mathrm{MeV}/c^2$
τ^+	$m(3\pi)$	$\in [400, 3500]\ \mathrm{MeV}/c^2$
	$\cos(\mathrm{DIRA})$	> 0.99
	χ^2_{vtx}	< 25
	$\min[m(\pi^+\pi^-)]$	$< 1670\,\mathrm{MeV}/c^2$
	n° of π with $p_{\mathrm{T}} > 300\,\mathrm{MeV}/c$	> 1
	$\max[\mathrm{DOCA}(\pi^+, \pi^-, \pi^+)]$	$< 0.15\,\mathrm{mm}$
	n° of π with $\chi^2_{\mathrm{IP}} > 5$	> 1
B^0	$m(D^{*-}) - m(3\pi)$	$\in \begin{cases} [-2579, 300]\ \mathrm{MeV}/c^2 \\ \mathrm{OR} \\ [720, 1721]\ \mathrm{MeV}/c^2 \end{cases}$
	$\mathrm{DOCA}(D^{*-}, 3\pi)$	$< 0.15\,\mathrm{mm}$
	$\cos(\mathrm{DIRA})$	> 0.995

to be greater than four times its uncertainty $\sigma_{\Delta z(3\pi, B^0)}$. Figure 3.1 shows how effective this requirement is in suppressing prompt $B \to D^{*-}3\pi X$ decays, namely by three orders of magnitude, resulting in an improvement of the signal-to-noise ratio by a factor 160. A schematic representation of the signal topology after applying the detached-vertex requirement is reported in Fig. 3.2. The 3π visible mass $m(3\pi)$ is required to be less than $1600\,\mathrm{MeV}/c^2$, since, looking at the distribution of this quantity in the simulation, only 1% of signal is present above this value. The q^2 variable, obtained by performing the partial reconstruction defined in Sec. 3.2.4, must be positive in order to remove events where the partial reconstruction provides

Table 3.3: List of requirements applied in the "cut"-based selection.

Variable	Requirement	Addressed background
$\Delta z(3\pi, B^0)/\sigma_{\Delta z(3\pi,B^0)}$	> 4	$B \to D^{*-}3\pi X$
$\Delta z(3\pi, \mathrm{PV})/\sigma_{\Delta z(3\pi,\mathrm{PV})}$	> 10	prompt charm
$\chi^2_{\mathrm{IP}}(\overline{D}^0)$	> 10	prompt charm
$\sqrt{[\mathrm{vtx_x}(3\pi)]^2 + [\mathrm{vtx_y}(3\pi)]^2}$	$\in [0.4, 6]$ mm	combinatorial
$\chi^2_{\mathrm{IP}}(\pi)$, π from τ^+	> 15	combinatorial
$\mathrm{PV}(\overline{D}^0)$	$= \mathrm{PV}(3\pi)$	combinatorial
$\chi^2_{\mathrm{vtx}}(3\pi)$	< 10	combinatorial
q^2	> 0	combinatorial
$m(D^{*-}) - m(\overline{D}^0)$	$\in [143, 148]$ MeV/c^2	combinatorial D^{*-}
$m(\overline{D}^0)$	$\in [1846, 1886]$ MeV/c^2	combinatorial $\overline{D}^0$
`ProbNNpi`(π), π from τ^+	> 0.6	misidentification
`ProbNNpi`(π^-), π^- from D^{*-}	> 0.1	misidentification
number of B^0 candidates	$= 1$	high track multiplicity
`ProbNNk`(π^-), π^- from τ^+	< 0.1	$D^+ \to K^-\pi^+\pi^+$
$m(3\pi)$	$< 1600\,\mathrm{MeV}/c^2$	double-charm
non-isolated tracks	$= 0$	double charm

non-physical results.

Additional topological requirements are imposed in order to suppress combinatorial background due to wrong 3π combination, such as on the χ^2_{vtx} of the 3π, the χ^2_{IP} of the pions coming from the τ^+ and the flight distance of the 3π in the transverse plane. Combinatorial background due to bad reconstruction of $\overline{D}^0$, D^{*-} or B^0 is addressed by requiring the associated PV of the $\overline{D}^0$ to be the same as that of the 3π, and by asking $m(\overline{D}^0)$ and $m(D^{*-}) - m(\overline{D}^0)$ to be in certain ranges. Requiring the 3π vertex to be significantly displaced from the PV and the χ^2_{IP} of the $\overline{D}^0$ to be high allows most of the background due to prompt charm decays to be removed.

Decays like $D^+ \to K^-\pi^+\pi^+$ and $D^+ \to K^-\pi^+\pi^+\pi^0$ contribute significantly to the $B \to D^{*-}D^+(X)$ background when the kaon is misidentified as a pion. Such decays are suppressed by applying requirements on `ProbNNpi` and `ProbNNk` of pions, where `ProbNNpi(k)` is the probability, computed through a neural network trained on simulation, for a detected particle to be a pion (kaon).

The number of candidates per event must be equal to one, in order to suppress five-prong backgrounds, which are mainly due to double-charm decays. In order to suppress further the double-charm background, which has the same topology as the signal, an isolation algorithm, which looks for additional charged or neutral particles

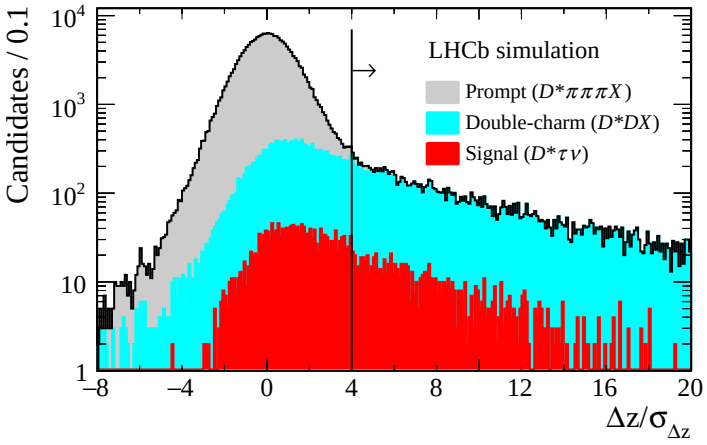

Figure 3.1: Distribution of the distance between the 3π and the B^0 vertices along the beam direction, $\Delta z(3\pi, B^0)$, divided by its uncertainty, from simulation. The vertical line shows the requirement used in the analysis to reject the prompt background component, which is represented by the grey area. The red and cyan areas correspond to signal and double-charm components, respectively.

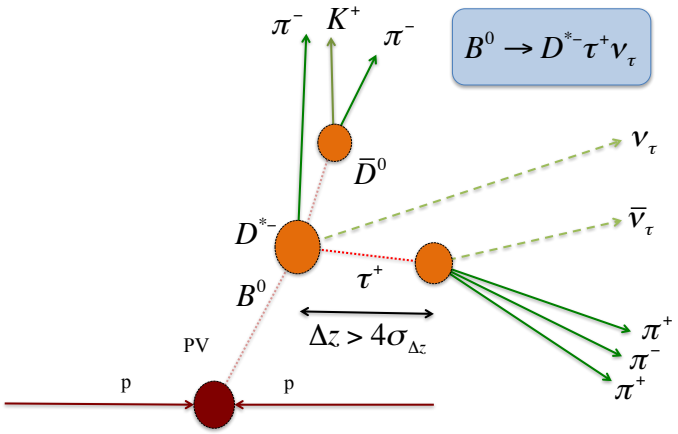

Figure 3.2: Schematic view of the topology of the signal decay, requiring $\Delta z(3\pi, B^0)/\sigma_{\Delta z(3\pi,B^0)} > 4$.

Table 3.4: List of requirements needed by a track to be selected by the charged-isolation algorithm.

Variable	Requirement
p_{T}	$> 250\,\mathrm{MeV}/c$
$\chi^2_{\mathrm{IP}}(\mathrm{PV})$	> 4
$\chi^2_{\mathrm{IP}}(B^0)$	< 25
$\chi^2_{\mathrm{IP}}(3\pi)$	< 25

produced in conjuction with the reconstructed particles, is used. The charged-isolation algorithm searches for extra tracks in the event which are compatible, according to the kinematic and topological criteria specified in Table 3.4, with coming from the τ^+ or B^0 vertices. If any of these non-isolated tracks are found, the B^0 candidate is rejected. The performance of the non-isolated-tracks requirement is evaluated on simulation using the $B^0 \to D^{*-} D^0 K^+(X_1)$ decay, with $D^0 \to K^- 3\pi(X_2)$, since this decay contains two extra kaons, one coming from the D^0 vertex (which is reconstructed as the 3π vertex) and the other from the B^0 vertex. The resulting measured rejection factor is 95%, and so the charged-isolation algorithm is very effective in suppressing the double-charm background. The selection efficiency of the charged-isolation algorithm on the $B^0 \to D^{*-} 3\pi$ data sample (see below for a description of the selection of the normalisation sample) is 80%. This value is in good agreement with the efficiency measured for the signal decay from simulation. This represents a good consistency check, as the charged-isolation algorithm is expected to have the same efficiency on signal and normalisation, due to the fact that both these channels have no additional charged tracks coming from the B^0 vertex.

Normalisation selection

The selection applied to obtain the normalisation sample is the same as that used for the signal, except for the requirement on $\Delta z(3\pi, B^0)$, which is replaced by $\Delta z(\overline{D}^0, 3\pi) > 4$, and the requirements on $m(3\pi)$ and q^2. All of the others requirements listed in Table 3.3 are applied. The invariant-mass distribution of the $D^* 3\pi$ system for events surviving the selection is reported in Fig. 3.3, which shows the clear peak due to the exclusive $B^0 \to D^{*-} 3\pi$ decay.

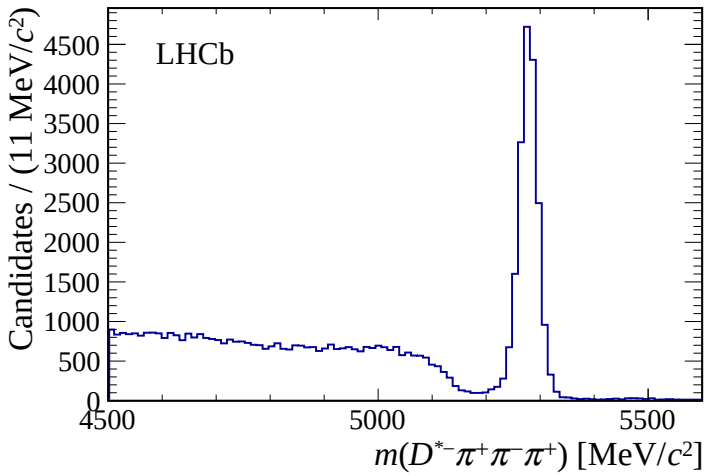

Figure 3.3: Distribution of the $D^{*-}3\pi$ invariant mass after the normalisation selection.

3.2.4 Reconstruction of the decay kinematics

The presence of two neutrinos in the signal decay or undetected particles in double-charm background decays makes the full reconstruction of the decay kinematics impossible. However, by appyling mass constraints and momentum conservation, it is possible to calculate with a good enough approximation the momenta of the various particles in the decay with two different techniques: one for the signal and one for the $B \to D^{*-} D_s^+(X)$ decay. While the former allows variables whose distributions are needed for the final fit to be computed, the latter provides variables that help to discriminate between signal and double-charm background decays.

Reconstruction in the signal hypothesis

Even if the total momenta of the τ^+ and the B^0 are not reconstructed because of the presence of the neutrinos in the decay, the τ^+ line of flight (and then the momentum direction) is known, since both the B^0 and τ^+ decay vertices are measured. The τ^+ momentum magnitude $\vec{p}_\tau$ is obtained up to a two-fold ambiguity by applying the mass constraint on the τ^+

$$|\vec{p}_\tau| = \frac{(m_{3\pi}^2 + m_\tau^2)|\vec{p}_{3\pi}| \cos\theta_{\tau,3\pi} \pm E_{3\pi}\sqrt{(m_\tau^2 - m_{3\pi}^2)^2 - 4m_\tau^2 |\vec{p}_{3\pi}|^2 \sin^2\theta_{\tau,3\pi}}}{2(E_{3\pi}^2 - |\vec{p}_{3\pi}|^2 \cos^2\theta_{\tau,3\pi})}, \quad (3.8)$$

where $\theta_{\tau,3\pi}$ is the unknown angle between the τ^+ line of flight and the 3π system momentum, m_τ is the nominal τ^+ mass and $|\vec{p}_{3\pi}|$, $m_{3\pi}$ and $E_{3\pi}$ are the momentum,

mass and energy of the 3π system, respectively. In order to solve the two-fold ambiguity, the value of $\theta_{\tau,3\pi}$ making the discriminant of Eq. (3.8) to vanish is chosen. This corresponds to the maximum allowed value of $\theta_{\tau,3\pi}$

$$\theta^{\max}_{\tau,3\pi} = \arcsin\left(\frac{m_\tau^2 - m_{3\pi}^2}{2m_\tau|\vec{p}_{3\pi}|}\right). \tag{3.9}$$

Once $|\vec{p}_\tau|$ is calculated, the same procedure is applied to estimate the B^0 momentum

$$|\vec{p}_{B^0}| = \frac{\left(m^2_{D^{*}\tau}+m^2_{B^0}\right)|\vec{p}_{D^{*}\tau}|\cos\theta_{B^0,D^{*}\tau} \pm E_{D^{*}\tau}\sqrt{\left(m^2_{B^0}-m^2_{D^{*}\tau}\right)^2 - 4m^2_{B^0}|\vec{p}_{D^{*}\tau}|^2\sin^2\theta_{B^0,D^{*}\tau}}}{2\left(E^2_{D^{*}\tau}-|\vec{p}_{D^{*}\tau}|^2\cos^2\theta_{B^0,D^{*}\tau}\right)}, \tag{3.10}$$

where all quantities are defined in the same way as in Eq. (3.8). The two-fold ambiguity is resolved again by choosing the value

$$\theta^{\max}_{B^0,D^{*}\tau} = \arcsin\left(\frac{m^2_{B^0} - m^2_{D^{*}\tau}}{2m_{B^0}|\vec{p}_{D^{*}\tau}|}\right). \tag{3.11}$$

The three-momentum and mass of the $D^{*-}\tau^+$ system used in Eq. (3.10) are calculated using the previously estimated τ^+ momentum $\vec{p}_\tau$.

Subsequently the exchanged four-momentum $q^2 = (p_{B^0} - p_{D^{*-}})^2$ and the τ^+ decay time t_τ are calculated. Even if $|\vec{p}_\tau|$ and $|\vec{p}_{B^0}|$ are computed with an approximation needed to solve the two-fold ambiguities due to the two mass constraints, q^2 and t_τ differ from their actual values with an accuracy which is sufficient to retain their discriminating power against double-charm backgrounds. Both these variables are in fact used in the fit performed to determine the signal yield. The difference between the reconstructed and the true value of q^2 divided by the true q^2 in signal simulated events is shown in Fig. 3.4, along with the resolution on the t_τ variable. The relative q^2 resolution is 18% full-width half-maximum, corresponding to an average resolution of $1.2\,\mathrm{GeV}^2/c^4$. The average resolution on t_τ is about 0.25 ps. No significant biases are observed.

An alternative approach consists in performing a minimisation of χ^2_{rec}, which is a function of the parameters describing the decay, namely the vertex positions and the momenta of the τ^+, D^{*-} and B^0, which are varied within their measured uncertainties. This χ^2_{rec} is a measure of how close the event kinematics are to those of a signal decay, *i.e.* a decay with two missing (quasi) massless particles. In this way the angles are not chosen to solve the two-fold ambiguities, but they are obtained by the output of the χ^2_{rec} minimisation. Since the χ^2_{rec} is expected to be lower for signal events, it is used as an input variable for the multivariate analysis described in Sec. 3.2.5.

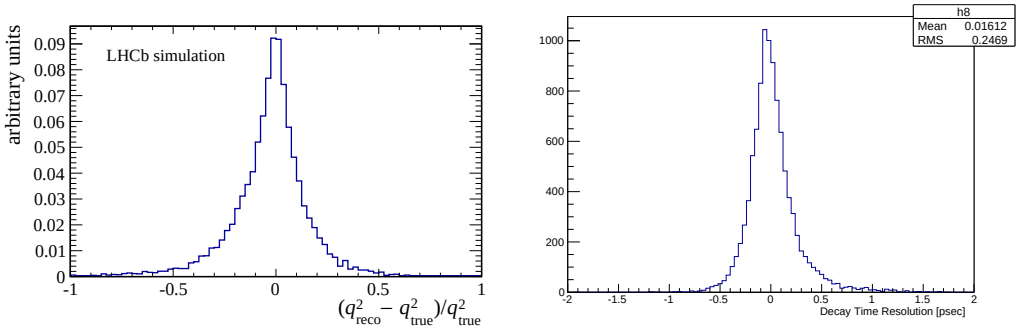

Figure 3.4: Difference observed in $3\pi\overline{\nu}_\tau$ signal simulated events (left) between the reconstructed and true q^2 variable divided by the true q^2 and (right) between the reconstructed and the true t_τ variable.

Reconstruction in the double-charm hypothesis

After applying the "cut"-based selection described in Sec. 3.2.3, the dominant source of background is represented by the double-charm decay $B^0 \to D^{*-} D_s^+(X_1)$, with $D_s^+ \to 3\pi X_2$, where X_2 is a system of unreconstructed particles, like $\pi^0, 2\pi^0, \pi^+\pi^-\pi^0$. The kinematics of this kind of decay can be reconstructed starting from the momentum conservation

$$|\vec{p}_{B^0}|\hat{u}_{B^0} = |\vec{p}_{D_s^+}|\hat{u}_{D_s^+} + \vec{p}_{D^{*-}}, \tag{3.12}$$

where $\vec{p}_{B^0}$, $\vec{p}_{D_s^+}$ and $\vec{p}_{D^{*-}}$ are the momenta of the mesons involved in the decay, and $\hat{u}_{B^0}$, $\hat{u}_{D_s^+}$ their unit vectors. These two unit vectors $\hat{u}_{B^0}$ and $\hat{u}_{D_s^+}$ correspond, approximately, to the direction of the lines joining the PV to the B^0 decay vertex and the B^0 decay vertex to the 3π vertex, respectively, and so they do not take into account the presence of unreconstructed particles in the D_s^+ decay. Equation (3.12) does not hold when extra particles are present in the B^0 decay, unless the additional particle is aligned with the D_s^+ momentum direction, as in the $B^0 \to D^{*-} D_s^{*+}$ decay, where the soft photon emitted in the D_s^{*+} decay is almost collinear with the D_s^+ momentum. In this case $\vec{p}_{D_s^+}$ refers to the momentum of the excited D_s^{*+} meson. The B^0 and D_s^+ momenta are obtained from Eq. (3.12) in two different ways, using vectorial or scalar product, denoted with the v and s subscripts:

$$P_{B^0,v} = \frac{|\vec{p}_{D^{*-}} \times \hat{u}_{D_s^+}|}{|\hat{u}_{B^0} \times \hat{u}_{D_s^+}|}, \tag{3.13a}$$

$$P_{B^0,s} = \frac{\vec{p}_{D^{*-}} \cdot \hat{u}_{B^0} - (\vec{p}_{D^{*-}} \cdot \hat{u}_{D_s^+})(\hat{u}_{B^0} \cdot \hat{u}_{D_s^+})}{1 - (\hat{u}_{B^0} \cdot \hat{u}_{D_s^+})^2} \tag{3.13b}$$

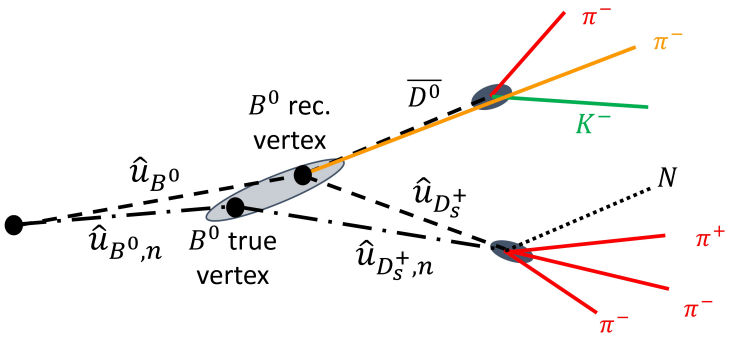

Figure 3.5: Illustration of the $B^0 \to D^{*-} D_s^+$ decay topology, with $D_s^+ \to 3\pi N$, where N stands for unreconstructed particles.

for the B^0 momentum and

$$P_{D_s^+,v} = \frac{|\vec{p}_{D^{*-}} \times \hat{u}_{B^0}|}{|\hat{u}_{D_s^+} \times \hat{u}_{B^0}|}, \tag{3.14a}$$

$$P_{D_s^+,s} = \frac{(\vec{p}_{D^{*-}} \cdot \hat{u}_{B^0})(\hat{u}_{B^0} \cdot \hat{u}_{D_s^+}) - \vec{p}_{D^{*-}} \cdot \hat{u}_{D_s^+}}{1 - (\hat{u}_{B^0} \cdot \hat{u}_{D_s^+})^2} \tag{3.14b}$$

for the D_s^+ momentum.

To take into account the presence of extra particles in the D_s^+ decay and its effect on the B^0 vertex determination, a correction to the B^0 vertex position is applied as a function of the 3π mass. The correction $dz = \mathrm{vtx}_z(B^0) - \mathrm{vtx}_z^{\mathrm{true}}(B^0)$ is parameterised as a second-order polynomial of $m(3\pi)$, with parameters determined from the double-charm simulated events. The B^0 vertex is then recomputed taking into account the correction dz, so new values of D_s^+ and B^0 momenta, called $P_{D_s^+,vn}$, $P_{D_s^+,sn}$, $P_{B^0,vn}$ and $P_{B^0,sn}$, are obtained. A schematic view of the $B^0 \to D^{*-} D_s^+$ decay topology, with $D_s^+ \to 3\pi X$, is shown in Fig. 3.5. The variables calculated with this approach provide discrimination between signal and $B^0 \to D^{*-} D_s^+(X)$ decays. They are therefore used as inputs to the multivariate analysis described in Sec. 3.2.5.

3.2.5 Multivariate analysis

To obtain the optimal rejection of the double-charm background, a multivariate analysis (MVA) based on a boosted decision tree (BDT) is implemented. Eighteen variables related to the charged and neutral isolation, the different resonant structures of $\tau^+ \to 3\pi\overline{\nu}_\tau$ and $D_s^+ \to 3\pi X$ decays, the topology and dynamics of the τ^+ and B^0

and the reconstruction techniques illustrated in Sec. 3.2.4 are used as inputs to the MVA.

In large part of $D_s^+ \to 3\pi X$ decay sample, one $\pi^+\pi^-$ pair comes from $\eta \to \pi^+\pi^-\pi^0$ or $\eta' \to \eta\pi^+\pi^-$ decays. In these intermediate decays the Q-value available to the $\pi^+\pi^-$ pair is less than 400 MeV, and so the $\pi^+\pi^-$ invariant mass is bound to be between 278 MeV/c^2 and 400 MeV/c^2, exhibiting a distinctive low-mass enhancement. For what concerns the signal $\tau^+ \to 3\pi\overline{\nu}_\tau$ decay, it proceeds through the $a_1(1260)^+ \to \rho^0(\to \pi^+\pi^-)\pi^+$ intermediate decay, and the maximum dipion mass will therefore show a ρ^0 peak. For these reasons the minimum and maximum values for the $\pi^+\pi^-$ masses are included in the BDT.

Background events where the 3π system is coming from D_s^+ decays are often accompanied by a large neutral energy from the rest of the D_s^+ decay, since the η meson tends to decay to purely neutral states as 2γ or $3\pi^0$. Photons are also produced when excited D_s^{*+} mesons decay to their ground state. A neutral-isolation algorithm is therefore used to measure the energy deposited in the ECAL in a cone of given opening $R = \sqrt{\Delta\eta + \Delta\varphi}$ around the 3π direction, where η is the pseudorapidity and φ is the azimuthal angle in the transverse plane. Three variables related to neutral energy are included in the MVA: the sum of the neutral energy contained in the cones with $R = 0.4$ and $R = 0.3$, $E_{0.4\mathrm{nc}}$ and $E_{0.3\mathrm{nc}}$ respectively, and the multiplicity of neutral objects in the cone with $R = 0.4$, $n_{0.4\mathrm{nc}}$. Two variables provided by the charged-isolation algorithm described in Sec. 3.2.3 are included in the MVA, namely the multiplicity $n_{0.2\mathrm{cc}}$ and energy $E_{0.2\mathrm{cc}}$ of charged objects in the cone with $R = 0.2$.

The distance in the transverse plane between the B^0 decay vertex and the PV, the visible τ^+ energy and the $D^{*-}3\pi$ invariant mass show discriminating power between signal and double-charm background, and so they are included in the MVA input list. Two variables obtained by reconstructing the signal are included as MVA inputs, namely the approximated energy of the neutrino emitted at the B^0 decay vertex, equal to the difference $|\vec{p}_{B^0}| - |\vec{p}_{D^{*-}}| - |\vec{p}_{\tau^+}|$, and the χ^2_{rec} of the reconstruction of the event, defined in Sec. 3.2.4. Six variables calculated by reconstructing double-charm hypothesis are used as well, namely

1. the B^0 momentum reconstructed using the scalar product method with the corrected B^0 vertex, $P_{B^0,sn}$;

2. the logarithm of the ratio between the reconstructed B^0 momentum (vector product method) and the visible one, $\log|P_{B^0,v}/|\vec{p}_{D^{*-}3\pi}||$;

3. the logarithm of the ratio between the reconstructed B^0 momentum (vector product method) and the visible one, with the corrected B^0 decay vertex, $\log|P_{B^0,vn}/|\vec{p}_{D^{*-}3\pi}||$;

4. the logarithm of the normalised difference between the estimates of the B^0 momentum, $\log|(P_{B^0,sn} - P_{B^0,vn})/P_{B^0,vn}|$;

5. the squared mass of the reconstructed neutral vector, m_N^2;

6. the reconstructed mass of the $D_{(s)}^{(*,**)}$ system, $m_{D_s^{(*,**)}}$.

The MVA is trained using the signal simulated events where the τ^+ decays into $3\pi\overline{\nu}_\tau$. The signal simulation where the τ^+ decays into $3\pi\pi^0\overline{\nu}_\tau$ is not included because it would decrease the MVA performance, since the neutral-isolation variables for this kind of signal are distributed as in the background. The background sample used in the training is made of double-charm simulated events. The distributions of the variables for both signal and background training samples are shown in Figs. 3.6-3.8. The MVA performance is shown in Fig. 3.9. The sample used to determine the signal yield is obtained by requiring the MVA output to be greater than -0.075, that is the value which, according to simulation, gives the lowest statistical uncertainty on the signal yield. The efficiency of this requirement on the $3\pi\overline{\nu}_\tau$ and the $3\pi\pi^0\overline{\nu}_\tau$ signal is 94% and 77%, respectively. No requirement on the MVA output is applied for the normalisation sample.

3.3 Control samples

Since the fit performed to determine the signal yields uses templates obtained from simulation, it is very important to verify the agreement between data and simulated double-charm decays. Control samples obtained from data are then built and used to check the level of agreement and, when needed, calculate the corrections to be applied to the simulation.

3.3.1 The $B \to D^{*-}D_s^+(X)$ control sample

A control sample of $B \to D^{*-}D_s^+(X)$ decays is obtained from data by selecting events in the exclusive $D_s^+ \to 3\pi$ peak, *i.e.* by requiring the $m(3\pi)$ to be around the nominal D_s^+ mass. These events include $B^0 \to D^{*-}D_s^{(*,**)+}$, $B^{0,-} \to D^{*-}D_s^+X^{0,-}$ and $B_s^0 \to D^{*-}D_s^+X$ decays. The first category includes $B \to D^{*-}D_s^+$ decays and

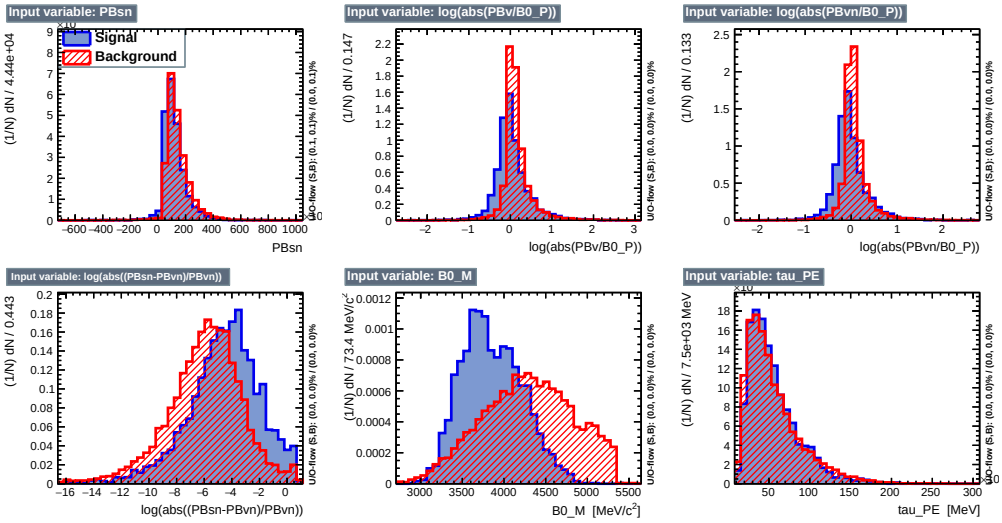

Figure 3.6: Subset of input MVA variables, namely (top left) $P_{B^0,sn}$, (top centre) $\log|P_{B^0,v}/|\vec{p}_{D^{*-}3\pi}||$, (top right) $\log|P_{B^0,vn}/|\vec{p}_{D^{*-}3\pi}||$, (bottom left) $\log|(P_{B^0,sn} - P_{B^0,vn})/P_{B^0,vn}|$, (bottom centre) the $D^{*-}3\pi$ invariant mass and (bottom right) the visible τ^+ energy. Signal (blue) and background (red) distributions are overlapped.

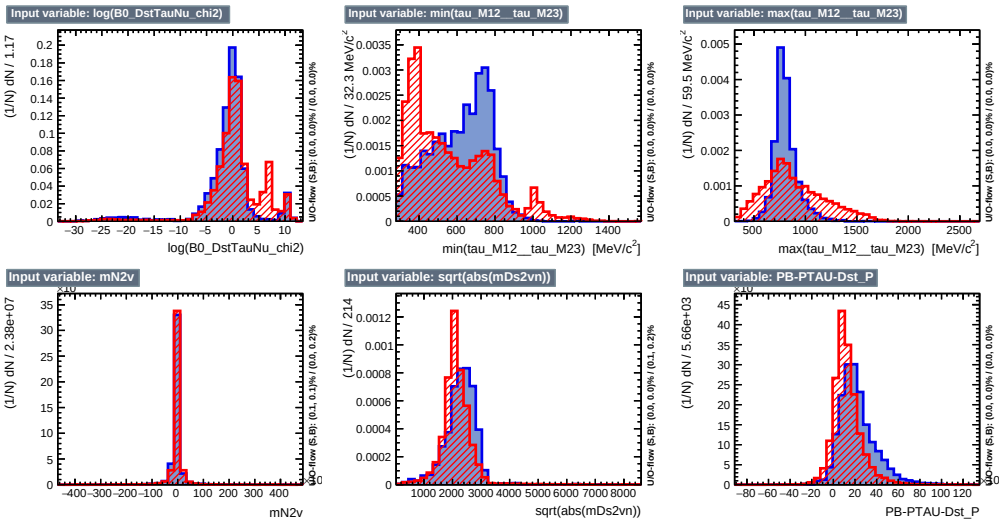

Figure 3.7: Subset of input MVA variables, namely (top left) $\log(\chi^2_{\rm rec})$, (top centre) $\min[m(\pi^+\pi^-)]$, (top right) $\max[m(\pi^+\pi^-)]$, (bottom left) m^2_N, (bottom centre) $m_{D_s^{(*,**)}}$ and (bottom right) the approximated neutrino energy. The same legend of Fig. 3.6 applies.

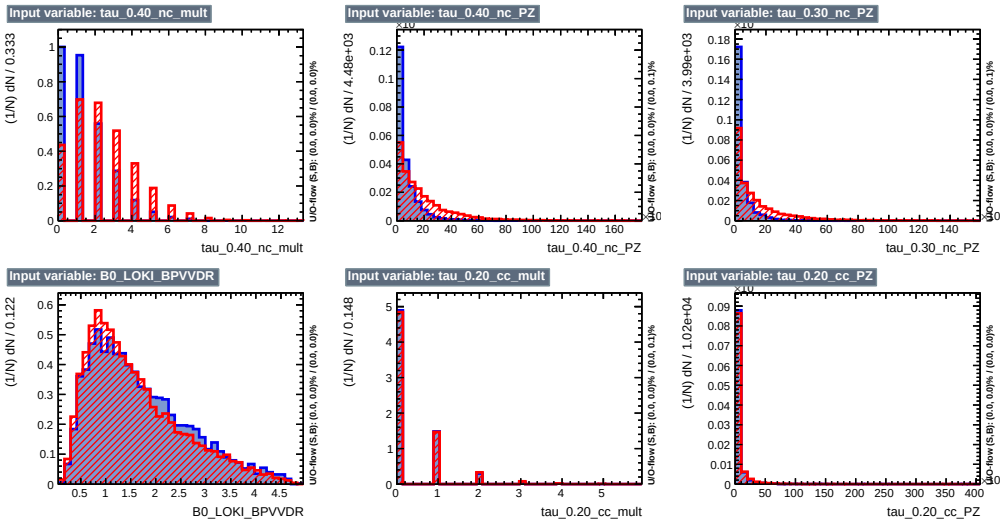

Figure 3.8: Subset of input MVA variables, namely (top left) $n_{0.4\text{nc}}$, (top centre) $E_{0.4\text{nc}}$, (top right) $E_{0.3\text{nc}}$, (bottom left) the distance in the transverse plane between the B^0 vertex and the PV, (bottom centre) $n_{0.2\text{cc}}$ and (bottom right) $E_{0.2\text{cc}}$. The same legend of Fig. 3.6 applies.

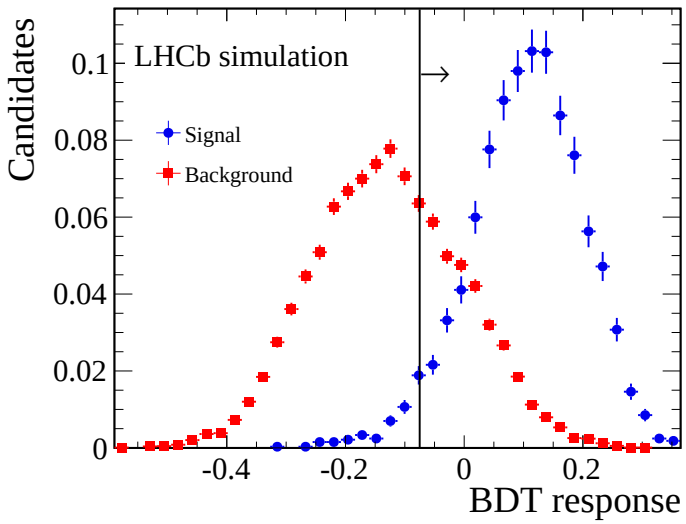

Figure 3.9: Distribution of the MVA response on the signal and background simulated samples. The black line shows the requirement applied to select the sample used for the final fit.

Table 3.5: Relative fractions of the various components obtained from the fit to the $B \to D^{*-} D_s^+(X)$ control sample. The values used in the simulation and the ratio of the two are also shown.

Parameter	Simulation	Fit	Ratio data/simulation
$f_{\text{c.b.}}$	—	0.014	—
$f_{D_s^+}$	0.54	0.594 ± 0.041	1.10 ± 0.08
$f_{D_{s0}^{*+}}$	0.08	$0.000^{+0.040}_{-0.000}$	$0.00^{+0.50}_{-0.00}$
$f_{D_{s1}^+}$	0.39	0.365 ± 0.053	0.94 ± 0.14
$f_{D_s^+ X}$	0.22	0.416 ± 0.069	1.89 ± 0.31
$f_{(D_s^+ X)_s}$	0.23	0.093 ± 0.027	0.40 ± 0.12

events where a neutral particle is emitted from an excited D_s^+ meson, namely a D_s^{*+}, a D_{s0}^{*+} or a D_{s1}^+. In the events belonging to the second category, the undetected particle originates from the $B^{0,-}$ decay or from an excited D^{*-} meson. The last category contains feed-down from the de-excitation of D^{*-} or D_s^+ mesons originating from the decay of a B_s^0 meson. The various relative fractions of these components are measured using the control sample by performing a template fit to the $m(D^{*-}3\pi)$ distribution, according to the model defined by the probability density function

$$\mathcal{P} = \frac{1 - f_{\text{c.b.}}}{k} \sum_i f_i \mathcal{P}_i + f_{\text{c.b.}} \mathcal{P}_{\text{c.b.}}, \tag{3.15}$$

where $f_{\text{c.b.}}$ and $\mathcal{P}_{\text{c.b.}}$ are the fraction and the template of the combinatorial background, while f_i and $\mathcal{P}_i$ are the fractions and the templates of the various components, with $i = D_s^+, D_s^{*+}, D_{s0}^{*+}, D_{s1}^+, D_s^+ X, (D_s^+ X)_s$ and $k = \sum_i f_i$. The various templates are obtained from simulation, except for the combinatorial background, which is obtained from the wrong sign sample $D^{*-}\pi^-\pi^+\pi^-$. The f_i fractions are free parameters of the fit, while $f_{\text{c.b.}}$ is fixed to a value extrapolated from the wrong-sign sample.

The fit result is shown in Fig. 3.10, and the resulting parameters are reported in Table 3.5. The ratios between the values of the different fractions measured in data and in simulation are reported in the same table. For the events belonging to the last two categories, discrepancies are found between the fractions used in the simulation and those measured on data. These ratios are used to correct and constrain the fractions of the various D_s^+ background components in the fit performed to obtain the signal yield (see Sec. 3.5.2).

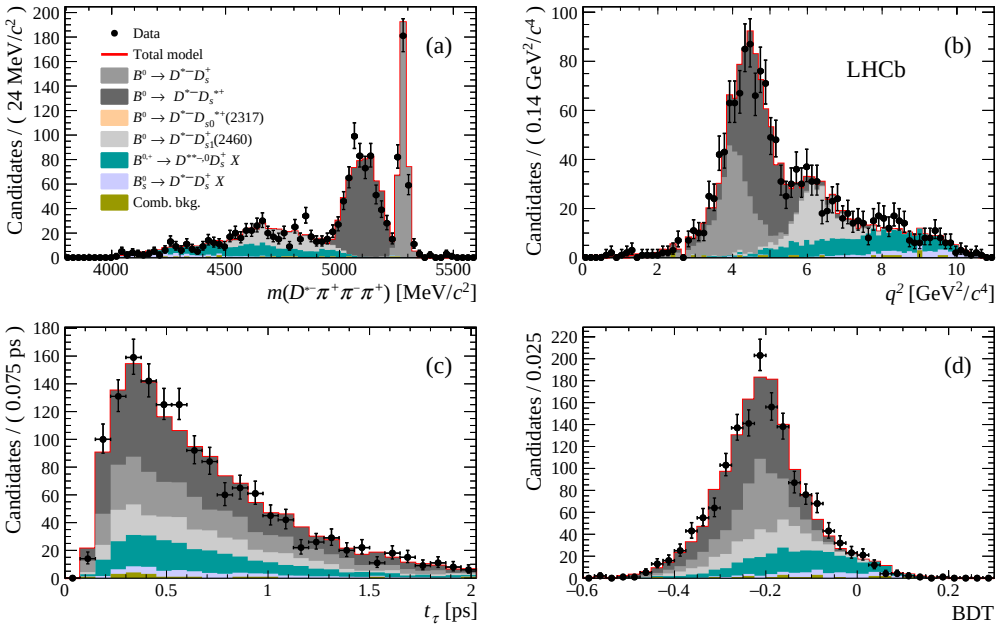

Figure 3.10: (a) Result of the fit to the $B \to D^{*-}D_s^+(X)$ control sample on the $m(D^{*-}3\pi)$ distribution. The post-fit model is projected on (b) q^2, (c) t_τ and (d) MVA output.

3.3.2 The $B \to D^{*-}D^0(X)$ control sample

A control sample for the $B \to D^{*-}D^0(X)$ decay is obtained by reversing the charged-isolation requirement described in Sec. 3.2.3, asking the isolation algorithm to find a kaon compatible with the 3π vertex, and the mass of the $K^-3\pi$ system to be in a window of $\pm 20\,\text{MeV}/c^2$ around the nominal D^0 mass (see Fig. 3.11).

The t_τ, q^2 and MVA output distributions in the control sample are compared to those of the corresponding simulated events in Fig. 3.12. A clear disagreement between data and simulation is seen in the q^2 and $m(D^{*-}D^0)$ distributions. In order to correct for such a disagreement, a linear function is used to fit the ratio between the q^2 distributions of the $B \to D^{*-}D^0(X)$ control sample and the corresponding simulation, shown in Fig. 3.13. The correction is therefore applied to the simulation before the determination of the template described in Sec. 3.5.2. Figure 3.14 shows the q^2 distribution after applying the correction.

3.3.3 The $B \to D^{*-}D^+(X)$ control sample

A control sample for the $B \to D^{*-}D^+(X)$ decay is obtained by reversing the `ProbNNk` requirement on the π^- coming from the τ^+ described in Sec. 3.2.3, requiring

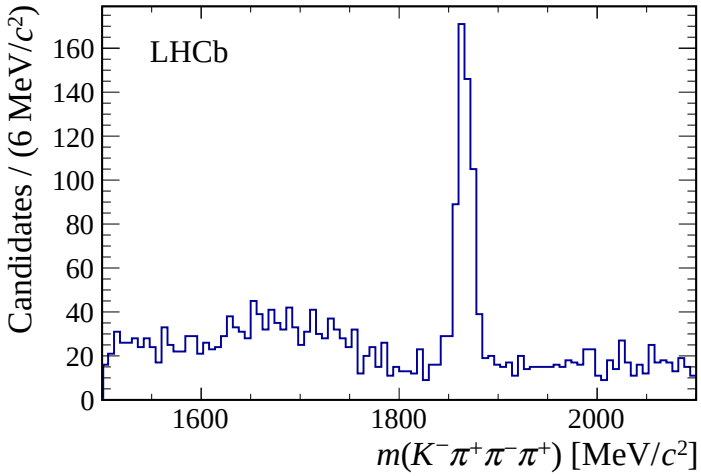

Figure 3.11: The $m(K^-3\pi)$ distribution for the D^0 candidates obtained by associating a charged kaon to the 3π vertex with the isolation algorithm.

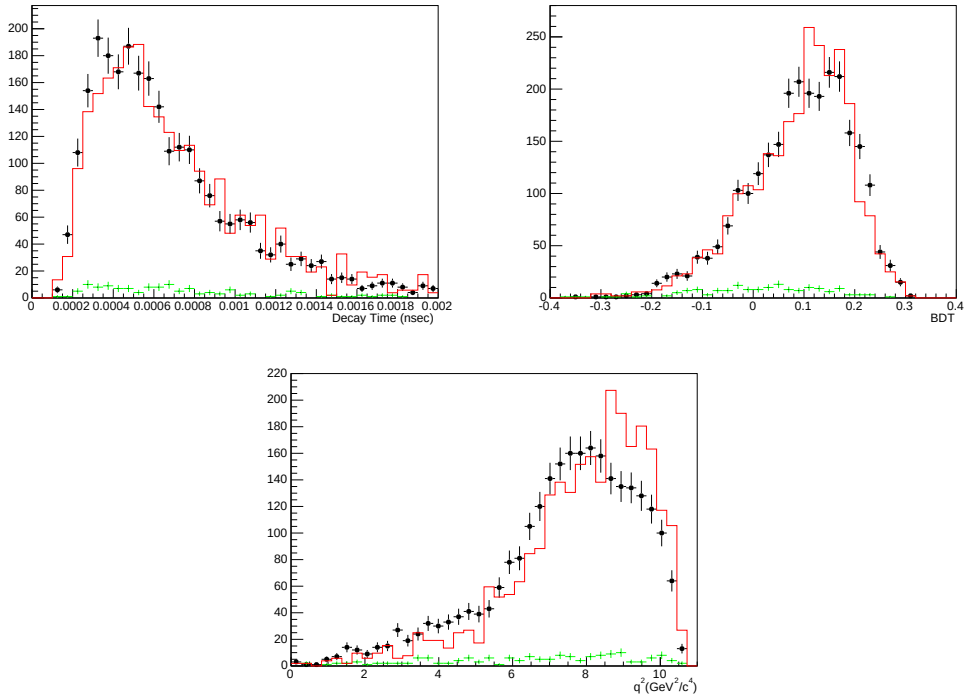

Figure 3.12: Distributions of (top left) t_τ, (top right) MVA response and (bottom) q^2 for the events of the $B \to D^{*-}D^0(X)$ control sample. Black points represent data, red histograms correspond to simulation. The combinatorial background, obtained using wrong-sign events, is shown in green.

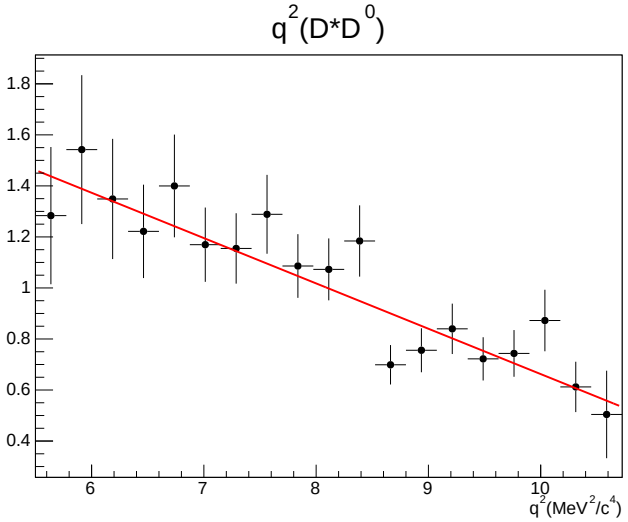

Figure 3.13: The ratio between the q^2 distributions of the $B \to D^{*-}D^0(X)$ control sample and the corresponding simulation. The fit to a linear function is shown in red.

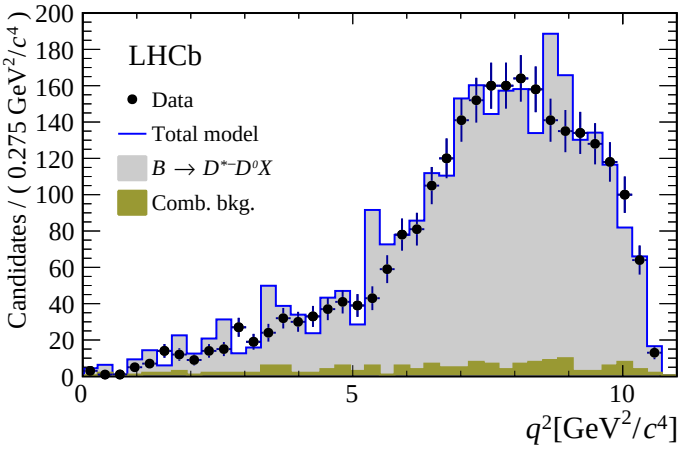

Figure 3.14: Distribution of q^2 for the events of the $B \to D^{*-}D^0(X)$ control sample after correcting for the disagreement between data and simulation.

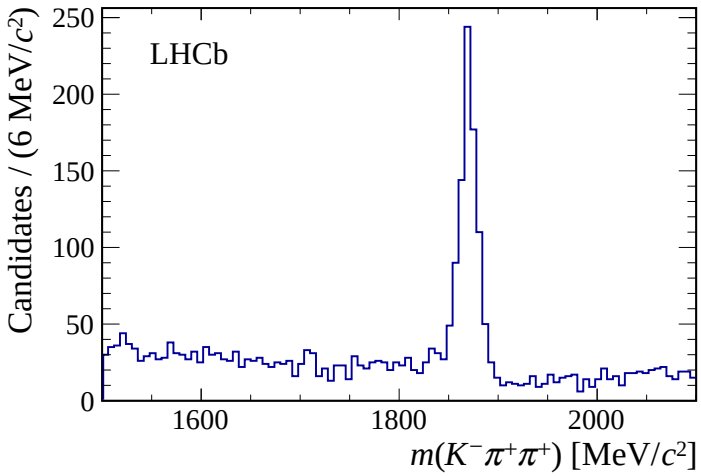

Figure 3.15: The $m(K^-\pi^+\pi^+)$ distribution for the D^+ candidates obtained by reversing the `ProbNNk`(π) requirement and assigning the kaon mass to the π^- coming from the τ^+.

`ProbNNk`(π^-) > 0.1, assigning the kaon mass to the π^- and requiring the mass of the $K^-\pi^+\pi^+$ system to be in a window of $\pm 20\,\text{MeV}/c^2$ around the nominal D^+ mass (see Fig. 3.15).

The t_τ, q^2 and MVA output distributions of this control sample are compared to those in the corresponding simulation in Fig. 3.16. A disagreement between data and simulation is observed. Because of the limited size of this sample, it is not possible to calculate a correction as in the case of the $B \to D^{*-}D^0(X)$ control sample. The same correction described in Sec. 3.3.2 is then applied, since the dominant $B \to D^{*-}DK$ decay is identical for both cases. The correction is then applied to the simulation before the determination of the template described in Sec. 3.5.2. Figure 3.17 shows the various distributions after applying the correction.

3.4 Corrections to simulation

Since the templates used in the fit performed to obtain the signal yield are obtained from simulation, all possible differences between data and simulation must be corrected for in order to reproduce the data and obtain the right values of the efficiencies. In the following, a description is given of the methods used to correct the signal, background and normalisation simulation and calculate the efficiency correction factors.

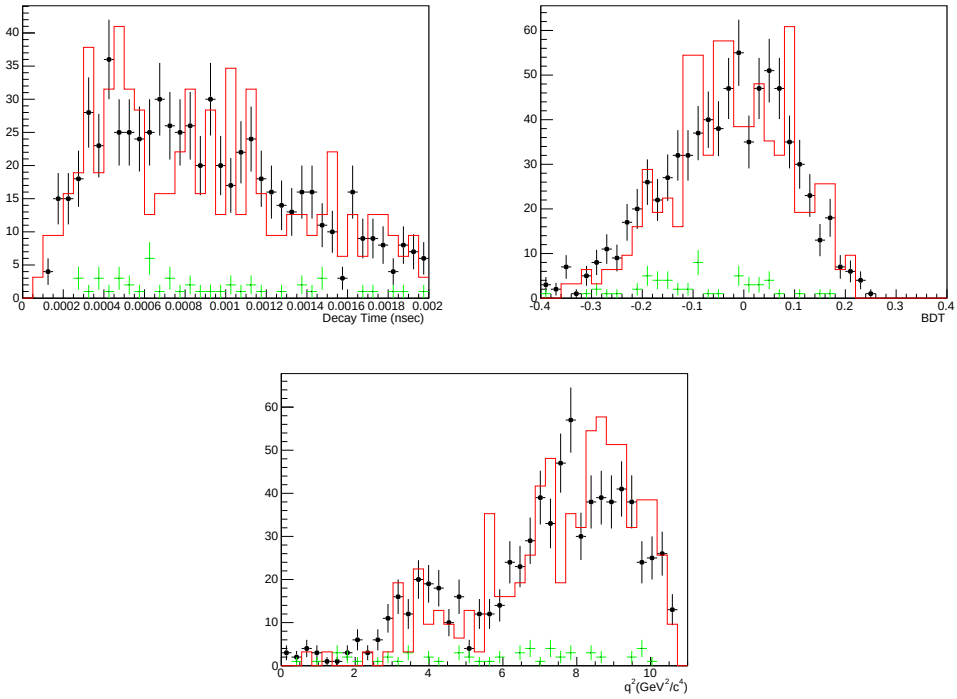

Figure 3.16: Distributions of (top left) t_τ, (top right) MVA response and (bottom) q^2 for the events of the $B \to D^{*-}D^+(X)$ control sample. Black points represent data, red histograms correspond to simulation. The combinatorial background, obtained using wrong-sign events, is shown in green.

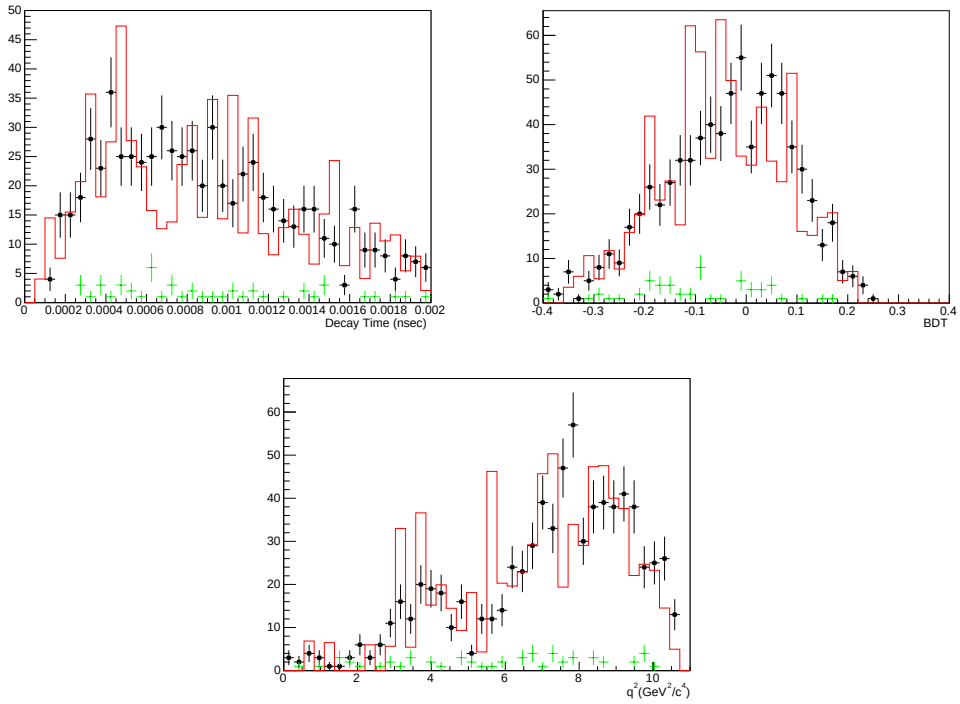

Figure 3.17: Distributions of (top left) t_τ, (top right) MVA response and (bottom) q^2 for the events of the $B \to D^{*-} D^+(X)$ control sample after applying the correction to account for disagreement between data and simulation. Black points represent data, red histograms correspond to simulation. The combinatorial background, obtained by wrong-sign events, is shown in green.

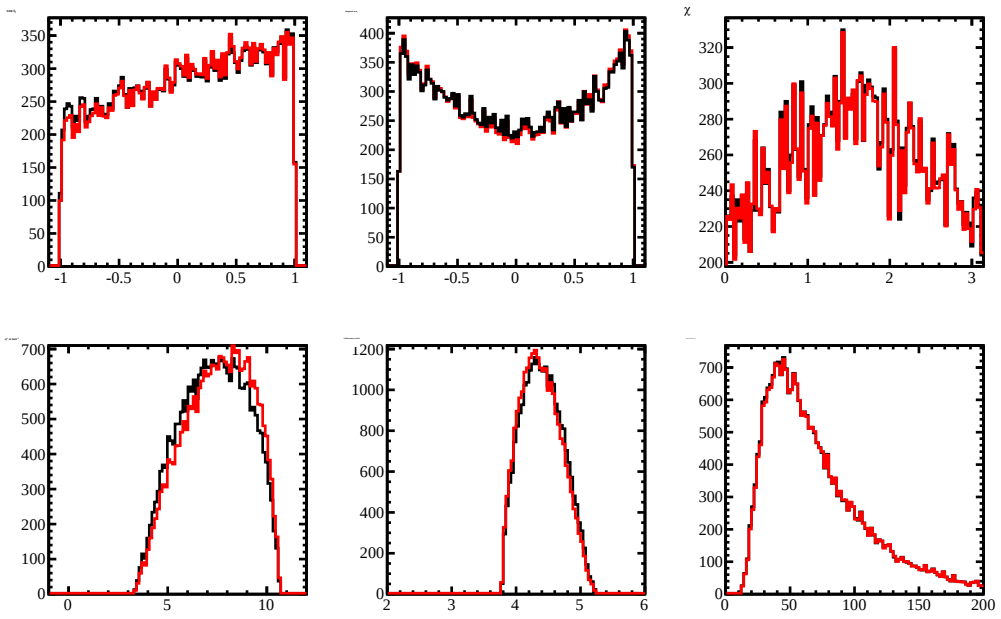

Figure 3.18: Distributions of generated (top left) τ^+ helicity angle, (top centre) D^{*-} helicity angle, (top right) azimuthal angle, (bottom left) q^2, (bottom centre) invariant $D^*3\pi$ mass and (bottom right) τ^+ momentum in simulation, (black histograms) before and (red histograms) after form-factor weighting.

3.4.1 Form factors

Signal simulation is generated with the ISGW2 model [95], which is known not to fully reproduce the distributions of the kinematic variables of the decay. Simulated signal events are therefore weighted in order to match the distributions predicted by the CLN parameterisation [41], by using the XslFF package [97]. The values of the form-factor ratios at zero recoil, defined in Sec. 1.4.1, are taken from their world average [6], $R_1(1) = 1.404 \pm 0.032$ and $R_2(1) = 0.854 \pm 0.020$, as well as the slope of the Isgur-Wise function $\rho^2 = 1.205 \pm 0.015 \pm 0.021$ and their correlations $\rho(\rho^2, R_1) = 0.566$, $\rho(R_1, R_2) = -0.759$, $\rho(R_2, \rho^2) = -0.807$. The scalar form-factor ratio at zero recoil and its uncertainty are calculated as in Ref. [38], giving $R_0(1) = 1.14 \pm 0.11$. Figure 3.18 shows the effect of the weighting on the kinematic variable distributions at the generator level, *i.e.* before simulating the interaction with the detector. Only the q^2 distribution is affected in a significant way. The weighting is performed before the application of the selection and the template extraction, so no further correction factors are needed.

3.4.2 PID

The PID performance is not correctly modelled by simulation, so weighting factors depending on the `ProbNN` variables used in the analysis must be applied to the simulation. In order to do that, the PIDCalib package [98] is used to evaluate event-by-event weights depending on the various `ProbNN` requirements, in bins of number of tracks in the event, momentum and pseudorapidity of the track on which the requirement is imposed. The calibration sample needed for this study is made of $D^{*+} \to D^0\pi^+$ decays, with $D^0 \to K^-\pi^+$, where the D^{*+} is produced promptly from the PV. This weighting procedure is applied before the production of the templates, and so further corrections are not necessary.

3.4.3 `L0Hadron` efficiency

The efficiency of `L0Hadron` is known to be not well modelled by the simulation. For this reason, the `L0Hadron` efficiency is measured on the normalisation sample and the corresponding simulation, in the B^0 region of the $m(D^{*-}3\pi)$ mass distribution. In order to evaluate the efficiency of a certain L0 trigger selection, the so-called TIS-TOS method is used: if in a sample of n events n_{TIS} is the number of events selected by a certain TIS trigger line and n_{TOS} is the number of events selected by a certain TOS trigger line, the efficiency of the TOS trigger selection is

$$\varepsilon_{\texttt{TOS}} = \frac{n_{\mathrm{TOS}}}{n} = \frac{n_{\mathrm{TOS}}}{n_{\mathrm{TIS}}} \cdot \frac{n_{\mathrm{TIS}}}{n} = \frac{n_{\mathrm{TOS}}}{n_{\mathrm{TIS}}} \cdot \varepsilon_{\texttt{TIS}}. \tag{3.16}$$

Since the TIS selection is independent of signal, its efficiency $\varepsilon_{\texttt{TIS}}$ on any subsample of the TOS triggered events is the same as that of the whole sample of selected events

$$\varepsilon_{\texttt{TIS}} = \varepsilon_{\texttt{TIS|TOS}} = \frac{n_{\mathrm{TOS\&TIS}}}{n_{\mathrm{TOS}}}, \tag{3.17}$$

where $n_{\mathrm{TOS\&TIS}}$ is the number of events triggered by both the TIS trigger line and the TOS trigger line under consideration. Hence Eq. (3.16) becomes

$$\varepsilon_{\texttt{TOS}} = \frac{n_{\mathrm{TOS\&TIS}}}{n_{\mathrm{TIS}}}. \tag{3.18}$$

In this case the TOS line is `L0Hadron` on the D^{*-} and the TIS line is `L0Global` on the B^0.

The comparison of the efficiency between data and simulation normalisation samples as a function of p_{T} of the 3π system is shown, along with the efficiency ratio

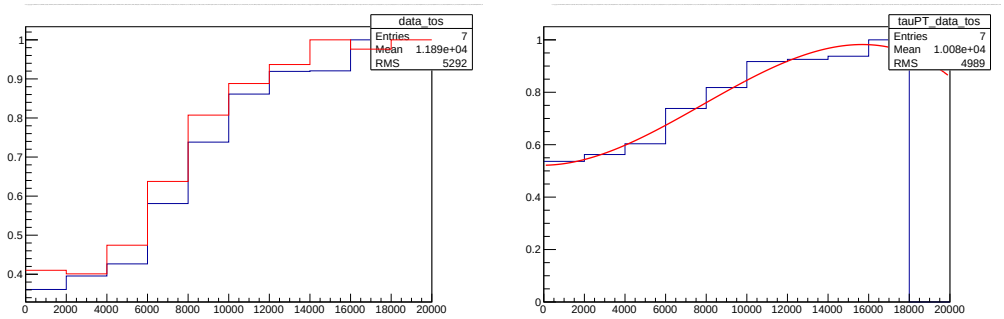

Figure 3.19: (left) `L0Hadron` efficiency as a function of $p_{\mathrm{T}}(3\pi)$ for (red) simulation and (blue) normalisation sample. (right) Efficiency ratio between data and simulation as function of $p_{\mathrm{T}}(3\pi)$, with the fit by a polynomial function shown in red.

between data and simulation, in Fig. 3.19. A disagreement is observed, especially for low values of p_{T}, hence a correction factor is calculated as function of $p_{\mathrm{T}}(3\pi)$ according to the data-simulation efficiency ratio, which is fitted by a polynomial function. The correction is therefore applied to the signal and normalisation simulated events, as a ratio between signal and normalisation efficiencies equal to

$$r_{\texttt{L0Hadron\_TOS}} = \frac{\varepsilon_{\texttt{L0Hadron\_TOS},\mathrm{sig}}}{\varepsilon_{\texttt{L0Hadron\_TOS},\mathrm{norm}}} \cdot \frac{\varepsilon_{\texttt{L0Hadron\_TOS},\mathrm{norm,MC}}}{\varepsilon_{\texttt{L0Hadron\_TOS},\mathrm{sig,MC}}} = 0.995 \pm 0.010,$$

where the uncertainty takes into account the statistical uncertainty due to the size of simulated samples and the calculation of the weights.

3.4.4 SPD multiplicity

The `L0Global_TIS` efficiency must be correctly reproduced by the simulation. In order to check this, the `L0Global_TIS` efficiency $\varepsilon_{\texttt{L0Global\_TIS}}$ is calculated in bins of the SPD hits multiplicity, which is a variable related to the whole event, hence expected to be correlated with the `L0Global_TIS` and not with the `L0Hadron_TOS`. The efficiency is calculated according to Eq. (3.17). The sample used for this study is the normalisation sample in the B^0 region of the $m(D^{*-}3\pi)$ mass distribution. First of all, a clear discrepancy is seen between data and simulation in the SPD multiplicity (nSPD) distribution, as shown in Fig. 3.20. A correction, equivalent to multiplying nSPD by a factor 1.4, is therefore applied to the simulation in order to match the nSPD distribution. The trigger efficiency ratio between data and simulation after the nSPD rescaling is reported in Fig. 3.21, and a good agreement

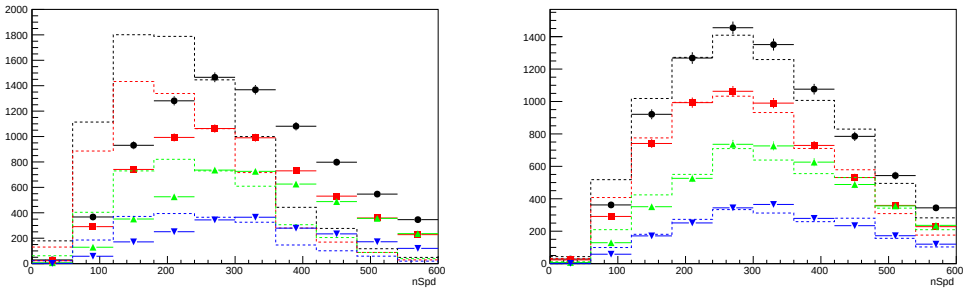

Figure 3.20: Comparison between the SPD multiplicity in simulation (dashed histograms) and data (full points) in the normalisation sample, (left) before and (right) after rescaling the SPD multiplicity. The various histograms/points correspond to (black) events firing `L0Hadron_TOS | L0Global_TIS`, (red) `L0Hadron_TOS`, (green) `L0Global_TIS` and (blue) `L0Hadron_TOS & L0Global_TIS`.

is observed. The nSPD rescaling translates to a correction factor to be applied to the ratio between signal and normalisation efficiencies equal to

$$r_{\texttt{L0Global\_TIS}} = \frac{\varepsilon_{\texttt{L0Global\_TIS,sig}}}{\varepsilon_{\texttt{L0Global\_TIS,norm}}} \cdot \frac{\varepsilon_{\texttt{L0Global\_TIS,norm,MC}}}{\varepsilon_{\texttt{L0Global\_TIS,sig,MC}}} = 1.031 \pm 0.011.$$

3.4.5 Feed-down from B_s^0

The component of the fit corresponding to the $B \to D^{**}\tau^+\nu_\tau$ decay does not take into account the $B_s^0 \to D_s^{**-}\tau^+\nu_\tau$ decay, with $D_s^{**-} \to D^{*-}K^0$, since it was chosen to keep the D^{**} contribution from B^0 and B^+ identical to what observed at B-factories, *i.e.* with no B_s^0 contribution. The contamination of this contribution is evaluated using simulation, and it corresponds to 3%. Hence, the efficiency ratio needs to be corrected by the factor $r_{B_s^0} = 1.030 \pm 0.015$, where the uncertainty is due to the poor knowledge of the branching fraction of the $B_s^0 \to D_s^{**-}\tau^+\nu_\tau$ decay.

3.4.6 Double-charm decays

The three pions in the $\tau^+ \to 3\pi\overline{\nu}_\tau$ decay come mostly from a $a_1(1260)^+$ resonance, which decay into $\rho^0\pi^+$. Since the dominant source of ρ^0 resonances in D_s^+ decays is due to $\eta' \to \rho^0\gamma$, and the dominant background of the analysis is due to $D_s^+ \to 3\pi X$ decays, it is very important to precisely control the η' contribution in D_s^+ decays, as all the various contributions of the type $D_s^+ \to R\pi^+$, $D_s^+ \to R(\to \pi^+\pi^- X)\pi^+\pi^0$ and $D_s^+ \to R3\pi$, where R denotes the intermediate states K^0_S, η, η', ϕ and ω.

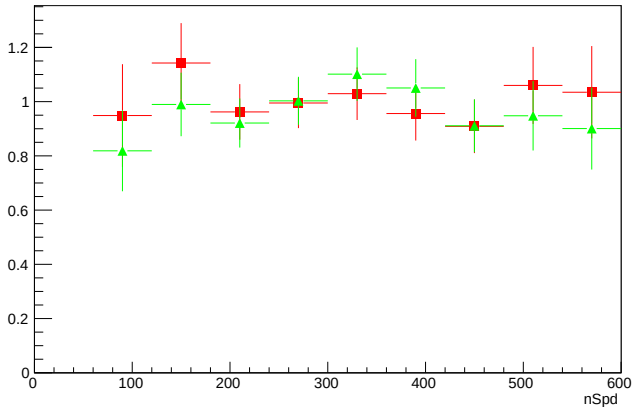

Figure 3.21: Data/simulation efficiency ratio of (red) `L0Hadron_TOS` and (green) `L0Global_TIS` evaluated on the normalisation sample.

In order to measure the relative fractions of the various contributions in data, the sample with MVA output smaller than -0.075, which is enriched in $B \to D^{*-} D_s^+(X)$ decays, is used. A simultaneous maximum-likelihood template fit is performed on the distributions of $\min[m(\pi^+\pi^-)]$, $\max[m(\pi^+\pi^-)]$, $m(\pi^+\pi^+)$ and $m(3\pi)$ in this low-MVA sample, where the shapes of all the various contributions are determined from simulation. The components used in the fit can be categorised in five groups

- D_s^+ decays where at least one pion originates from a η meson decay, as $D_s^+ \to \eta\pi^+$ and $D_s^+ \to \eta\rho^+$ decays;
- D_s^+ decays where at least one pion is produced in the decay of a η' meson;
- D_s^+ decays where at least one pion originates from an intermediate resonance different from η and η', as ω and ϕ;
- D_s^+ decays where the three pions do not originate from an intermediate state;
- decays where the three pions do not come from the decay of a D_s^+ meson.

The various relative fractions are free parameters in the fit, except for those related to $D_s^+ \to \phi 3\pi$ and $D_s^+ \to \tau^+(\to 3\pi(N)\overline{\nu}_\tau)\nu_\tau$ decays, whose branching fractions are known with 10% precision. The result of the fit is shown in Fig. 3.22, and the relative fractions of the various contributions in the decays involving a D_s^+ are reported in Table 3.6. For each component a correction factor, given by the ratio between the

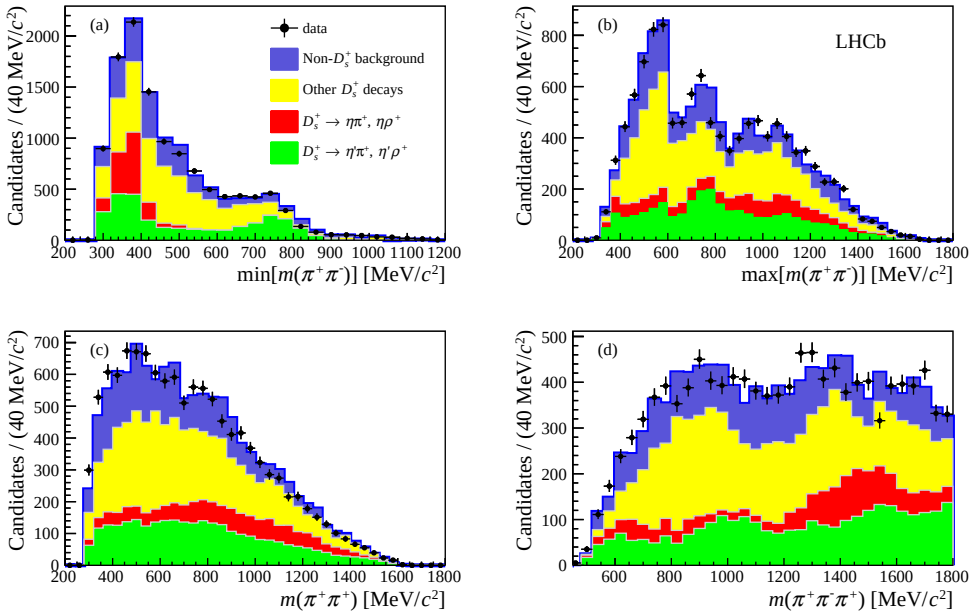

Figure 3.22: Fit to the distributions of (a) min$[m(\pi^+\pi^-)]$, (b) max$[m(\pi^+\pi^-)]$, (c) $m(\pi^+\pi^+)$ and (d) $m(3\pi)$ in the data sample obtained requiring the MVA output below -0.075.

measured fraction and that observed in simulation, is calculated. All correction factors are therefore applied to simulated sample of $B \to D^{*-} D_s^+(X)$.

In order to correct for differences between data and simulation in q^2 distributions of $B \to D^{*-} D^{0,+}(X)$ decays, a linear weighting in q^2 is performed using the control sample. The procedure is described in Secs. 3.3.2-3.3.3.

3.4.7 $m(3\pi)$ distribution in simulation

A difference between the $m(3\pi)$ distribution for the normalisation sample is seen between data and simulation, as shown in Fig. 3.23. The simulation is therefore weighted to obtain an agreement between the two samples.

3.5 Extraction of signal and normalisation yields

The procedures to determine the normalisation and the signal yields are here described.

Table 3.6: Results of the fit to the D_s^+ decay model. The relative contribution of each decay with respect to the total number of $D_s^+ \to 3\pi X$ decays is reported, along with the correction to be applied to the simulation.

D_s^+ decay	Fraction	Correction
$\eta\rho^+$	0.109 ± 0.016	0.88 ± 0.13
$\eta\pi^+$	0.047 ± 0.014	0.75 ± 0.23
$\eta'\rho^+$	0.179 ± 0.016	0.710 ± 0.063
$\eta'\pi^+$	0.138 ± 0.015	0.808 ± 0.088
$\phi\rho^+$, $\omega\rho^+$	0.043 ± 0.022	0.28 ± 0.14
$\phi\pi^+$, $\omega\pi^+$	0.163 ± 0.021	1.588 ± 0.208
$\eta 3\pi$	0.104 ± 0.021	1.81 ± 0.36
$\eta' 3\pi$	0.0835 ± 0.0102	5.39 ± 0.66
$\omega 3\pi$	0.0415 ± 0.0122	5.19 ± 1.53
$K^0 3\pi$	0.0204 ± 0.0139	1.0 ± 0.7
$\phi 3\pi$	0.0141	0.97
$\tau^+(\to 3\pi(N)\overline{\nu}_\tau)\nu_\tau$	0.0135	0.97
$X_{\text{nr}} 3\pi$	0.038 ± 0.005	6.69 ± 0.94

3.5.1 Determination of the normalisation yield

To obtain the normalisation yield, an unbinned maximum-likelihood fit is performed on the clean B^0 peak of the $m(D^{*-}3\pi)$ distribution reported in Fig. 3.3. The mass range between $5150\,\text{MeV}/c^2$ and $5400\,\text{MeV}/c^2$ is considered, with the signal component described by the sum of a Gaussian function and a Crystal Ball function [99], with the mean shared by the two functions. The background component is described by an exponential function. The result of the fit, split by year, is illustrated in Fig. 3.24. The measured total number of $B^0 \to D^{*-}3\pi$ events is 17808 ± 143.

Looking at the $m(3\pi)$ distribution for candidates with $m(D^{*-}3\pi)$ between $5200\,\text{MeV}/c^2$ and $5350\,\text{MeV}/c^2$, reported in Fig. 3.25, a peak around $2000\,\text{MeV}/c^2$, due to $B^0 \to D^{*-}D_s^+$ decays, with $D_s^+ \to 3\pi$, is visible. The number of such decays, obtained from a fit to the $m(3\pi)$ distribution with a Gaussian function used to describe the signal and an exponential function to model the background, is equal to 151 ± 22. This number must then be subtracted in order to obtain the yield of the pure $B^0 \to D^{*-}3\pi$ decays. The normalisation yield is therefore equal to

$$N_{\text{norm}} = 17657 \pm 143\ \text{stat}) \pm 22\ (D_s^+\ \text{sub}).$$

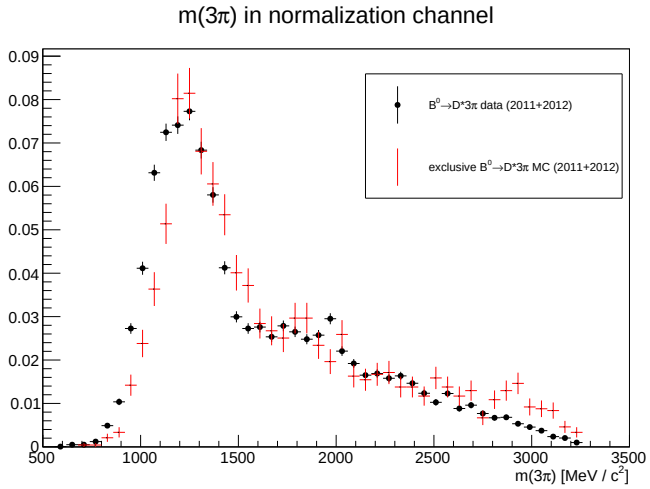

Figure 3.23: Normalised distribution of $m(3\pi)$ for (black) data and (red) simulation for the normalisation sample.

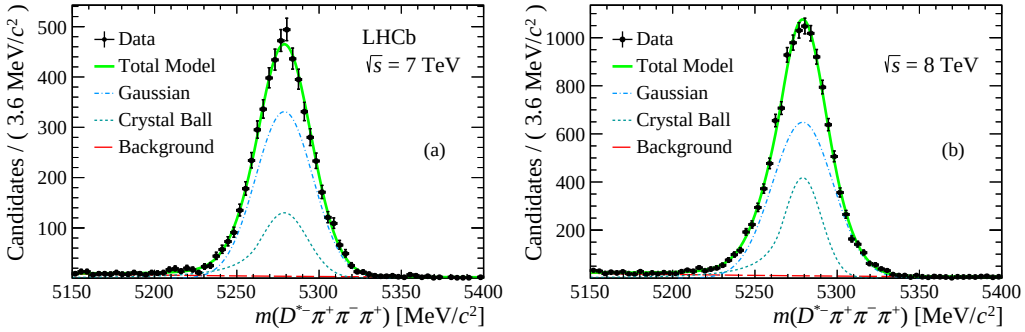

Figure 3.24: Fit to the $m(D^{*-}3\pi)$ distribution after the normalisation selection for (left) 2011 and (right) data sample.

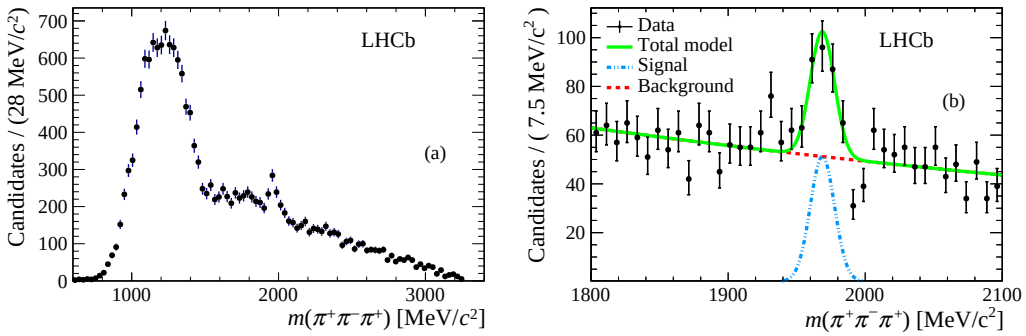

Figure 3.25: (left) $m(3\pi)$ distribution for candidates with $m(D^{*-}3\pi)$ between 5200 MeV/c^2 and 5350 MeV/c^2. (right) Fit of the same distribution in the D_s^+ mass region.

3.5.2 Determination of the signal yield

The fit model

The signal yield is determined by performing a three-dimensional binned maximum likelihood template fit to the distributions of t_τ, q^2 and MVA output. To model the various signal and background contributions in the data sample, fifteen templates extracted from the corresponding simulated samples are produced, with eight bins in t_τ, eight bins in q^2 and four bins in the MVA output. The list of the fifteen components and their normalisations is reported in Table 3.7. The various normalisations are expressed as a function of the following parameters

- $N_{\rm sig}$: the free parameter equal to the yield of signal candidates.
- $f_{\tau\to 3\pi\nu}$: the fraction of $\tau^+ \to 3\pi\overline{\nu}_\tau$ signal candidates with respect to the sum of the $\tau^+ \to 3\pi\overline{\nu}_\tau$ and $\tau^+ \to 3\pi\pi^0\overline{\nu}_\tau$ components. This parameter is fixed to 0.78, according to the ratio between the branching fractions and the efficiencies of the two modes.
- $f_{D^{**}\tau\nu}$: the ratio between the yields of $B \to D^{**}\tau^+\nu_\tau$ decay and signal candidates. Its value is fixed to 0.11, and it is computed assuming that the ratio of the decay rates lies between the predictions of Ref. [38] (0.06) and the ratio of available phase space (0.18), taking into account their different efficiencies.
- $N_{D^0}^{\rm sv}$: the yield of $B \to D^{*-}D^0X$ decays, where the three pions originate from the D^0 decay vertex. A Gaussian constraint with 5% width is applied on this

parameter, since the expected yield is estimated from the yield determined from the $D^0 \to K^+3\pi$ control sample yield scaled by the efficiency evaluated using simulation.

- $f_{D^0}^{v_1 v_2}$: the ratio of $B \to D^{*-}D^0X$ decays where at least one pion originates from the D^0 decay vertex and the other pion(s) from a different vertex, normalised to $N_{D^0}^{\mathrm{sv}}$. This is a free parameter.

- N_{D_s}: free parameter equal to the yield of double-charm background events involving a D_s^+.

- $f_{D_s^+}$, $f_{D_{s0}^{*+}}$, $f_{D_{s1}^+}$, $f_{D_s^+X}$, $f_{(D_s^+X),s}$ and k: parameters constrained to the fractions seen in simulation and corrected by the ratios reported in Table 3.5 and the efficiencies.

- f_{D^+}: free parameter representing the ratio of $B \to D^{*-}D^+X$ decays with respect to double-charm background events involving a D_s^+.

- $N_{B\to D^*3\pi X}$: yield of $B \to D^{*-}3\pi X$ events where the three pions come from the B decay vertex. This value is constrained by a Gaussian function with 5% width to the exclusive $B^0 \to D^{*-}3\pi$ yield observed in data and scaled by the ratio between $B^0 \to D^{*-}3\pi$ and inclusive $B \to D^{*-}3\pi X$ decays, measured in simulation and corrected for efficiencies.

- $N_{\mathrm{not}B}$: yield of combinatorial background events where the D^{*-} and the 3π system come from different B decays. This parameter is fixed by using the number of the wrong-sign events in the region of $m(D^{*-}\pi^-\pi^+\pi^-)$ greater than $5100\,\mathrm{MeV}/c^2$.

- $N_{\mathrm{not}D^*}$: the yield of the combinatorial background due to fake D^{*-}. Its value is fixed by extrapolating the number of events from the $\overline{D}^0$ mass sidebands.

Study of the fit bias

Because of the limited size of simulated samples used to determine the templates, the presence of empty bins in the templates introduces a bias in the value of the signal yield obtained from the fit. To study this effect, a method involving kernel density estimators (KDE) [100] is used. For each simulated sample, a three-dimensional histogram is produced and transformed to a smoothed template. These templates

Table 3.7: Summary of the fit components and their corresponding normalisations, grouped according to the legend in Fig. 3.27.

Fit component	Normalisation
$B^0 \to D^{*-}\tau^+(\to 3\pi\overline{\nu}_\tau)\nu_\tau$	$N_{\text{sig}} \times f_{\tau\to 3\pi\nu}$
$B^0 \to D^{*-}\tau^+(\to 3\pi\pi^0\overline{\nu}_\tau)\nu_\tau$	$N_{\text{sig}} \times (1 - f_{\tau\to 3\pi\nu})$
$B \to D^{**}\tau^+\nu_\tau$	$N_{\text{sig}} \times f_{D^{**}\tau\nu}$
$B^0 \to D^{*-}D_s^+$	$N_{D_s} \times f_{D_s^+}/k$
$B^0 \to D^{*-}D_s^{*+}$	$N_{D_s} \times 1/k$
$B^0 \to D^{*-}D_{s0}^*(2317)^+$	$N_{D_s} \times f_{D_{s0}^{*+}}/k$
$B^{0,+} \to D^{**}D_s^+X$	$N_{D_s} \times f_{D_s^+X}/k$
$B_s^0 \to D^{*-}D_s^+X$	$N_{D_s} \times f_{(D_s^+X),s}/k$
$B \to D^{*-}D^+X$	$N_{D_s} \times f_{D^+}$
$B^0 \to D^{*-}D_{s1}(2460)^+$	$N_{D_s} \times f_{D_{s1}^+}/k$
$B \to D^{*-}3\pi X$	$N_{B\to D^*3\pi X}$
$B \to D^{*-}D^0X$ different vertices	$N_{D^0}^{\text{sv}} \times f_{D^0}^{v_1v_2}$
$B \to D^{*-}D^0X$ same vertex	$N_{D^0}^{\text{sv}}$
combinatorial B	$N_{\text{not}B}$
combinatorial D^{*-}	$N_{\text{not}D^*}$

are combined to form a fit model in the same way as done for the baseline model. The new model is then used to generate 1000 pseudo datasets with a certain signal yield hypothesis. The study is repeated for different signal yield hypotheses, and the bias on the signal yield as a function of the generated signal yield is obtained, as shown in Fig. 3.26.

Results of the fit

The results of the fit are reported in Table 3.8 and Fig. 3.27. The χ^2 per degree of freedom is equal to 1.15, considering 12 free parameters and 236 non-empty bins in the templates. The signal yield obtained from the fit is 1336 ± 86, which corresponds to a bias of +40. Hence the yield of the $B^0 \to D^{*-}\tau^+\nu_\tau$ decay in the sample is equal to

$$N_{\text{sig}} = 1296 \pm 86.$$

The fit projection on t_τ and q^2 distributions in bins of the MVA output is shown in Fig. 3.28. A good agreement is observed between data and the post-fit model in the distributions of the most discriminating variables of the MVA, namely $\min[m(\pi^+\pi^-)]$ and $m(D^{*-}3\pi)$, as illustrated in Fig. 3.29.

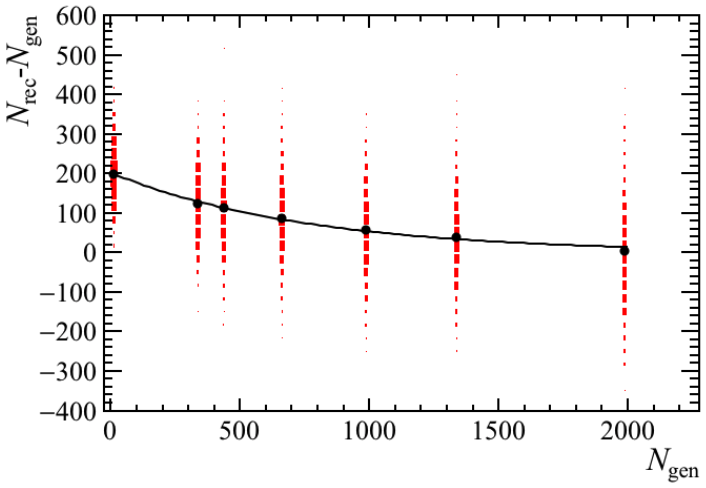

Figure 3.26: Difference between the signal yield obtained from the fits to the pseudo datasets and the generated yield, as a function of the generated value.

Table 3.8: Fit results for the three-dimensional fit. The constraints on the parameters $f_{D_s^+}$, $f_{D_{s0}^{*+}}$, $f_{D_{s1}^+}$, $f_{D_s^+X}$ and $f_{D_s^+X,s}$ are applied taking into account their correlations.

Parameter	Fit result	Constraint
N_{sig}	1336 ± 86	
$f_{\tau\to 3\pi\nu}$	0.78	0.78 (fixed)
$f_{D^{**}\tau\nu}$	0.11	0.11 (fixed)
$N_{D^0}^{\text{sv}}$	445 ± 22	445 ± 22
$f_{D^0}^{v_1 v_2}$	0.41 ± 0.22	
N_{D_s}	6835 ± 166	
f_{D^+}	0.245 ± 0.020	
$N_{B\to D^*3\pi X}$	424 ± 21	443 ± 22
$f_{D_s^+}$	0.494 ± 0.028	0.467 ± 0.032
$f_{D_{s0}^{*+}}$	$0^{+0.010}_{-0.000}$	$0^{+0.042}_{-0.000}$
$f_{D_{s1}^+}$	0.384 ± 0.044	0.444 ± 0.064
$f_{D_s^+X}$	0.836 ± 0.077	0.647 ± 0.107
$f_{(D_s^+X),s}$	0.159 ± 0.034	0.138 ± 0.040
$N_{\text{not}B}$	197	197 (fixed)
$N_{\text{not}D^*}$	243	243 (fixed)

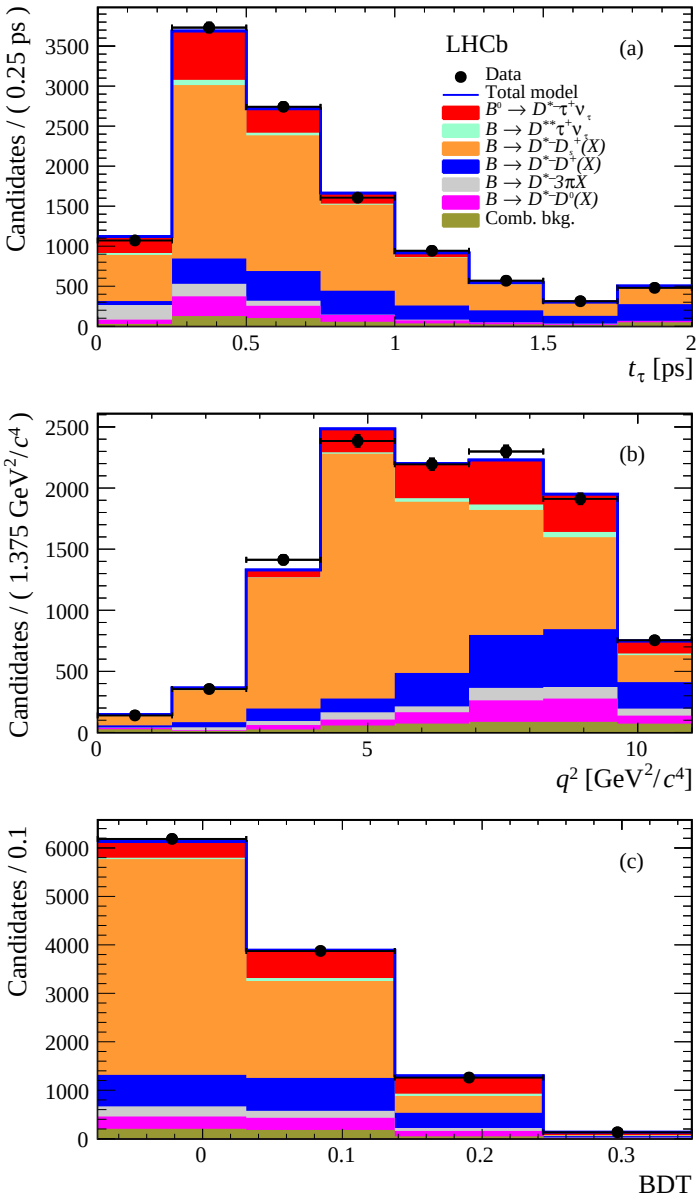

Figure 3.27: Projection of the fit on the (a) t_τ, (b) q^2 and (c) MVA output distributions.

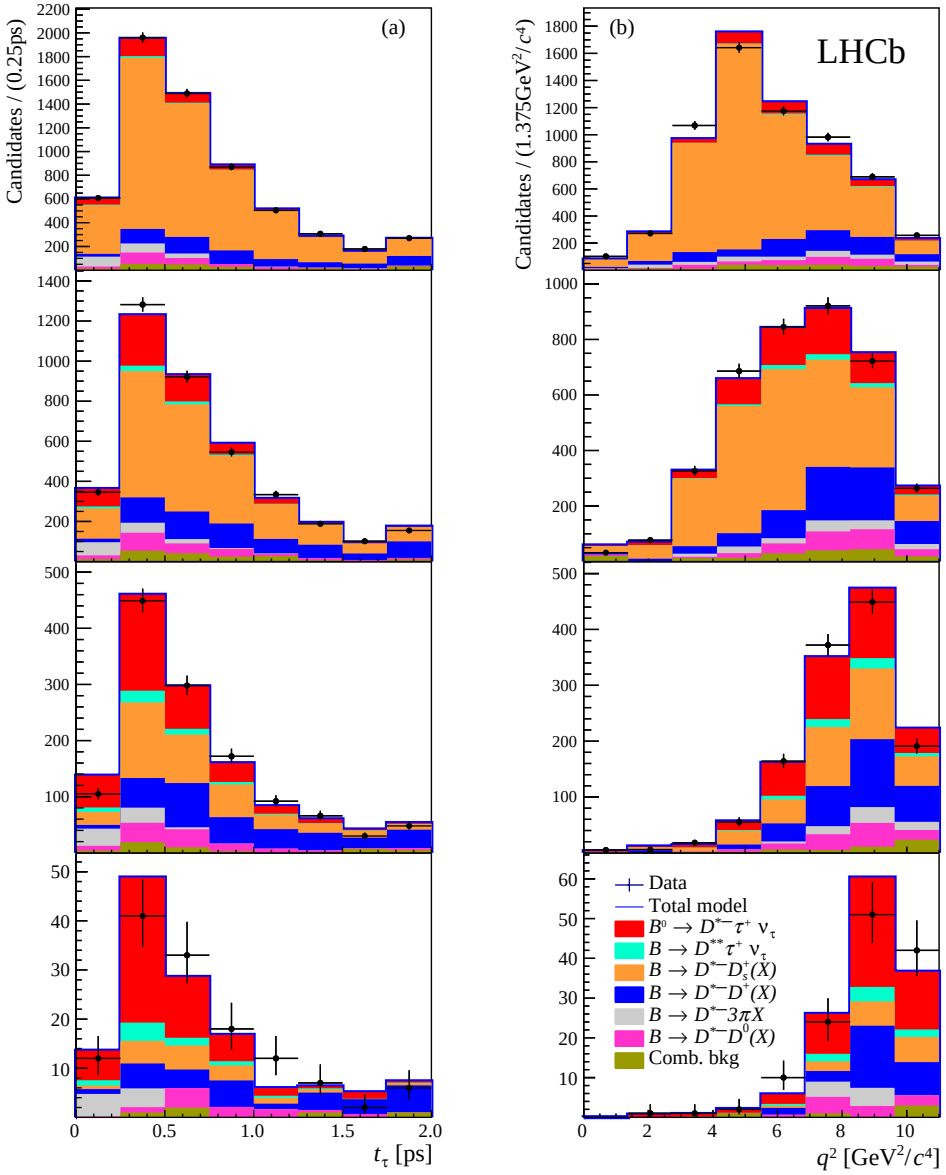

Figure 3.28: Projection of the fit on the (a) t_τ and (b) q^2 distributions in the four bins of the MVA response, with increasing values of the MVA output from top to bottom. The fit components are described in the legend.

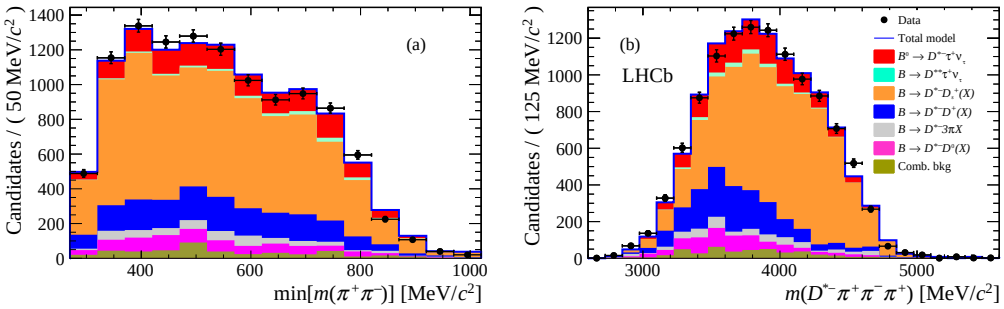

Figure 3.29: Projection of the post-fit model on (a) min$[m(\pi^+\pi^-)]$ and (b) $m(D^{*-}3\pi)$ distributions.

3.6 Evaluation of systematic uncertainties

The evaluation of the various systematic uncertainties is described in the following Section. The sources of systematic uncertainties are related to signal and background modelling, fit procedure, evaluation of the efficiencies and determination of the normalisation yield. In the following, the procedures to evaluate all the relative systematic uncertainties on $\mathcal{K}(D^*)$ are described.

3.6.1 Signal model

Form factors

To assign a systematic uncertainty due to the knowledge of the form factors, 100 pseudoexperiments are performed by extracting randomly the values of $R_0(1)$, $R_1(1)$, $R_2(1)$ and ρ^2 from a multi-Gaussian distribution based on the values and correlations reported in Sec. 3.4.1 (here $R_0(1)$ is assumed to be uncorrelated with the other parameters). The standard deviation of the distribution of the signal yield values obtained from the fits to the pseudoexperiments gives a 0.7% relative systematic uncertainty. The relative difference between the efficiencies on the signal with and without the weighting is 1.0%, and this value is assigned as relative systematic uncertainty related to the effect of the form factors weighting.

τ^+ polarisation

The TAUOLA model used to simulate the signal decays does not reproduce correctly the τ^+ polarisation. For this reason, a comparison at the generator level is performed between signal decays generated with TAUOLA and those where the τ^+ decay model is described by EvtGen [101], which takes into account the polarisation. Since the $\tau^+ \to 3\pi\overline{\nu}_\tau$ decays proceeds mostly through $a_1(1260)^+ \to 3\pi$, the sensitivity to the polarisation in this channel is negligible. For this reason, the study is performed only for $\tau^+ \to 3\pi\pi^0\overline{\nu}_\tau$ decays. The relative change in the efficiency is 1.5% which, scaled by the relative fraction of the $\tau^+ \to 3\pi\pi^0\overline{\nu}_\tau$ component with respect to the total signal component, translates to a relative systematic uncertainty on $\mathcal{K}(D^*)$ equal to 0.4%.

Other τ^+ decays

The simulated sample of $B^0 \to D^{*-}\tau^+\nu_\tau$, where the τ^+ decays inclusively, is used to estimate the contamination of τ^+ decays which are different from the signal decay. The observed number of non-signal events surviving the full selection corresponds to 1% of the total, and this value is taken as a relative systematic uncertainty.

$f_{\tau\to 3\pi\nu}$ evaluation

In the fit performed to obtain the signal yield, the fraction $f_{\tau\to 3\pi\nu}$ is fixed to 0.78 (see Table 3.8). Taking into account the uncertainties of the branching fractions and the efficiencies used to compute this value, an uncertainty of 0.01 is assigned to $f_{\tau\to 3\pi\nu}$. Two alternative fits are then performed, the first one by applying a Gaussian constraint to 0.78 ± 0.01 on $f_{\tau\to 3\pi\nu}$, the second one by fixing its value to that obtained from the first fit. The square root of the difference between the squared uncertainties of the signal yields obtained with the two fits results in a relative systematic uncertainty equal to 0.7%.

3.6.2 Background model

D_s^+ decay model

As explained in Sec. 3.3.1, the control sample obtained selecting candidates with low-MVA response is used to correct the composition of the $D_s^+ \to 3\pi X$ decay in the simulation. In order to assign a systematic uncertainty related to this procedure, 1000 alternative templates for each D_s^+ component are built performing a Gaussian extraction for the relative fraction of each sub-decay of the $D_s^+ \to 3\pi X$ decay, based on the values listed in Table 3.6. The alternative templates are then used to fit the data, and the standard deviation of the distribution of the difference between the signal yields of the alternative and the baseline fits, divided by that of the baseline, is taken as a relative systematic uncertainty, namely 2.5%.

Double-charm background composition

In order to evaluate the uncertainty due to the knowledge of the template shapes of the double-charm background components, alternative templates are produced by weighting the distributions of four variables strongly correlated with the fit variables, namely the masses $\min[m(\pi^+\pi^-)]$, $\max[m(\pi^+\pi^-)]$, $m(D^{*-}3\pi)$ and $m(3\pi)$. For each

double-charm background template, two alternative templates are built by applying a linear weighting on the mass distributions, corresponding to the values ± 1 of certain nuisance parameters. The weighting is not applied to the $\min[m(\pi^+\pi^-)]$, $\max[m(\pi^+\pi^-)]$ and $m(3\pi)$ distributions of the components involving the D_s^+, since a systematic uncertainty for the D_s^+ decay model calculated by using these distributions is already assigned. A fit is then performed by interpolating between the nominal and alternative templates, allowing the nuisance parameters to float between -1 and 1. The fit is repeated fixing the values of the nuisance parameters to those obtained in the previous step, and the square root of the difference between the squared uncertainties of the signal yields obtained with the two fits allows a relative systematic uncertainty equal to 2.9% to be assessed.

A systematic uncertainty is assigned to take into account the statistical uncertainty of the relative fractions $f_{D_s^+}$, $f_{D_{s0}^{*+}}$, $f_{D_{s1}^+}$, $f_{D_s^+X}$, $f_{(D_s^+X),s}$. The baseline fit is repeated by fixing the values of these fractions to those obtained in the baseline fit, and the square root of the difference between the squared uncertainties of the signal yield obtained with this fit and the baseline one gives a relative systematic uncertainty of 2.6%.

Prompt $B \to D^{*-}3\pi X$ background

The uncertainty related to the knowledge of the shape and normalisation of the $B \to D^{*-}3\pi X$ background component is evaluated in the same way as for the double-charm background, *i.e.* by interpolating the template and repeating the fit after leaving fixed the normalisation. The assigned relative systematic uncertainty is 2.8%.

Combinatorial background

The template interpolation is used also to evaluate the systematic uncertainty related to the shape of the combinatorial background, giving a relative systematic uncertainty of 0.7%. Since the normalisation of the combinatorial background is fixed in the baseline fit, an alternative fit with a Gaussian constraint with a 30% width on $N_{\mathrm{not},B}$ and N_{not,D^*} is performed, giving a systematic uncertainty equal to 0.1%.

Feed-down from $D^{**}_{(s)}$

In order to evaluate the contamination due to the feed-down from $B \to D^{**}\tau^+\nu_\tau$ decays, a sample of reconstructed $B^+ \to D_1(2420)^0\tau^+\nu_\tau$ decays is built by requiring the isolation algorithm to find a pion compatible with the B decay vertex. The $B^+ \to D_1(2420)^0\tau^+\nu_\tau$ yield is then obtained by fitting the $m(D_1(2420)^0) - m(D^{*-})$ distribution, scaled by a factor evaluated from simulation to get un upper limit on the yield of all $B \to D^{**}\tau^+\nu_\tau$ decays in data. The observed contamination corresponds to a relative systematic uncertainty of 2.3%.

Finally a relative systematic uncertainty of 1.5% is obtained for the contamination of $B_s^0 \to D_s^{**}\tau^+\nu_\tau$ decays, according to the uncertainty on $r_{B_s^0}$ (see Sec. 3.4.5).

3.6.3 Fit model

Finite size of simulated samples

In order to evaluate the systematic uncertainty due the size of simulated samples, new templates are produced by sampling from the original ones, varied bin-by-bin according to a Poisson distribution. The procedure is repeated 500 times, each time fitting the data with the model built with the alternative templates. The associated relative systematic uncertainty corresponds to the standard deviation of the distribution of the 500 signal yields, and it is equal to 4.1%.

Bias evaluation

In Sec. 3.5.2 the procedure needed to evaluate the bias on the signal yield obtained from the fit has been described. The three-dimensional probability density functions are built using a KDE approach, which depends on a given smoothing parameter. Alternative tests are performed with different smoothing parameters, resulting in a 1.3% relative difference in the signal yield, which is therefore assigned as a relative systematic uncertainty.

3.6.4 Selection efficiency

3.6.4.1 Uncertainty related to the size of the simulated samples

The uncertainty of the selection efficiencies on signal and normalisation, evaluated using simulated events, depends on the size of the simulated samples. The efficiencies and their uncertainties are reported in Table 3.10. The uncertainty of the signal

efficiency gives a relative systematic uncertainty of 1.7%, while for the normalisation the contribution is 1.6%.

Stripping selection

A systematic uncertainty must be assessed to take into account possible differences in stripping efficiency between data and simulated events. To this end, various tests performed by changing the requirements used in the stripping selection, and the maximum relative deviation of the efficiency ratio between signal and normalisation results to be 2%, which is taken as a relative systematic uncertainty.

Trigger efficiency

The relative systematic uncertainty associated to the correction factor for the `L0Hadron_TOS` trigger selection $r_{\texttt{L0Hadron\_TOS}} = 0.995 \pm 0.010$ is 1%. In the same way, the relative systematic uncertainty associated to the correction factor for the `L0Global_TIS` trigger selection $r_{\texttt{L0Global\_TIS}} = 1.031 \pm 0.011$ is 1%.

PID requirements

The correction introduced in Sec. 3.4.2, applied to simulated events to describe correctly the effects of the requirements on `ProbNN`, depends on the chosen binning scheme in the number of tracks in the event, momentum and pseudorapidity of the track. Two alternative binning schemes are tested, with half and twice the number of the bins. The resulting correction factors lead to a relative systematic uncertainty of 1.3%.

Offline selection

The systematic uncertainty associated to the knowledge of the relative efficiencies corresponding to the different signal and normalisation vertex topologies is evaluated as in the following. The simulated sample of inclusive $D^{*-}3\pi X$ is split into three regions, between -4σ and -2σ, between -2σ and 2σ and between 2σ and 4σ, where σ is the uncertainty on the distance between the B^0 and the τ^+ decay vertices along the beam direction. Then, for the candidates with $m(D^{*-}3\pi)$ in the $B^0 \to D^{*-}3\pi$ peak region, the ratio between the number of candidates in the outer regions and that of candidates in the inner region is computed. The same ratio is calculated for candidates outside the $B^0 \to D^{*-}3\pi$ peak, which show a signal-like behaviour.

The whole procedure is performed also on data, and the difference between the ratios measured in data and in simulation, for both events inside and outside the $B^0 \to D^{*-}3\pi$ peak region, is calculated. The corresponding relative difference in the signal-background efficiency ratio, equal to 2%, is taken as a systematic uncertainty.

Charged-isolation requirement

Comparing the efficiency of the charged-isolation requirement obtained in the normalisation sample with that measured in the corresponding simulation, a relative difference of 1% is seen, and this value is taken as a relative systematic uncertainty.

3.6.5 Normalisation yield and model

The systematic uncertainty of the normalisation yield is evaluated with alternative fit configurations: the fit is also performed on a different mass range or requiring the mean value of the signal functions to be the same between the 2011 and 2012 data samples. The maximum difference between signal yields in alternative and nominal configurations is used to assess a systematic uncertainty on the normalisation yield equal to $\sqrt{64^2 + 22^2} = 68$, which, since $N_{\text{norm}} = 17657$, gives a relative uncertainty of 0.4%. To take into account other possible unknown resonant contributions in the $B^0 \to D^*3\pi$ decay, a conservative 1% relative systematic uncertainty is assessed.

A systematic uncertainty is assessed for the weighting procedure, described in Sec. 3.4.7, performed to match the $m(3\pi)$ distribution for the normalisation sample between data and simulation. A relative difference of 2% in the efficiency on the normalisation is seen with and without applying the weighting, so this value is assigned as a relative systematic uncertainty.

3.6.6 Summary of systematic uncertainties

A summary of the various relative systematic uncertainties for the measurement of $\mathcal{K}(D^*)$ is reported in Table 3.9. The total relative systematic uncertainty, obtained as the quadratic sum of all contributions, is 9.1%.

3.7 Results

The value of $\mathcal{K}(D^*)$ is calculated by using Eq. (3.7), with all the needed yields, efficiencies, correction factors and branching fractions listed in Table 3.10. The

efficiencies are evaluated using simulation and the efficiency ratio must be divided by the various correction factors. The branching fractions of $\tau^+ \to 3\pi\overline{\nu}_\tau$ and $\tau^+ \to 3\pi\pi^0\overline{\nu}_\tau$ decays are taken from Ref. [26]. The resulting $\mathcal{K}(D^*)$ is therefore

$$\mathcal{K}(D^*) = 1.97 \pm 0.13 \text{ (stat)} \pm 0.18 \text{ (syst)},$$

where the first uncertainty is statistical and the second systematic.

The branching fraction of the $B^0 \to D^{*-}\tau^+\nu_\tau$ decay is then calculated according to Eq. (3.1)

$$\mathcal{B}(B^0 \to D^{*-}\tau^+\nu_\tau) = (1.42 \pm 0.094 \text{ (stat)} \pm 0.129 \text{ (syst)} \pm 0.054 \text{ (ext)})\%,$$

where the first uncertainty is statistical, the second systematic and the third due to the knowledge of the $B^0 \to D^{*-}3\pi$ branching fraction, which is obtained from the weighted average of the measurements performed by LHCb [88], BaBar [89] and Belle [90]: $\mathcal{B}(B^0 \to D^{*-}3\pi) = (0.721 \pm 0.028)\%$. The value of $\mathcal{B}(B^0 \to D^{*-}\tau^+\nu_\tau)$ measured in this analysis is compatible with the previous measurements [26].

The value of $\mathcal{R}(D^*)$ is obtained by dividing $\mathcal{B}(B^0 \to D^{*-}\tau^+\nu_\tau)$ by the known branching fraction $\mathcal{B}(B^0 \to D^{*-}\mu^+\nu_\mu) = (4.88 \pm 0.10)\%$ [6], resulting in

$$\mathcal{R}(D^*) = 0.291 \pm 0.019 \text{ (stat)} \pm 0.026 \text{ (syst)} \pm 0.013 \text{ (ext)},$$

which corresponds to one of the most precise single measurements of $\mathcal{R}(D^*)$ and to the first one performed with the three-prong decay of the τ lepton. This measurement is fully compatible with previous determinations, summarised in Sec. 1.4.2.

Comparing the result with the theoretical calculations listed in Table 1.2, the measured value is higher than the predictions, with a difference spanning from 0.9 standard deviations, corresponding to the less precise prediction [48], to 1.1 standard deviations [38]. The combination with the previous measurement by LHCb [59], taking into account the correlations between the systematic uncertainties due to form factors, τ polarisation and $B \to D^{**}\tau^+\nu_\tau$ contamination, is equal to $\mathcal{R}(D^*) = 0.310 \pm 0.016 \text{ (stat)} \pm 0.022 \text{ (syst)}$, higher than the SM expectation with a difference ranging from 1.8 to 2.1 standard deviations. Figure 3.30 gives an illustration of the various measurements and theoretical calculations of $\mathcal{R}(D^*)$, while Fig. 3.31 shows a similar comparison for the combination of $\mathcal{R}(D)$ and $\mathcal{R}(D^*)$. Combining the measured values of $\mathcal{R}(D)$ and $\mathcal{R}(D^*)$, and taking into account their correlation -0.203, a difference with respect to the SM prediction (using the $\mathcal{R}(D^*)$ prediction with the largest theoretical uncertainty) of 3.6 standard deviations is obtained.

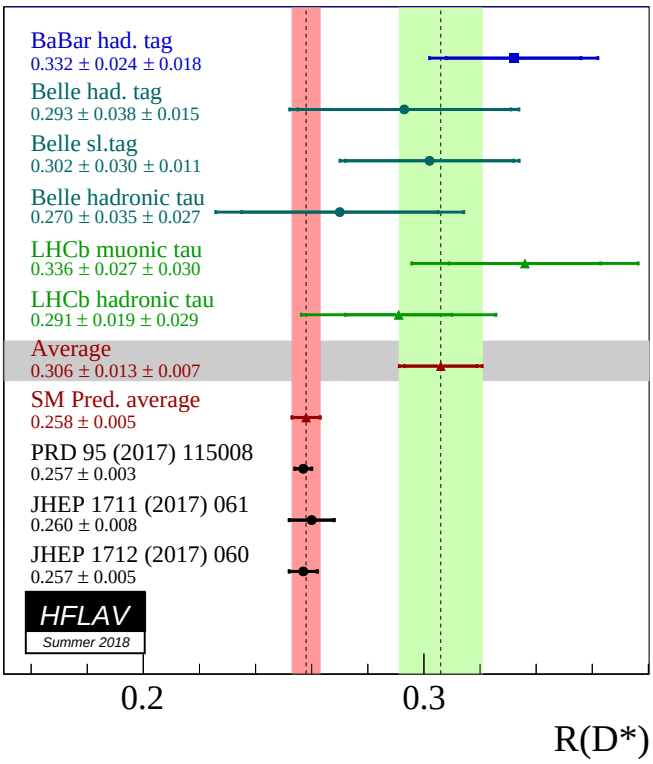

Figure 3.30: Summary of the current status of experimental measurements and theoretical predictions of $\mathcal{R}(D^*)$.

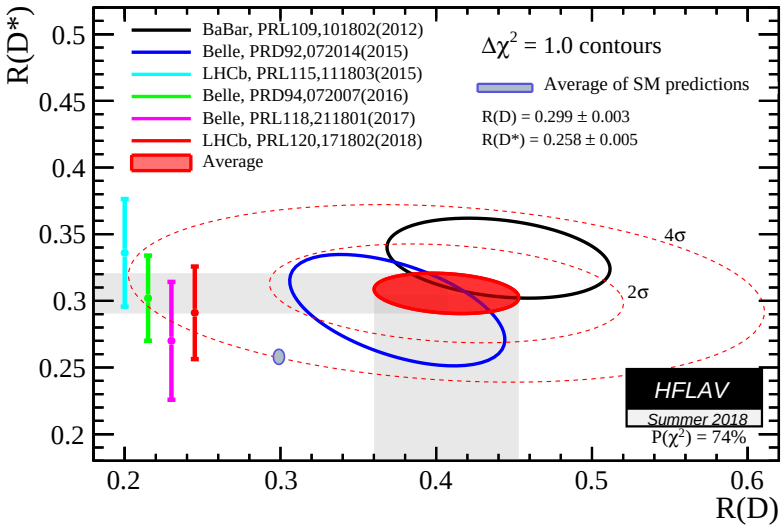

Figure 3.31: Graphical view of the current status of experimental measurements and theoretical predictions of $\mathcal{R}(D^*)$ and $\mathcal{R}(D)$.

The new technique presented in this thesis, developed to reconstruct semitauonic decays with $\tau^+ \to 3\pi(\pi^0)\overline{\nu}_\tau$ transitions, can potentially be applied to the semitauonic decays of the other b hadrons, as B^+, B_s^0, B_c^+ and Λ_b^0. The inclusion of the data collected by LHCb during Run 2 will result in an overall uncertainty on $\mathcal{R}(D^*)$ measured by using the $\tau^+ \to 3\pi(\pi^0)\overline{\nu}_\tau$ decay comparable to that of the current world average.

The measurement of $\mathcal{B}(B^0 \to D^{*-}\tau^+\nu_\tau)$ and $\mathcal{R}(D^*)$ described in this thesis has been published in two papers [102, 103].

Table 3.9: List of the relative systematic uncertainties for the measurement of $\mathcal{K}(D^*)$.

Uncertainty source	**Value [%]**
Form factors (template shapes)	0.7
Form factors (efficiency)	1.0
τ^+ polarisation	0.4
Other τ^+ decays	1.0
$f_{\tau\to 3\pi\nu}$	0.7
$D_s^+ \to 3\pi X$ decay model	2.5
double-charm background template shapes	2.9
$B \to D^{*-} D_s^+(X)$ and $B \to D^{*-} D^0(X)$ composition	2.6
$B \to D^{*-} 3\pi X$ shape and normalisation	2.8
Combinatorial background (shape)	0.7
Combinatorial background (normalisation)	0.1
$B \to D^{**}\tau^+\nu_\tau$ contamination	2.3
$B_s^0 \to D_s^{**}\tau^+\nu_\tau$ contamination	1.5
Size of simulation in the fit	4.1
Bias due to empty bins in templates	1.3
Stripping selection	2.0
`L0Hadron_TOS`	1.0
`L0Global_TIS`	1.0
Offline selection	2.0
Particle identification	1.3
Charged-isolation algorithm	1.0
Signal efficiencies (size of simulation samples)	1.7
Normalisation channel efficiency (size of simulation samples)	1.6
Normalisation yield	1.0
Modeling of 3π dynamics in $B^0 \to D^{*-} 3\pi$	2.0
Total uncertainty	9.1

Table 3.10: Values needed to calculate $\mathcal{K}(D^*)$.

Parameter	Value
N_{sig}	1296 ± 86
N_{norm}	$17657 \pm 143 \pm 64 \pm 22$
$\varepsilon_{\text{sig},3\pi\overline{\nu}_\tau,\text{MC}}$	$(6.08 \pm 0.06) \times 10^{-5}$
$\varepsilon_{\text{sig},3\pi\pi^0\overline{\nu}_\tau,\text{MC}}$	$(3.23 \pm 0.05) \times 10^{-5}$
$\varepsilon_{\text{norm,MC}}$	$(20.0 \pm 0.4) \times 10^{-5}$
$r_{\texttt{LOHadron\_TOS}}$	0.995±0.010
$r_{B_s^0}$	1.030±0.015
$r_{\texttt{LOGlobal\_TIS}}$	1.031 ± 0.011
$\mathcal{B}\ (\tau^+ \to 3\pi\overline{\nu}_\tau)$	$(9.07 \pm 0.05)\%$
$\mathcal{B}\ (\tau^+ \to 3\pi\pi^0\overline{\nu}_\tau)$	$(4.74 \pm 0.05)\%$

Chapter 4

Measurement of ΔA_{CP}

The measurement of $\Delta A_{CP} \equiv A_{CP}(D^0 \to K^+K^-) - A_{CP}(D^0 \to \pi^+\pi^-)$ performed using data collected with the LHCb detector during Run 2 is described in this chapter. After the explanation of the analysis strategy in Sec. 4.1, a description of the data sample and of the selection criteria is given in Sec. 4.2. The procedure used to determine the raw asymmetries is discussed in Sec. 4.3. The various studies performed to evaluate the systematic uncertainties are described in Sec. 4.4, while an overview of the cross-checks to test the robustness and consistency of the measurement is given in Sec. 4.5. In Sec. 4.6, the measurement of the average D^0 decay time, needed for the interpretation of the result in terms of direct and indirect *CP* asymmetries, is reported. Finally, the results are summarised in Sec. 4.7.

4.1 Analysis strategy

The raw asymmetry of D^0 decays to a *CP* eigenstate f is defined as

$$A_{\text{raw}}(f) = \frac{N(D^0 \to f) - N(\overline{D}^0 \to f)}{N(D^0 \to f) + N(\overline{D}^0 \to f)}, \tag{4.1}$$

where $N(D^0 \to f)$ and $N(\overline{D}^0 \to f)$ are the reconstructed yields of D^0 and $\overline{D}^0$ mesons, respectively, decaying into the final state f. Since f is a *CP* eigenstate, it is not possible to deduce the flavour of the D^0 meson at production from its decay products. The D^0 flavour is therefore inferred by looking at the accompanying particles in the decay where the D^0 is produced. This process, called *flavour tagging*, is performed in two ways.

Prompt tag: it consists of looking at the charge of the pion in the $D^{*+} \to D^0\pi^+$ and $D^{*-} \to \overline{D}^0\pi^-$ decays, where the $D^{*\pm}$ mesons are produced promptly from

pp collisions. The positive charge of the pion identifies a D^0, while the negative charge corresponds to a $\overline{D}^0$.

Semileptonic tag: this method uses D^0 mesons produced in flavour-specific decays of B mesons, $\overline{B}^0,\ B^- \to D^0\mu^- X$ or $B^0,\ B^+ \to \overline{D}^0\mu^+ X$. In this case a negative muon is associated to D^0, while a positive muon identifies a $\overline{D}^0$.

The two tagging procedures use two independent samples, from now on referred to as *prompt* and *semileptonic* samples, and the measurement of ΔA_{CP} is therefore performed independently on the two samples.

The raw asymmetry defined in Eq. (4.1) is not equal to the physical *CP* asymmetry defined in Eq. (1.70), since other asymmetries need to be taken into account. The fact that the detector response is not perfectly symmetric and that cross-sections of particles and antiparticles while interacting with the detector material are different is responsible for a detection asymmetry of the hadron h^+

$$A_{\rm D}(h^+) = \frac{\varepsilon(h^+) - \varepsilon(h^-)}{\varepsilon(h^+) + \varepsilon(h^-)}, \tag{4.2}$$

where $\varepsilon(h^\pm)$ is the reconstruction efficiency of the $h^\pm$ hadron integrated over its momentum distribution. There is also an asymmetry due to different production rates of D^0 and $\overline{D}^0$, which is defined as

$$A_{\rm P}(D^0) = \frac{\sigma(D^0) - \sigma(\overline{D}^0)}{\sigma(D^0) + \sigma(\overline{D}^0)}, \tag{4.3}$$

where $\sigma(D^0)$ and $\sigma(\overline{D}^0)$ are the inclusive production cross-sections of D^0 and a $\overline{D}^0$ in *pp* collisions, respectively. For D^0 mesons originating from prompt D^* mesons, the production asymmetry $A_{\rm P}(D^0)$ is equal to $A_{\rm P}(D^{*+})$, while for D^0 mesons produced in B decays the effective D^0 production asymmetry in semileptonic B decays is

$$A_{\rm P,eff}(D^0) = f(\overline{B}^0) D A_{\rm P}(\overline{B}^0) + [1 - f(\overline{B}^0)] A_{\rm P}(B^-), \tag{4.4}$$

where $f(\overline{B}^0)$ is the fraction of $\overline{B}^0$ mesons in the sample with respect to the total number of $\overline{B}$, $A_{\rm P}(\overline{B}^0)$ and $A_{\rm P}(B^-)$ are the production asymmetries of $\overline{B}^0$ and B^-, D is the dilution factor due to B^0-$\overline{B}^0$ mixing (see Sec. 4.4.2).

The number of reconstructed D^0 and $\overline{D}^0$ candidates with the prompt tag is proportional to reconstruction efficiencies (assuming they are factorisable), production rates, branching fractions

$$N(D^0 \to f) \propto \sigma(D^{*+})\varepsilon(\pi^+)\Gamma(D^0 \to f), \tag{4.5a}$$

$$N(\overline{D}^0 \to f) \propto \sigma(D^{*-})\varepsilon(\pi^-)\Gamma(\overline{D}^0 \to f). \tag{4.5b}$$

According to Eqs. (1.70), (4.2), (4.3) and (4.5), the raw asymmetry defined in Eq. (4.1) can be written as

$$A_{\rm raw}(f) = \frac{A_{CP}(f) + A_{\rm P}(D^{*+}) + A_{\rm D}(\pi^+) + A_{CP}(f)A_{\rm P}(D^{*+})A_{\rm D}(\pi^+)}{1 + A_{\rm P}(D^{*+})A_{CP}(f) + A_{\rm P}(D^{*+})A_{\rm D}(\pi^+) + A_{CP}(f)A_{\rm D}(\pi^+)}. \quad (4.6)$$

As the $A_{\rm P}(D^{*+})$ value is expected to be 1% (because $A_{\rm P}(D^+)$ is order of 1% [104]) and also $A_{\rm D}(\pi^+)$ is of the same order, Eq. (4.6) can be written, up to $\mathcal{O}(10^{-6})$, as

$$A_{\rm raw}(f) = A_{CP}(f) + A_{\rm P}(D^{*+}) + A_{\rm D}(\pi^+). \quad (4.7)$$

In an analogous way, for the semileptonic channel the raw asymmetry is equal to

$$A_{\rm raw}(f) = A_{CP}(f) + A_{\rm P,eff}(D^0) + A_{\rm D}(\mu^-). \quad (4.8)$$

This means that the difference between the two raw asymmetries is equal to the difference between the *CP* asymmetries

$$\Delta A_{\rm raw} = A_{\rm raw}(K^+K^-) - A_{\rm raw}(\pi^+\pi^-) = A_{CP}(K^+K^-) - A_{CP}(\pi^+\pi^-) = \Delta A_{CP}, \quad (4.9)$$

since production and detection asymmetries are independent of the final state. However, these nuisance asymmetries vary as function of the decay kinematics. Hence, if the kinematic distributions are different between the reconstructed $D^0 \to K^+K^-$ and $D^0 \to \pi^+\pi^-$ decays, the nuisance asymmetries may not fully cancel in the difference. To remove possible residual effects due to production and detection asymmetries, a weighting technique is applied to equalise the relevant kinematic distributions, as described in Sec. 4.2.4.

To calculate the raw asymmetries, a fit is performed on the $m(D^0\pi)$ distribution for the prompt sample and $m(D^0)$ for the semileptonic sample, after splitting the D^0 candidates according to the tag, as explained in Sec. 4.3. The data sample is split on the basis of data-taking year and magnet polarity (*MagUp* or *MagDown*, depending on whether the main component of the magnetic field is directed upward or downward), and the measurement is performed independently on each subsample, combining the results at the end.

4.2 Data sample and selection

The analysis is based on the data recorded by LHCb using the Turbo data stream, described in Sec. 2.5.3. In the prompt case, the analysis is based on the data sample

collected during 2015, 2016, 2017 and 2018, whereas in that of the semileptonic mode, as the corresponding Turbo trigger line was introduced only one year later, 2016, 2017 and 2018 data are used. For this analysis three D^0 decay modes are considered: $D^0 \to \pi^+\pi^-$, $D^0 \to K^+K^-$ and $D^0 \to K^-\pi^+$. In the prompt mode, the D^* meson is asked to come from the PV and to be fully reconstructed. In the case of the semileptonic mode, only the D^0 and the μ are reconstructed. The main handles on the authenticity of semileptonic decays are the significant impact parameter of the muon with respect to the PV and the good quality of its common vertex with a D^0 meson.

In the following, a detailed description of the various criteria required by the relevant trigger lines (Sec. 4.2.1) and by the offline selection (Sec. 4.2.2) is reported. A description of the simulated samples is given in Sec. 4.2.3.

4.2.1 Trigger selection

The following trigger criteria are required on the prompt sample.

L0 trigger: `L0Global_TOS` on the D^0 or `L0Global_TIS` on the D^*, which means that the event is accepted if at least one track coming from the D^0 fires any L0 trigger or if any particles not originating from the D^* fires any L0 trigger.

HLT1 trigger: `Hlt1TrackMVA_TOS` or `Hlt1TwoTrackMVA_TOS` on the D^0, *i.e.* at least one particle from the D^0 must fire the `Hlt1TrackMVA` or the `Hlt1TwoTrackMVA` triggers. The `Hlt1TrackMVA` line looks for a single track with good reconstruction quality, high p_{T} and significant IP with respect to the PV. The `Hlt1TwoTrackMVA` line looks for couples of long tracks which are both characterised by good reconstruction quality and high momentum, and are consistent with the decay of a high p_{T} particle significantly displaced from the PV.

For what concerns the semileptonic sample, the requirements are given in the following.

L0 trigger: `L0Muon_TOS` on the muon, *i.e.* the muon must fire the `L0Muon` trigger.

HLT1 trigger: `Hlt1TrackMuon_TOS` or `Hlt1TrackMuonMVA_TOS` on the muon, or `Hlt1TrackMVA_TOS` or `Hlt1TwoTrackMVA_TOS` on the B, which means that the muon must fire either the `Hlt1TrackMuon` or `Hlt1TrackMuonMVA` lines or any

particle coming from the B meson must trigger either the `Hlt1TrackMVA` or `Hlt1TwoTrackMVA` lines. Both `Hlt1TrackMuon` and `Hlt1TrackMuonMVA` lines look for a muon with high p_{T} and high χ^2_{IP} with respect to the PV. The difference between them is that the `Hlt1TrackMuonMVA` line uses a set of parameters optimised with a MVA.

The reconstruction of the D^* and B candidates is performed directly by the Turbo lines in the HLT2 stage. For the prompt mode, three Turbo lines, one for each D^0 decay mode, reconstruct a D^0 meson by combining two tracks identified as pions, kaons, or a kaon and a pion, into a common vertex detached from the PV. The D^0 is then combined with a *soft pion* π_s, *i.e.* a pion with low momentum, to form the D^* meson candidate. The requirements asked by the Turbo lines are reported in Table 4.1. The variables involved are related to reconstruction quality (P_{track}(Ghost) and χ^2_{track}/ndof), kinematics (p and p_{T}), topology (χ^2_{IP}) and particle identification ($\mathrm{DLL}_{K\pi}$). The reconstructed D^0 and D^* candidates must satisfy some requirements on the invariant masses, the decay-vertex quality (χ^2_{vertex}/ndof), the distance of the decay vertex from the PV in terms of χ^2 (χ^2_{VD}), the transverse momentum of the decay products, the DIRA and the DOCA (as defined in Sec. 3.2.1).

Similar requirements are applied to the tracks used to reconstruct the D^0 and the B candidates, the latter obtained by combining the D^0 with a muon, in the semileptonic mode. The detailed list of requirements is reported in Table 4.2. Among the variables involved in the selection, the corrected mass of the B candidate $m_{\mathrm{corr}}(B)$ is present. This variable is defined as $m_{\mathrm{corr}}(B) = \sqrt{m(B)^2 + p_{\mathrm{T}}(B)^2} + p_{\mathrm{T}}(B)$, where $m(B)$ is the visible invariant mass of the B meson and $p_{\mathrm{T}}(B)$ is its visible momentum transverse to the flight direction. The corrected mass partially recovers the missing energy due to the invisible neutrino and unreconstructed particles, since from the flight direction and the momentum direction it is possible, owing to momentum conservation, to calculate the missing momentum transverse to the flight direction.

4.2.2 Offline selection

The events surviving the trigger selections are further filtered by applying a set of offline requirements, as described in the following.

Prompt sample

Before applying the offline selection requirements, the data sample has been processed using the DecayTreeFitter (DTF) package [105]. The DTF algorithm enables a

Table 4.1: Selection requirements applied in the Turbo selection for $D^0 \to K^+K^-$, $D^0 \to \pi^+\pi^-$ and $D^0 \to K^-\pi^+$ decays in the prompt sample.

Particle	Variable	Selection requirement
K, π from D^0	$P_{\text{track}}(\text{Ghost})$	< 0.4
	$\chi^2_{\text{track}}/\text{ndof}$	< 3
	p	$> 5\,\text{GeV}/c$
	p_{T}	$> 800\,\text{MeV}/c$
	χ^2_{IP}	> 4
	$\text{DLL}_{K\pi}(K)$	> 5
	$\text{DLL}_{K\pi}(\pi)$	< 5
soft π from D^*	$P_{\text{track}}(\text{Ghost})$ (2015, 2016)	< 0.4
	$P_{\text{track}}(\text{Ghost})$ (2017, 2018)	< 0.25
	$\chi^2_{\text{track}}/\text{ndof}$	< 3
	p	$> 1\,\text{GeV}/c$
	p_{T} (2015, 2016)	$> 100\,\text{MeV}/c$
	p_{T} (2017, 2018)	$> 200\,\text{MeV}/c$
D^0	$m(D^0)$	$\in [1715, 2015]\,\text{MeV}/c^2$
	$\chi^2_{\text{vertex}}/\text{ndof}$	< 10
	χ^2_{VD}	> 25
	cos(DIRA)	> 0.99985
	DOCA	$< 0.1\,\text{mm}$
	p_{T}	$> 2\,\text{GeV}/c$
	$\max[p_{\text{T}}(h^+), p_{\text{T}}(h^-)]$	$> 1\,\text{GeV}/c$
D^*	$m(D^*) - m(D^0)$	$\in [130, 160]\ \text{MeV}/c^2$
	$\chi^2_{\text{vertex}}/\text{ndof}$	< 25

constraint on the D^* to be applied, asking its decay vertex to coincide with the associated PV. Such a constraint improves the D^* mass resolution and gives a slight gain in the precision of the measured A_{raw}. To discard D^* candidates where the fits do not converge or have poor quality, the condition $0 < \chi^2_{\text{DTF}} < 150$ is required. The offline selection, whose requirements are reported in Table 4.3, is based on: the D^0 invariant mass $m(D^0)$ to select the signal region, corresponding to about three standard deviations of the signal mass distribution around the nominal value of the D^0 mass; the χ^2_{IP} in order to select events where the D^0 comes from a PV; the $\text{DLL}_{K\pi}$ of the D^0 decay products to reduce the background due to misidentified particles. In addition, low-statistics regions at the edges of the kinematic distributions of the D^0 meson and the π_s, which could affect the weighting procedure described in Sec. 4.2.4, are vetoed.

Table 4.2: Selection requirements applied in the Turbo selection for $D^0 \to K^+K^-$, $D^0 \to \pi^+\pi^-$ and $D^0 \to K^-\pi^+$ decays in the semileptonic sample.

Particle	Variable	Selection requirement
K, π from D^0	$P_{\text{track}}(\text{Ghost})$	< 0.4
	p	$> 2\,\text{GeV}/c$
	p_{T}	$> 200\,\text{MeV}/c$
	χ^2_{IP}	> 9
	$\text{DLL}_{K\pi}(K)$	> 5
	$\text{DLL}_{K\pi}(\pi)$	< 0
μ from B	$P_{\text{track}}(\text{Ghost})$	< 0.4
	p	$> 3\,\text{GeV}/c$
	p_{T}	$> 1\,\text{GeV}/c$
	χ^2_{IP}	> 9
	$\text{DLL}_{\mu\pi}$	> 0
D^0	$m(D^0)$	$\in [1775, 1955]\,\text{MeV}/c^2$
	$\chi^2_{\text{vertex}}/\text{ndof}$	< 9
	χ^2_{VD}	> 9
B	$m(B)$	$\in [2300, 10000]\,\text{MeV}/c^2$
	$m_{\text{corr}}(B)$	$\in [2800, 8500]\,\text{MeV}/c^2$
	$\chi^2_{\text{vertex}}/\text{ndof}$	< 9
	$\cos(\text{DIRA})$	> 0.999
	χ^2_{DOCA}	< 10

Furthermore, to exclude kinematic regions where a large soft-pion detection asymmetry is present, a set of *fiducial requirements* is applied, resulting in about 34% of discarded candidates. Owing to these, no kinematic regions with detection asymmetries larger than order of 1% are kept. A graphical representation of the fiducial requirements together with the distribution of A_{raw} as a function of $(p_z(\pi_s),\ p_x(\pi_s))$ for *MagDown* and *MagUp* data samples is reported in Fig. 4.1. The raw asymmetry shown in these plots is obtained by performing the ratio between the difference and the sum of the bidimensional $(p_z(\pi_s),\ p_x(\pi_s))$ distributions for the D^0 and the $\overline{D}^0$ candidates, after background removal performed with the *sPlot* technique [106] using the fit model described in Sec. 4.3.1. Some regions with 100% asymmetry are clearly visible: this is due to the fact that soft pions with a certain charge and values of p_x and p_z are deviated by the magnetic field outside the detector acceptance, while the same does not happen for pions with equal p_x and p_z values

Table 4.3: Offline selection requirements applied to the candidates surviving the trigger selection for the prompt mode.

Variable	Selection requirement
$m(D^0)$	[1844,1887] MeV/c^2
$\chi^2_{\rm IP}(D^0)$	< 9
$\mathrm{DLL}_{K\pi}$ of π from D^0	< -5
Fiducial requirements	see Eq. (4.10)
$p(\pi_s)$	$< 20\,\mathrm{GeV}/c$
$p_{\rm T}(\pi_s)$	$< 2\,\mathrm{GeV}/c$
$\eta(\pi_s)$	$\in [2, 5]$
$p(D^0)$	$< 200\,\mathrm{GeV}/c$
$p_{\rm T}(D^0)$	$< 20\,\mathrm{GeV}/c$
$\eta(D^0)$	$\in [2, 5]$

but opposite charge. The set of fiducial requirements is defined by

$$\begin{aligned} &|p_x| < \alpha(p_z - p_0) \\ &|p_y/p_z| > 0.02 \quad \text{OR} \quad |p_x| < p_1 - \beta_1 p_z \quad \text{OR} \quad |p_x| > p_2 + \beta_2 p_z, \end{aligned} \tag{4.10}$$

with $\alpha = 0.317$, $p_0 = 2400\,\mathrm{MeV}/c$, $p_1 = 418\,\mathrm{MeV}/c$, $p_2 = 497\,\mathrm{MeV}/c$, $\beta_1 = 0.01397$ and $\beta_2 = 0.01605$.

Some events contain more than one D^* candidate after the full selection. They share mostly the same reconstructed D^0 candidate but different soft pions. When this happens, a random candidate is kept per event. This results in removing about 10% of the candidates.

Semileptonic sample

Candidates in the semileptonic sample surviving the trigger selection are further processed using the DTF algorithm, without applying the vertex constraint on the PV. The offline selection for the semileptonic sample consists in a set of requirements followed by a MVA-based selection. The list of requirements is reported in Table 4.4. They include: the distance of the D^0 and B decay vertices along the z direction ($\mathrm{vtx}_z(D^0) - \mathrm{vtx}_z(B)$), in order to suppress combinatorial background where the D^0 vertex is reconstructed backwards with respect to the B; the χ^2/ndf of the DTF separately performed on the D^0 and the B; the invariant mass and the corrected mass of the B ($m(B)$ and $m_{\rm corr}(B)$); and the $\mathrm{DLL}_{K\pi}$ of the D^0 decay products to

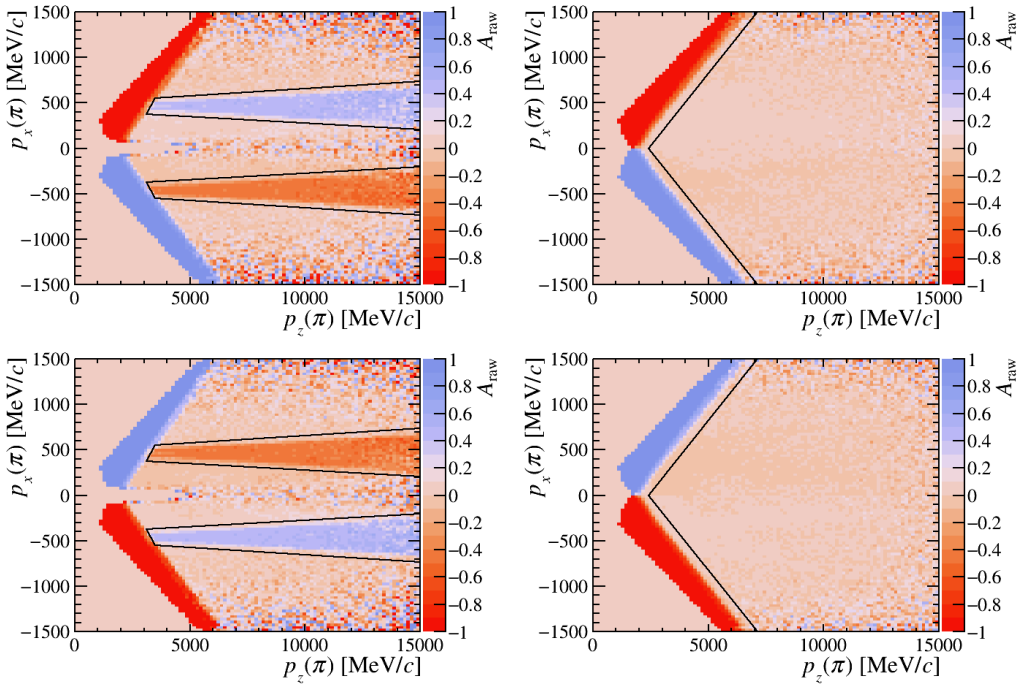

Figure 4.1: Raw asymmetries in bins of (p_z, p_x) of the soft pion for the prompt case, for the (top) *MagUp* and (bottom) *MagDown* samples. The plots on the left include only candidates with $|p_y/p_z| < 0.02$, and the fiducial requirements used to exclude the kinematic region surrounding the beam pipe, characterized by large values of the raw asymmetry, are indicated as black lines (in addition to the forementioned requirement $|p_y/p_z| < 0.02$). The plots on the right include all candidates but those excluded by the beam-pipe fiducial requirements, and the black lines indicate the fiducial requirements used to exclude regions at the boundary of the detector acceptance. Only the distributions for $D^0 \to K^+K^-$ decays are shown, as an example, since those for $D^0 \to \pi^+\pi^-$ decays are very similar.

reduce the background due to misidentified particles. A J/ψ- and $\psi(2S)$-veto is applied to suppress events where one muon originating from a $J/\psi \to \mu^+\mu^-$ decay is misidentified as a kaon or pion (the $B^0 \to J/\psi\, K\pi$ decay is an example of this kind of background): the invariant mass of the pair formed by the muon and the D^0 decay product with opposite charge is calculated and, if the considered D^0 decay product satisfies the *IsMuon* criterion (defined in Sec. 2.4.3) and the calculated invariant mass is in a $\pm 45\,\text{MeV}/c^2$ window around the J/ψ nominal mass or $\pm 55\,\text{MeV}/c^2$ around the $\psi(2S)$ nominal mass, the B candidate is discarded.

Similarly to what done in the prompt case for the soft-pion kinematics, a set of fiducial requirements is applied to the muon p_x and p_z in order to remove regions

Table 4.4: Offline selection applied to the events surviving the trigger selection for the semileptonic modes.

Variable	Selection requirement
DTF χ^2/ndf(B)	$[0, 9.5]$
DTF χ^2/ndf(D^0)	$[0, 6.5]$
$m(B)$	$\in [2.5, 5]\,\mathrm{GeV}/c^2$
$m_{\mathrm{corr}}(B)$	$< 6\,\mathrm{GeV}/c^2$
$\mathrm{vtx}_z(D^0) - \mathrm{vtx}_z(B)$	$> 0\,\mathrm{mm}$
$\mathrm{DLL}_{K\pi}(\pi)$	< -2
$\mathrm{DLL}_{K\pi}(K)$	> 5
J/ψ veto	see text in Sec. 4.2.2
Fiducial requirements	see Eq. (4.11)

where a large muon detection asymmetry is present

$$\begin{aligned} &|p_x| < 0.315 \cdot p_z - 1032.5\,\mathrm{MeV}/c, \\ &|p_x| > 1000\,\mathrm{MeV}/c \quad \mathrm{OR} \quad |p_x| < 700\,\mathrm{MeV}/c. \end{aligned} \tag{4.11}$$

Figure 4.2 illustrates the regions removed by the fiducial requirements. The fraction of removed events is 12% for the $D^0 \to \pi^+\pi^-$ mode and 10% for the $D^0 \to K^+K^-$ mode.

After the "cut"-based selection, a non negligible fraction of background events is still present. An MVA based on a BDT is therefore implemented to improve the precision of the measured A_{raw}. Two different trainings, one for the $D^0 \to K^+K^-$ mode and one for the $D^0 \to \pi^+\pi^-$ mode, are performed. For both channels the $D^0 \to K^-\pi^+$ sample is used as signal proxy in the training, while the sidebands of the $m(D^0)$ distribution of the two decay modes are considered as background. The $D^0 \to K^-\pi^+$ sample is chosen because it includes a negligible amount of background, as shown in Fig. 4.3, and it has kinematic properties very similar to the signal. The training is performed using events lying in the $[1844, 1884]\,\mathrm{MeV}/c^2$ window of $m(D^0)$. For the background, the sideband for the $D^0 \to \pi^+\pi^-$ mode is defined by the $[1900, 1950]\,\mathrm{MeV}/c^2$ window, while for the $D^0 \to K^+K^-$ the window is $[1900, 1920]\,\mathrm{MeV}/c^2$. In this mass region, most of the candidates are purely combinatorial. For both signal and background samples, half of the events are used for training and the other for the evaluation of the MVA efficiency and performance.

The variables used for the training are: the two DTF χ^2/ndf, one for the B and one for the D^0; the D^0 flight distance with respect to the PV in terms of

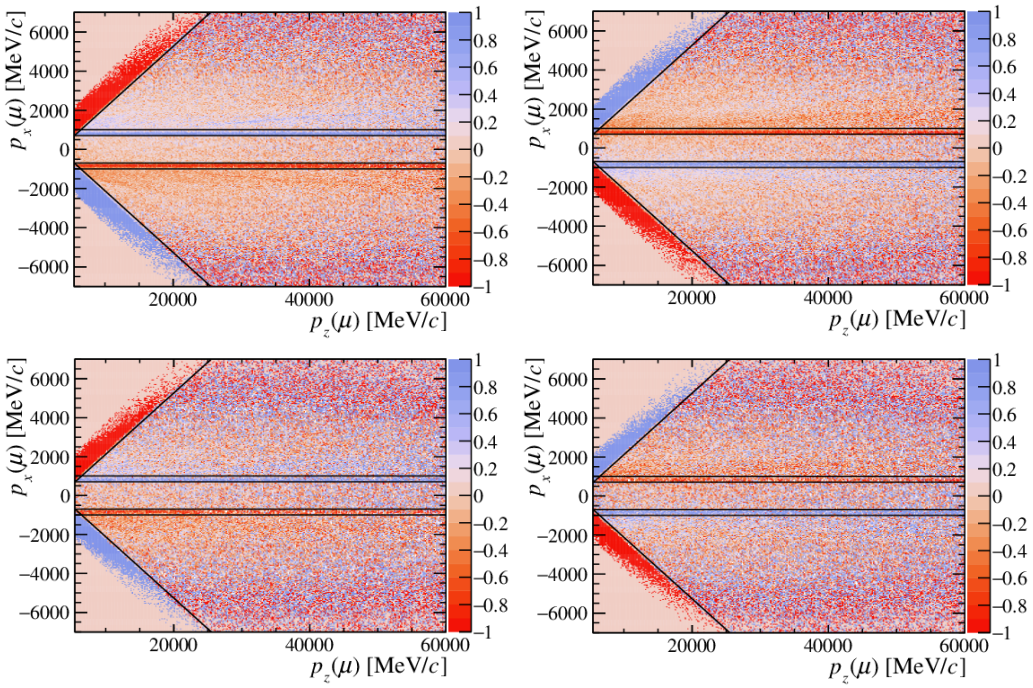

Figure 4.2: Raw asymmetry distributions as a function of p_x and p_z of the muon for (top) $D^0 \to K^+K^-$ and (bottom) $D^0 \to \pi^+\pi^-$ decays, and for 2016 (left) *MagUp* and (right) *MagDown* data samples. The black lines show the boundaries of the large raw asymmetry regions which are excluded by the fiducial requirements.

χ^2 ($\log[\chi^2_{\rm FD}(D^0)]$); the $\chi^2_{\rm IP}$ of the D^0 decay products ($\log[\chi^2_{\rm IP}(h^\pm)]$); the transverse momentum of the D^0 decay products ($p_{\rm T}(h^\pm)$); the distance between the D^0 and the B decay vertices along z divided by its uncertainty ($\Delta z(D^0, B)/\sigma_{\Delta z(D^0,B)}$ as defined in Sec. 3.2.3); the invariant mass and the corrected mass of the B ($m(B)$ and $m_{\rm corr}(B)$); and the SPD hit multiplicity. The distributions of the BDT input variables in the samples used for training are shown in Figs. 4.4 and 4.5.

The BDT algorithm assigns to each candidate a numerical factor ($\mu_{\rm BDT}$) ranging between -1 and $+1$ depending on whether the candidate is considered more likely to be background or signal, respectively. The optimal separation between signal and background events is then achieved by choosing an appropriate threshold for $\mu_{\rm BDT}$. The threshold is chosen to maximise a predefined score function, namely $S/\sqrt{S+B}$, where S is the number of signal candidates and B the number of background candidates lying within the $[1818, 1918]\,{\rm MeV}/c^2$ window of $m(D^0)$. The resulting thresholds are 0.0 and -0.1 for the $D^0 \to \pi^+\pi^-$ and $D^0 \to K^+K^-$ decays, respectively. The BDT requirement has 90% (75%) signal efficiency and rejects

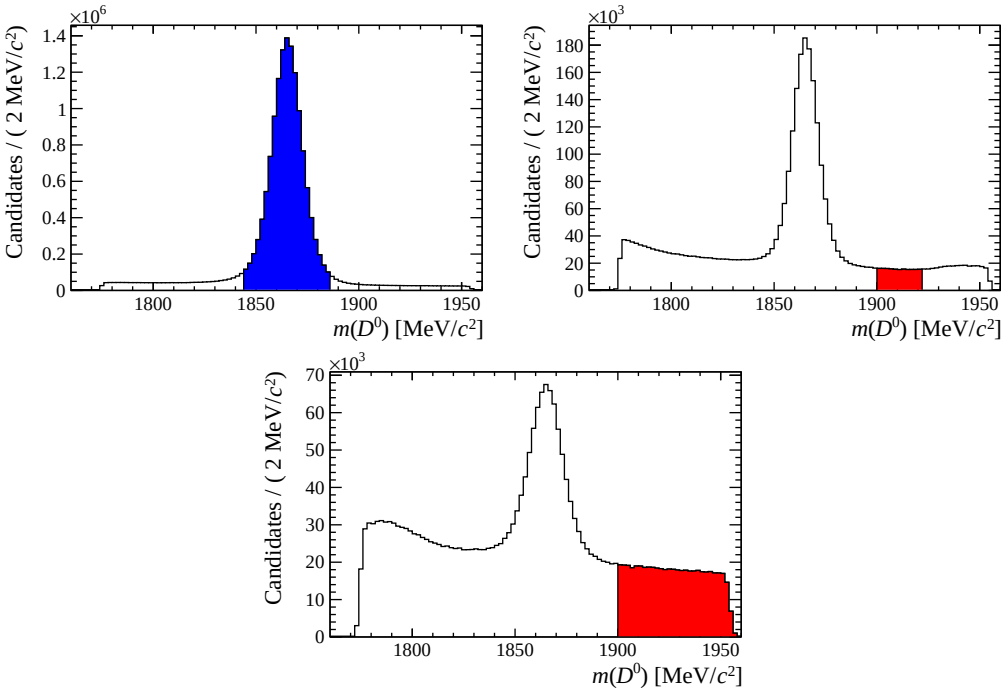

Figure 4.3: The $m(D^0)$ distribution for the (left) $D^0 \to K^-\pi^+$, (centre) $D^0 \to K^+K^-$ and (right) $D^0 \to \pi^+\pi^-$ samples. The 2016 *MagDown* data sample is reported as an example. The signal region is highlighted in blue and the background regions in red. The amount of background candidates in the $D^0 \to K^-\pi^+$ signal region is very small and for this reason the candidates around the peak are used as a signal proxy while training the MVA.

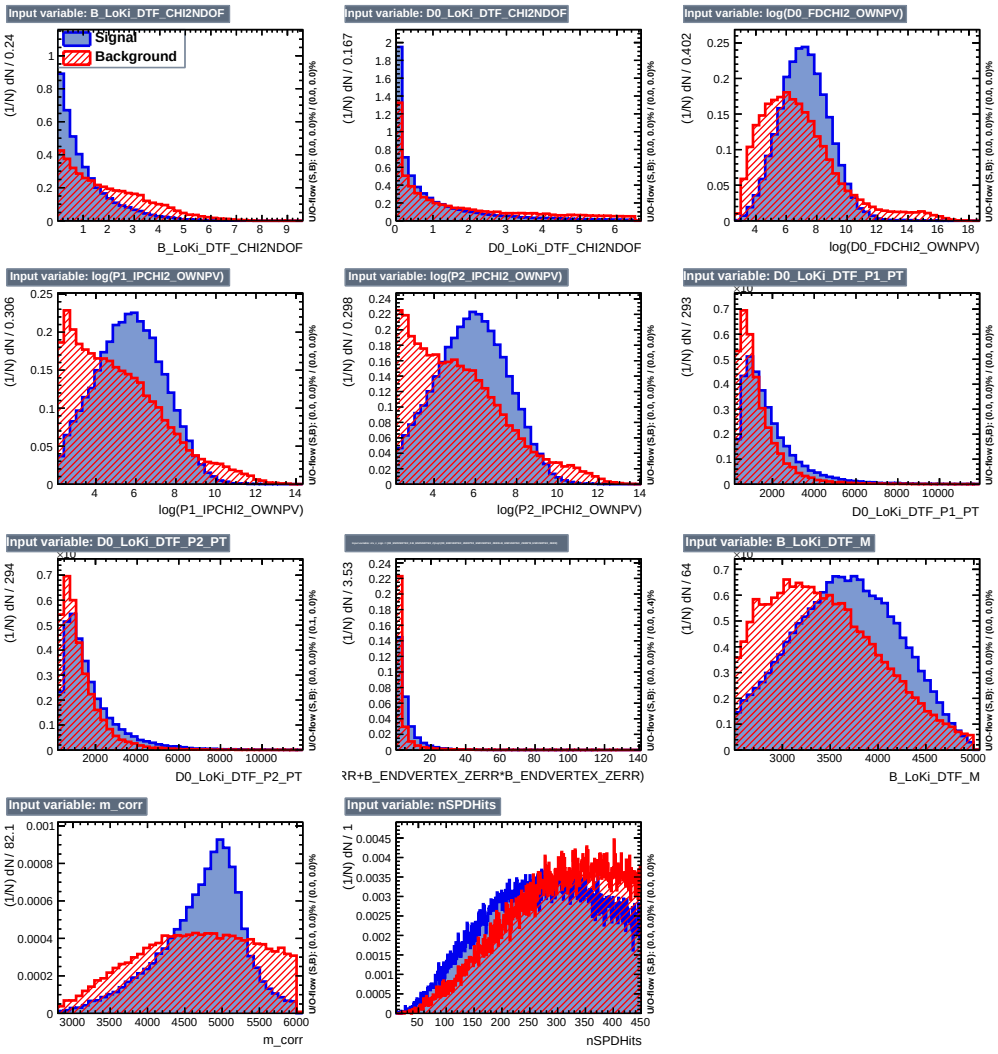

Figure 4.4: Distributions of the variables used in the BDT training for the $D^0 \to \pi^+\pi^-$ decay: (blue) signal and (red) background. The 2016 data sample is used as an example.

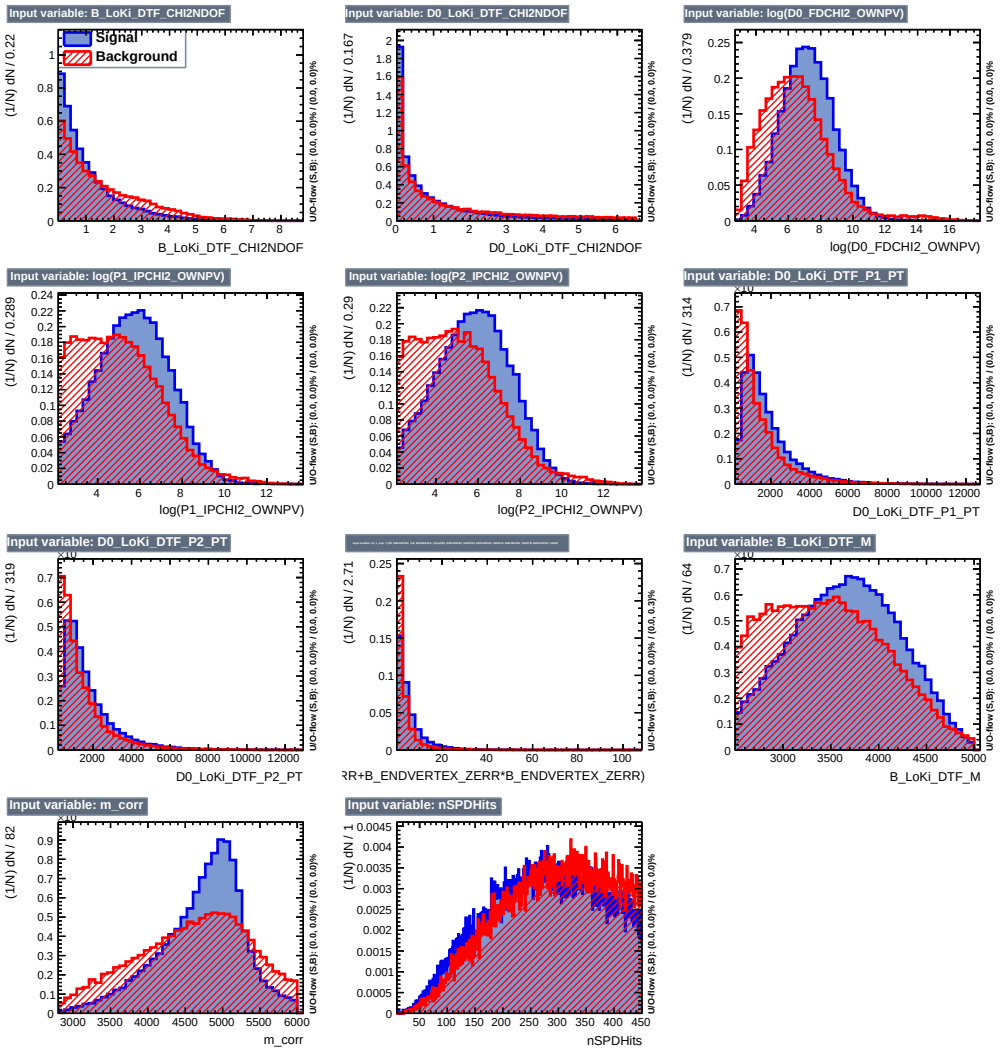

Figure 4.5: Distributions of the variables used in the BDT training for the $D^0 \to K^+K^-$ decay: (blue) signal and (red) background. The 2016 data sample is used as an example.

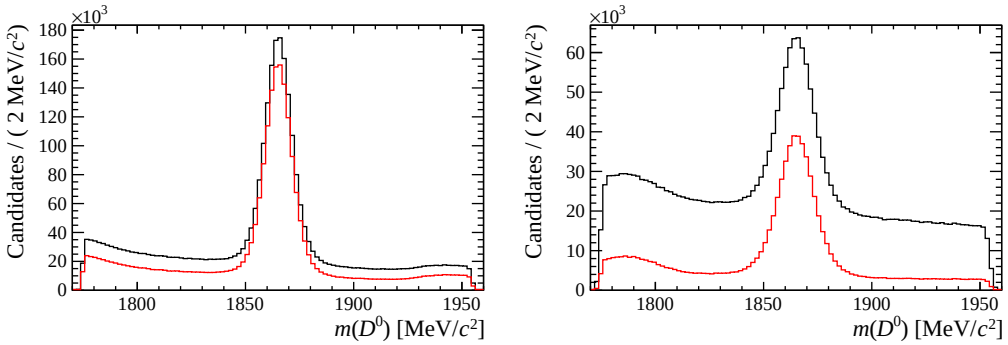

Figure 4.6: The $m(D^0)$ distribution (black) before and (red) after the BDT requirement, for (left) $D^0 \to K^+K^-$ and (right) $D^0 \to \pi^+\pi^-$. The 2016 *MagDown* data sample is used as an example.

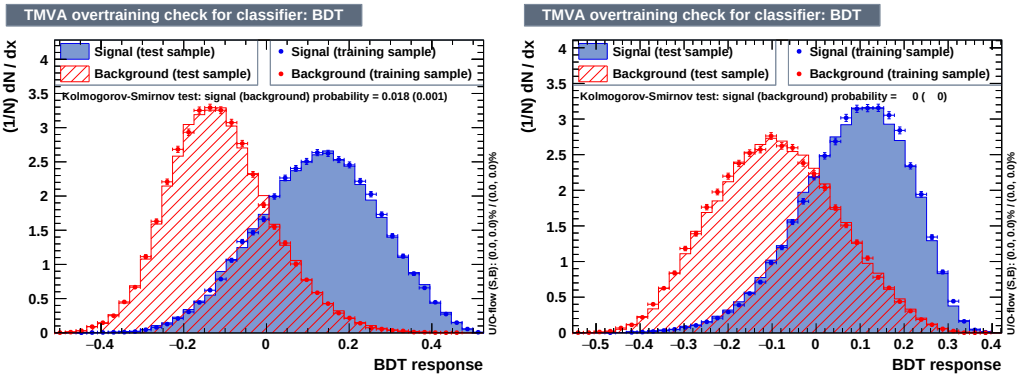

Figure 4.7: Distributions of the BDT response for (left) $D^0 \to \pi^+\pi^-$ and (right) $D^0 \to K^+K^-$: (blue) signal and (red) background training samples. The 2016 data sample is used as an example.

55% (85%) of background candidates for the $D^0 \to K^+K^-$ ($D^0 \to \pi^+\pi^-$) decay. Figure 4.6 shows the $m(D^0)$ distribution before and after the BDT requirement. The distributions of the BDT response for signal and background candidates are shown in Fig. 4.7.

Finally, if an event contains more than one B candidate after the full selection, only one candidate is kept by a random choice. The fraction of candidates removed in this way amounts to 0.4%.

4.2.3 Simulated samples

Two simulated samples are used for the two prompt decay modes $D^0 \to K^+K^-$ and $D^0 \to \pi^+\pi^-$. They are generated by simulating the 2016 data-taking conditions, and

the amount of fully reconstructed true decays is equal to $5.21 \cdot 10^5$ and $4.75 \cdot 10^5$ for the $D^0 \to K^+K^-$ and $D^0 \to \pi^+\pi^-$ modes, respectively. These samples are used to fix the parameters of an alternative fit model for the signal, as described in Sec. 4.4.2.

Four samples of simulated $D^0 \to K^-\pi^+\pi^0$, $D^0 \to \pi^- e^+ \nu_e$, $D^0 \to \pi^-\mu^+\nu_\mu$ and $D_s^+ \to K^-K^+\pi^+$ decays are generated with the RapidSim application [107], which enables the kinematic properties of the generated decays to be reproduced by means of a fast simulation, taking into account the resolution and the acceptance of the detector. The samples generated with RapidSim are used to evaluate the systematic uncertainty associated to the peaking background, as reported in Sec. 4.4.1.

4.2.4 Kinematic weighting

Production and detection asymmetries depend on the kinematic distributions of the particle in question, thus the two decay channels $D^0 \to K^+K^-$ and $D^0 \to \pi^+\pi^-$ must have the same kinematic distributions in order for such asymmetries to cancel in the difference. In the following, the procedure to create samples with the same kinematic distributions is explained. The procedure used to evaluate systematic uncertainties due to the weighting process is explained in Sec. 4.4.

Prompt mode

A kinematic weighting procedure is applied to $D^0 \to K^+K^-$ decay candidates in order to match the kinematic distributions of the $D^0 \to \pi^+\pi^-$ sample, separately for both the magnet polarities and the years of data taking. To determine the weights, normalised three-dimensional distributions of momentum p, transverse momentum p_{T}, and azimuthal angle φ of the D^* candidates are used. The distributions are taken from background-subtracted $D^0 \to K^+K^-$ and $D^0 \to \pi^+\pi^-$ events, where the signal weights have been obtained using the *sPlot* technique [106] with the fit model described in Sec. 4.3.1. The binning scheme used for the distribution is a uniform $40 \times 40 \times 40$.

The distributions of pseudorapidity and azimuthal angle of the D^*, before and after weighting, are shown in Fig. 4.8. Other kinematic distributions of the D^* and the soft pion are reported in App. A.1. The distributions of both the D^* and the soft pion match very well once the weights are applied.

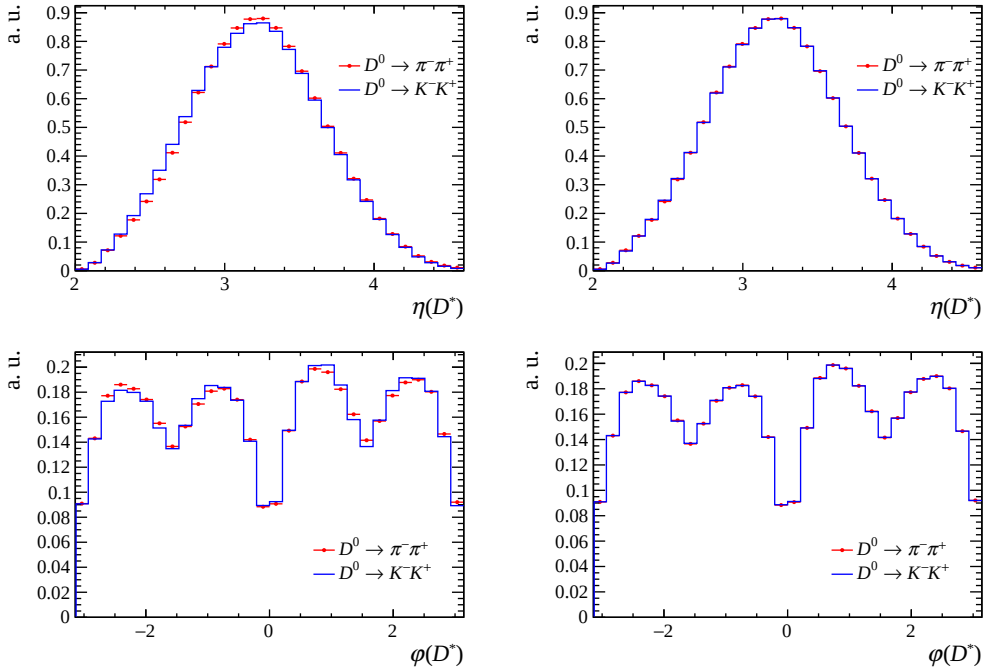

Figure 4.8: Distributions of η and φ of the D^* meson for $D^0 \to K^+K^-$ and $D^0 \to \pi^+\pi^-$ candidates, (left) before and (right) after weighting, for the prompt mode.

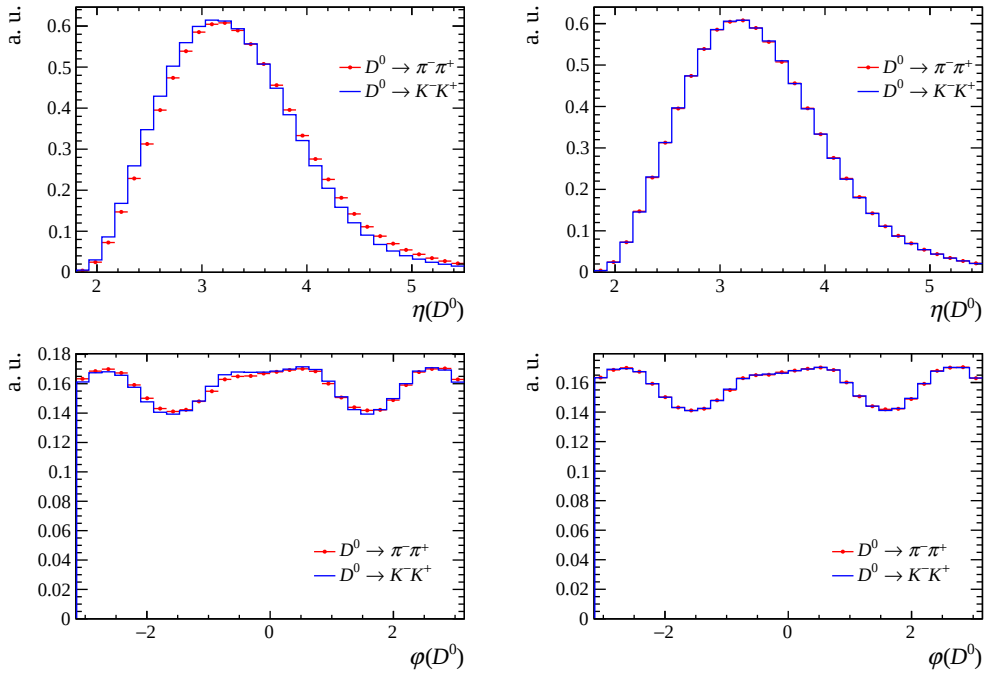

Figure 4.9: Comparison of η and φ of the D^0 meson between $D^0 \to K^+K^-$ and $D^0 \to \pi^+\pi^-$ candidates (left) before and (right) after weighting, for the semileptonic mode.

Semileptonic mode

Similarly to the prompt case, the weighting procedure is applied also to the semileptonic mode on the p, p_{T} and φ distributions of the D^0 meson. The distributions of the D^0 meson pseudorapidity and azimuthal angle, before and after weighting, are shown in Fig. 4.9. Other kinematic distributions of the the μ and the $D^0\mu$ system are reported in App. A.2. An overall good agreement is observed after the weighting.

4.3 Determination of raw asymmetries

The measurement of the raw asymmetries for the prompt and semileptonic modes is described in the following.

4.3.1 Prompt case

The raw asymmetries are measured by means of binned χ^2 fits to $m(D^0\pi)$ invariant-mass spectra, with $m(D^0\pi)$ defined as

$$m(D^0\pi) \equiv \left(m_{D^0}^2 + m_\pi^2 + 2\sqrt{m_{D^0}^2 + |\vec{p}_{D^0}|^2} \cdot \sqrt{m_\pi^2 + |\vec{p}_\pi|^2} - 2\vec{p}_{D^0} \cdot \vec{p}_\pi \right)^{\frac{1}{2}}, \quad (4.12)$$

This equation does not rely on any mass hypotheses on the D^0 decay products. The calculation is made using the nominal D^0 mass m_{D^0} [26] and the reconstructed momenta of the D^0 meson and soft pion. The sample is split according to the charge of the soft pion, that defines the charge of the D^* meson. The signal component is parameterised with the following probability density function (PDF) for D^{*+} $(+)$ and D^{*-} $(-)$ decays

$$\begin{aligned}\mathcal{P}_\pm^{\text{sig}}(m) = \Theta(m - m_{\text{trsh}}) \cdot \big[& f_J \mathcal{J}(m; \mu_J, \sigma_J, \delta_J, \sigma_J) + f_1 G(m; \mu_1^\pm, \sigma_1) \\ & + f_2 G(m; \mu_2^\pm, \sigma_2) + (1 - f_J - f_1 - f_2) G(m; \mu_3^\pm, \sigma_3) \big],\end{aligned} \quad (4.13)$$

where Θ stands for the Heaviside function, $G(m; \mu, \sigma)$ is a Gaussian function with mean μ and standard deviation σ and $\mathcal{J}$ is a Johnson function [108] defined as

$$\mathcal{J}(m; \mu_J, \sigma_J, \delta_J, \gamma_J) = \frac{e^{-\frac{1}{2}\left[\gamma_J + \delta_J \sinh^{-1}\left(\frac{m-\mu_J}{\sigma_J}\right)\right]^2}}{\sqrt{1 + \left(\frac{m-\mu_J}{\sigma_J}\right)^2}}. \quad (4.14)$$

The value $m_{\text{trsh}} = 2004.4\,\text{MeV}/c^2$ corresponds to the minimum value allowed for $m(D^0\pi)$ and it is fixed in the fit. All other parameters entering Eq. (4.13) are left free to be adjusted by the fit.

The background PDF shares the same parameters between D^{*+} and D^{*-} decays, and it is given by

$$\mathcal{P}^{\text{bkg}}(m) = \Theta(m - m_{\text{trsh}}) \cdot (m - m_{D^0} - m_\pi)^a e^{-b(m - m_{D^0} - m_\pi)}, \quad (4.15)$$

where a and b are free parameters in the fit.

The total extended PDF is defined as follows

$$\mathcal{P}(q,m) = \frac{1}{2\left(N_{\rm sig}^{\rm tot} + N_{\rm bkg}^{\rm tot}\right)} \left[\left(1 + qA_{\rm raw}\right) N_{\rm sig}^{\rm tot} \cdot \mathcal{P}_q^{\rm sig}(m) + \left(1 + qA_{\rm bkg}\right) N_{\rm bkg}^{\rm tot} \cdot \mathcal{P}^{\rm bkg}(m) \right], \tag{4.16}$$

which is a function of $m(D^0\pi)$ and of the discrete tag $q = \pm 1$, that identifies the $D^{*\pm}$ final state. Namely, $q = +1$ corresponds to D^{*+} and $q = -1$ to D^{*-}. The parameters $A_{\rm raw}$ and $A_{\rm bkg}$ are the raw asymmetries of signal and background components, defined as

$$A_{\rm raw} = \frac{N_{\rm sig}(D^{*+}) - N_{\rm sig}(D^{*-})}{N_{\rm sig}^{\rm tot}}, \tag{4.17a}$$

$$A_{\rm bkg} = \frac{N_{\rm bkg}(D^{*+}) - N_{\rm bkg}(D^{*-})}{N_{\rm bkg}^{\rm tot}}, \tag{4.17b}$$

where $N_{\rm sig}^{\rm tot}$ and $N_{\rm bkg}^{\rm tot}$ are the total yields of signal and background candidates.

The fit is performed separately for each decay mode, data-taking year and magnet polarity, but simultaneously to the D^{*+} and D^{*-} candidates. In Figs. 4.10–4.11 the D^* invariant-mass distributions with the results of the fits overlaid are shown for the 2018 sample, as an example. The results of the fits to the 2015, 2016 and 2017 samples are reported in App. B.1. The raw asymmetries obtained from the fits are reported in Table 4.5. Table 4.6 reports the signal yields obtained for each year and magnet polarity.

The average values of $\Delta A_{CP}^{\rm prompt}$ between the two polarities are $(-0.130 \pm 0.142)\%$, $(-0.207 \pm 0.061)\%$, $(-0.184 \pm 0.057)\%$ and $(-0.166 \pm 0.056)\%$, where the uncertainties are statistical only, for the 2015, 2016, 2017 and 2018 data samples, respectively.

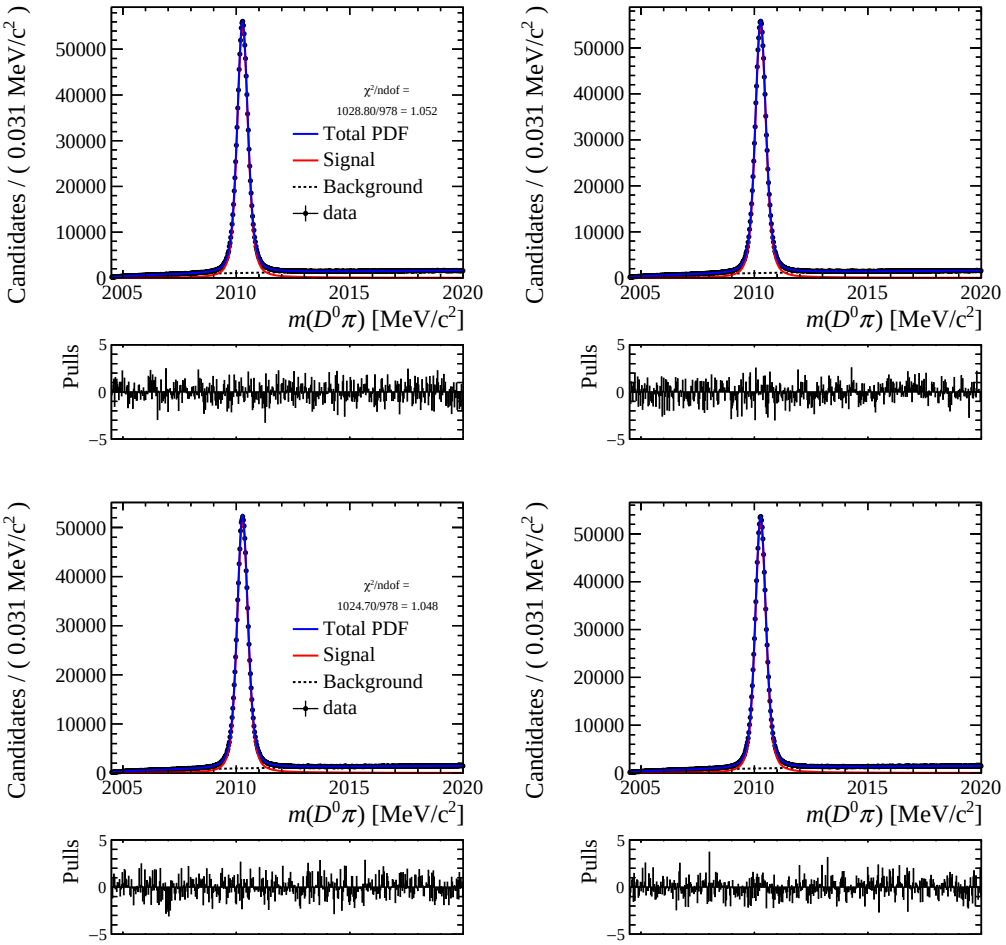

Figure 4.10: Invariant-mass distributions of 2018 prompt $D^0 \to \pi^+\pi^-$ events for (top left) positively tagged *MagDown* events, (top right) negatively tagged *MagDown* events, (bottom left) positively tagged *MagUp* events and (bottom right) negatively tagged *MagUp* sample. The result of the fit is overlaid.

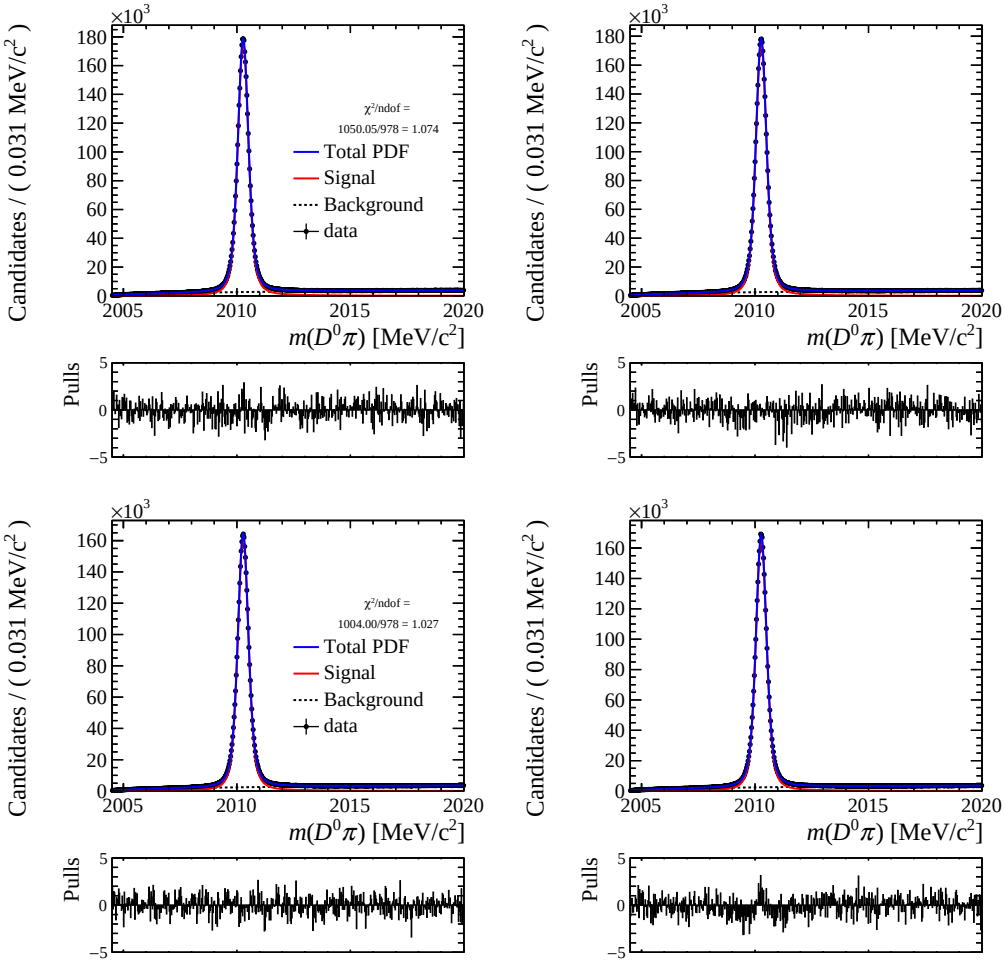

Figure 4.11: Invariant-mass distributions of 2018 prompt $D^0 \to K^+K^-$ events for (top left) positively tagged *MagDown* events, (top right) negatively tagged *MagDown* events, (bottom left) positively tagged *MagUp* events and (bottom right) negatively tagged *MagUp* sample. The result of the fit is overlaid.

Table 4.5: Measured values of A_{raw} and ΔA_{CP} in the prompt case.

Sample	$A_{\text{raw}}^{\text{prompt}}(K^+K^-)$ [%] (no weights)	$A_{\text{raw}}^{\text{prompt}}(K^+K^-)$ [%]	$A_{\text{raw}}^{\text{prompt}}(\pi^+\pi^-)$ [%]
2015 Down	0.060 ± 0.086	0.054 ± 0.093	0.411 ± 0.157
2015 Up	-1.195 ± 0.108	-1.132 ± 0.117	-1.347 ± 0.192
2016 Down	0.002 ± 0.041	0.004 ± 0.042	0.206 ± 0.073
2016 Up	-1.345 ± 0.043	-1.362 ± 0.044	-1.149 ± 0.075
2017 Down	-0.090 ± 0.038	-0.064 ± 0.039	0.086 ± 0.069
2017 Up	-1.328 ± 0.039	-1.332 ± 0.040	-1.113 ± 0.070
2018 Down	-0.006 ± 0.037	-0.001 ± 0.038	0.116 ± 0.068
2018 Up	-1.324 ± 0.039	-1.335 ± 0.040	-1.118 ± 0.070

Sample	$\Delta A_{CP}^{\text{prompt}}$ [%] (no weights)	$\Delta A_{CP}^{\text{prompt}}$ [%]
2015 Down	-0.351 ± 0.179	-0.357 ± 0.182
2015 Up	0.152 ± 0.220	0.215 ± 0.225
average	-0.151 ± 0.139	-0.130 ± 0.142
2016 Down	-0.204 ± 0.084	-0.202 ± 0.084
2016 Up	-0.196 ± 0.087	-0.212 ± 0.087
average	-0.200 ± 0.060	-0.207 ± 0.061
2017 Down	-0.176 ± 0.079	-0.150 ± 0.080
2017 Up	-0.214 ± 0.080	-0.219 ± 0.081
average	-0.195 ± 0.056	-0.184 ± 0.057
2018 Down	-0.122 ± 0.078	-0.117 ± 0.079
2018 Up	-0.205 ± 0.080	-0.217 ± 0.080
average	-0.163 ± 0.056	-0.166 ± 0.056

Table 4.6: Measured signal yields in the prompt case.

Sample	$N_{\text{sig}}^{\text{tot}}(KK)$ [$\times 10^3$]	$N_{\text{sig}}^{\text{tot}}(\pi\pi)$ [$\times 10^3$]
2015 Down	1468 ± 10	484 ± 3
2015 Up	934 ± 9	319 ± 6
2016 Down	6524 ± 19	2156 ± 10
2016 Up	5955 ± 20	2033 ± 11
2017 Down	7356 ± 16	2342 ± 14
2017 Up	7041 ± 15	2308 ± 12
2018 Down	7754 ± 19	2419 ± 11
2018 Up	7376 ± 16	2322 ± 12

4.3.2 Semileptonic case

The value of the raw asymmetry is measured by performing a binned χ^2 fit to the D^0 invariant mass distribution. The sample is split in positively ($\overline{D}^0$ associated with μ^+) and negatively (D^0 associated with μ^-) tagged events. The signal PDF is parameterised by a convolution of the sum of two Gaussian functions with a function parameterising the final-state QED radiation, namely

$$\mathcal{P}^{\rm sig}_{\pm}(m) = \int_0^{+\infty} (m')^s \left(f_1 \cdot G(m+m';\mu^{\pm},\sigma_1) + (1-f_1)\cdot G(m+m';\mu^{\pm},\sigma_2)\right) {\rm d}m'. \tag{4.18}$$

In this mode the D^0 invariant mass spectrum presents also a residual component of misidentified $D^0 \to K^-\pi^+$ background which, if not included in the fit, can bias the final result. This component is modelled with a Gaussian function ($\mathcal{P}^{\rm mis}(m)$) with mean value outside the fit invariant mass region, such that only one Gaussian tail (the right one for the $D^0 \to \pi^+\pi^-$ decays and the left one for the $D^0 \to K^+K^-$ decays) is used to describe this component. The combinatorial background is described with an exponential distribution ($\mathcal{P}^{\rm bkg}(m)$). The total extended PDF is defined similarly to the prompt mode as

$$\begin{aligned}\mathcal{P}(q,m) = \frac{1}{2\left(N^{\rm tot}_{\rm sig} + N^{\rm tot}_{\rm bkg} + N^{\rm tot}_{\rm mis}\right)} \big[&(1+qA_{\rm raw})\, N^{\rm tot}_{\rm sig}\cdot \mathcal{P}^{\rm sig}_q(m) \\ &+ (1+qA_{\rm bkg})\, N^{\rm tot}_{\rm bkg}\cdot \mathcal{P}^{\rm bkg}(m) \\ &+ (1+qA_{\rm mis})\, N^{\rm tot}_{\rm mis}\cdot \mathcal{P}^{\rm mis}(m)\big]\,,\end{aligned} \tag{4.19}$$

which is a function of $m(D^0)$ and of the discrete tag $q = \pm 1$, that identifies the negatively and positively tagged candidates.

The fit is performed separately for each decay mode, data-taking year and magnet polarity, but simultaneously to the negatively and positively tagged candidates. In Figs. 4.12 and 4.13 the $m(D^0)$ invariant-mass distributions are shown for the 2018 data sample with the results of the fits overlaid, as an example. The results of the fits to the 2016 and 2017 samples are reported in App. B.2. The results are summarised in Table 4.7, and the related signal yields are reported in Table 4.8. The average values of $\Delta A^{\rm SL}_{CP}$ are equal to $(-0.173 \pm 0.141)\%$, $(0.046 \pm 0.133)\%$ and $(-0.143 \pm 0.129)\%$, where the uncertainties are statistical only, for the 2016, 2017 and 2018 data samples, respectively.

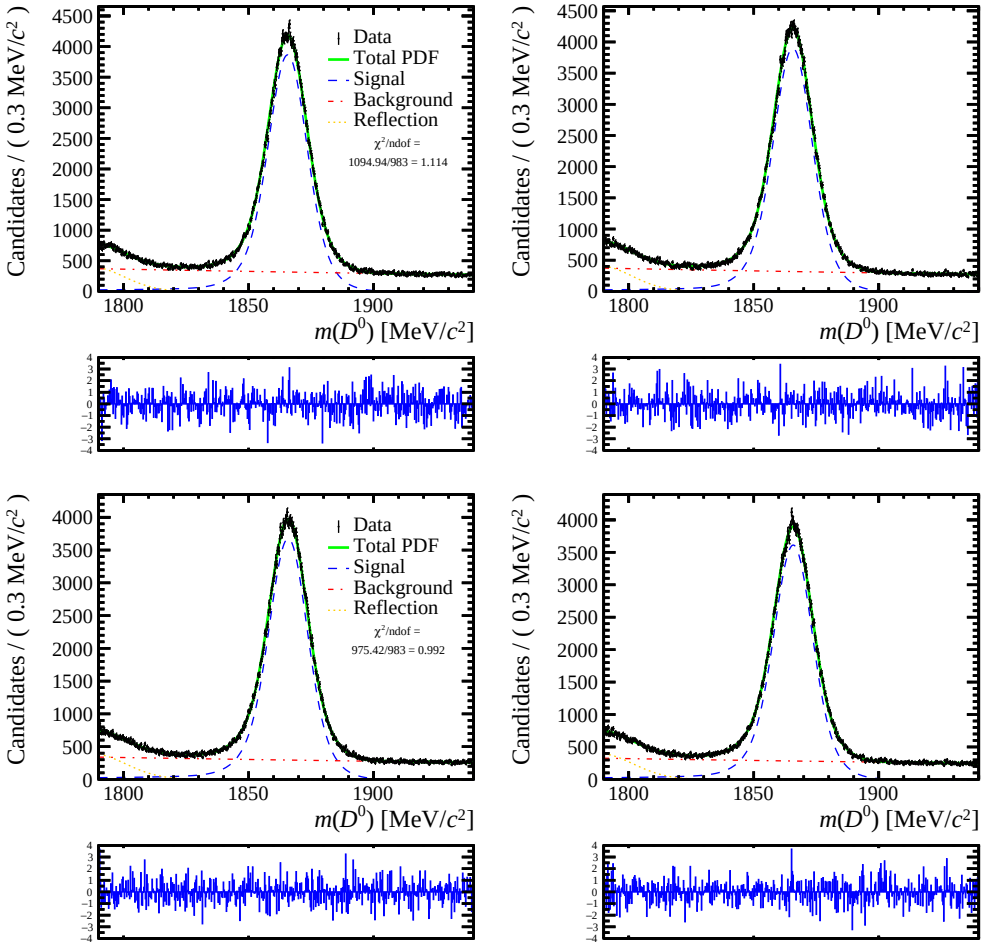

Figure 4.12: Invariant-mass distributions for $D^0 \to \pi^+\pi^-$ candidates in the semileptonic sample for (top left) positively tagged 2018 *MagDown* events, (top right) negatively tagged 2018 *MagDown* sample, (bottom left) positively tagged 2018 *MagUp* events and (bottom right) negatively tagged 2018 *MagUp* sample. The result of the fit is overlaid.

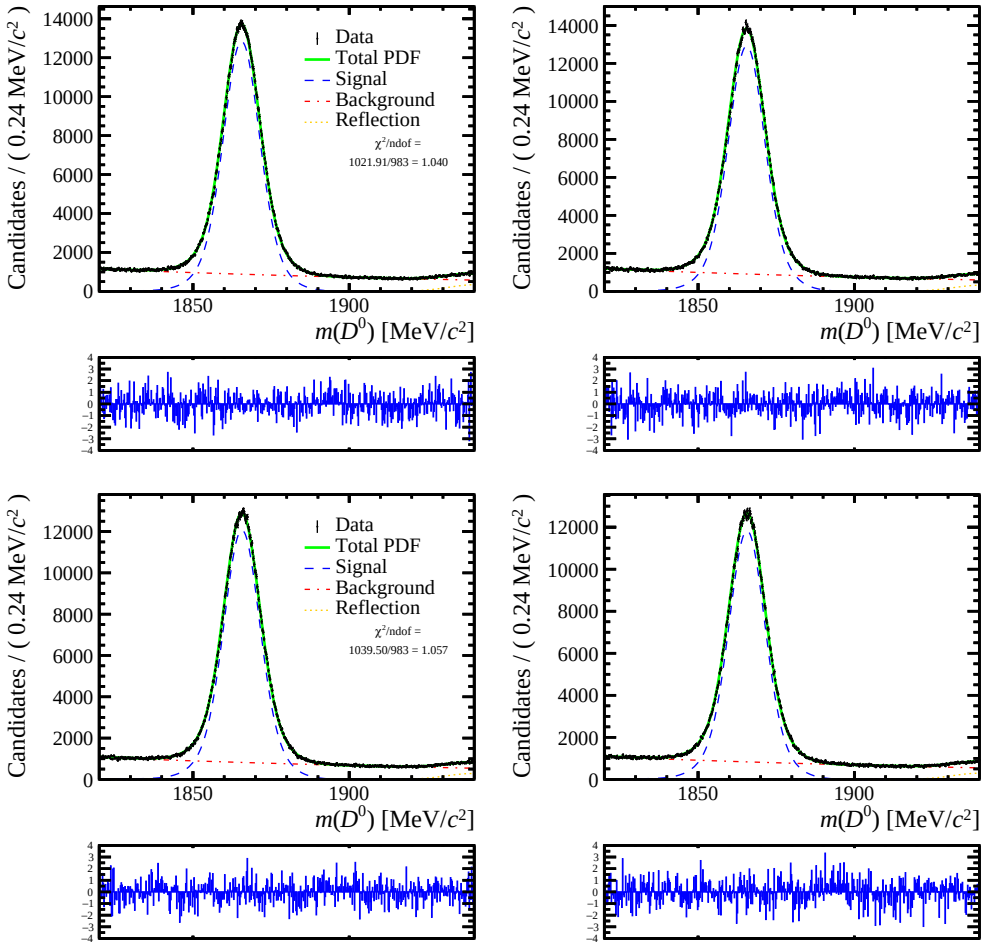

Figure 4.13: Invariant-mass distributions for $D^0 \to K^+K^-$ candidates in the semileptonic sample for (top left) positively tagged 2018 *MagDown* events, (top right) negatively tagged 2018 *MagDown* sample, (bottom left) positively tagged 2018 *MagUp* events and (bottom right) negatively tagged 2018 *MagUp* sample. The result of the fit is overlaid.

Table 4.7: Measured values of A_{raw} and ΔA_{CP} in the semileptonic case.

Sample	$A^{\text{SL}}_{\text{raw}}(K^+K^-)$ [%] (no weights)	$A^{\text{SL}}_{\text{raw}}(K^+K^-)$ [%]	$A^{\text{SL}}_{\text{raw}}(\pi^+\pi^-)$ [%]
2016 Down	0.018 ± 0.101	0.051 ± 0.108	0.031 ± 0.184
2016 Up	-0.522 ± 0.089	-0.574 ± 0.096	-0.250 ± 0.162
2017 Down	0.070 ± 0.088	0.134 ± 0.095	0.027 ± 0.161
2017 Up	-0.590 ± 0.090	-0.590 ± 0.097	-0.572 ± 0.164
2018 Down	0.350 ± 0.085	0.309 ± 0.091	0.460 ± 0.155
2018 Up	-1.001 ± 0.088	-1.014 ± 0.094	-0.880 ± 0.160

Sample	$\Delta A^{\text{SL}}_{CP}$ [%] (no weights)	$\Delta A^{\text{SL}}_{CP}$ [%]
2016 Down	-0.013 ± 0.209	0.019 ± 0.213
2016 Up	-0.272 ± 0.185	-0.324 ± 0.189
average	-0.158 ± 0.139	-0.173 ± 0.141
2017 Down	0.043 ± 0.184	0.107 ± 0.187
2017 Up	-0.018 ± 0.187	-0.018 ± 0.190
average	0.133 ± 0.131	0.046 ± 0.133
2018 Down	-0.110 ± 0.178	-0.151 ± 0.179
2018 Up	-0.121 ± 0.182	-0.134 ± 0.185
average	-0.155 ± 0.127	-0.143 ± 0.129

Table 4.8: Measured signal yields in the semileptonic case.

Sample	$N^{\text{tot}}_{\text{sig}}(KK)$ [$\times 10^2$]	$N^{\text{tot}}_{\text{sig}}(\pi\pi)$ [$\times 10^2$]
2016 Down	11494 ± 20	4040 ± 20
2016 Up	14835 ± 23	5318 ± 30
2017 Down	15557 ± 23	5232 ± 25
2017 Up	14903 ± 23	5061 ± 22
2018 Down	16854 ± 24	5586 ± 26
2018 Up	15661 ± 23	5253 ± 24

4.3.3 Validation of the fit model

In order to check that there are no biases due to the fit procedure, 5000 pseudo-experiments are generated, using the PDF of the total fit model, with parameters fixed to the central values resulting from the fit, for each subsample. The same fit model is then fitted to the data of the 5000 pseudoexperiments. The distributions of the canonical pulls obtained from the fits, reported in Fig. 4.14, show no biases.

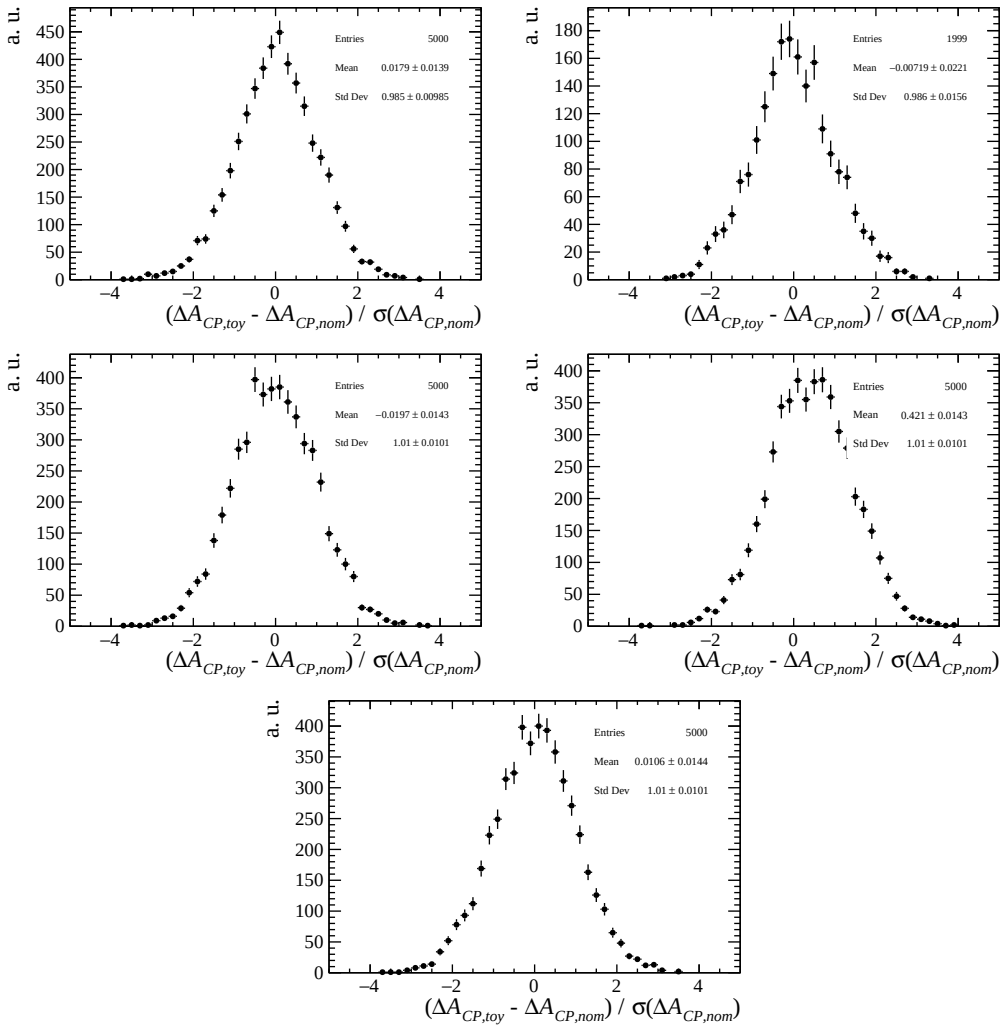

Figure 4.14: Distribution of canonical pulls obtained from fit to pseudoexperiments, for (top left) prompt 2015 sample, (top right) prompt 2016 sample, (middle left), prompt 2017 and 2018 sample, (middle right) semileptonic 2016 sample and (bottom) semileptonic 2017 and 2018 sample.

4.4 Study of systematic uncertainties

Two sources of systematic uncertainties affecting the determination of ΔA_{CP} are considered for both prompt and semileptonic measurements: the signal and background modelling and the weighting procedure. For the prompt channel two further sources are studied: the contamination from secondary D^0 decays and the presence of peaking background. Finally, an evaluation of the systematic uncertainties associated to the mistag rate and the cancellation of the D^0 effective production asymmetry is performed in the semileptonic case.

4.4.1 Prompt case

Fit model

The systematic uncertainty associated to the choice of the fit model for signal and background is evaluated by generating 1000 pseudoexperiments according to the central values resulting from the fit to data, and then fitting the baseline and alternative fit models to them. This procedure is applied for each subsample, and the weighted average of ΔA_{CP} is considered to evaluate the difference between the baseline and the alternative fit models for each pseudoexperiment.

The alternative models which are used are described in the following.

- Three Gaussian functions plus a bifurcated (*i.e.* with two different widths on the left and the right sides of the mean) Gaussian function for the signal.
- The function described by Eq. (4.18), but with triple Gaussian functions instead of two, for the signal.
- First-order polynomial times a phase-space function for the background, *i.e.*

$$\mathcal{P}_{\text{bkg}}(m) = \frac{1}{m^2} \cdot (1 + p_1 \cdot m) \cdot \sqrt{[m^2 - (m_{D^0} + m_{\pi_s})^2]\,[m^2 - (m_{D^0} - m_{\pi_s})^2]}. \tag{4.20}$$

- Background template extracted from the invariant mass distribution obtained by combining D^0 candidates with random soft pions coming from other events.
- Three Gaussian functions with a radiative tail for signal, D^0 plus random-π_s template for background.
- The baseline background function with tag-dependent parameters.

Table 4.9: RMS of $\delta(\Delta A_{CP})$ for each alternative fit model for the prompt case.

Fit model	**Systematic uncertainty** [%]
Bifurcated Gaussian	0.003
Triple Gaussian + radiative tail	0.004
Polynomial × phase space	0.004
D^0 + random-π_s	0.003
Triple Gaussian + radiative tail, D^0 + random-π_s	0.004
Background tag-dependent parameters	0.006

Table 4.10: Differences between ΔA_{CP} obtained with baseline and alternative fit models on data in the prompt case.

Fit model	**Difference from baseline** ΔA_{CP} [%]
Bifurcated Gaussian	0.001
Triple Gaussian + radiative tail	0.002
Polynomial × phase space	0.003
D^0 + random-π_s	0.004
Triple Gaussian + radiative tail, D^0 + random-π_s	0.003
Background tag-dependent parameters	0.001

The distributions of the difference between ΔA_{CP} values obtained with alternative and baseline fits, $\delta(\Delta A_{CP}) \equiv \Delta A_{CP}^{\text{alt}} - \Delta A_{CP}^{\text{base}}$, are shown in Fig. 4.15, and the root-mean-square (RMS) values are reported in Table 4.9. The maximum deviation observed is 0.006%, and it is assigned as a systematic uncertainty.

A test is performed using the alternative models to fit the data, obtaining the differences between alternative and baseline ΔA_{CP} values reported in Table 4.10. For each model, the difference is smaller or similar to the corresponding systematic uncertainty.

Weighting procedure

The kinematic weighting procedure is described in Sec. 4.2.4. In order to evaluate a systematic uncertainty related to the uncertainty on the weighting function due to limited statistics, the weighting procedure is repeated using 300 different weighting functions calculated by randomly extracting, event by event, a new weight from a Gaussian function centred at the nominal value of the weight with standard deviation equal to its uncertainty. This is done for each subsample, and the results are then averaged. The distribution of the difference between ΔA_{CP} values obtained with this procedure and the baseline is reported in Fig. 4.16. The assigned systematic

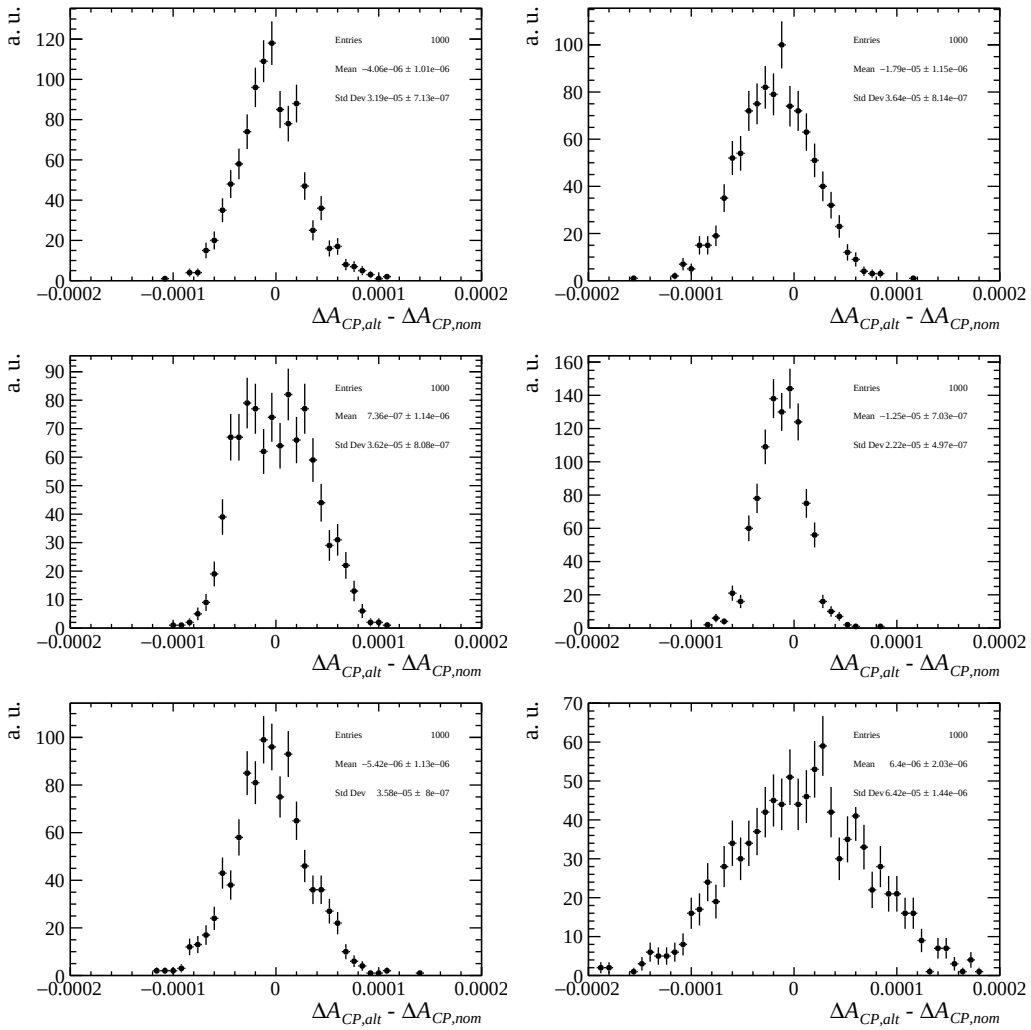

Figure 4.15: Distributions of the difference between the ΔA_{CP} values obtained with the baseline and the various fit models for the prompt case, namely: (top left) bifurcated Gaussian, (top right) triple Gaussian functions + radiative tail, (middle left) polynomial × phase space, (middle right) D^0 + random-π_s, (bottom left) triple Gaussian functions + radiative tail combined with D^0 + random-π_s and (bottom right) background tag-dependent parameters.

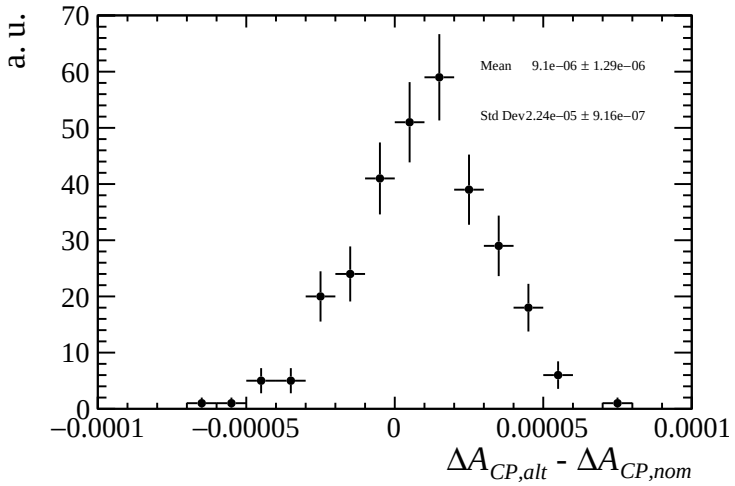

Figure 4.16: Distribution of the difference between the ΔA_{CP} values measured with different weighting functions and the ΔA_{CP} value obtained from the baseline fit for the prompt case.

uncertainty is the RMS of this distribution, *i.e.* 0.002%.

Contamination from secondary D^0 decays

The requirement imposed on the D^0 impact parameter, *i.e.* $\chi^2_{\rm IP}(D^0) < 9$, is needed to reject secondary D^0 decays. However, a certain fraction of secondary decays, $f_{\rm sec}$, is still present. If this fraction is different between the $D^0 \to K^+K^-$ and $D^0 \to \pi^+\pi^-$ decays, an imperfect cancellation of the charm-meson production asymmetries can occur, generating a bias on ΔA_{CP}. In fact, the raw asymmetries for the prompt and secondary decays are equal to

$$A^{\rm prompt}_{\rm raw}(h^+h^-) = A_{\rm P}(D^{*+}) + A_{CP}(h^+h^-) + A^{\rm prompt}_{\rm D}(\pi^+), \tag{4.21}$$

$$A^{\rm sec}_{\rm raw}(h^+h^-) = A^{\rm sec}_{\rm P}(D^{*+}) + A_{CP}(h^+h^-) + A^{\rm sec}_{\rm D}(\pi^+), \tag{4.22}$$

where $A_{\rm P}(D^{*+})$ is the D^{*+} production asymmetry and $A^{\rm sec}_{\rm P}(D^{*+})$ is the production asymmetry of D^{*+} mesons originating from B decays. The detection asymmetry of the pion may be slightly different between prompt and secondary decays because of different momentum distribution in secondary decays. The measured difference of raw asymmetries between $D^0 \to K^+K^-$ and $D^0 \to \pi^+\pi^-$ decays is therefore equal to

$$\begin{aligned}\Delta A = &[(1 - f^{K^+K^-}_{\rm sec})A^{\rm prompt}_{\rm raw}(K^+K^-) + f^{K^+K^-}_{\rm sec} A^{\rm sec}_{\rm raw}(K^+K^-)] \\ &- [(1 - f^{\pi^+\pi^-}_{\rm sec})A^{\rm prompt}_{\rm raw}(\pi^+\pi^-) + f^{\pi^+\pi^-}_{\rm sec} A^{\rm sec}_{\rm raw}(\pi^+\pi^-)].\end{aligned} \tag{4.23}$$

If the fractions $f_{\rm sec}^{K^+K^-}$ and $f_{\rm sec}^{\pi^+\pi^-}$ of secondary D^0 decays is different between the $D^0 \to K^+K^-$ and $D^0 \to \pi^+\pi^-$ samples, this results in a systematic shift $\Delta_{\rm sec}$ on the ΔA_{CP} value, given by

$$\Delta_{\rm sec} = f_{\rm sec}^{K^+K^-}[A_{\rm raw}^{\rm sec}(K^+K^-) - A_{\rm raw}^{\rm prompt}(K^+K^-)] - f_{\rm sec}^{\pi^+\pi^-}[A_{\rm raw}^{\rm sec}(\pi^+\pi^-) - A_{\rm raw}^{\rm prompt}(\pi^+\pi^-)]. \tag{4.24}$$

If 2ε is the difference between $f_{\rm sec}^{K^+K^-}$ and $f_{\rm sec}^{\pi^+\pi^-}$, the two fractions can be written as

$$f_{\rm sec}^{K^+K^-} = f_{\rm sec} + \varepsilon, \tag{4.25a}$$

$$f_{\rm sec}^{\pi^+\pi^-} = f_{\rm sec} - \varepsilon, \tag{4.25b}$$

and, taking into account that

$$A_{\rm raw}^{\rm sec}(K^+K^-) - A_{\rm raw}^{\rm sec}(\pi^+\pi^-) = A_{\rm raw}^{\rm prompt}(K^+K^-) - A_{\rm raw}^{\rm prompt}(\pi^+\pi^-) = \Delta A_{CP}, \tag{4.26}$$

Eq. (4.24) can be written as

$$\begin{aligned}\Delta_{\rm sec} &= \varepsilon[A_{\rm raw}^{\rm sec}(K^+K^-) + A_{\rm raw}^{\rm sec}(\pi^+\pi^-) - A_{\rm raw}^{\rm prompt}(K^+K^-) - A_{\rm raw}^{\rm prompt}(\pi^+\pi^-)] \\ &= \frac{f_{\rm sec}^{K^+K^-} - f_{\rm sec}^{\pi^+\pi^-}}{2}[A_{\rm raw}^{\rm sec}(K^+K^-) - A_{\rm raw}^{\rm prompt}(K^+K^-) \\ &\qquad + A_{\rm raw}^{\rm sec}(\pi^+\pi^-) - A_{\rm raw}^{\rm prompt}(\pi^+\pi^-)].\end{aligned} \tag{4.27}$$

To estimate the secondary fractions for events with $\chi^2_{\rm IP}(D^0) < 9$, a fit to the D^0 transverse impact parameter (TIP) distribution is performed on the background-subtracted data samples without the $\chi^2_{\rm IP}$ requirement. The TIP is defined as the distance of closest approach of the trajectory of the D^0 meson to the beam axis

$$\text{TIP} = \frac{\hat{n}_z \wedge \vec{p}}{|\hat{n}_z \wedge \vec{p}|} \cdot (\vec{x}_{\rm DV} - \vec{x}_{\rm PV}), \tag{4.28}$$

where $\vec{p}$ is the momentum vector of the D^0 meson, $\hat{n}_z$ is the unit vector along the z direction (beam axis) and $\vec{x}_{\rm DV}$ and $\vec{x}_{\rm PV}$ are the vectors defining the position of the D^0 decay vertex and of the PV, respectively. As the baseline analysis makes use of a requirement on $\chi^2_{\rm IP}(D^0)$, the relation between the $\chi^2_{\rm IP}(D^0)$ and the TIP variables must be studied. Figure 4.17 shows that when imposing $\chi^2_{\rm IP}(D^0) < 9$ the TIP distribution is almost included in the range $|\text{TIP}| < 50\,\mu\text{m}$. For this reason, the fit is performed in the range $|\text{TIP}| < 200\,\mu\text{m}$ to determine accurately the contribution of secondary D^0 decays in the tails of the TIP distributions. The yields of the prompt

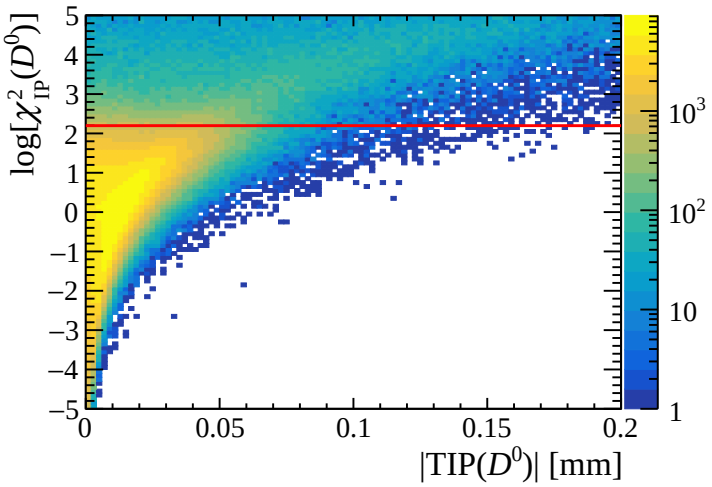

Figure 4.17: Distribution of $\chi^2_{\rm IP}(D^0)$ vs |TIP| for the *MagDown* 2016 sample. The red line shows the baseline requirement on $\chi^2_{\rm IP}(D^0)$.

and secondary components are then obtained by integrating the fitted functions extrapolated in the range $|\text{TIP}| < 50\,\mu\text{m}$.

The TIP distribution of the prompt component is described by a resolution model (R) made of two Gaussian functions with a common mean

$$\begin{aligned} F_{\rm prompt}(\text{TIP}) &= R(\text{TIP};\mu,\sigma_1,\sigma_2,f_1) \\ &= f_1\, G(\text{TIP};\mu,\sigma_1) + (1-f_1)\, G(\text{TIP};\mu,\sigma_2). \end{aligned} \tag{4.29}$$

The secondary component is modelled with a symmetric exponential

$$S(x;\lambda) = \frac{e^{-\frac{|x|}{\lambda}}}{2\lambda}, \tag{4.30}$$

convolved with the same function of the prompt component

$$F_{\rm sec}(\text{TIP}) = S(\text{TIP};\lambda) \otimes R(\text{TIP};\mu,\sigma_1,\sigma_2,f_1). \tag{4.31}$$

Since the parameters of these models, μ, σ_1, σ_2, f_1 and λ, depend on the measured decay time t, the data sample is divided in four bins of t/τ (where τ is the nominal D^0 lifetime [26]), namely $t/\tau < 1.5$, $1.5 < t/\tau < 3.0$, $3.0 < t/\tau < 4.5$ and $t/\tau > 4.5$. To have a better knowledge of the resolution model, the fit to the TIP distribution is performed on the larger $D^0 \to K^-\pi^+$ control sample using the same binning scheme. The parameters of the resolution model so obtained are then fixed in the fits to the

Table 4.11: Fraction of candidates coming from secondary D^0 decays with respect to the total number of candidates, requiring $|\text{TIP}| < 50\,\mu\text{m}$. No requirements on $\chi^2_{\text{IP}}(D^0)$ are applied.

Results from the fit to the TIP	2015 and 2016 [%]	2017 and 2018 [%]
$f_{\text{sec}}^{K^+K^-}$	11.79 ± 0.04	11.12 ± 0.03
$f_{\text{sec}}^{\pi^+\pi^-}$	12.91 ± 0.09	10.98 ± 0.06
$f_{\text{sec}}^{K^+K^-} - f_{\text{sec}}^{\pi^+\pi^-}$	-1.1 ± 0.1	0.14 ± 0.07
$A_{\text{raw}}^{\text{sec}}(K^+K^-) - A_{\text{raw}}^{\text{prompt}}(K^+K^-)$	-0.26 ± 0.21	0.03 ± 0.15
$A_{\text{raw}}^{\text{sec}}(\pi^+\pi^-) - A_{\text{raw}}^{\text{prompt}}(\pi^+\pi^-)$	0.12 ± 0.42	-0.43 ± 0.29

$D^0 \to K^+K^-$ and $D^0 \to \pi^+\pi^-$ samples. For each t/τ bin, the yields of the D^{*+} and D^{*-} candidates, for both prompt and secondary components, are obtained from the fit. The study is performed on the 2015 plus 2016 and on 2017 plus 2018 data sets separately.

Figures 4.18 and 4.19 show the TIP distributions for $D^0 \to K^-\pi^+$, $D^0 \to K^+K^-$ and $D^0 \to \pi^+\pi^-$ candidates with the results of the fits overlaid. For each decay mode, the sum across all the t/τ bins of the various prompt and secondary yields, split by tag, allows the total fraction of secondary decays and the total raw asymmetries to be calculated. The results are reported in Table 4.11 and are used to evaluate $\Delta_{\text{sec}}(2015 + 2016) = (-0.0008 \pm 0.0026)\%$ for the 2015 and 2016 sample, which leads to a systematic uncertainty of 0.003%, by summing in quadrature the mean and the uncertainty of Δ_{sec}. For the 2017 and 2018 sample, $\Delta_{\text{sec}}(2017 + 2018) = (-0.00029 \pm 0.00027)\%$, resulting in a systematic uncertainty of 0.0004%, which is negligible. Conservatively, the systematic uncertainty due to secondary D^0 decays assigned to the full Run-2 data sample is chosen to be that one obtained with the 2015 and 2016 sample, *i.e.* 0.003%.

Peaking background

Partially or mis-reconstructed D^0 mesons from a D^* may peak in the $m(D^0\pi)$ invariant mass distribution and mimic the signal. In order to assess a systematic uncertainty due to the fact that this is ignored in the baseline fit, fits to the $m(D^0)$ invariant mass spectra are performed considering all events in the full $m(D^0\pi)$ window $[2004.5, 2020]\,\text{MeV}/c^2$. The values of raw asymmetry and yield of the peaking background obtained from the fits are used as inputs to pseudoexperiments from which the systematic uncertainty is evaluated.

In the $D^0 \to K^+K^-$ case, the fit is performed considering the following compo-

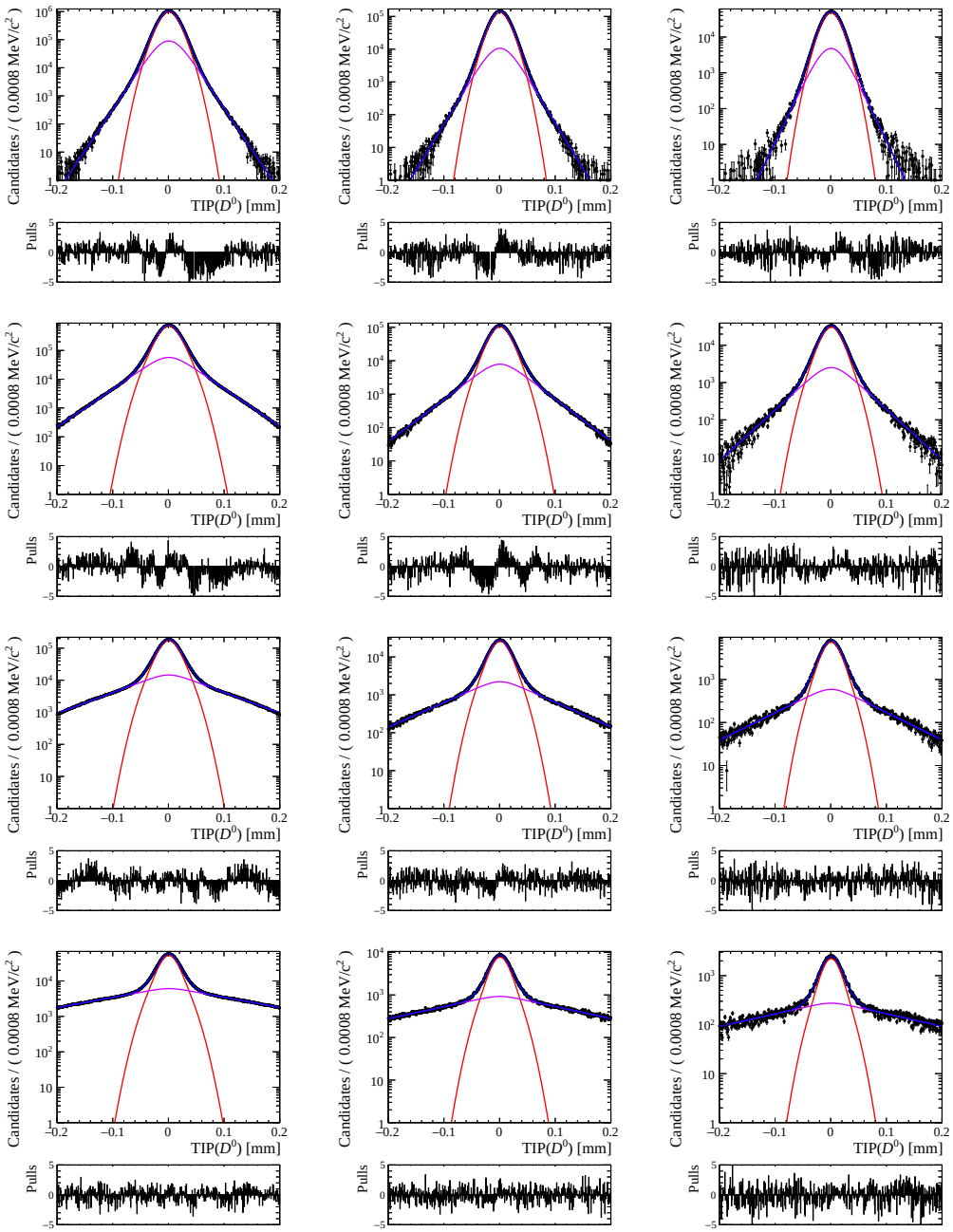

Figure 4.18: Fits to the TIP distributions for (left) $D^0 \to K^-\pi^+$, (centre) $D^0 \to K^+K^-$ and (right) $D^0 \to \pi^+\pi^-$ 2015 and 2016 samples, in the various t/τ bins, starting from the top: $t/\tau < 1.5$, $1.5 < t/\tau < 3.0$, $3.0 < t/\tau < 4.5$, $t/\tau > 4.5$. The prompt component is shown in red and the secondary in violet.

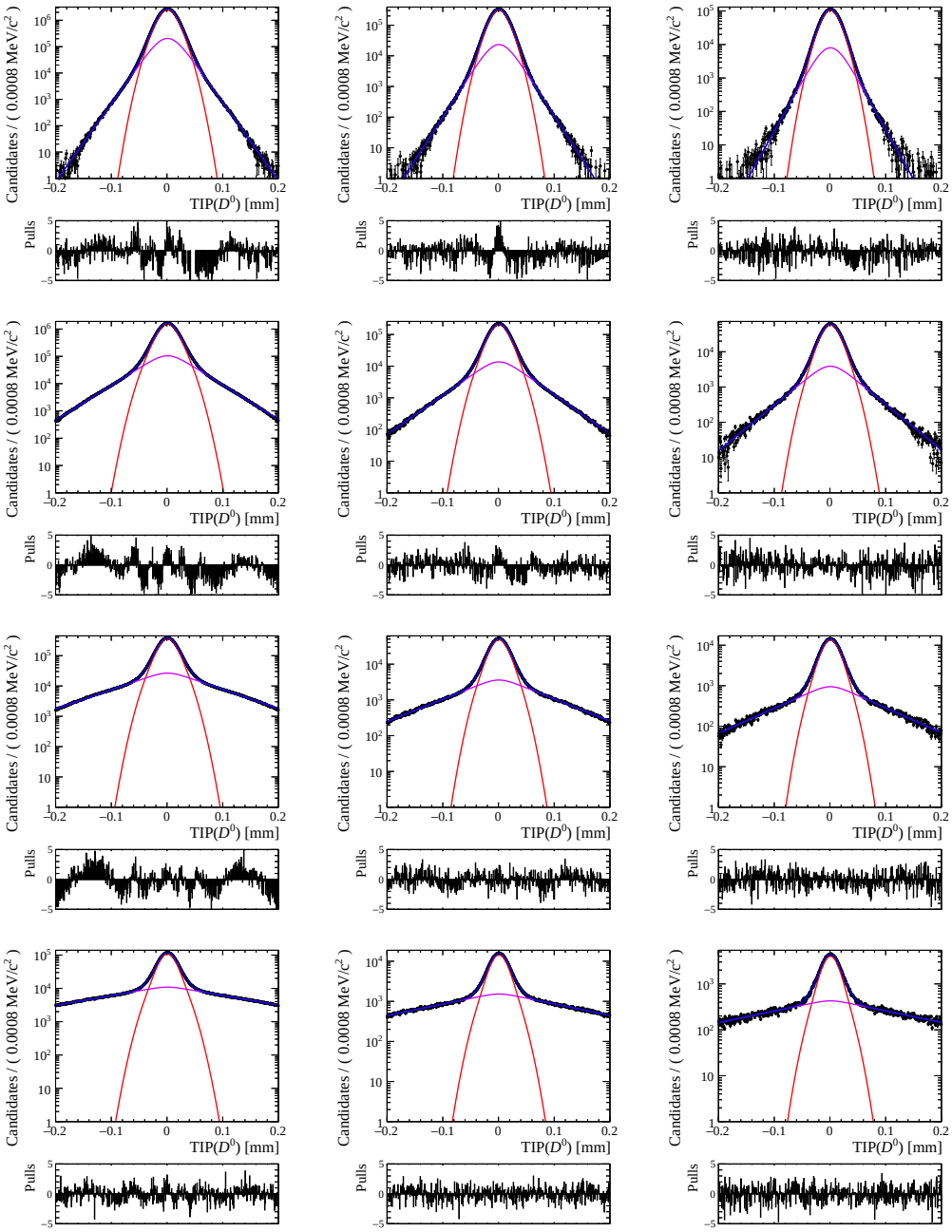

Figure 4.19: Fits to the TIP distributions for (left) $D^0 \to K^-\pi^+$, (centre) $D^0 \to K^+K^-$ and (right) $D^0 \to \pi^+\pi^-$ 2017 and 2018 samples, in the various t/τ bins, starting from the top: $t/\tau < 1.5$, $1.5 < t/\tau < 3.0$, $3.0 < t/\tau < 4.5$, $t/\tau > 4.5$. The prompt component is shown in red and the secondary in violet.

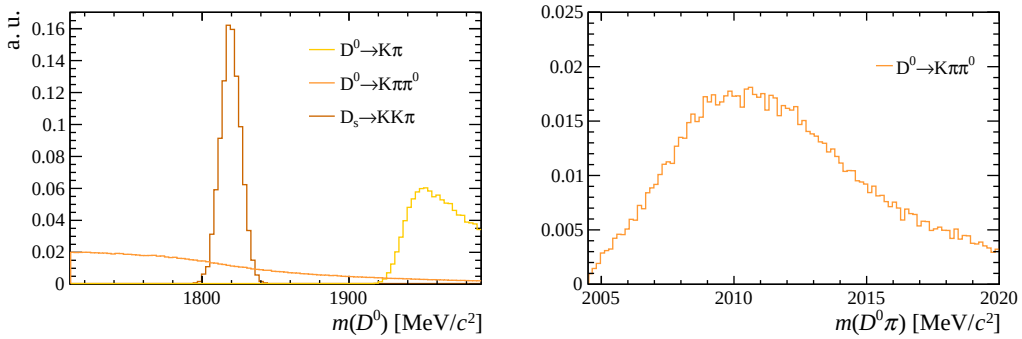

Figure 4.20: Normalised distributions of (left) $m(K^+K^-)$ and (right) $m(D^0\pi)$ for the various main background components simulated with RapidSim. The baseline requirement on $m(K^+K^-)$ is applied to the events in the $m(D^0\pi)$ spectrum.

nents.

- The signal, modelled with a double Gaussian function and a radiative tail, described by Eq. (4.18). The parameter s, that governs the radiative tail, is fixed to the value obtained from the baseline fit to the semileptonic sample.
- The $D^0 \to K^-\pi^+$ decay, where the pion is misidentified as a kaon. This background is modelled with a Landau function.
- The $D^0 \to K^-\pi^+\pi^0$ decay, where the charged pion is misidentified as a kaon and the π^0 is not reconstructed. The shape of this component, obtained from the fast simulation performed with the RapidSim tool as described in Sec. 4.2.3, is modelled with a Landau function, and is shown in Fig. 4.20.
- The $D_s^+ \to K^-K^+\pi^+$ decay, where the π^+ mimics a soft pion. As checked by means of the fast simulation, a Gaussian function is used to model the shape of this component, which is reported in Fig. 4.20.
- The combinatorial background, described by a constant function.

Among the various components listed above, only the $D^0 \to K^-\pi^+\pi^0$ decay shows a peaking structure in the $m(D^0\pi)$ distribution for the events in the $m(K^+K^-)$ signal window, as shown in Fig. 4.20. Figure 4.21 reports the $m(D^0\pi)$ spectrum with the result of the fit superimposed. The measured yield of $D^0 \to K^-\pi^+\pi^0$, extrapolated to the signal region, is $5.5{\cdot}10^5$, with a raw asymmetry $A_{\rm raw}(K^-\pi^+\pi^0) = (-0.45{\pm}0.07)\%$.

In the $D^0 \to \pi^+\pi^-$ case, the following decays are considered.

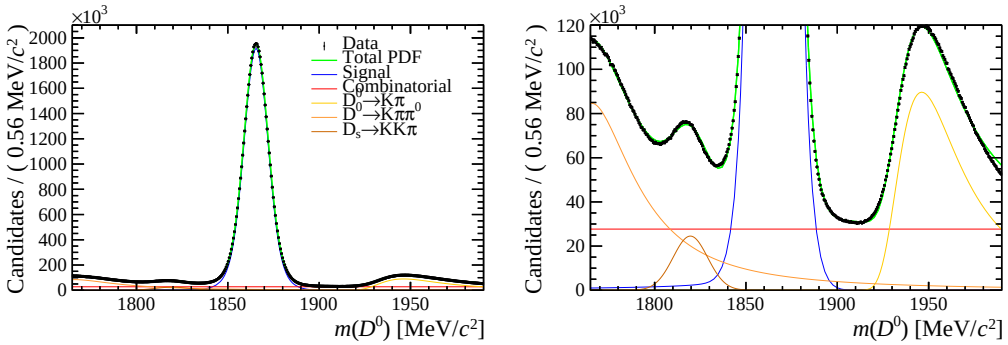

Figure 4.21: Invariant-mass distribution for $D^0 \to K^+K^-$ candidates, with the result of the fit superimposed. The plot on the right is a magnification of that on the left.

- The signal, modelled with a double Gaussian function and a radiative tail, described by Eq. (4.18). The parameter s, that governs the radiative tail, is fixed to the value obtained from the baseline fit to the semileptonic sample.
- The $D^0 \to K^-\pi^+$ decay, where the kaon is misidentified as a pion. This background is modelled with an Argus function [109] convolved with a Gaussian function.
- The $D^0 \to \pi^-\ell^+\nu_\ell$ decay, with the lepton misidentified as a pion and the neutrino not reconstructed. The shape of this background, obtained from the fast simulation, is shown in Fig. 4.22.
- The combinatorial background, described by a constant function.

Only the $D^0 \to \pi^-\ell^+\nu_\ell$ decay exhibits a peaking behaviour in $m(D^0\pi)$, as shown in Fig. 4.22. Figure 4.23 reports the $m(D^0\pi)$ spectrum with the result of the fit superimposed. The measured yield of $D^0 \to \pi^-\ell^+\nu_\ell$ decay, extrapolated to the signal region, is $6.9 \cdot 10^3$, with a raw asymmetry $A_{\rm raw}(K^-\pi^+\pi^0) = (0.82 \pm 0.95)\%$.

The last step consists in generating 1000 pseudoexperiments according to the baseline results. A fit to each sample is done using the baseline model and an alternative model that includes also the peaking background. The difference of the values of ΔA_{CP} obtaining using the two fit models are shown in Fig. 4.24. The RMS of the distribution amounts to 0.003%, and this is taken as a systematic uncertainty.

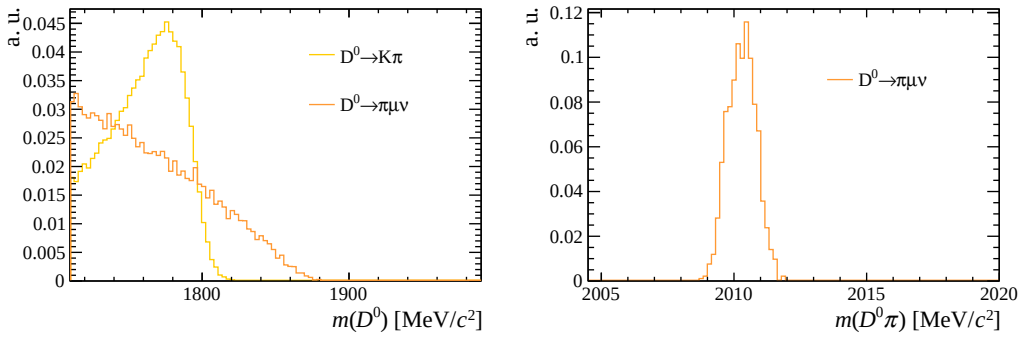

Figure 4.22: Normalised distributions of (left) $m(\pi^+\pi^-)$ and (right) $m(D^0\pi)$ for the main background components simulated with RapidSim. The baseline requirement on $m(\pi^+\pi^-)$ is applied to the events in the $m(D^0\pi)$ spectrum.

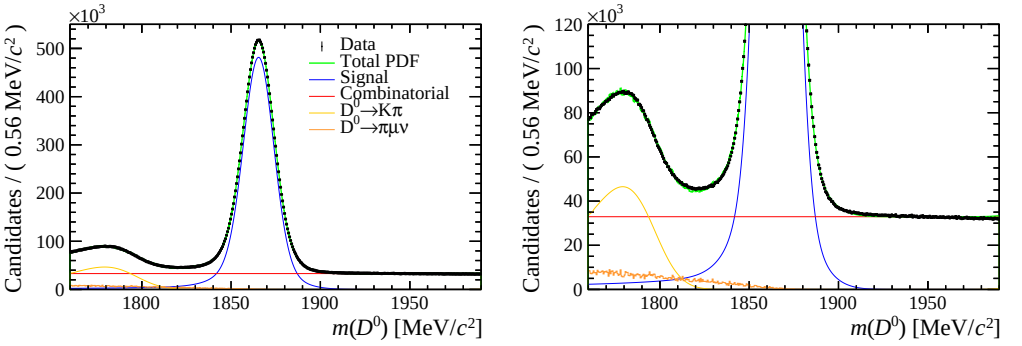

Figure 4.23: Invariant-mass distribution for $D^0 \to \pi^+\pi^-$ candidates, with the result of the fit superimposed. The plot on the right is a magnification of that on the left.

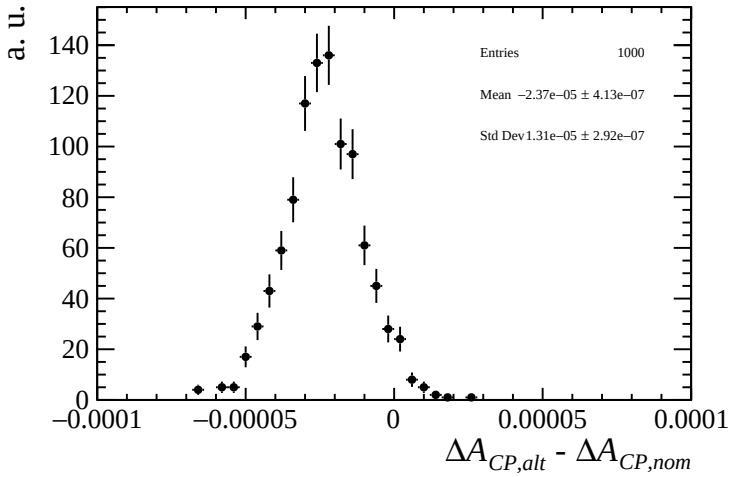

Figure 4.24: Distribution of the difference between the ΔA_{CP} values obtained with and without considering the peaking background in the fit model.

Table 4.12: Sum in quadrature of mean and variance of $\delta(\Delta A_{CP})$ for each alternative fit model in the semileptonic case.

Fit model	**Systematic uncertainty** [%]
Crystal Ball + Gaussian	0.002
Double Gaussian	0.012
Polynomial with different parameters for each tag	0.016
Polynomial with same parameters for each tag	0.004
Exponential with different parameters for each tag	0.013
Triple Gaussian + radiative tail	0.004

4.4.2 Semileptonic case

Fit model

To assess a systematic uncertainty related to the choice of the fit model, the same procedure described for the prompt case is repeated, using the following alternative fit models

- Crystal Ball [99] plus Gaussian function for the signal;
- double Gaussian function for the signal;
- first-order polynomial for the background with different parameters for each tag;
- first-order polynomial for the background with same parameters for each tag;
- exponential function for the background with different parameters for each tag;
- triple Gaussian function convolved with a radiative tail for the signal, with parameters fixed from simulation except for the means.

One example of a fit to a simulated sample is shown in Fig. 4.25. The distributions of $\delta(\Delta A_{CP})$ for the various fit models are shown in Fig. 4.26, and the associated uncertainties reported in Table 4.12. The assigned systematic uncertainty is 0.02%, corresponding to the maximum of the sums in quadrature of the means and the variances of the distributions for the various alternative fit models.

A test is performed using the alternative models to fit the data, obtaining the differences between alternative and baseline ΔA_{CP} values reported in Table 4.13.

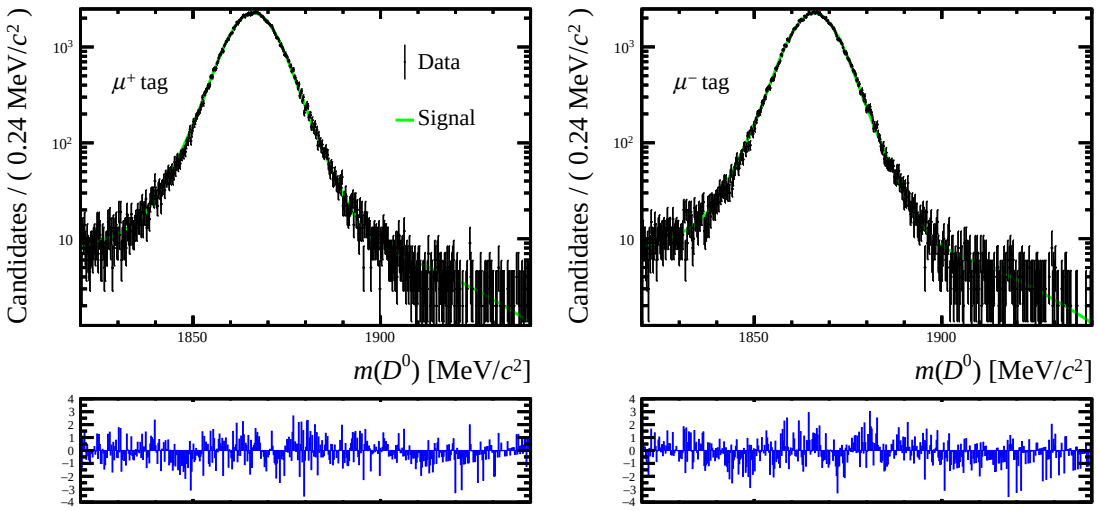

Figure 4.25: Fits to $D^0 \to K^+K^-$ simulated decays for the *MagUp* configuration. The PDF used is the same of the triple Gaussian functions convolved with a radiative tail.

Table 4.13: Differences between ΔA_{CP} obtained with baseline and alternative fit models for the semileptonic mode.

Fit model	**Difference with baseline ΔA_{CP} [%]**
Crystal Ball + Gaussian	0.002
Double Gaussian	0.015
Polynomial with different parameters for each tag	0.013
Polynomial with same parameters for each tag	0.004
Exponential with different parameters for each tag	0.013
Triple Gaussian + radiative tail	0.004

For each model, the difference is smaller or of the same order as the corresponding systematic uncertainty.

Weighting procedure

The method used to evaluate a systematic uncertainty associated to the weighting procedure is the same as in the prompt case, explained in Sec. 4.4.1. The distribution of the difference between the values of ΔA_{CP} obtained with alternative weighting functions and the baseline is shown in Fig. 4.27. The RMS of the distribution, equal to 0.01%, is assigned as a systematic uncertainty.

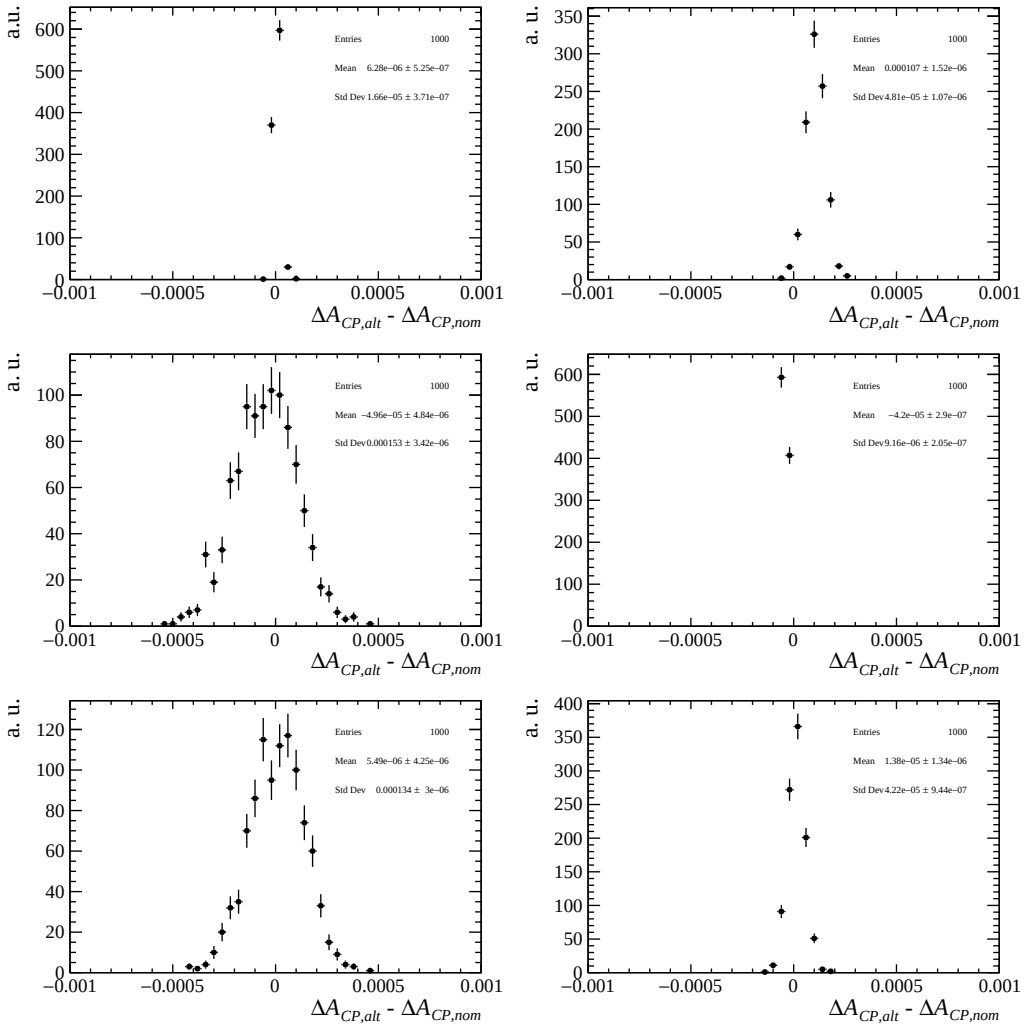

Figure 4.26: Distributions of the difference between the ΔA_{CP} values obtained with the baseline and the various fit models for the semileptonic case, namely (top left): Crystal Ball + Gaussian, (top right) double Gaussian, (middle left) polynomial with different parameters between tags, (middle right) polynomial with common parameters between tags, (bottom left) exponential with different parameters between tags and (bottom right) triple Gaussian + radiative tail.

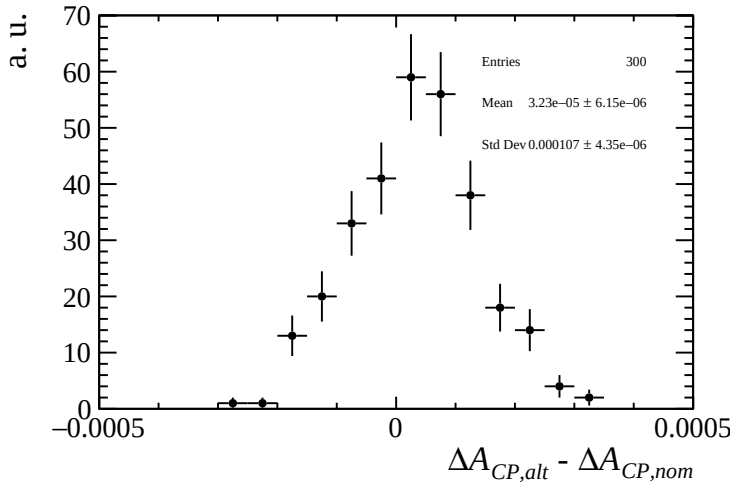

Figure 4.27: Distribution of the difference between the ΔA_{CP} values obtained with alternative weighting functions and the baseline for the semileptonic case.

Mistag rate estimation

In the semileptonic case the probability to tag a D^0 ($\overline{D}^0$) with a positive (negative) muon is defined as

$$\omega_{D^0} = \mathcal{P}(\mu^+|D^0), \tag{4.32a}$$
$$\omega_{\overline{D}^0} = \mathcal{P}(\mu^-|\overline{D}^0), \tag{4.32b}$$

and the average mistag rate and mistag difference are defined as

$$\omega = \frac{\omega_{D^0} + \omega_{\overline{D}^0}}{2}, \tag{4.33a}$$
$$\Delta\omega = \omega_{D^0} - \omega_{\overline{D}^0}. \tag{4.33b}$$

It is possible to show that the mistag rate, which is expected to be of the order of 1%, modifies $A_{\text{raw}}(K^+K^-)$ and $A_{\text{raw}}(\pi^+\pi^-)$ as follows

$$A_{\text{raw}}(f) = (1-2\omega)[A_{CP}(f) + A_{\text{P,eff}}(D^0)] + A_D(\mu^-) - \Delta\omega. \tag{4.34}$$

Therefore ΔA_{CP} becomes

$$\Delta A_{CP} = (1-2\omega)(A_{\text{raw}}(K^+K^-) - A_{\text{raw}}(\pi^+\pi^-)). \tag{4.35}$$

The mistag rate is measured directly on data using the $D^0 \to K^-\pi^+$ decay from semileptonic B-meson decays. The assumption is that the reconstruction efficiency

Table 4.14: The D^0 mixing parameters from Ref. [110].

Results		Correlations					
Parameter	Fit value	R_D^+	y'^+	x'^{2+}	R_D^-	y'^-	x'^{2-}
R_D^+ $[10^{-3}]$	3.454 ± 0.045	1.000	−0.935	0.843	−0.012	−0.003	0.002
y'^+ $[10^{-3}]$	5.01 ± 0.74		1.000	−0.963	−0.003	0.004	−0.003
$(x'^+)^2$ $[10^{-3}]$	0.061 ± 0.037			1.000	0.002	−0.003	0.003
R_D^- $[10^{-3}]$	3.454 ± 0.045				1.000	−0.935	0.846
y'^- $[10^{-3}]$	5.54 ± 0.74					1.000	−0.964
$(x'^-)^2$ $[10^{-3}]$	0.016 ± 0.039						1.000

of the muon factorises with the reconstruction efficiency of the D^0, and so the mistag rate does not depend on the D^0 final state. A D^0 meson mainly decays into the $K^-\pi^+$ final state. This is called *right-sign* (RS) decay. A small fraction ($\mathcal{O}(10^{-3})$) of D^0 mesons may also decay to the so-called *wrong-sign* (WS) final state $K^+\pi^-$. This state is accessible either by the direct doubly-Cabibbo-suppressed $D^0 \to K^-\pi^+$ decay or by D^0–$\overline{D}^0$ mixing followed by the Cabibbo-favoured decay $\overline{D}^0 \to K^+\pi^-$. The time-dependent ratios of WS decays for D^0 (+) and $\overline{D}^0$ (–) are given by

$$R^{\pm}(t) \simeq R_D^{\pm} + \sqrt{R_D^{\pm}}\, y'^{\pm} \left(\frac{t}{\tau}\right) + \frac{x'^{\pm 2} + y'^{\pm 2}}{4} \left(\frac{t}{\tau}\right)^2, \tag{4.36}$$

while the average ratio is given by

$$R^{\pm} = R_D^{\pm} + \left\langle \frac{t}{\tau} \right\rangle \sqrt{R_D^{\pm}}\, y'^{\pm} + \left\langle \left(\frac{t}{\tau}\right)^2 \right\rangle \frac{x'^{\pm 2} + y'^{\pm 2}}{2}, \tag{4.37}$$

where $\langle t \rangle$ is the average of the decay-time distribution observed on events where the D^0 does not oscillate, and τ is the average lifetime of the D^0 meson, taken from Ref. [26]. $R_D^{\pm}$, $x'^{\pm 2}$ and y' have been measured by LHCb for D^0 and $\overline{D}^0$ mesons separately [110], and their values are reported in Table 4.14. From their values, $R^{\pm}$ can be calculated to be

$$R^+ = (3.899 \pm 0.060) \cdot 10^{-3},$$
$$R^- = (3.891 \pm 0.062) \cdot 10^{-3}.$$

In order to measure the mistag rate, the $D^0 \to K^-\pi^+$ sample is divided in four subsamples, according to the charges of the K, π and μ

- $K^-\pi^+\mu^-$: it includes correctly tagged RS D^0 decays and wrongly tagged WS $\overline{D}^0$ decays, called $\mu^-_{\rm RS}$;

Table 4.15: Measured values of the mistag rates. The values are computed neglecting the correlation between ω_{D^0} and $\omega_{\overline{D}^0}$, since this is very small.

$\omega_{D^0}[\%]$	$\omega_{\overline{D}^0}[\%]$	$\rho(\omega_{D^0}, \omega_{\overline{D}^0})$	$\omega[\%]$	$\Delta\omega[\%]$
BDT_{KK}				
1.747 ± 0.003	1.753 ± 0.004	0.003	1.750 ± 0.002	-0.005 ± 0.004
$\text{BDT}_{\pi\pi}$				
1.270 ± 0.002	1.274 ± 0.002	0.004	1.272 ± 0.002	-0.005 ± 0.003

- $K^+\pi^-\mu^+$: it includes correctly tagged RS $\overline{D}^0$ decays and wrongly tagged WS D^0 decays, called μ^+_{RS};

- $K^+\pi^-\mu^-$: it includes correctly tagged WS D^0 decays and wrongly tagged RS $\overline{D}^0$ decays, called μ^-_{WS};

- $K^-\pi^+\mu^+$: it includes correctly tagged WS $\overline{D}^0$ decays and wrongly tagged RS D^0 decays, called μ^+_{WS}.

It is possible to parameterise the signal yields of these four samples as a function of ω_{D^0}, $\omega_{\overline{D}^0}$, $R^\pm$ and number of RS D^0 and $\overline{D}^0$ decays:

$$N(\mu^-_{\text{RS}}) = (1-\omega_{D^0})N({D^0}_{RS}) + \omega_{\overline{D}^0} R^- N({\overline{D}^0}_{RS}), \tag{4.38a}$$
$$N(\mu^+_{\text{RS}}) = (1-\omega_{\overline{D}^0})N({\overline{D}^0}_{RS}) + \omega_{D^0} R^+ N({D^0}_{RS}), \tag{4.38b}$$
$$N(\mu^-_{\text{WS}}) = (1-\omega_{D^0})R^+ N({D^0}_{RS}) + \omega_{\overline{D}^0} N({\overline{D}^0}_{RS}), \tag{4.38c}$$
$$N(\mu^+_{\text{WS}}) = (1-\omega_{\overline{D}^0})R^- N({\overline{D}^0}_{RS}) + \omega_{D^0} N({D^0}_{RS}). \tag{4.38d}$$

The values of ω_{D^0} and $\omega_{\overline{D}^0}$ are measured from a simultaneous fit to the four subsamples. The values of $R^\pm$ are fixed in the fits to the values reported above. The fit model is the same as that previously described in Sec. 4.3.2. However, due to the large number of signal events, an additional Gaussian function is added to the signal PDF for a better agreement between model and data. The fit is performed separately for each BDT requirement (BDT_{KK} and $\text{BDT}_{\pi\pi}$). The $m(D^0)$ spectra are shown in Figs. 4.28 and 4.29 with the results of the fits superimposed, while the results are summarised in Table 4.15.

Differences are present for the values of the mistag rate between the two BDT_{KK} and $\text{BDT}_{\pi\pi}$ selections. For this reason, Eq. (4.35) does not hold and needs to be

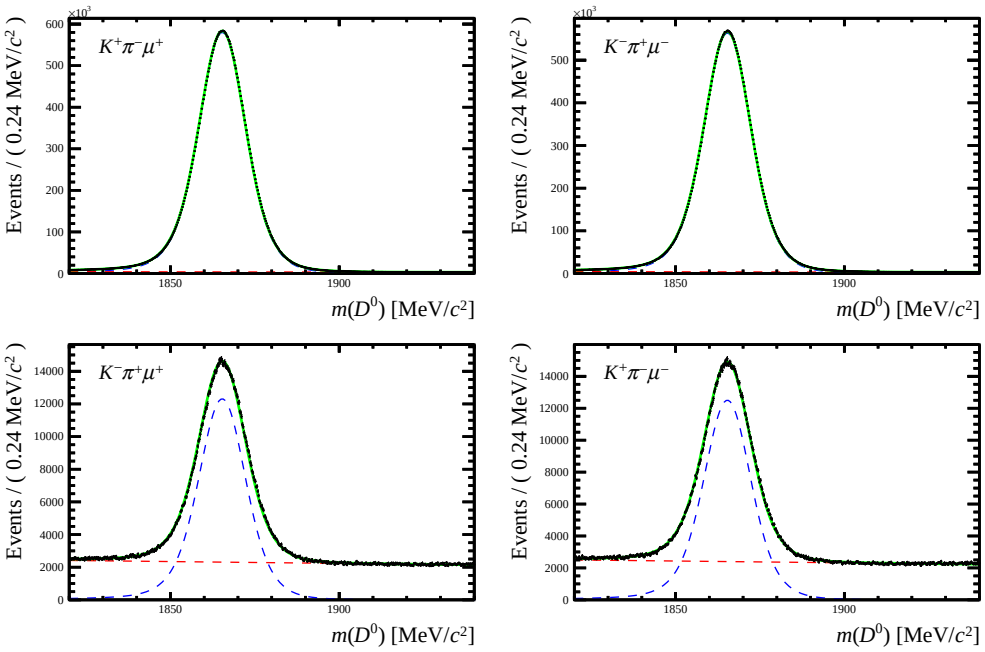

Figure 4.28: Distributions of $m(D^0)$ for (top left) $\mu^+_{\rm RS}$, (top right) $\mu^-_{\rm RS}$, (bottom left) $\mu^+_{\rm WS}$ and (bottom right) $\mu^-_{\rm WS}$. The results of the fits are overlaid to the distributions. The BDT$_{KK}$ selection is used.

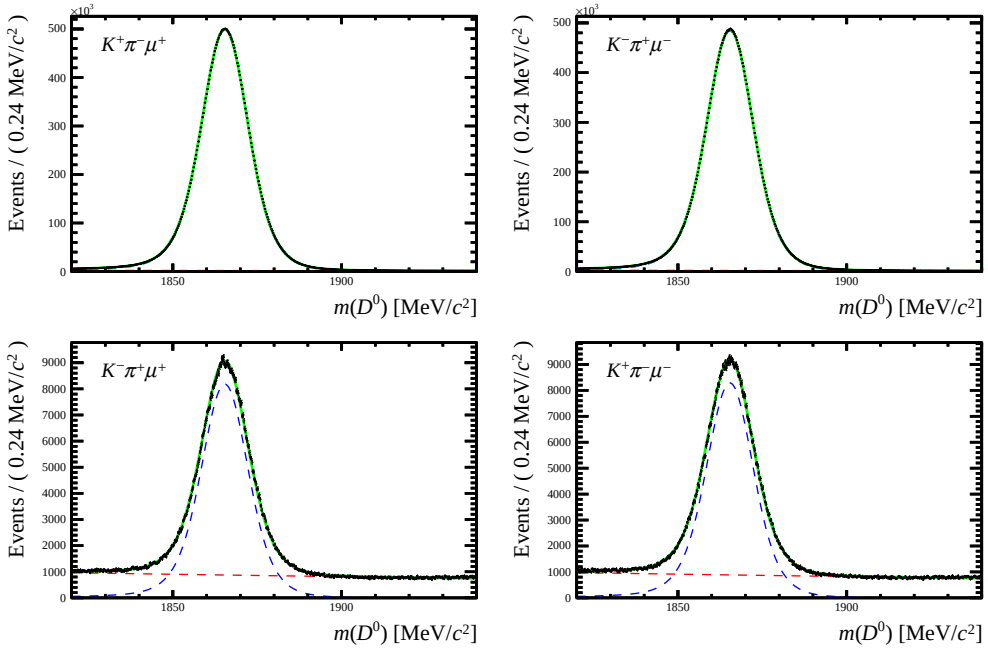

Figure 4.29: Distributions of $m(D^0)$ for (top left) $\mu^+_{\rm RS}$, (top right) $\mu^-_{\rm RS}$, (bottom left) $\mu^+_{\rm WS}$ and (bottom right) $\mu^-_{\rm WS}$. The results of the fits are overlaid to the distributions. The BDT$_{\pi\pi}$ selection is used.

modified as

$$\begin{aligned}\Delta A_{CP} = \Delta A_{\rm raw} &+ 2\omega_{KK} A_{CP}(K^+K^-) - 2\omega_{\pi\pi}[A_{CP}(K^+K^-) - \Delta A_{CP}] \\ &+ 2A_{\rm P,eff}(D^0)(\omega_{KK} - \omega_{\pi\pi}) + \Delta\omega_{KK} - \Delta\omega_{\pi\pi},\end{aligned} \tag{4.39}$$

where ω_{KK} ($\omega_{\pi\pi}$) and $\Delta\omega_{KK}$ ($\Delta\omega_{\pi\pi}$) are the mistag rates and mistag differences measured with the BDT$_{KK}$ (BDT$_{\pi\pi}$) selection. Therefore, the bias due to the mistag rate, δ_ω, is defined as

$$\begin{aligned}\delta_\omega = \Delta A_{CP} - \Delta A_{\rm raw} = &2\omega_{KK} A_{CP}(K^+K^-) - 2\omega_{\pi\pi}[A_{CP}(K^+K^-) - \Delta A_{CP}] \\ &+ 2A_{\rm P,eff}(D^0)(\omega_{KK} - \omega_{\pi\pi}) + \Delta\omega_{KK} - \Delta\omega_{\pi\pi},\end{aligned} \tag{4.40}$$

and it is estimated using the mistag measurements reported in Table 4.15, as well as the values of $A_{CP}(K^+K^-)$ and ΔA_{CP} measured by LHCb [66]. The value of $A_{\rm P,eff}(D^0)$ is conservatively assumed not to be larger than 3% [111]. The resulting systematic uncertainty is 0.04%.

B^0 production fraction

As shown in Eq. (4.4), the effective D^0 production asymmetries in semileptonic B decays depends also on a dilution factor D, which is equal to

$$D = 1 - 2\mathcal{P}_{\rm osc}, \tag{4.41}$$

where $\mathcal{P}_{\rm osc}$ is the probability that the B^0 meson oscillates. The value of D computed assuming no decay-time acceptance is equal to 0.628. So far $A_{\rm P,eff}(D^0)$ has been assumed to be equal between $D^0 \to K^+K^-$ and $D^0 \to \pi^+\pi^-$, but there could be a residual asymmetry due to different reconstruction efficiencies of $\overline{B}^0$ and B^- in the two cases, which could affect the value of $f(\overline{B}^0)$. A difference in $f(\overline{B}^0)$ is responsible for a bias in the value of $\Delta A_{\rm P,eff}(D^0)$, and then ΔA_{CP}, equal to

$$\Delta A_{\rm P,eff}(D^0) = \Delta f(\overline{B}^0)[A_{\rm P}(\overline{B}^0)D - A_{\rm P}(B^-)]. \tag{4.42}$$

According to studies performed in Ref. [66] using simulation, the difference $\Delta f(\overline{B}^0)$ is estimated to be (0.34 ± 0.18)%. Assuming conservatively a value for $\Delta f(\overline{B}^0)$ of 1% and using $A_{\rm P}(\overline{B}^0) = (0.88 \pm 0.47)$% and $A_{\rm P}(B^-) = (0.54 \pm 0.28)$% (weighted averages between 7 and 8 TeV results) [111], $\Delta A_{\rm P,eff}(D^0)$ is equal to (0.0001 ± 0.0058)%. The assigned systematic uncertainty is the sum in quadrature of the central value and the uncertainty of $\Delta A_{\rm P,eff}(D^0)$, *i.e.* 0.006%.

Table 4.16: Summary of the systematic uncertainties.

Source	**Prompt** [%]	**Semileptonic** [%]
Fit model	0.006	0.02
Weighting	0.002	0.01
Mistag rate	–	0.04
Secondary D^0	0.003	–
B^0 fraction	–	0.01
Decay time acceptance	–	0.02
Peaking background	0.005	–
Total	0.009	0.05

Difference in decay-time acceptance

If there is a decay-time acceptance, assumed to be modelled by a step function, the oscillation probability reported in Eq. (4.41) is equal to

$$\mathcal{P}_{\text{osc}} = \frac{\Gamma_d}{2} \int_{t_0}^{\infty} e^{-\Gamma_d t}(1 - \cos(\Delta m_d t))\text{t}, \tag{4.43}$$

where t_0 is the minimum reconstructed decay time, slightly different between $D^0 \to K^+K^-$ and $D^0 \to \pi^+\pi^-$. The related systematic uncertainty is taken unchanged from the Run-1 measurement [66], where it was estimated to be maximally 0.02%.

4.4.3 Summary of systematic uncertainties

The total systematic uncertainty in the prompt case is 0.009%, while in the semileptonic case it is 0.05%. The various contributions are summarised in Table 4.16.

4.5 Cross-checks

Many cross-checks are performed to verify the stability and robustness of the measurement of ΔA_{CP}. Section 4.5.1 describes the measurement of ΔA_{CP} as a function of various kinematic variables and data-taking periods, while in Sec. 4.5.2 an overview of measurements with alternative selection criteria is given. In Sec. 4.5.3 an important cross-check on ΔA_{bkg} in the prompt case is presented.

4.5.1 Dependence of ΔA_{CP} on kinematics and data-taking period

ΔA_{CP} is a physical observable which must not depend on the kinematics of the involved decays. In order to investigate whether there are any variations of ΔA_{CP} over the running period and as a function of relevant kinematic variables, the data sample is divided into blocks of runs and bins of kinematic and geometrical variables, and ΔA_{CP} is measured in each block and bin. In App. C, the values of ΔA_{CP} as a function of the various variables are shown. This study shows an excellent stability of ΔA_{CP} and no significant deviations from flatness, for both the prompt and the semileptonic cases.

4.5.2 Alternative selection criteria

The effect of various alternative selection criteria is studied, namely: tighter $\mathrm{DLL}_{K\pi}$ requirements; looser fiducial selection; weighting with alternative binnings on the variables used to calculate the weighting function; and no removal of multiple candidates. In all these tests the alternative ΔA_{CP} values result fully compatible with those obtained with the baseline procedure.

4.5.3 Test of ΔA_{bkg}

The value of ΔA_{bkg} is defined as the difference between the background raw asymmetries $A_{\mathrm{bkg}}(K^+K^-)$ and $A_{\mathrm{bkg}}(\pi^+\pi^-)$. For the prompt case, in the absence of physical backgrounds, one would expect a value of ΔA_{bkg} compatible with zero. The value of $A_{\mathrm{bkg}}(h^+h^-)$ is measured by performing the fit to the data sample where the background is weighted and by counting the background events in the $m(D^0\pi)$ sideband $[2020, 2035]\,\mathrm{MeV}/c^2$ which is not included in the baseline fit. The values of ΔA_{bkg} are reported in Table 4.17. By combining all the independent measurements, a value of $\Delta A_{\mathrm{bkg}} = (-0.023 \pm 0.041)\%$ is obtained, which differs from zero by 0.6 standard deviations.

4.6 Average decay time

It is necessary to measure the average decay time of reconstructed signal events in each decay mode to allow for an interpretation of ΔA_{CP} in terms of direct and indirect *CP* violation, shown in Eq. (1.86). The time-integrated *CP* asymmetries for

Table 4.17: Values of $\Delta A_{\rm bkg}$ for the various data samples.

Sample	$\boldsymbol{\Delta A_{\rm bkg}}$ **[%] (baseline fit)**	$\boldsymbol{\Delta A_{\rm bkg}}$ **[%] (sidebands only)**
2015	-0.422 ± 0.214	-0.234 ± 0.243
2016	-0.122 ± 0.090	0.026 ± 0.110
2017	0.133 ± 0.096	-0.065 ± 0.118
2018	0.121 ± 0.095	-0.149 ± 0.117
Total	-0.023 ± 0.041	

$D^0 \to K^+K^-$ and $D^0 \to \pi^+\pi^-$ decays are mainly sensitive to direct *CP* violation, but they receive also a small contribution from indirect *CP* violation, whose size depends on the average of the reconstructed decay time of the D^0 meson.

The average decay time for selected events is determined by using the *sPlot* background-subtraction technique with a fit to the $m(D^0\pi)$ distribution in the prompt case and to the $m(D^0)$ distribution in the semileptonic case, as reported in Sec. 4.3. The background-subtracted distributions of the decay time of the D^0 meson for the prompt samples are shown in Fig. 4.30. The average decay times are directly computed from the distributions, and are equal to

$$\langle t_{KK} \rangle^{\pi-\text{tagged}} = (0.73748 \pm 0.00007)\,\text{ps},$$
$$\langle t_{\pi\pi} \rangle^{\pi-\text{tagged}} = (0.68263 \pm 0.00012)\,\text{ps},$$

where the uncertainties are statistical only.

To evaluate the relative difference of the decay time between the two channels, the nominal D^0 lifetime $\tau_{hh} = (0.4072 \pm 0.0016)\,\text{ps}$ is used. The choice of fixing the lifetime to 0.4072 ps is justified in the following way. As the final states K^+K^- and $\pi^+\pi^-$ are *CP* even, if one ignores *CP* violation, the initial state has to be *CP* even as well. The lifetime difference for *CP*-even and *CP*-odd states is given through the width splitting parameter y_{CP}. In practice, the definition of y_{CP} is

$$y_{CP} = \frac{\tau_{K\pi}}{\tau_{hh}} - 1, \tag{4.44}$$

and then

$$\tau_{hh} = \frac{\tau_{K\pi}}{y_{CP} + 1}. \tag{4.45}$$

Using $\tau = (0.4101 \pm 0.0015)\,\text{ps}$ [26] and $y_{CP} = (0.705 \pm 0.111)\%$, obtained by combining the HFLAV-2016 world average [6] with the latest LHCb result [112], $\tau_{hh} = (0.4072 \pm 0.0016)\,\text{ps}$ is obtained. The presence of secondary D^0 mesons affects

the average lifetime according to

$$\begin{aligned} \langle t_{hh} \rangle^{\pi-\text{tagged}} &= (1 - f_{\text{sec}}^{h^+h^-}) \langle t_{hh} \rangle^{\pi-\text{tagged,corr}} + f_{\text{sec}}^{h^+h^-} \langle t_{hh} \rangle^{\text{sec}} \\ \Rightarrow \langle t_{hh} \rangle^{\pi-\text{tagged,corr}} &= \frac{\langle t_{hh} \rangle^{\pi-\text{tagged}} - f_{\text{sec}}^{h^+h^-} \langle t_{hh} \rangle^{\text{sec}}}{1 - f_{\text{sec}}^{h^+h^-}}, \end{aligned} \tag{4.46}$$

where $\langle t_{hh} \rangle^{\pi-\text{tagged,corr}}$ is the actual average decay time of the prompt decays and $\langle t_{hh} \rangle^{\text{sec}}$ is the average decay time of the secondary decays. The values of $f_{\text{sec}}^{h^+h^-}$ are measured on the full Run-2 sample according to the procedure described in Sec. 4.4.1: $f_{\text{sec}}^{K^+K^-} = (11.57 \pm 0.02)\%$ and $f_{\text{sec}}^{\pi^+\pi^-} = (12.73 \pm 0.05)\%$. The values of $\langle t_{hh} \rangle^{\text{sec}}$ are taken from Ref. [67] and correspond to $\langle t_{KK} \rangle = 1.065\,\text{ps}$ and $\langle t_{\pi\pi} \rangle = 0.971\,\text{ps}$. A systematic uncertainty on $(\Delta \langle t \rangle / \tau)^{\pi-\text{tagged}}$ is assigned by taking the difference between the values of $(\Delta \langle t \rangle / \tau)^{\pi-\text{tagged}}$ with and without the correction due to the presence of secondary D^0 decays, and is equal to 0.0019. In the same way, a systematic uncertainty equal to 0.1 is assigned to $(\overline{\langle t \rangle}/\tau)^{\pi-\text{tagged}}$. The systematic uncertainty due to the uncertainty on τ_{hh} is equal to 0.0005 for $(\Delta \langle t \rangle / \tau)^{\pi-\text{tagged}}$ and 0.0069 for $(\overline{\langle t \rangle}/\tau)^{\pi-\text{tagged}}$.

Combining all these information, the relative difference between the decay times is (from now τ_{hh} is simply referred as τ)

$$\frac{\Delta \langle t \rangle}{\tau}^{\pi-\text{tagged}} = \frac{\langle t_{KK} \rangle^{\pi-\text{tagged}} - \langle t_{\pi\pi} \rangle^{\pi-\text{tagged}}}{\tau} = (13.47 \pm 0.20)\%,$$

while the average is

$$\frac{\overline{\langle t \rangle}}{\tau}^{\pi-\text{tagged}} = \frac{\langle t_{KK} \rangle^{\pi-\text{tagged}} + \langle t_{\pi\pi} \rangle^{\pi-\text{tagged}}}{2\tau} = 1.74 \pm 0.10,$$

where the uncertainties include statistical and systematic contributions.

The same procedure is repeated with the semileptonic sample, and the background-subtracted distributions of decay time for these events are shown in Fig. 4.31. The corresponding average decay times are

$$\begin{aligned} \langle t_{KK} \rangle^{\mu-\text{tagged}} &= (0.49177 \pm 0.00017)\,\text{ps}, \\ \langle t_{\pi\pi} \rangle^{\mu-\text{tagged}} &= (0.49313 \pm 0.00028)\,\text{ps}. \end{aligned}$$

The systematic uncertainty due to the uncertainty on τ is negligible on $(\Delta \langle t \rangle / \tau)^{\mu-\text{tagged}}$ and 0.0048 on $(\overline{\langle t \rangle}/\tau)^{\mu-\text{tagged}}$. Hence the relative decay-time difference is

$$\frac{\Delta \langle t \rangle}{\tau}^{\mu-\text{tagged}} = \frac{\langle t_{KK} \rangle^{\mu-\text{tagged}} - \langle t_{\pi\pi} \rangle^{\mu-\text{tagged}}}{\tau} = (-0.33 \pm 0.08)\%,$$

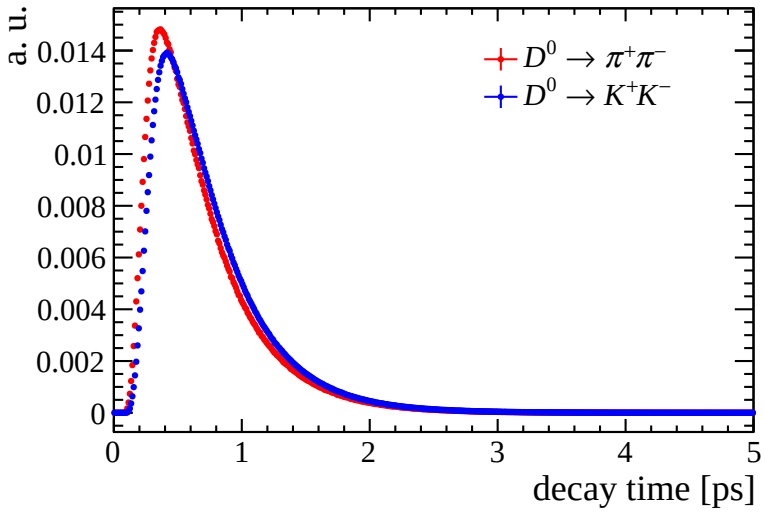

Figure 4.30: Background-subtracted decay-time distributions in the prompt case.

and the average is

$$\frac{\overline{\langle t \rangle}^{\mu-\text{tagged}}}{\tau} = \frac{\langle t_{KK} \rangle^{\mu-\text{tagged}} + \langle t_{\pi\pi} \rangle^{\mu-\text{tagged}}}{2\tau} = 1.209 \pm 0.005,$$

where again the uncertainties include statistical and systematic contributions.

In summary, the following decay-time relative differences and averages are measured to be

$$\begin{aligned}
\frac{\Delta \langle t \rangle^{\pi-\text{tagged}}}{\tau} &= (13.47 \pm 0.20)\%, \\
\frac{\overline{\langle t \rangle}^{\pi-\text{tagged}}}{\tau} &= 1.74 \pm 0.10, \\
\frac{\Delta \langle t \rangle^{\mu-\text{tagged}}}{\tau} &= (-0.33 \pm 0.08)\%, \\
\frac{\overline{\langle t \rangle}^{\mu-\text{tagged}}}{\tau} &= 1.209 \pm 0.005.
\end{aligned}$$

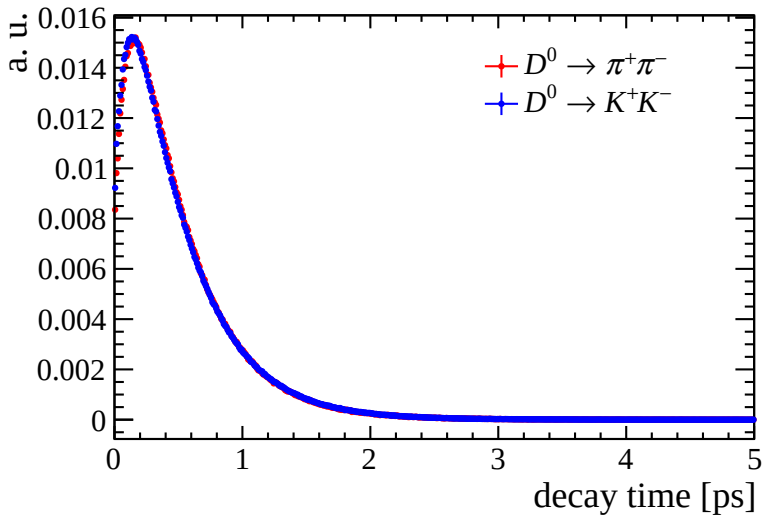

Figure 4.31: Background-subtracted decay-time distributions in the semileptonic case.

4.7 Final results and interpretation

The values of ΔA_{CP} measured with the prompt tag are

$$\begin{aligned}
\Delta A_{CP}^{\text{prompt,2015}} &= (-0.130 \pm 0.142)\%, \\
\Delta A_{CP}^{\text{prompt,2016}} &= (-0.207 \pm 0.061)\%, \\
\Delta A_{CP}^{\text{prompt,2017}} &= (-0.184 \pm 0.057)\%, \\
\Delta A_{CP}^{\text{prompt,2018}} &= (-0.166 \pm 0.056)\%,
\end{aligned}$$

where the uncertainties are statistical only, and their weighted average, now including the systematic uncertainty, is

$$\Delta A_{CP}^{\text{prompt}} = (-0.182 \pm 0.032\ (\text{stat}) \pm 0.009\ (\text{syst}))\%.$$

The values of ΔA_{CP} measured with the semileptonic tag are

$$\begin{aligned}
\Delta A_{CP}^{\text{SL,2016}} &= (-0.173 \pm 0.141)\%, \\
\Delta A_{CP}^{\text{SL,2017}} &= (\ \ 0.046 \pm 0.133)\%, \\
\Delta A_{CP}^{\text{SL,2018}} &= (-0.143 \pm 0.129)\%,
\end{aligned}$$

and the resulting average is

$$\Delta A_{CP}^{\text{SL}} = (-0.088 \pm 0.077\ (\text{stat}) \pm 0.050\ (\text{syst}))\%.$$

Table 4.18: Summary of ΔA_{CP} measurements for the full LHCb data taking.

	Run 1		Run 2	
Tag	**Prompt**	**SL**	**Prompt**	**SL**
$\Delta A_{CP} \times 10^4$	$-10 \pm 8 \pm 3$	$14 \pm 16 \pm 8$	$-18.2 \pm 3.2 \pm 0.9$	$-8.8 \pm 7.7 \pm 5.0$
$\Delta \langle t \rangle / \tau$	0.1153 ± 0.0019	0.014 ± 0.004	0.1347 ± 0.0020	-0.0033 ± 0.0008
$\overline{\langle t \rangle}/\tau$	2.095 ± 0.016	1.075 ± 0.004	1.74 ± 0.10	1.209 ± 0.005

The results are summarised in Table 4.18, along with those obtained from Run-1 analyses [66, 67]. The combination of Run-1 and Run-2 measurements is

$$\Delta A_{CP} = (-15.4 \pm 2.9) \cdot 10^{-4}.$$

The significance of the deviation from zero corresponds to 5.3 standard deviations. This is the first observation of *CP* violation in the decay of a charm hadron.

The effective value for $\Delta \langle t \rangle / \tau$ corresponding to the combination of Run-1 and Run-2 results is obtained by a weighted average of the single values, where the weights are evaluated in terms of the uncertainties on the ΔA_{CP} measurements. In fact, Eq. (1.86) holds for the combination if

$$\Delta A_{CP} = \frac{\sum_i w_i \Delta A_{CP i}}{\sum_i w_i}, \tag{4.47}$$

$$\frac{\Delta \langle t \rangle}{\tau} = \frac{\sum_i w_i (\Delta \langle t \rangle / \tau)_i}{\sum_i w_i}, \tag{4.48}$$

$$\frac{\overline{\langle t \rangle}}{\tau} = \frac{\sum_i w_i (\overline{\langle t \rangle}/\tau)_i}{\sum_i w_i}, \tag{4.49}$$

where $\Delta A_{CP i}$, $(\Delta \langle t \rangle / \tau)_i$ and $(\overline{\langle t \rangle}/\tau)_i$ are the values obtained from the various subsamples and the weights are $w_i = \frac{1}{\sigma_i^2(\Delta A_{CP})}$. The relative difference and the average of the lifetime measured on the Run-1 and Run-2 samples are (the uncertainties are irrelevant for the interpretation of ΔA_{CP} at the current level of precision)

$$\frac{\Delta \langle t \rangle}{\tau} = 0.1155,$$
$$\frac{\overline{\langle t \rangle}}{\tau} = 1.7107.$$

By using the combined Run-1 and Run-2 values of $\Delta \langle t \rangle / \tau(D^0)$ and $\overline{\langle t \rangle}/\tau(D^0)$, along with the LHCb averages $y_{CP} = (5.7 \pm 1.5) \cdot 10^{-3}$ [112,113] and $A_\Gamma = (-2.8 \pm 2.8) \cdot$

10^{-4} [114, 115] – see Eq. (1.86) and the associated footnote – it is possible to derive $\Delta a_{CP}^{\rm dir} = (-15.6 \pm 2.9) \cdot 10^{-4}$, which also shows that, as expected, ΔA_{CP} is primarily sensitive to direct *CP* violation. The overall improvement in precision brought by the present analysis to the knowledge of $\Delta a_{CP}^{\rm dir}$ is apparent when comparing with the value obtained from previous measurements, $\Delta a_{CP}^{\rm dir} = (-13.4 \pm 7.0) \cdot 10^{-4}$ [6].

Conclusions

This thesis presents the measurement of the branching fraction of the $B^0 \to D^{*-}\tau^+\nu_\tau$ decay using for the first time τ-lepton decays to final states with three charged pions, namely $\tau^+ \to 3\pi\overline{\nu}_\tau$ and $\tau^+ \to 3\pi\pi^0\overline{\nu}_\tau$. The analysis has been performed using a data sample collected with the LHCb detector during the LHC Run 1, at the centre-of-mass energies of 7 and 8 TeV, corresponding to an integrated luminosity of $3\,\text{fb}^{-1}$. The result is

$$\mathcal{B}(B^0 \to D^{*-}\tau^+\nu_\tau) = (1.42 \pm 0.094 \pm 0.129 \pm 0.054)\%,$$

where the first uncertainty is statistical, the second systematic and the third due to the knowledge of the branching fraction of the decay used as a normalisation, $B^0 \to D^{*-}3\pi$. By taking the ratio between $\mathcal{B}(B^0 \to D^{*-}\tau^+\nu_\tau)$ and $\mathcal{B}(B^0 \to D^{*-}\mu^+\nu_\mu)$, the value of $\mathcal{R}(D^*) \equiv \mathcal{B}(B^0 \to D^{*-}\tau^+\nu_\tau)/\mathcal{B}(B^0 \to D^{*-}\ell^+\nu_\ell)$, which represents an important test of lepton-flavour universality, is then determined to be

$$\mathcal{R}(D^*) = 0.291 \pm 0.019 \pm 0.026 \pm 0.013,$$

corresponding to one of the most precise single measurements of this quantity and to the first performed with the three-prong decay of the τ lepton. The same convention as for the $\mathcal{B}(B^0 \to D^{*-}\tau^+\nu_\tau)$ result is followed for the three uncertainties. The result is compatible with previous determinations and with the Standard Model expectation. When combining this result with those already existing for $\mathcal{R}(D)$ and $\mathcal{R}(D^*)$, depending on the theoretical prediction, a discrepancy of at least 3.6 standard deviations is found with respect to the Standard Model.

A second, independent measurement is the main subject of the thesis. This is on the difference between the *CP* asymmetries in $D^0 \to K^+K^-$ and $D^0 \to \pi^+\pi^-$ decays, performed using data collected by LHCb during the LHC Run 2 at a centre-of-mass energy of 13 TeV, corresponding to an integrated luminosity of $6\,\text{fb}^{-1}$. The measured value of $\Delta A_{CP} \equiv A_{CP}(K^+K^-) - A_{CP}(\pi^+\pi^-)$, obtained by reconstructing D^0 mesons

originating from prompt $D^{*+} \to D^0\pi^+$ decays or from semileptonic $B \to D^0\mu\nu X$ decays, are

$$\Delta A_{CP}^{\text{prompt}} = (-18.2 \pm 3.2 \pm 0.9) \cdot 10^{-4},$$
$$\Delta A_{CP}^{\text{semileptonic}} = (-8.8 \pm 7.7 \pm 5.0) \cdot 10^{-4},$$

where the first uncertainties are statistical and the second systematic. The average of the two results is

$$\Delta A_{CP} = (-17.1 \pm 3.0 \pm 1.0) \cdot 10^{-4},$$

representing the most sensitive search for direct *CP* violation in the charm sector to date. By combining with previous LHCb measurements based on Run-1 data, the value of ΔA_{CP} results to be

$$\Delta A_{CP} = (-15.4 \pm 2.9) \cdot 10^{-4},$$

which differs from zero by 5.3 standard deviations. This is the first observation of *CP* violation in the decay of a charm hadron. As the value of ΔA_{CP} is mostly sensitive to direct *CP* violation, this ΔA_{CP} average can be translated with small corrections to $\Delta A_{CP}^{\text{dir}} \equiv A_{CP}^{\text{dir}}(K^+K^-) - A_{CP}^{\text{dir}}(\pi^+\pi^-) = (-15.6 \pm 2.9) \cdot 10^{-4}$, where $A_{CP}^{\text{dir}}(K^+K^-)$ and $A_{CP}^{\text{dir}}(\pi^+\pi^-)$ parameterise direct *CP* violation in the respective D^0 decay modes.

The result on $\mathcal{R}(D^*)$ led already to two distinct publications [102, 103], whereas a paper on the measurement of ΔA_{CP} is planned to be published in March 2019.

Appendix A

Kinematic distributions before and after the weighting

A.1 Prompt case

The distributions of p and p_{T} of the D^* meson, before and after weighting, are shown in Fig. A.1. Figures A.2–A.3 report the distributions of the pseudorapidity, azimuthal angle, p and p_{T} of the soft pion.

A.2 Semileptonic case

The comparison of the distributions of p and p_{T} of the D^0 before and after weighting is shown in Fig. A.4. The distributions of pseudorapidity, azimuthal angle, p and p_{T} of the μ are reported in Figs. A.5–A.6.

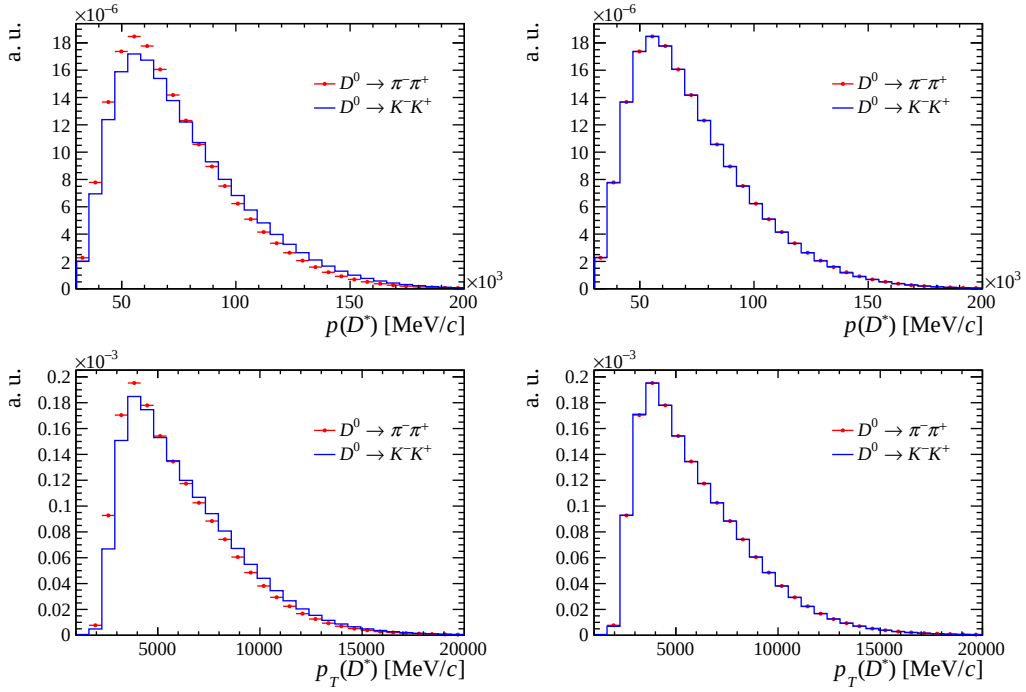

Figure A.1: Distributions of p and p_{T} of the D^* meson for $D^0 \to K^+K^-$ and $D^0 \to \pi^+\pi^-$ candidates, (left) before and (right) after weighting, for the prompt mode.

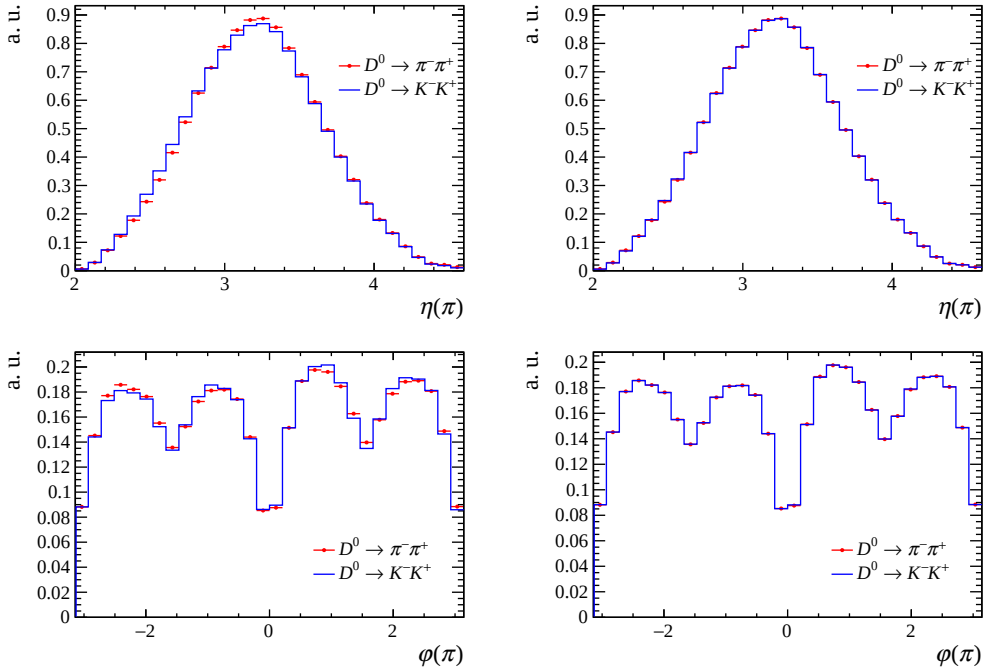

Figure A.2: Distributions of η and φ of the soft pion for $D^0 \to K^+K^-$ and $D^0 \to \pi^+\pi^-$ candidates, (left) before and (right) after weighting, for the prompt mode.

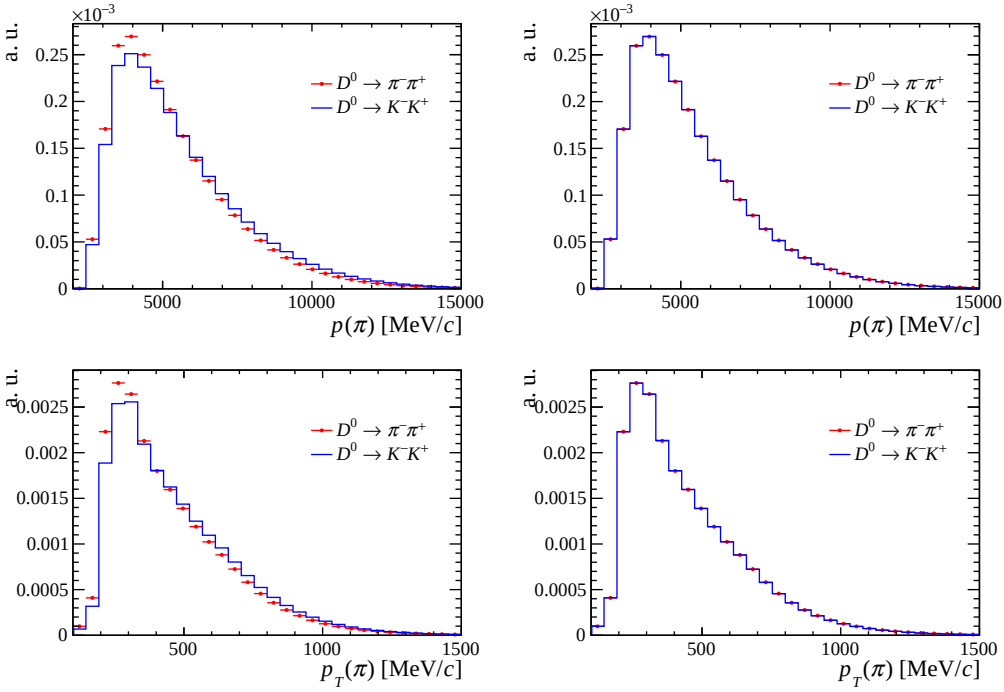

Figure A.3: Distributions of p and p_{T} of the soft pion for $D^0 \to K^+K^-$ and $D^0 \to \pi^+\pi^-$ candidates, (left) before and (right) after weighting, for the prompt mode.

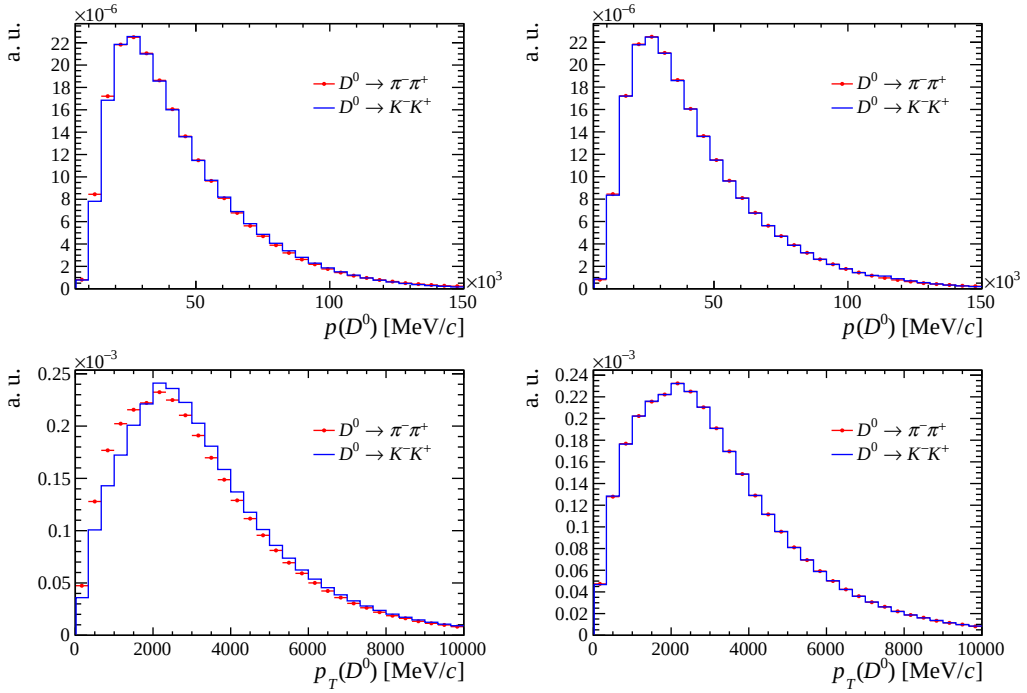

Figure A.4: Comparison of p and p_{T} of the D^0 meson between $D^0 \to K^+K^-$ and $D^0 \to \pi^+\pi^-$ candidates (left) before and (right) after weighting, for the semileptonic mode.

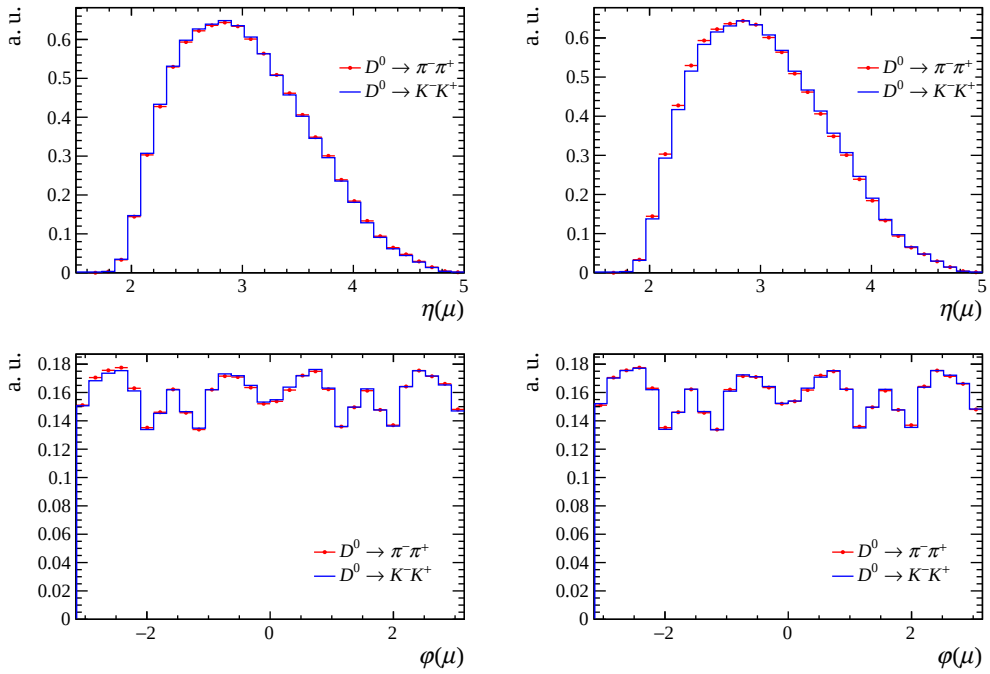

Figure A.5: Comparison of η and φ of the muon between $D^0 \to K^+K^-$ and $D^0 \to \pi^+\pi^-$ candidates (left) before and (right) after weighting, for the semileptonic mode.

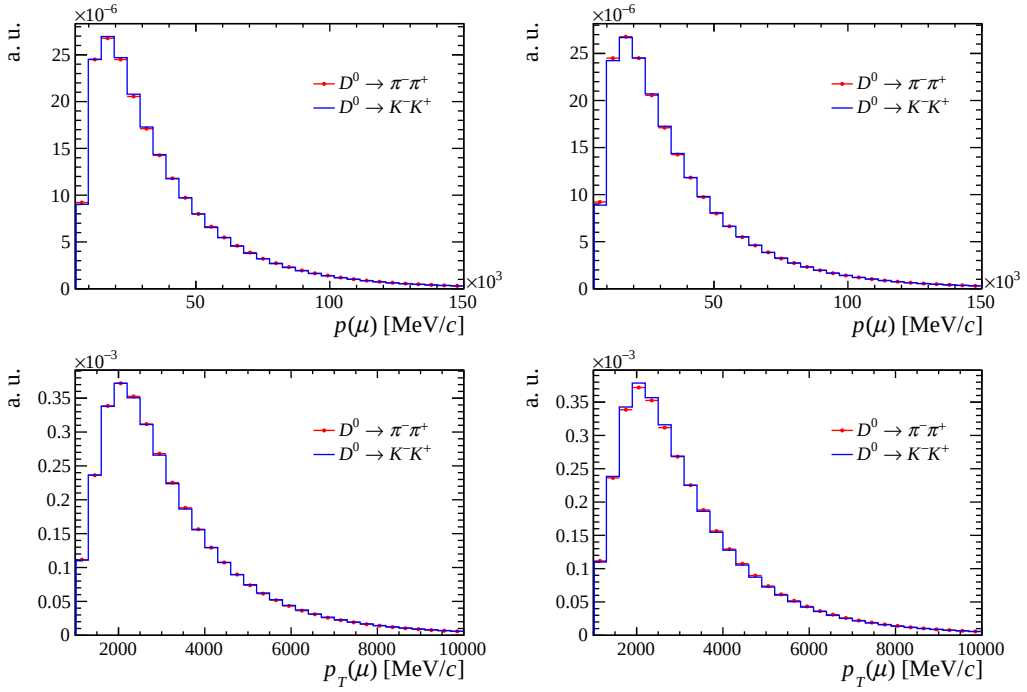

Figure A.6: Comparison of p and p_{T} of the muon between $D^0 \to K^+K^-$ and $D^0 \to \pi^+\pi^-$ candidates (left) before and (right) after weighting, for the semileptonic mode.

Appendix B

Plots of fits

In this Appendix the result of all the baseline fits are shown.

B.1 Prompt case

In Figs. B.1–B.6 the D^* invariant mass distributions with the results of the fits overlaid are shown for the 2015, 2016 and 2017 data sample.

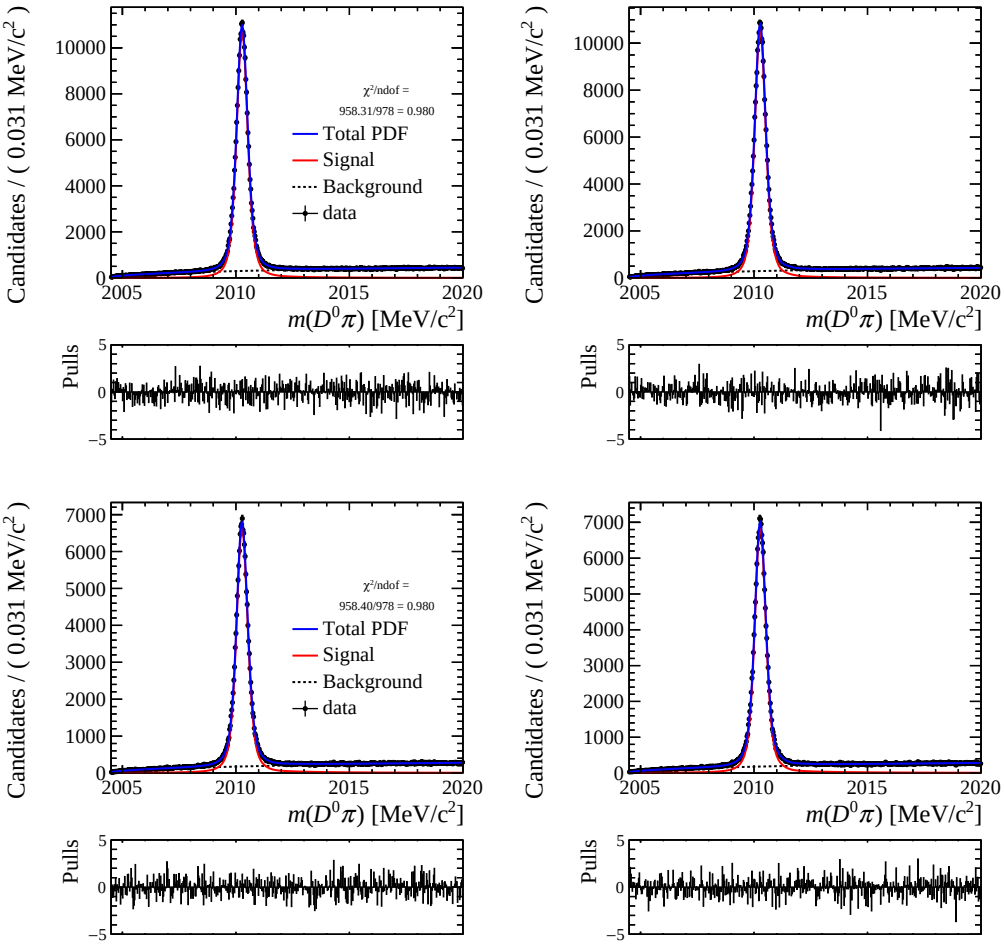

Figure B.1: Invariant-mass distributions of 2015 prompt $D^0 \to \pi^+\pi^-$ events for (top left) positively tagged *MagDown* events, (top right) negatively tagged *MagDown* events, (bottom left) positively tagged *MagUp* events and (bottom right) negatively tagged *MagUp* sample. The result of the fit is overlaid.

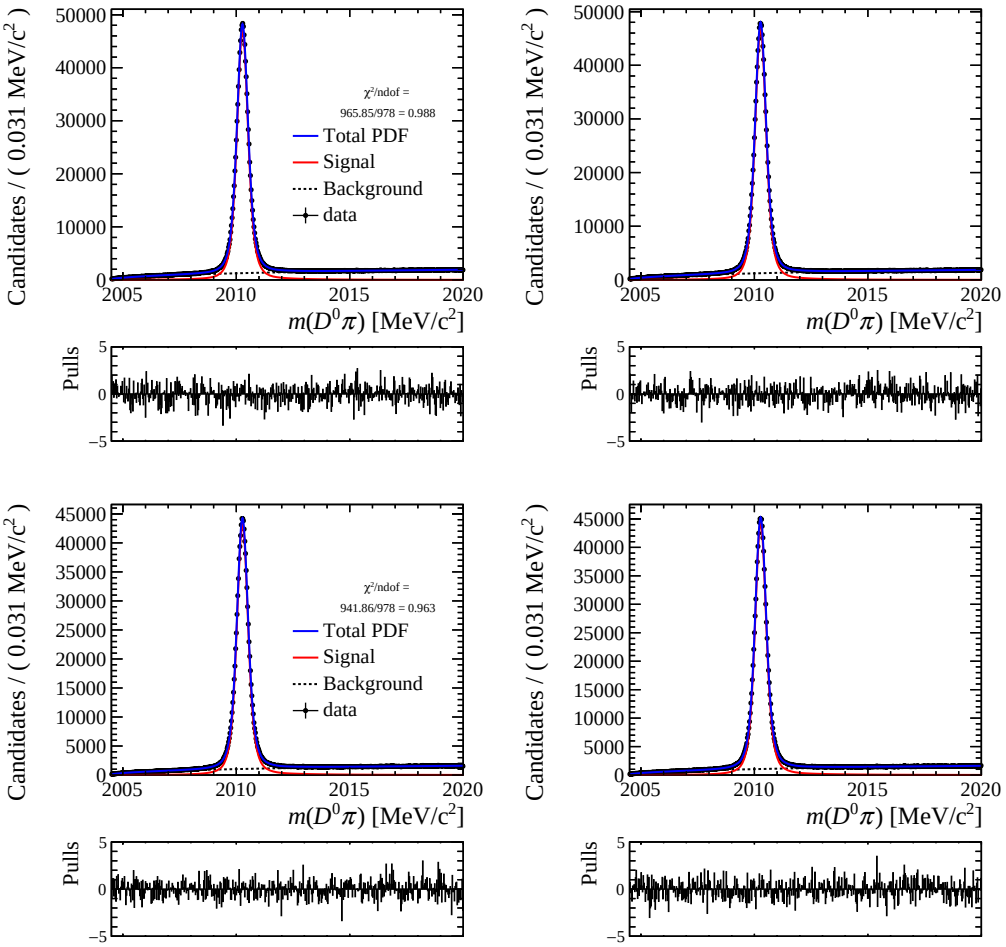

Figure B.2: Invariant-mass distributions of 2016 prompt $D^0 \to \pi^+\pi^-$ events for (top left) positively tagged *MagDown* events, (top right) negatively tagged *MagDown* events, (bottom left) positively tagged *MagUp* events and (bottom right) negatively tagged *MagUp* sample. The result of the fit is overlaid.

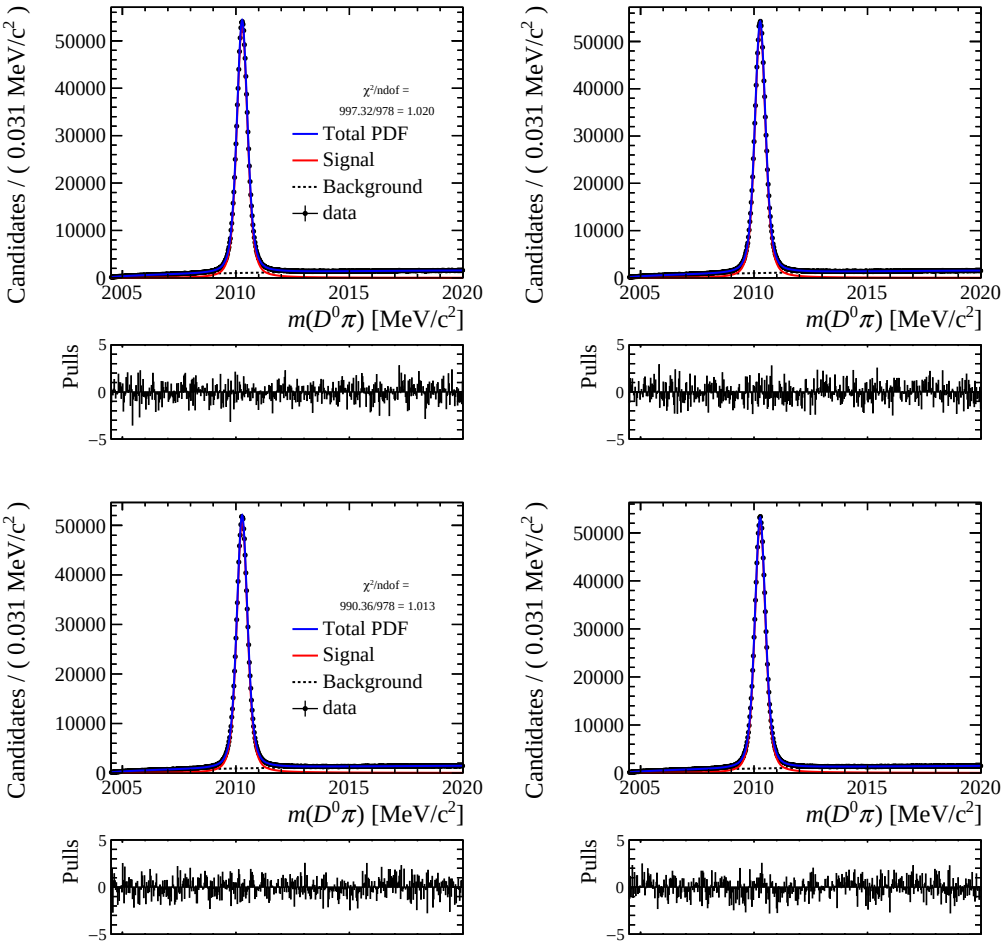

Figure B.3: Invariant-mass distributions of 2017 prompt $D^0 \to \pi^+\pi^-$ events for (top left) positively tagged *MagDown* events, (top right) negatively tagged *MagDown* events, (bottom left) positively tagged *MagUp* events and (bottom right) negatively tagged *MagUp* sample. The result of the fit is overlaid.

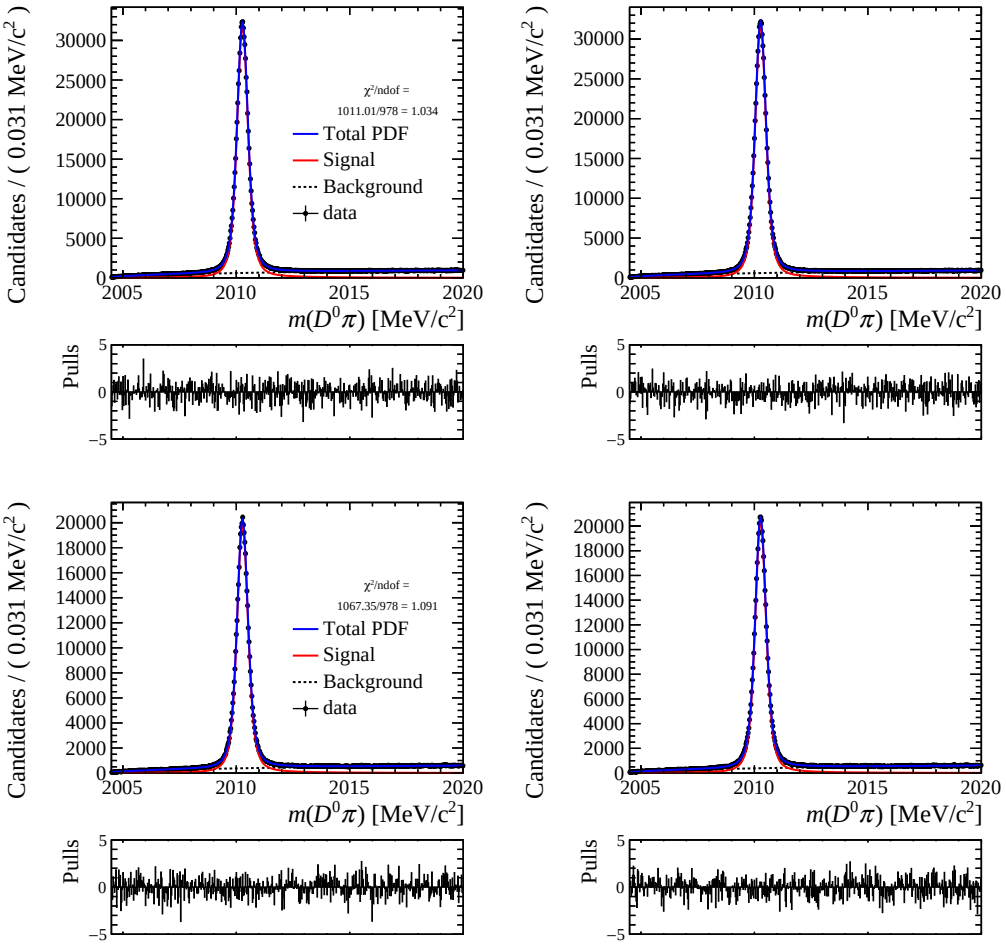

Figure B.4: Invariant-mass distributions of 2015 prompt $D^0 \to K^+K^-$ events for (top left) positively tagged *MagDown* events, (top right) negatively tagged *MagDown* events, (bottom left) positively tagged *MagUp* events and (bottom right) negatively tagged *MagUp* sample. The result of the fit is overlaid.

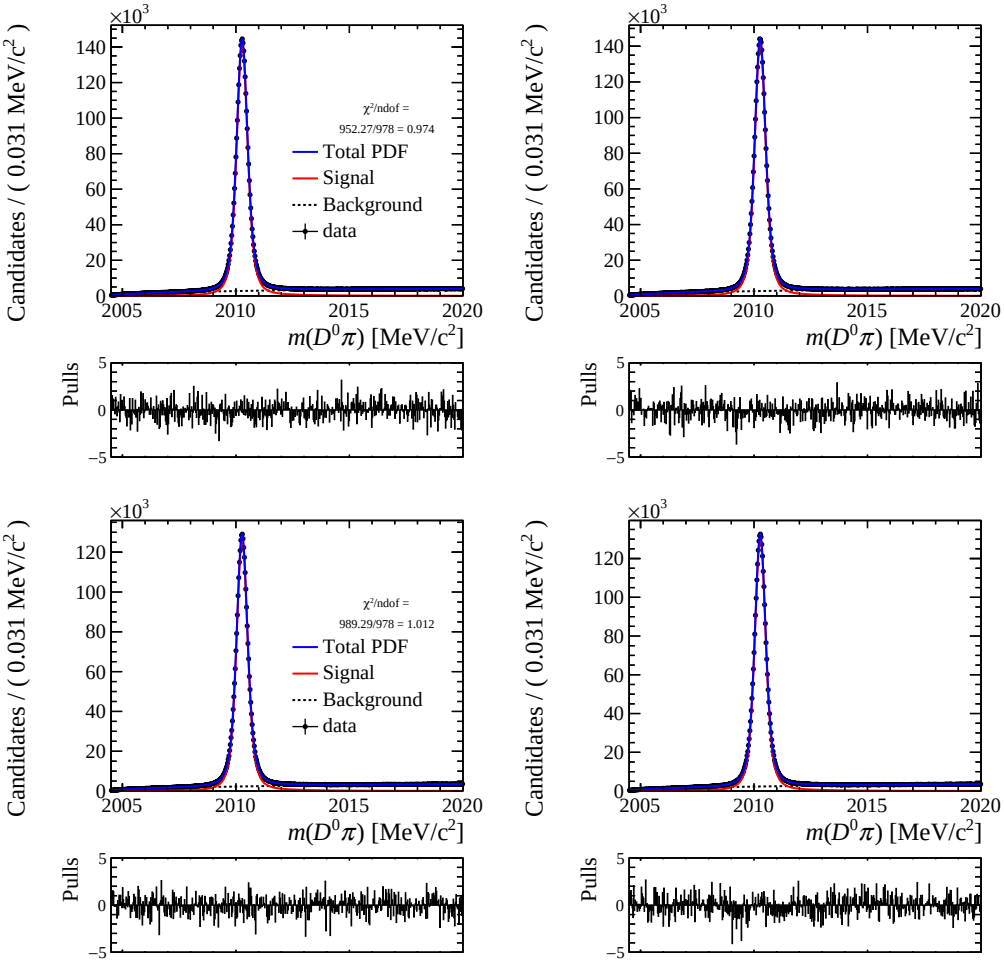

Figure B.5: Invariant-mass distributions of 2016 prompt $D^0 \to K^+K^-$ events for (top left) positively tagged *MagDown* events, (top right) negatively tagged *MagDown* events, (bottom left) positively tagged *MagUp* events and (bottom right) negatively tagged *MagUp* sample. The result of the fit is overlaid.

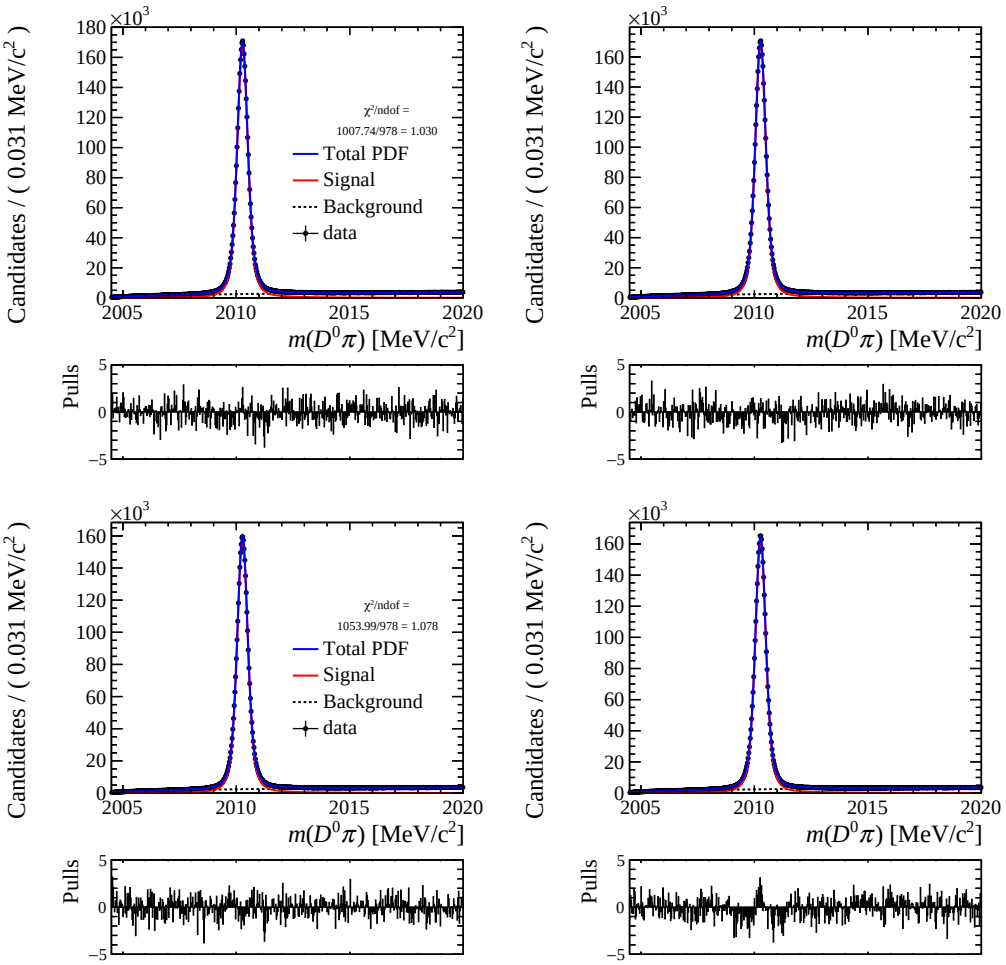

Figure B.6: Invariant-mass distributions of 2017 prompt $D^0 \to K^+K^-$ events for (top left) positively tagged *MagDown* events, (top right) negatively tagged *MagDown* events, (bottom left) positively tagged *MagUp* events and (bottom right) negatively tagged *MagUp* sample. The result of the fit is overlaid.

B.2 Semileptonic case

In Figs. B.7–B.10 the D^0 invariant mass distributions with the results of the fits overlaid are shown for the 2016 and 2017 data sample.

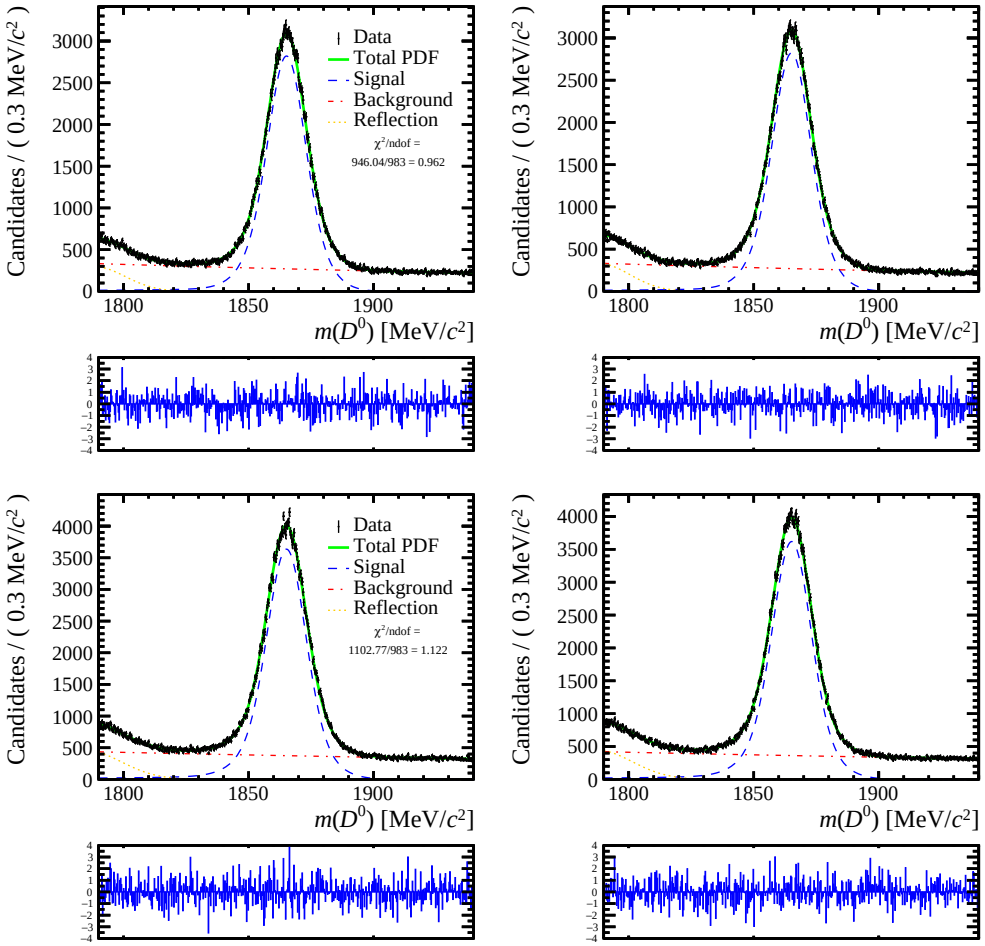

Figure B.7: Invariant-mass distributions for semileptonic $D^0 \to \pi^+\pi^-$ sample for (top left) positively tagged 2016 *MagDown* events, (top right) negatively tagged 2016 *MagDown* sample, (bottom left) positively tagged 2016 *MagUp* events and (bottom right) negatively tagged 2016 *MagUp* sample. The result of the fit is overlaid.

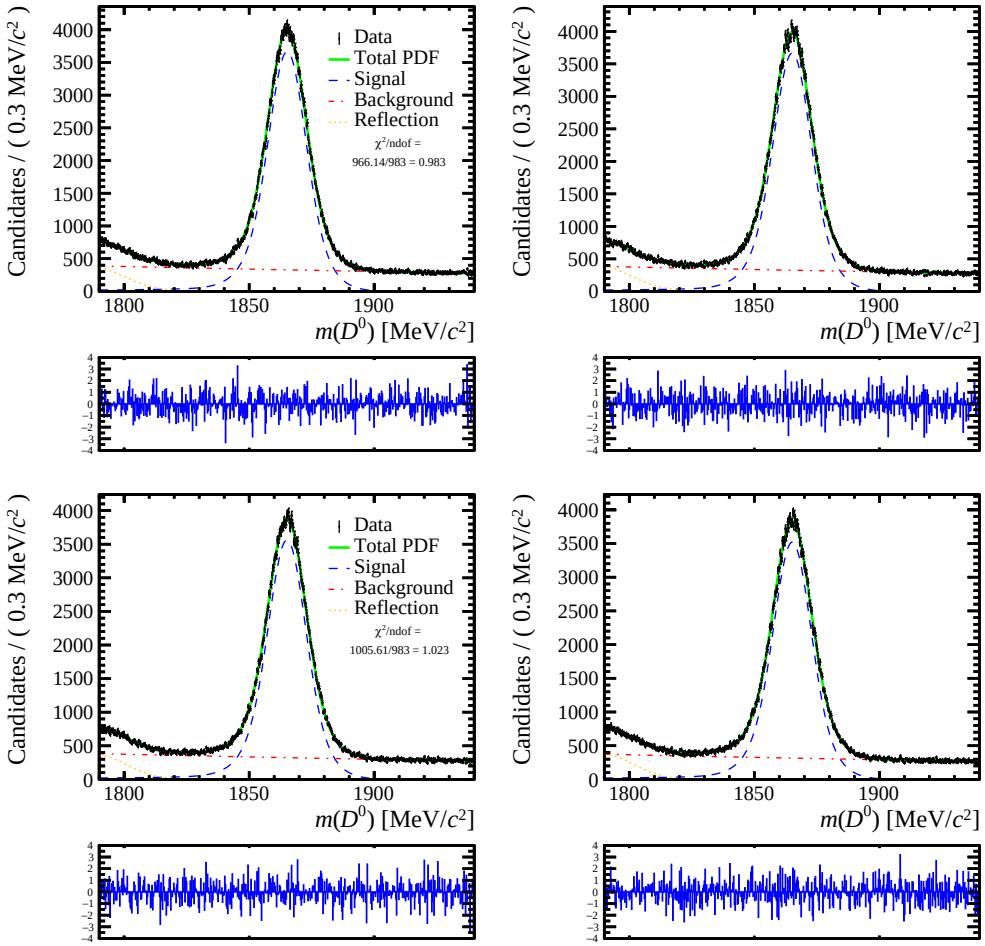

Figure B.8: Invariant-mass distributions for semileptonic $D^0 \to \pi^+\pi^-$ sample for (top left) positively tagged 2017 *MagDown* events, (top right) negatively tagged 2017 *MagDown* sample, (bottom left) positively tagged 2017 *MagUp* events and (bottom right) negatively tagged 2017 *MagUp* sample. The result of the fit is overlaid.

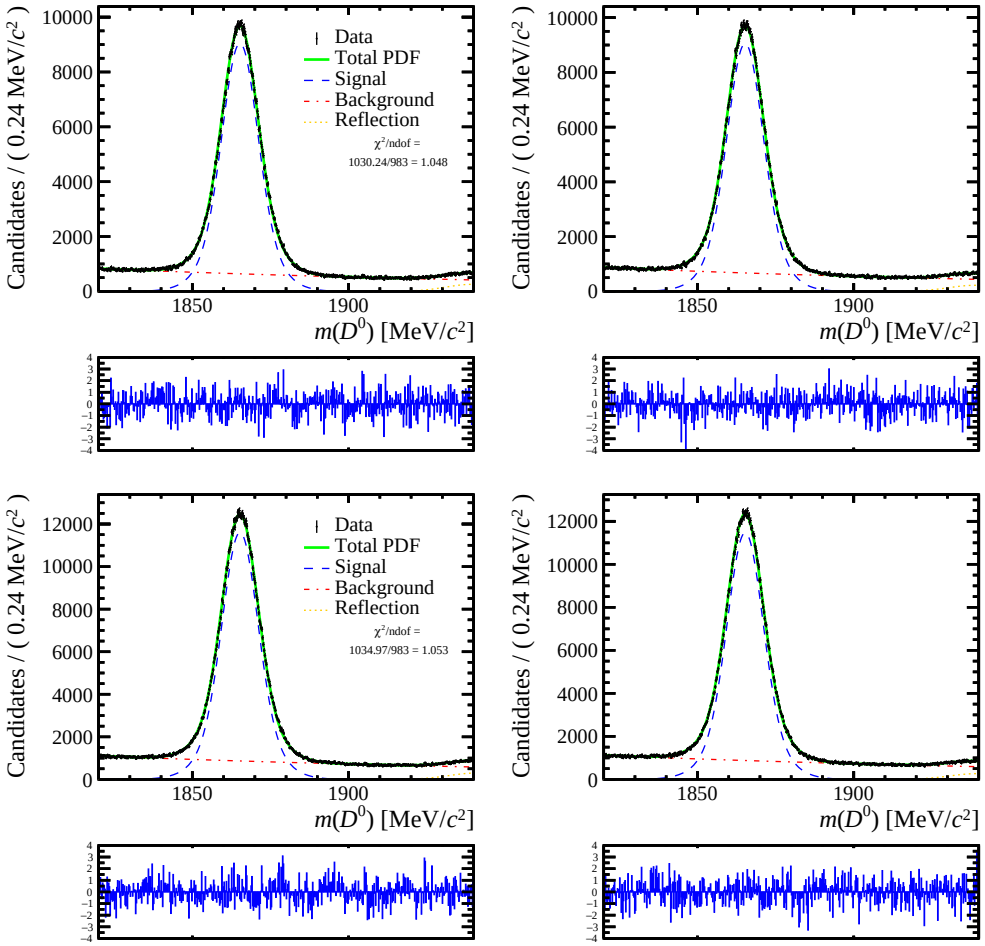

Figure B.9: Invariant-mass distributions for semileptonic $D^0 \to K^+K^-$ sample for (top left) positively tagged 2016 *MagDown* events, (top right) negatively tagged 2016 *MagDown* sample, (bottom left) positively tagged 2016 *MagUp* events and (bottom right) negatively tagged 2016 *MagUp* sample. The result of the fit is overlaid.

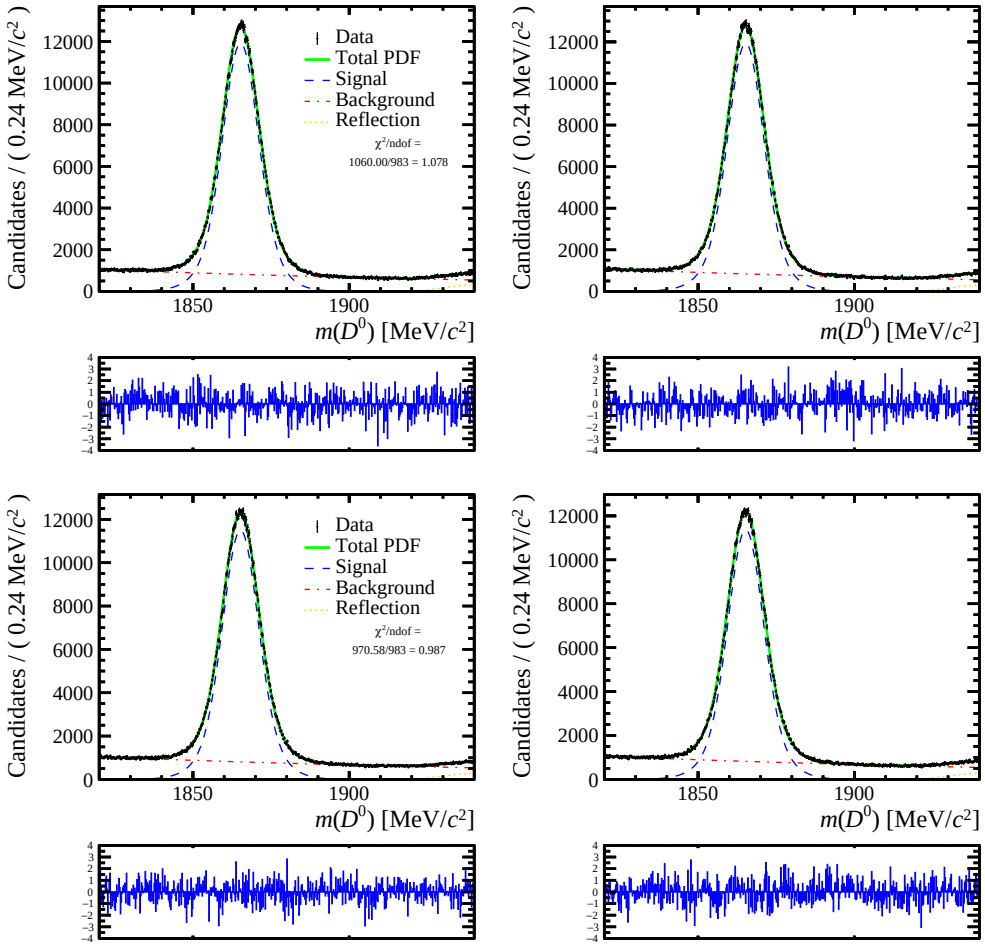

Figure B.10: Invariant-mass distributions for semileptonic $D^0 \to K^+K^-$ sample for (top left) positively tagged 2017 *MagDown* events, (top right) negatively tagged 2017 *MagDown* sample, (bottom left) positively tagged 2017 *MagUp* events and (bottom right) negatively tagged 2017 *MagUp* sample. The result of the fit is overlaid.

Appendix C

Raw asymmetries as a function of variables and data-taking period

Here various plots showing the values of ΔA_{CP} in bins of kinematic and geometrical variables are reported, to study the stability of the measurement.

C.1 Prompt case

To investigate whether there are any variations of ΔA_{CP} over the running period, the data sample is divided into blocks of runs, and ΔA_{CP} is measured in each block. The result is reported in Fig. C.1.

In Figs. C.2-C.7 similar plots, but a as a function of the relevant kinematic and geometrical variables, are shown, namely: the number of PVs, the number of hits in the SPD detector, the soft pion ghost track probability, the azimuthal angle of the D^0 meson and the soft pion, the D^0-meson lifetime, the $\chi^2_{\rm IP}$ of the D^0 meson and the soft pion, the χ^2 of the common vertex between the D^0 meson and the soft pion, the transverse momentum of the D^0 meson and the soft pion, the soft pion momentum along z, the D^0-meson flight distance and the pseudorapidity of the D^0 meson and the soft pion. On each plot the χ^2/ndf and $p-$value obtained by the comparison with the baseline Run–2 ΔA_{CP} value, represented by a flat line, are reported. This study shows an excellent stability of ΔA_{CP} and no significant deviations from flatness.

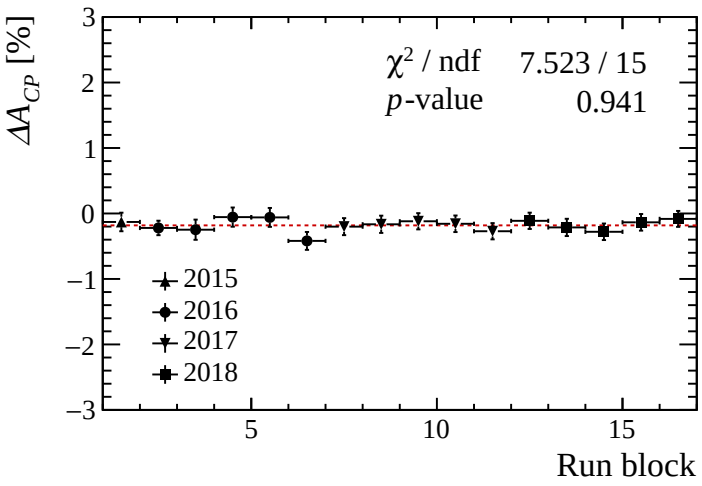

Figure C.1: ΔA_{CP} as a function of run blocks for the prompt case.

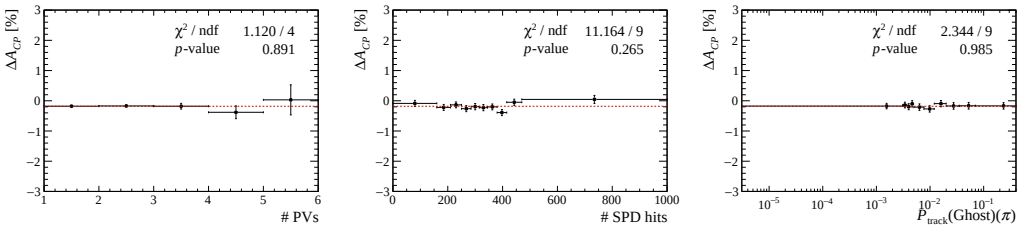

Figure C.2: ΔA_{CP} as a function of (left) number of PVs, (centre) number of SPD hits and (right) soft pion ghost track probability, for the prompt case.

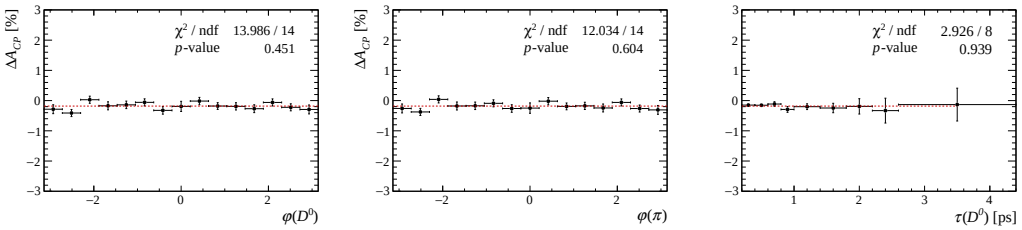

Figure C.3: ΔA_{CP} as a function of (left) D^0 azimuthal angle, (centre) soft pion azimuthal angle and (right) D^0 lifetime, for the prompt case.

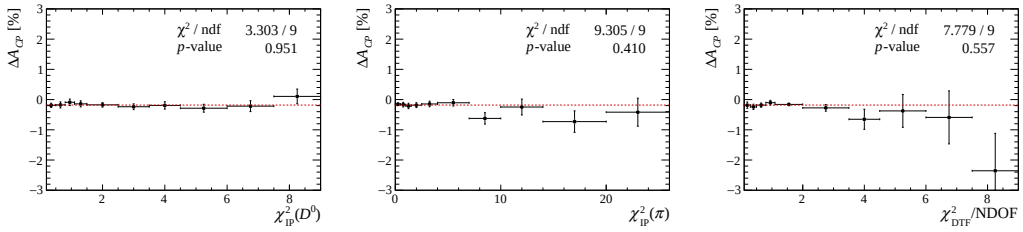

Figure C.4: ΔA_{CP} as a function of (left) D^0 $\chi^2_{\rm IP}$, (centre) soft pion $\chi^2_{\rm IP}$ and (right) $\chi^2_{\rm vtx}$/ndf between D^0 and soft pion, for the prompt case.

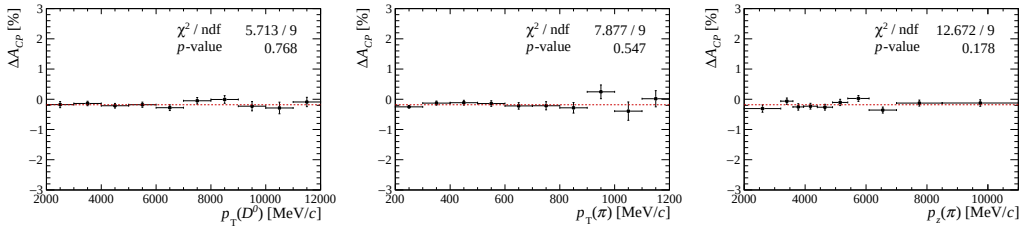

Figure C.5: ΔA_{CP} as a function of (left) D^0 transverse momentum, (centre) soft pion transverse momentum and (right) soft pion momentum along z, for the prompt case.

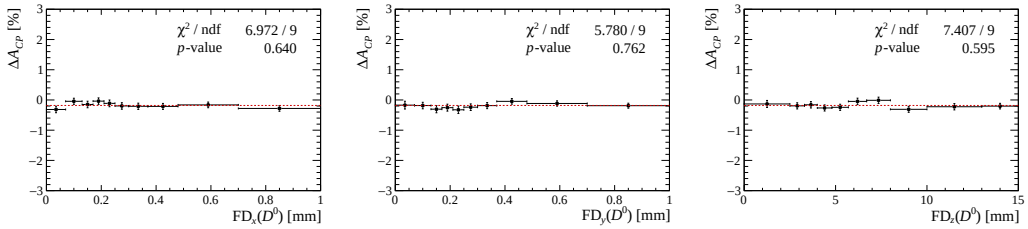

Figure C.6: ΔA_{CP} as a function of D^0 flight distance along (left) x, (centre) y and (right) z, for the prompt case.

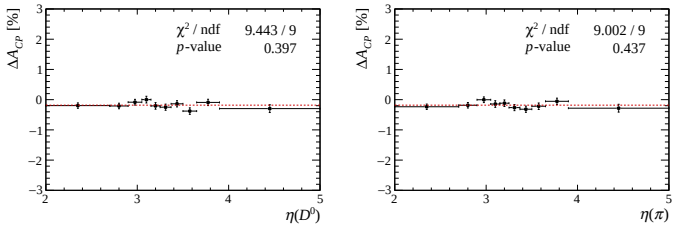

Figure C.7: ΔA_{CP} as a function of (left) D^0 pseudorapidity and (right) soft pion pseudorapidity, for the prompt case.

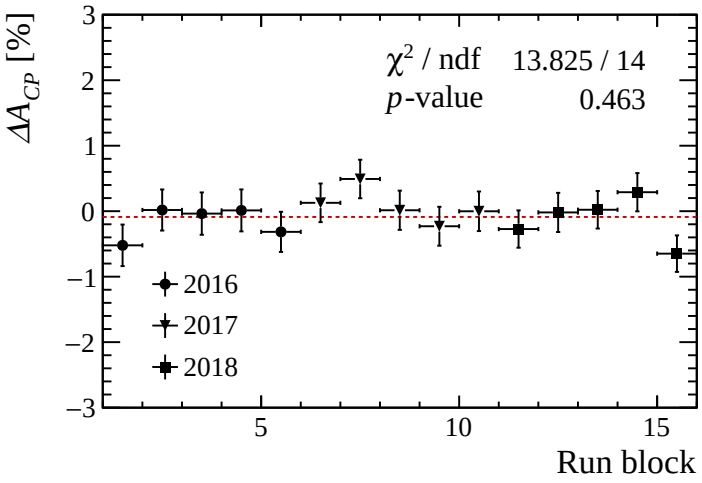

Figure C.8: ΔA_{CP} as a function of run blocks for the semileptonic case.

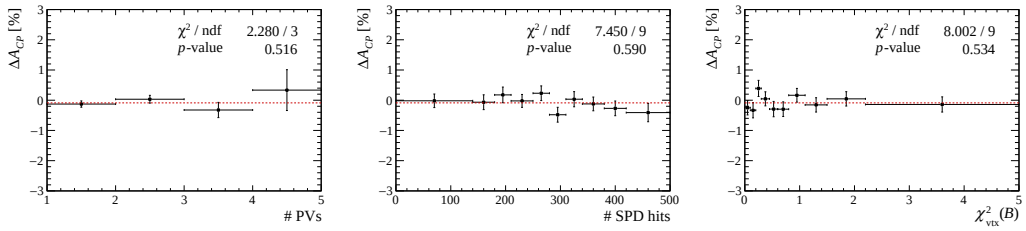

Figure C.9: ΔA_{CP} as a function of (left) number of PVs, (centre) number of SPD hits and (right) $\chi^2_{\rm vtx}$/ndf between D^0 and muon, for the semileptonic case.

C.2 Semileptonic case

Stability checks are performed on the semileptonic sample too. The values of ΔA_{CP} are measured in bins of: blocks of runs, the number of PVs, the number of SPD hits, the χ^2 of the common vertex between the D^0 meson and the muon, the $\chi^2_{\rm IP}$ of the D^0 meson and muon, the B flight distance, the azimuthal angle of the D^0 meson and muon, the lifetime of the D^0 meson, the pseudorapidity of the D^0 meson and muon and the transverse momentum of the D^0 meson and muon. The results are shown in Figs. C.8-C.13. Like in the prompt case, this study shows an excellent stability of ΔA_{CP} and no significant deviations from flatness.

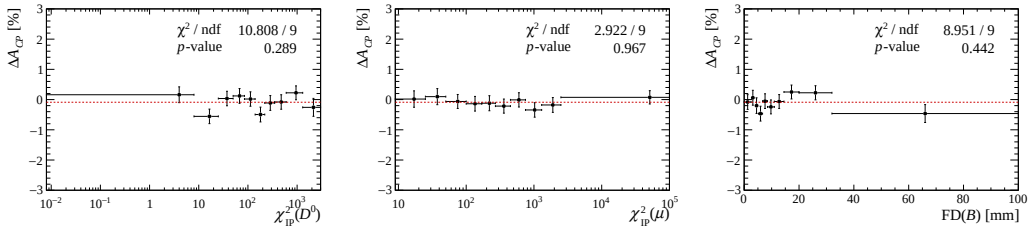

Figure C.10: ΔA_{CP} as a function of (left) D^0 χ^2_{IP}, (centre) muon χ^2_{IP} and (right) B flight distance, for the semileptonic case.

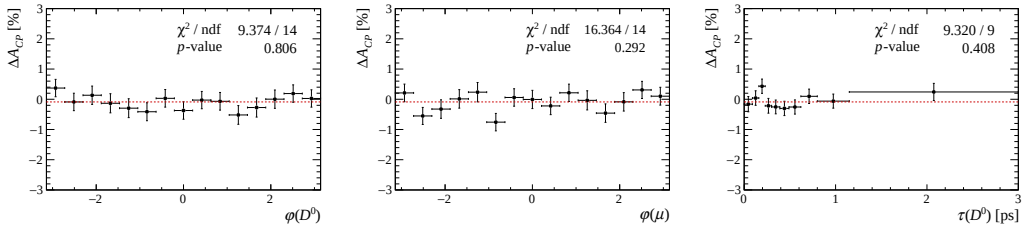

Figure C.11: ΔA_{CP} as a function of (left) D^0 azimuthal angle, (centre) muon azimuthal angle and (right) D^0 lifetime, for the semileptonic case.

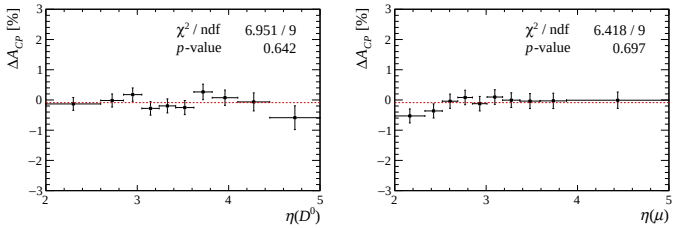

Figure C.12: ΔA_{CP} as a function of (left) D^0 pseudorapidity and (right) muon pseudorapidity, for the semileptonic case.

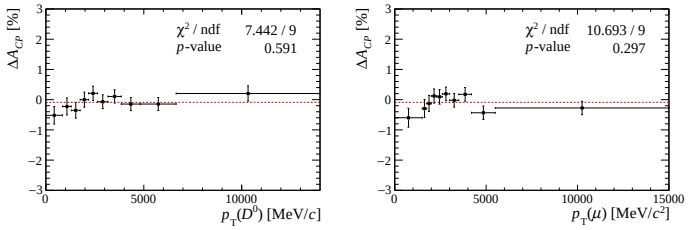

Figure C.13: ΔA_{CP} as a function of (left) D^0 transverse momentum and (right) muon transverse momentum, for the semileptonic case.

Bibliography

[1] LHCb collaboration, R. Aaij *et al.*, *Differential branching fractions and isospin asymmetries of $B \to K^* \mu^+ \mu^-$ decays*, JHEP **06** (2014) 133, arXiv:1403.8044.

[2] LHCb collaboration, R. Aaij *et al.*, *Angular analysis and differential branching fraction of the decay $B_s^0 \to \phi \mu^+ \mu^-$*, JHEP **09** (2015) 179, arXiv:1506.08777.

[3] LHCb collaboration, R. Aaij *et al.*, *Angular analysis of the $B^0 \to K^{*0} \mu^+ \mu^-$ decay using $3\,fb^{-1}$ of integrated luminosity*, JHEP **02** (2016) 104, arXiv:1512.04442.

[4] Belle collaboration, S. Wehle *et al.*, *Lepton-flavor-dependent angular analysis of $B \to K^* \ell^+ \ell^-$*, Phys. Rev. Lett. **118** (2017) 111801, arXiv:1612.05014.

[5] LHCb collaboration, R. Aaij *et al.*, *Test of lepton universality using $B^+ \to K^+ \ell^+ \ell^-$ decays*, Phys. Rev. Lett. **113** (2014) 151601, arXiv:1406.6482.

[6] Heavy Flavor Averaging Group, Y. Amhis *et al.*, *Averages of b-hadron, c-hadron, and τ-lepton properties as of summer 2016*, arXiv:1612.07233, updated results and plots available at http://www.slac.stanford.edu/xorg/hflav/.

[7] Y. Grossman, A. L. Kagan, and Y. Nir, *New physics and CP violation in singly Cabibbo suppressed D decays*, Phys. Rev. **D75** (2007) 036008, arXiv:hep-ph/0609178.

[8] A. A. Petrov, *Implications of CP violation in charmed hadrons*, J. Phys. Conf. Ser. **556** (2014) 012057.

[9] P. Santorelli, *CP violation in nonleptonic two-body decays of D mesons*, PoS **CHARM2016** (2017) 019.

[10] A. Khodjamirian and A. A. Petrov, *Direct CP asymmetry in $D \to \pi^-\pi^+$ and $D \to K^-K^+$ in QCD-based approach*, Phys. Lett. **B774** (2017) 235, arXiv:1706.07780.

[11] A. Salam, *Weak and electromagnetic interactions*, Conf. Proc. **C680519** (1968) 367.

[12] S. Weinberg, *A model of leptons*, Phys. Rev. Lett. **19** (1967) 1264.

[13] S. L. Glashow, *Partial symmetries of weak interactions*, Nucl. Phys. **22** (1961) 579.

[14] F. Englert and R. Brout, *Broken symmetry and the mass of gauge vector mesons*, Phys. Rev. Lett. **13** (1964) 321.

[15] P. W. Higgs, *Broken symmetries and the masses of gauge bosons*, Phys. Rev. Lett. **13** (1964) 508.

[16] MINOS, D. G. Michael *et al.*, *Observation of muon neutrino disappearance with the MINOS detectors and the NuMI neutrino beam*, Phys. Rev. Lett. **97** (2006) 191801, arXiv:hep-ex/0607088.

[17] MINOS, P. Adamson *et al.*, *Measurement of neutrino nscillations with the MINOS detectors in the NuMI beam*, Phys. Rev. Lett. **101** (2008) 131802, arXiv:0806.2237.

[18] MINOS, P. Adamson *et al.*, *Measurement of the neutrino mass splitting and flavor mixing by MINOS*, Phys. Rev. Lett. **106** (2011) 181801, arXiv:1103.0340.

[19] T2K, K. Abe *et al.*, *First muon-neutrino disappearance study with an off-axis beam*, Phys. Rev. **D85** (2012) 031103, arXiv:1201.1386.

[20] T2K, K. Abe *et al.*, *Measurement of neutrino oscillation parameters from muon neutrino disappearance with an off-axis beam*, Phys. Rev. Lett. **111** (2013) 211803, arXiv:1308.0465.

[21] Super-Kamiokande, K. Abe *et al.*, *Evidence for the appearance of atmospheric tau neutrinos in Super-Kamiokande*, Phys. Rev. Lett. **110** (2013) 181802, arXiv:1206.0328.

[22] OPERA, N. Agafonova *et al.*, *Final results of the OPERA experiment on ν_τ appearance in the CNGS neutrino beam*, Phys. Rev. Lett. **120** (2018) 211801, arXiv:1804.04912, [Erratum: Phys. Rev. Lett.121,no.13,139901(2018)].

[23] N. Cabibbo, *Unitary symmetry and leptonic decays*, Phys. Rev. Lett. **10** (1963) 531.

[24] M. Kobayashi and T. Maskawa, *CP violation in the renormalizable theory of weak interaction*, Prog. Theor. Phys. **49** (1973) 652.

[25] L. Wolfenstein, *Parametrization of the Kobayashi-Maskawa matrix*, Phys. Rev. Lett. **51** (1983) 1945.

[26] Particle Data Group, M. Tanabashi *et al.*, *Review of particle physics*, Phys. Rev. **D98** (2018) 030001.

[27] S. L. Glashow, J. Iliopoulos, and L. Maiani, *Weak interactions with lepton-hadron symmetry*, Phys. Rev. **D2** (1970) 1285.

[28] K. G. Wilson, *Confinement of quarks*, Phys. Rev. **D10** (1974) 2445.

[29] E. Eichten and B. R. Hill, *An effective field theory for the calculation of matrix elements involving heavy quarks*, Phys. Lett. **B234** (1990) 511.

[30] H. Georgi, *An effective field theory for heavy quarks at low energies*, Phys. Lett. **B240** (1990) 447.

[31] B. Grinstein, *The static quark effective theory*, Nucl. Phys. **B339** (1990) 253.

[32] T. Mannel, W. Roberts, and Z. Ryzak, *A derivation of the heavy quark effective Lagrangian from QCD*, Nucl. Phys. **B368** (1992) 204.

[33] I. I. Balitsky, V. M. Braun, and A. V. Kolesnichenko, *Radiative decay $\Sigma^+ \to p\gamma$ in quantum chromodynamics*, Nucl. Phys. **B312** (1989) 509.

[34] V. M. Braun and I. E. Filyanov, *QCD sum rules in exclusive kinematics and pion wave function*, Z. Phys. **C44** (1989) 157.

[35] V. L. Chernyak and I. R. Zhitnitsky, *B meson exclusive decays into baryons*, Nucl. Phys. **B345** (1990) 137.

[36] P. Ball, V. M. Braun, and H. G. Dosch, *Form-factors of semileptonic D decays from QCD sum rules*, Phys. Rev. **D44** (1991) 3567.

[37] DELPHI, OPAL, LEP Electroweak, ALEPH, L3, S. Schael *et al.*, *Electroweak measurements in electron-positron collisions at W-boson-pair energies at LEP*, Phys. Rept. **532** (2013) 119, arXiv:1302.3415.

[38] S. Fajfer, J. F. Kamenik, and I. Nisandzic, *On the $B \to D^* \tau \bar{\nu}_\tau$ sensitivity to new physics*, Phys. Rev. **D85** (2012) 094025, arXiv:1203.2654.

[39] N. Isgur and M. B. Wise, *Weak decays of heavy mesons in the static quark approximation*, Phys. Lett. **B232** (1989) 113.

[40] N. Isgur and M. B. Wise, *Weak transition form-factors between heavy mesons*, Phys. Lett. **B237** (1990) 527.

[41] I. Caprini, L. Lellouch, and M. Neubert, *Dispersive bounds on the shape of $\overline{B} \to D^{(*)} \ell \overline{\nu}$ form-factors*, Nucl. Phys. **B530** (1998) 153, arXiv:hep-ph/9712417.

[42] Belle collaboration, W. Dungel *et al.*, *Measurement of the form factors of the decay $B^0 \to D^{*-} \ell^+ \nu_\ell$ and determination of the CKM matrix element $|V_{cb}|$*, Phys. Rev. **D82** (2010) 112007, arXiv:1010.5620.

[43] M. Neubert, Z. Ligeti, and Y. Nir, *QCD sum rule analysis of the subleading Isgur-Wise form-factor $\chi_2(v \cdot v')$*, Phys. Lett. **B301** (1993) 101, arXiv:hep-ph/9209271.

[44] M. Neubert, Z. Ligeti, and Y. Nir, *The subleading Isgur-Wise form-factor $\chi_3(v \cdot v')$ to order α_s in QCD sum rules*, Phys. Rev. **D47** (1993) 5060, arXiv:hep-ph/9212266.

[45] Z. Ligeti, Y. Nir, and M. Neubert, *The subleading Isgur-Wise form-factor $\xi_3(v \cdot v')$ and its implications for the decays $\overline{B} \to D^{(*)} \ell \nu_\tau$*, Phys. Rev. **D49** (1994) 1302, arXiv:hep-ph/9305304.

[46] Belle collaboration, A. Abdesselam *et al.*, *Precise determination of the CKM matrix element $|V_{cb}|$ with $\bar{B}^0 \to D^{*+} \ell^- \bar{\nu}_\ell$ decays with hadronic tagging at Belle*, arXiv:1702.01521.

[47] F. U. Bernlochner, Z. Ligeti, M. Papucci, and D. J. Robinson, *Combined analysis of semileptonic B decays to D and D^*: $R(D^{(*)})$, $|V_{cb}|$, and new physics*, Phys. Rev. **D95** (2017) 115008, arXiv:1703.05330, [Erratum: Phys. Rev.D97,no.5,059902(2018)].

[48] D. Bigi, P. Gambino, and S. Schacht, *$R(D^*)$, $|V_{cb}|$, and the heavy quark symmetry relations between form factors*, JHEP **11** (2017) 061, arXiv:1707.09509.

[49] C. G. Boyd, B. Grinstein, and R. F. Lebed, *Precision corrections to dispersive bounds on form-factors*, Phys. Rev. **D56** (1997) 6895, arXiv:hep-ph/9705252.

[50] S. Jaiswal, S. Nandi, and S. K. Patra, *Extraction of $|V_{cb}|$ from $B \to D^{(*)}\ell\nu_\ell$ and the Standard Model predictions of $R(D^{(*)})$*, JHEP **12** (2017) 060, arXiv:1707.09977.

[51] S. Aoki *et al.*, *Review of lattice results concerning low-energy particle physics*, Eur. Phys. J. **C77** (2017) 112, arXiv:1607.00299.

[52] D. Bigi and P. Gambino, *Revisiting $B \to D\ell\nu$*, Phys. Rev. **D94** (2016) 094008, arXiv:1606.08030.

[53] BaBar collaboration, J. P. Lees *et al.*, *Evidence for an excess of $\bar{B} \to D^{(*)}\tau^-\bar{\nu}_\tau$ decays*, Phys. Rev. Lett. **109** (2012) 101802, arXiv:1205.5442.

[54] BaBar collaboration, J. P. Lees *et al.*, *Measurement of an excess of $\bar{B} \to D^{(*)}\tau^-\bar{\nu}_\tau$ decays and implications for charged Higgs bosons*, Phys. Rev. **D88** (2013) 072012, arXiv:1303.0571.

[55] Belle collaboration, M. Huschle *et al.*, *Measurement of the branching ratio of $\bar{B} \to D^{(*)}\tau^-\bar{\nu}_\tau$ relative to $\bar{B} \to D^{(*)}\ell^-\bar{\nu}_\ell$ decays with hadronic tagging at Belle*, Phys. Rev. **D92** (2015) 072014, arXiv:1507.03233.

[56] Belle collaboration, Y. Sato *et al.*, *Measurement of the branching ratio of $\bar{B}^0 \to D^{*+}\tau^-\bar{\nu}_\tau$ relative to $\bar{B}^0 \to D^{*+}\ell^-\bar{\nu}_\ell$ decays with a semileptonic tagging method*, Phys. Rev. **D94** (2016) 072007, arXiv:1607.07923.

[57] Belle collaboration, S. Hirose *et al.*, *Measurement of the τ lepton polarization and $R(D^*)$ in the decay $\bar{B} \to D^*\tau^-\bar{\nu}_\tau$*, Phys. Rev. Lett. **118** (2017) 211801, arXiv:1612.00529.

[58] Belle collaboration, S. Hirose *et al.*, *Measurement of the τ lepton polarization and $R(D^*)$ in the decay $\bar{B} \to D^*\tau^-\bar{\nu}_\tau$ with one-prong hadronic τ decays at Belle*, Phys. Rev. **D97** (2018) 012004, arXiv:1709.00129.

[59] LHCb collaboration, R. Aaij *et al.*, *Measurement of the ratio of branching fractions $\mathcal{B}(\overline{B}^0 \to D^{*+}\tau^-\overline{\nu}_\tau)/\mathcal{B}(\overline{B}^0 \to D^{*+}\mu^-\overline{\nu}_\mu)$*, Phys. Rev. Lett. **115** (2015) 111803, Publisher's Note ibid. **115** (2015) 159901, arXiv:1506.08614.

[60] R. D. Peccei and H. R. Quinn, *CP conservation in the presence of instantons*, Phys. Rev. Lett. **38** (1977) 1440.

[61] C. Jarlskog, *Commutator of the quark mass matrices in the standard electroweak model and a measure of maximal CP violation*, Phys. Rev. Lett. **55** (1985) 1039.

[62] A. A. Petrov, *Charm mixing in the Standard Model and beyond*, Int. J. Mod. Phys. **A21** (2006) 5686, arXiv:hep-ph/0611361.

[63] E. Golowich, J. Hewett, S. Pakvasa, and A. A. Petrov, *Implications of D^0-$\overline{D}^0$ mixing for new physics*, Phys. Rev. **D76** (2007) 095009, arXiv:0705.3650.

[64] D. Du, *CP violation for neutral charmed meson decays to CP eigenstates*, Eur. Phys. J. **C50** (2007) 579, arXiv:hep-ph/0608313.

[65] M. Gersabeck *et al.*, *On the interplay of direct and indirect CP violation in the charm sector*, J. Phys. **G39** (2012) 045005, arXiv:1111.6515.

[66] LHCb collaboration, R. Aaij *et al.*, *Measurement of CP asymmetry in $D^0 \to K^-K^+$ and $D^0 \to \pi^-\pi^+$ decays*, JHEP **07** (2014) 041, arXiv:1405.2797.

[67] LHCb collaboration, R. Aaij *et al.*, *Measurement of the difference of time-integrated CP asymmetries in $D^0 \to K^-K^+$ and $D^0 \to \pi^-\pi^+$ decays*, Phys. Rev. Lett. **116** (2016) 191601, arXiv:1602.03160.

[68] L. Evans and P. Bryant, *LHC machine*, JINST **3** (2008) S08001.

[69] E. Mobs, *The CERN accelerator complex. Complexe des accélérateurs du CERN*, https://cds. cern. ch/record/2197559 (2016), General Photo.

[70] LHCb collaboration, A. A. Alves Jr. *et al.*, *The LHCb detector at the LHC*, JINST **3** (2008) S08005.

[71] LHCb collaboration, R. Aaij *et al.*, *Measurement of the b-quark production cross-section in 7 and 13 TeV pp collisions*, Phys. Rev. Lett. **118** (2017) 052002, Erratum ibid. **119** (2017) 169901, arXiv:1612.05140.

[72] LHCb collaboration, R. Aaij *et al.*, *Prompt charm production in pp collisions at* $\sqrt{s} = 7$ *TeV*, Nucl. Phys. **B871** (2013) 1, arXiv:1302.2864.

[73] LHCb collaboration, R. Aaij *et al.*, *Measurements of prompt charm production cross-sections in pp collisions at* $\sqrt{s} = 13$ *TeV*, JHEP **03** (2016) 159, Erratum ibid. **09** (2016) 013, Erratum ibid. **05** (2017) 074, arXiv:1510.01707.

[74] F. Follin and D. Jacquet, *Implementation and experience with luminosity levelling with offset beam*, in *Proceedings, ICFA Mini-Workshop on Beam-Beam Effects in Hadron Colliders (BB2013): CERN, Geneva, Switzerland, March 18-22 2013*, pp. 183–187, 2014. arXiv:1410.3667. doi: 10.5170/CERN-2014-004.183.

[75] LHCb collaboration, *LHCb VELO (VErtex LOcator): Technical Design Report*, CERN-LHCC-2001-011.

[76] R. Aaij *et al.*, *Performance of the LHCb Vertex Locator*, JINST **9** (2014) P09007, arXiv:1405.7808.

[77] LHCb collaboration, *LHCb inner tracker: Technical Design Report*, CERN-LHCC-2002-029.

[78] LHCb collaboration, *LHCb outer tracker: Technical Design Report*, CERN-LHCC-2001-024.

[79] LHCb, R. Aaij *et al.*, *LHCb detector performance*, Int. J. Mod. Phys. **A30** (2015) 1530022, arXiv:1412.6352.

[80] LHCb collaboration, *LHCb RICH: Technical Design Report*, CERN-LHCC-2000-037.

[81] LHCb RICH Group, M. Adinolfi *et al.*, *Performance of the LHCb RICH detector at the LHC*, Eur. Phys. J. **C73** (2013) 2431, arXiv:1211.6759.

[82] LHCb collaboration, *LHCb calorimeters: Technical Design Report*, CERN-LHCC-2000-036.

[83] LHCb collaboration, *LHCb muon system: Technical Design Report*, CERN-LHCC-2001-010.

[84] F. Archilli *et al.*, *Performance of the Muon Identification at LHCb*, JINST **8** (2013) P10020, arXiv:1306.0249.

[85] LHCb collaboration, *LHCb trigger system: Technical Design Report*, CERN-LHCC-2003-031.

[86] R. Fruhwirth, *Application of Kalman filtering to track and vertex fitting*, Nucl. Instrum. Meth. **A262** (1987) 444.

[87] R. Aaij *et al.*, *Tesla : an application for real-time data analysis in High Energy Physics*, Comput. Phys. Commun. **208** (2016) 35.

[88] LHCb collaboration, R. Aaij *et al.*, *Study of* $B^0 \to D^{*-}\pi^+\pi^-\pi^+$ *and* $B^0 \to D^{*-}K^+\pi^-\pi^+$ *decays*, Phys. Rev. **D87** (2013) 092001, arXiv:1303.6861.

[89] BaBar collaboration, J. P. Lees *et al.*, *Measurement of the* $B^0 \to D^{*-}\pi^+\pi^-\pi^+$ *branching fraction*, Phys. Rev. **D94** (2016) 091101, arXiv:1609.06802.

[90] Belle collaboration, G. Majumder *et al.*, *Observation of* $B^0 \to D^{*-}(5\pi)^+$, $B^+ \to D^{*-}(4\pi)^{++}$ *and* $B^+ \to \overline{D}^{*0}(5\pi)^+$, Phys. Rev. **D70** (2004) 111103, arXiv:hep-ex/0409008.

[91] Z. Was, *TAUOLA for simulation of tau decay and production: perspectives for precision low energy and LHC applications*, Nucl. Phys. Proc. Suppl. **218** (2011) 249, arXiv:1101.1652.

[92] N. Davidson *et al.*, *Universal interface of TAUOLA technical and physics documentation*, Comput. Phys. Commun. **183** (2012) 821, arXiv:1002.0543.

[93] I. M. Nugent *et al.*, *Resonance chiral Lagrangian currents and experimental data for* $\tau^- \to \pi^-\pi^-\pi^+\nu_\tau$, Phys. Rev. **D88** (2013) 093012, arXiv:1310.1053.

[94] BaBar collaboration, I. M. Nugent, *Invariant mass spectra of* $\tau^- \to h^-h^-h^+\nu_\tau$ *decays*, Nucl. Phys. Proc. Suppl. **253-255** (2014) 38, arXiv:1301.7105.

[95] D. Scora and N. Isgur, *Semileptonic meson decays in the quark model: An update*, Phys. Rev. **D52** (1995) 2783, arXiv:hep-ph/9503486.

[96] A. Puig, *The LHCb trigger in 2011 and 2012*, LHCb-PUB-2014-046.

[97] D. Cote, S. Brunet, P. Taras, and B. Viaud, *Reweighting of the form-factors in exclusive $B \to X\ell\nu_\ell$ decays*, Eur. Phys. J. **C38** (2004) 105, arXiv:hep-ex/0409046.

[98] L. Anderlini *et al.*, *The PIDCalib package*, Tech. Rep. LHCb-PUB-2016-021. CERN-LHCb-PUB-2016-021, CERN, Geneva, Jul, 2016.

[99] T. Skwarnicki, *A study of the radiative cascade transitions between the Upsilon-prime and Upsilon resonances*, PhD thesis, Institute of Nuclear Physics, Krakow, 1986, DESY-F31-86-02.

[100] K. S. Cranmer, *Kernel estimation in high-energy physics*, Comput. Phys. Commun. **136** (2001) 198, arXiv:hep-ex/0011057.

[101] D. J. Lange, *The EvtGen particle decay simulation package*, Nucl. Instrum. Meth. **A462** (2001) 152.

[102] LHCb collaboration, R. Aaij *et al.*, *Measurement of the ratio of the $\mathcal{B}(B^0 \to D^{*-}\tau^+\nu_\tau)$ and $\mathcal{B}(B^0 \to D^{*-}\mu^+\nu_\mu)$ branching fractions using three-prong τ-lepton decays*, Phys. Rev. Lett. **120** (2018) 171802, arXiv:1708.08856.

[103] LHCb collaboration, R. Aaij *et al.*, *Test of lepton flavor universality by the measurement of the $B^0 \to D^{*-}\tau^+\nu_\tau$ branching fraction using three-prong τ decays*, Phys. Rev. **D97** (2018) 072013, arXiv:1711.02505.

[104] LHCb collaboration, R. Aaij *et al.*, *Measurement of the $D^\pm$ production asymmetry in 7 TeV pp collisions*, Phys. Lett. **B718** (2013) 902, arXiv:1210.4112.

[105] W. D. Hulsbergen, *Decay chain fitting with a Kalman filter*, Nucl. Instrum. Meth. **A552** (2005) 566, arXiv:physics/0503191.

[106] M. Pivk and F. R. Le Diberder, *sPlot: A statistical tool to unfold data distributions*, Nucl. Instrum. Meth. **A555** (2005) 356, arXiv:physics/0402083.

[107] G. A. Cowan, D. C. Craik, and M. D. Needham, *RapidSim: an application for the fast simulation of heavy-quark hadron decays*, Comput. Phys. Commun. **214** (2017) 239, arXiv:1612.07489.

[108] N. L. Johnson, *Systems of frequency curves generated by methods of translation*, Biometrika **36** (1949) 149.

[109] ARGUS, H. Albrecht *et al.*, *Measurement of the polarization in the decay B —> J / psi K**, Phys. Lett. **B340** (1994) 217.

[110] LHCb collaboration, R. Aaij *et al.*, *Updated determination of D^0-$\overline{D}^0$ mixing and CP violation parameters with $D^0 \to K^+\pi^-$ decays*, Phys. Rev. **D97** (2018) 031101, arXiv:1712.03220.

[111] LHCb collaboration, R. Aaij *et al.*, *Measurement of B^0, B_s^0, B^+ and Λ_b^0 production asymmetries in 7 and 8 TeV pp collisions*, Phys. Lett. **B774** (2017) 139, arXiv:1703.08464.

[112] LHCb collaboration, R. Aaij *et al.*, *Measurement of the charm-mixing parameter y_{CP}*, Phys. Rev. Lett. **122** (2019) 011802, arXiv:1810.06874.

[113] LHCb collaboration, R. Aaij *et al.*, *Measurement of mixing and CP violation parameters in two-body charm decays*, JHEP **04** (2012) 129, arXiv:1112.4698.

[114] LHCb collaboration, R. Aaij *et al.*, *Measurement of indirect CP asymmetries in $D^0 \to K^-K^+$ and $D^0 \to \pi^-\pi^+$ decays*, JHEP **04** (2015) 043, arXiv:1501.06777.

[115] LHCb collaboration, R. Aaij *et al.*, *Measurement of the CP violation parameter A_Γ in $D^0 \to K^+K^-$ and $D^0 \to \pi^+\pi^-$ decays*, Phys. Rev. Lett. **118** (2017) 261803, arXiv:1702.06490.